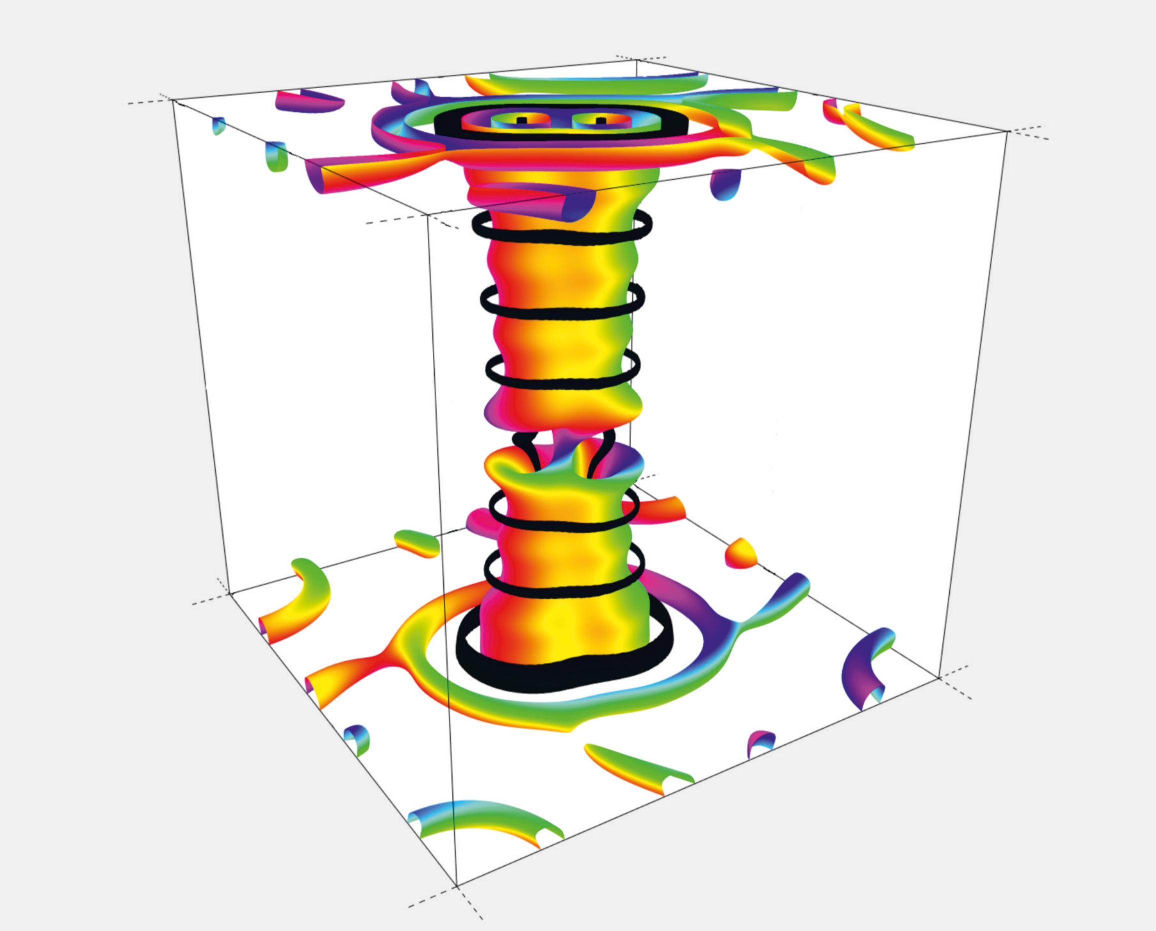

Diversity of chiral magnetic solitons

Vladyslav Kuchkin

Information
Band / Volume 88
ISBN 978-3-95806-665-6

Mitglied der Helmholtz-Gemeinschaft

JÜLICH
Forschungszentrum

Schriften des Forschungszentrums Jülich
Reihe Information / Information Band / Volume 88

Forschungszentrum Jülich GmbH
Peter Grünberg Institut (PGI)
Quanten-Theorie der Materialien (PGI-1/IAS-1)

Diversity of chiral magnetic solitons

Vladyslav Kuchkin

Schriften des Forschungszentrums Jülich
Reihe Information / Information Band / Volume 88

ISSN 1866-1777 ISBN 978-3-95806-665-6

Bibliografische Information der Deutschen Nationalbibliothek.
Die Deutsche Nationalbibliothek verzeichnet diese Publikation in der
Deutschen Nationalbibliografie; detaillierte Bibliografische Daten
sind im Internet über http://dnb.d-nb.de abrufbar.

Herausgeber und Vertrieb:	Forschungszentrum Jülich GmbH Zentralbibliothek, Verlag 52425 Jülich Tel.: +49 2461 61-5368 Fax: +49 2461 61-6103 zb-publikation@fz-juelich.de www.fz-juelich.de/zb
Umschlaggestaltung:	Grafische Medien, Forschungszentrum Jülich GmbH
Druck:	Grafische Medien, Forschungszentrum Jülich GmbH
Copyright:	Forschungszentrum Jülich 2022

Schriften des Forschungszentrums Jülich
Reihe Information / Information, Band / Volume 88

D 82 (Diss. RWTH Aachen University, 2022)

ISSN 1866-1777
ISBN 978-3-95806-665-6

Vollständig frei verfügbar über das Publikationsportal des Forschungszentrums Jülich (JuSER)
unter www.fz-juelich.de/zb/openaccess.

Abstract

This thesis is devoted to the theoretical study of *chiral ferromagnets* [1]. The main properties of any ferromagnet are usually defined by the competition of Heisenberg exchange interaction with the other energy terms, e.g., anisotropy or demagnetizing fields. In the case of chiral ferromagnets, the key energy term is the Dzyaloshinskii-Moria interaction (DMI). The interplay between exchange interaction and DMI leads to many exciting properties distinguishing chiral magnets from many other magnetic systems. One of the most thrilling properties of chiral magnets is their ability to host an extraordinary wide diversity of stable well-localized vortex-like spin textures, also known as *skyrmions* (Sk). They are magnetic solitons – solutions of the corresponding non-linear model of chiral magnet [2] which is akin to a similar model in nuclear physics developed by Tony Skyrme [3]. Currently, Sks are under intensive study by different scientific groups and are the "hot topic" of modern magnetism. The high attention to Sks is heated up by their possible utilization in computational devices. For instance, Sks have excellent potential for application in neuromorphic and reservoir computing. Additionally, investigation of Sks is of academic interest, allowing us to extend our knowledge about non-linear models and solitons in general.

In this work, I study the various properties of chiral magnetic Sks by combining well-established analytical methods and different advanced numerical methods. A significant part of the presented work is devoted to investigating the static properties of Sks, such as stability regions, inter-solitonic interactions, and homotopy transformations. The most intriguing part of these studies is related to the role of the tilted magnetic field on Sks. As it turned out, one can learn a lot about Sks in experimental and theoretical studies by manipulating the direction of the external magnetic field. Among the dynamic properties of Sks, I pay the most attention to the current-induced motion and thermal generation of Sks. The results for Sk motion induced by electric current are based on a quite general analysis of the symmetry and topology of Sks, and thus are general for all possible solutions allowed by this model. In the chapter devoted to the thermal generation of Sks, I present an approach for the generation of a new type of Sks solution which has not been experimentally observed so far. The presented approach allows moving further in constructing more complicated magnetic textures and can be thought of as a guideline for experimental verification of the theoretical prediction. Besides the static and dynamic properties of magnetic solitons in chiral magnets, in this thesis, I have also considered other interesting problems related to the properties of chiral magnets themselves. The first one is related to the problem of an analytically solvable model for the dynamics of the cone phase in the presence of an electric current. The second problem is related to the equilibrium magnetization distribution when the free sample boundaries are taken into account. I found that under certain conditions, this problem has a fully analytical

solution. The final part of my thesis is related to a new type of 3D solitons in chiral magnets. The discovery of these solutions, to a certain extent, was motivated by the analysis of homotopies of 2D Sk solutions. However, the central results of this chapter can be obtained even without referring to 2D systems. I strongly believe that the results presented in thesis will motivate further study of chiral magnets and trigger other researchers' interest in this topic.

Kurzzusammenfassung

Diese Dissertation widmet sich der theoretischen Untersuchung von *chiralen Ferromagneten* [1]. Die Haupteigenschaften jedes Ferromagneten werden normalerweise durch die Konkurrenz der Heisenberg-Austauschwechselwirkung mit den anderen Energietermen definiert, z. B. Anisotropie oder entmagnetisierende Felder. Im Fall von chiralen Ferromagneten ist der entscheidende Energieterm die Dzyaloshinskii-Moria-Wechselwirkung (DMI). Das Zusammenspiel zwischen Austauschwechselwirkung und DMI führt zu vielen spannenden Eigenschaften, die chirale Magnete von vielen anderen magnetischen Systemen unterscheiden. Eine der aufregendsten Eigenschaften chiraler Magnete ist ihre Fähigkeit, eine außerordentlich große Vielfalt an stabilen, gut lokalisierten, wirbelartigen Spintexturen zu beherbergen, die auch als *Skyrmionen* (Sk) bekannt sind. Sie sind magnetische Solitonen – Lösungen des entsprechenden nichtlinearen Modells des chiralen Magneten [2], das einem ähnlichen Modell in der Kernphysik ähnelt, das von Tony Skyrme [3] entwickelt wurde. Derzeit werden Sks von verschiedenen wissenschaftlichen Gruppen intensiv untersucht und sind das „heiße Thema“ des modernen Magnetismus. Die hohe Aufmerksamkeit für Sks wird durch ihre mögliche Verwendung in Computergeräten aufgeheizt. Beispielsweise haben Sks ein hervorragendes Potenzial für die Anwendung im neuromorphen und Reservoir-Computing. Darüber hinaus ist die Untersuchung von Sks von akademischem Interesse, was es uns ermöglicht, unser Wissen über nichtlineare Modelle und Solitonen im Allgemeinen zu erweitern.

In dieser Arbeit untersuche ich die verschiedenen Eigenschaften chiraler magnetischer Sks, indem ich etablierte analytische Methoden und verschiedene fortschrittliche numerische Methoden kombiniere. Ein bedeutender Teil der vorgestellten Arbeit widmet sich der Untersuchung der statischen Eigenschaften von Sks, wie z. B. Stabilitätsregionen, intersolitonische Wechselwirkungen und Homotopietransformationen. Der faszinierendste Teil dieser Studien bezieht sich auf die Rolle des geneigten Magnetfelds auf Sks. Wie sich herausstellte, kann man in experimentellen und theoretischen Studien viel über Sks lernen, indem man die Richtung des externen Magnetfelds manipuliert. Unter den dynamischen Eigenschaften von Sks widme ich der strominduzierten Bewegung und thermischen Erzeugung von Sks die größte Aufmerksamkeit. Die Ergebnisse für die durch elektrischen Strom induzierte Sk-Bewegung basieren auf einer ziemlich allgemeinen Analyse der Symmetrie und Topologie von Sks und sind daher allgemein für alle möglichen Lösungen, die dieses Modell zulässt. Im Kapitel zur thermischen Erzeugung von Sks stelle ich einen Ansatz zur Erzeugung einer neuartigen Sks-Lösung vor, der bisher noch nicht experimentell beobachtet wurde. Der vorgestellte Ansatz ermöglicht einen weiteren Fortschritt bei der Konstruktion komplizierterer magnetischer Texturen und kann als Richtlinie für die experimentelle Überprüfung der theoretischen Vorhersage angesehen werden. Neben den statischen und dynamischen Eigenschaften magnetischer Solitonen in chiralen Mag-

neten habe ich in dieser Dissertation auch andere interessante Probleme im Zusammenhang mit den Eigenschaften chiraler Magnete selbst betrachtet. Die erste betrifft das Problem eines analytisch lösbaren Modells für die Dynamik der Kegelphase in Gegenwart eines elektrischen Stroms. Das zweite Problem hängt mit der Gleichgewichtsmagnetisierungsverteilung zusammen, wenn die freien Probengrenzen berücksichtigt werden. Ich habe festgestellt, dass dieses Problem unter bestimmten Bedingungen eine vollständig analytische Lösung hat. Der letzte Teil meiner Doktorarbeit befasst sich mit einer neuen Art von 3D-Solitonen in chiralen Magneten. Die Entdeckung dieser Lösungen wurde bis zu einem gewissen Grad durch die Analyse von Homotopien von 2D-Sk-Lösungen motiviert. Die zentralen Ergebnisse dieses Kapitels lassen sich aber auch ohne Bezugnahme auf 2D-Systeme gewinnen. Ich bin fest davon überzeugt, dass die in der Dissertation präsentierten Ergebnisse weitere Untersuchungen zu chiralen Magneten anregen und das Interesse anderer Forscher an diesem Thema wecken werden.

Acknowledgements

First of all I am grateful to Deutsche Forschungsgemeinschaft (DFG) for the financial support through SPP 2137 “Skyrmionic” Grant Nos. KI 2078/1-1. I would like to thank Prof. Stefan Blügel for providing me with the excellent opportunity to research and write my Dissertation at the Forschungszentrum Jülich. His inspirational advice, in many ways, have influenced the research I have been doing.

The biggest acknowledgement deserves my scientific advisor Dr. Nikolai Kiselev. Endless scientific discussions of various subjects in physics and his enormous support in my undertakings have been very fruitful and changed my view on modern magnetism. I have learnt a lot.

I would like to thank Prof. Bernd Schroers for accepting to be the second referee of my thesis for the examination.

Next, I would like to thank a large number of people I have been collaborating with. I am thankful to Dr. Philipp Rybakov, Dr. Pavel Bessarab, Prof. Bernd Schroers, Dr. Bruno Barton-Singer, Dr. Andrii Savchenko, Dr. Juba Bouaziz and Dr. Moritz Salermann for highly professional help in solving different problems I have met during my work.

Proofreaders of my thesis were Dr. Sebastián A. Díaz and Thórný Sigurjónsdóttir to whom I am very grateful.

I have had many administrative issues working at the Forschungszentrum Jülich, and I am thankful to Mrs. Ute Winkler for resolving all of them.

Finally, I am grateful to my family and friends for their diversified support.

Contents

List of Figures

List of Tables

Nomenclature

2π-DW	2π-domain wall
BP	Bloch point
CA	chiral antikink
CD	chiral droplet
CK	chiral kink
DDI	dipole-dipole interaction
DMI	Dzyaloschinskii-Moria interaction
DW	domain wall
EL	Euler-Lagrange
FM	ferromagnet
GNEB	geodesic nudge elastic band
LLG	Landau-Lifshitz-Gilbert
MC	Monte-Carlo
MEP	minimum energy path
PBC	periodic boundary condition
PDE	partial differential equation
Sk	skyrmion
Ql	quasilinearization

Introduction

Magnetic materials have been attracting people's attention since ancient times. One of the first known facts of utilizing magnets is the discovery of the compass in China in 4th-century BC. A significant amount of time has passed until people found more efficient applications for magnetic materials. The critical moment in the history of magnetism is the year 1819 when Oersted revealed the connection between electrical and magnetic fields. The discovery of Oersted gave a strong impetus to the study of magnetic phenomena. For instance, the Biot-Savart law revealed the connection between electric current and generated magnetic field. Many other fundamental laws have been discovered as well. Many of them still remain the basis of electromagnetism until now. The most complete and elegant version of the electromagnetic theory that we still use today was derived by Maxwell [4]. Maxwell equations have many essential consequences that influenced not only the development of magnetism but also other branches of physics such as quantum mechanics and relativistic physics.

While the Maxwell equations perfectly describe electromagnetic phenomena on the macroscopic scale, the theory developed in 1935 by Landau and Lifshits [5] has allowed the description of magnetic phenomena to go to the microscopic level. Up to now, the Landau-Lifshitz-Gilbert (LLG) equation describing the dynamics of magnetic moments remains the primary tool of *micromagnetism*. Accompanied by the Maxwell equations, the LLG equation allows us to describe all of the most essential properties of magnetic materials. Although we know that one can understand the origin of magnetic phenomena only in terms of quantum physics, the micromagnetic theory that belongs to classical physics can still be effectively applied to describe the phenomena observed in micro and nanoscale magnetic systems. Micromagnetism is often called a phenomenological theory. It means that it contains certain constants that can not be derived or explained in terms of micromagnetic theory itself. The density-functional theory [6, 7] often plays the role of a bridge between the quantum theory of magnetism and the classical micromagnetic theory. Interestingly, pure mathematical theories such as group theory [8] and symmetries [9] are widely used in micromagnetics, for instance, when discussing magnetic crystals of various crystallographic classes.

Magnetic materials have found application in quite diverse technologies from mechanical systems to electric engines, microelectronics, computational, and data storage devices. The discovery of the giant magneto-resistance effect by Peter Grünberg [10] and Albert Fert [11] has revolutionized data-storage technology. Until now, most of the hard disk drives in all big data centers use the advantages of this effect. There were also many attempts to combine semiconducting electronics and magnetic materials to build computational units of a new type. The prominent example is magnetic bubble memory chips [12], which were popular at the beginning of 1970 but fail in competition with semiconducting devices. With the discovery of magnetic skyrmions – nanoscale magnetic solitons in chiral magnets, the concept similar to bubble memory devices got a second wind [13, 14]. Additionally, skyrmions are considered as potentially attractive objects for a relatively new and conceptually different approach known as neuromorphic calculation [15].

The magnetic materials I studied throughout the thesis are called chiral magnets. They have been intensively studied for almost 40 years with the theoretical work of Bogdanov, and Yablonskiui [2], which predicted the stability of topological solitons in these materials. A few years later, Bogdanov and Hubert [16] discovered in this model a new type of solitons now known as $k\pi$-skyrmions. For almost 20 years, these solutions were the only ones people hoped to observe in experiments. Recent theoretical works of Rybakov and Kiselev [17] and Foster with coworkers [18] have demonstrated a new class of non-axially symmetric solitons, called skyrmion bags. These new solutions were a big step forward from $k\pi$-skyrmions because they allowed obtaining solitons with arbitrary topological charge, Q. In many ways, these solutions inspired me in my study of chiral skyrmions and have led to the discovery of another type of solutions – skyrmions with chiral kinks [19]. The study of the skyrmion diversity and the static and dynamic properties of these skyrmions are the main subjects of my thesis.

An essential aspect of chiral skyrmions is related to specific materials in which they can be experimentally observed. Many magnetic systems such as bulk crystals, free-standing films, and multilayers can be attributed to chiral magnets. The first two types belong to 3D systems, and the last one corresponds to quasi 2D systems. The most studied materials of 3D chiral magnets are different Si- and Ge-based alloys with B20 crystal symmetry, such as MnSi [20, 21], FeGe [22, 23, 24], $Mn_{1-x}Fe_xGe$ [25], $Mn_{1-x}Fe_xSi$ [26] and $Fe_{1-x}Co_xSi$ [27] or helimagnetic insulator Cu_2OsO_3 [28]. Experimentally these materials, especially bulk crystals, are often studied by neutron diffraction techniques. Direct imaging of magnetic skyrmions is often performed by transmission electron microscopy in Lorentz mode or by means of the off-axis electron holography technique. The latter one allows reconstruction of the magnetic induction field and the analyzing of the inner structure of magnetic skyrmions.

Utilizing magnetic skyrmions as information carriers or for calculation purposes represent the practical part of the motivation to their study. However, there is an additional pure academic interest in skyrmions caused mainly by their topological properties. Generally, the model of the chiral magnet to some extent represents a unique physical model. In particular, the discussed below diversity of different solitons in chiral magnets is not common for most of the other physical models. A similar variety of particles is demonstrated, perhaps, only by the model of elementary particles but a strict theoretical model describing all these particles is absent. That is not the case for chiral skyrmions where such a model is known. Although particle physics is a quantum model and magnetism is a classical one, one still can not deny a rich diversity of localized solitons which is common for both models. The topological charge conservation law plays a role, similar to conservation laws of various charges in particle physics. The aforementioned ideas of similarity between the model of elementary particles and chiral magnetic skyrmions are fascinating enough. Nevertheless, in my thesis, I do not discuss these similarities. Instead, I mainly concentrate on exploring 2D and 3D skyrmions, which can help advance our understanding of non-linear models in general.

The thesis is organized as follows. In the beginning, I briefly introduce the chiral magnet model and show the primary methods used to study it. I use a combination of various analytical and advanced numerical methods. The interconnection between chapters containing the results of my work is presented in the diagram below. The arrow directions show the inheritance and interconnections of the chapters. The chapter in which I discuss the diversity of skyrmions represents the central part of the work, which opens many questions I address in further chapters. Together with chapters placed in red blocks, it represents the study of 2D systems of chiral magnets. Chapters in green blocks relate to 3D chiral magnets

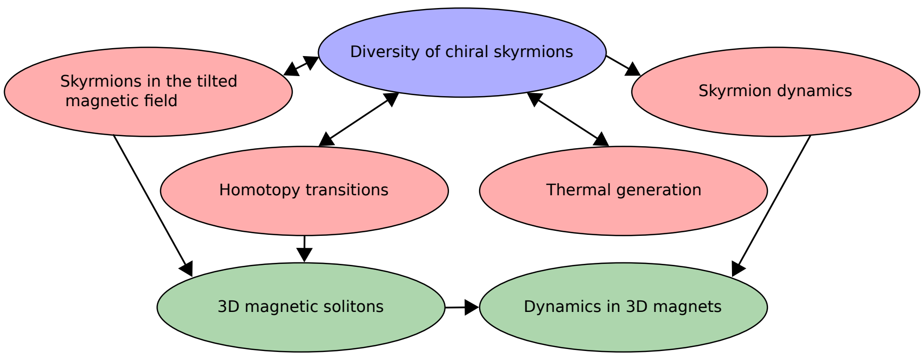

1 Model and methods

This Chapter contains the description of the model of the chiral magnet and the methods used in the thesis. **Section** 1.1 contains the description of atomistic (discrete) and micromagnetic (continual) models of chiral ferromagnet as well as the approach for the comparison and validation of the results obtained with both models. Typically, the solution of a micromagnetic problem leads to the Euler-Lagrange (EL) equations and the LLG equation employed to study the statistic and dynamical properties of magnetic solitons. I provide the general form of the EL and LLG equations for chiral magnets in a separate section, **Section** 1.2, that also includes the derivation of the Thiele equation and basic concepts of homotopy classification of localized solutions. At the end of **Section** 1.2, I also discuss the Bogomol'nyi point – the case corresponding to a particular value of external field and anisotropy at which the model of chiral magnet becomes analytically solvable, and Sk solutions can be written in very general form employing complex value functions. **Section** 1.3 includes a description of the methods used for the numerical solution of EL and LLG equations and the method for direct energy minimization. I also provide the description for the high accuracy quasilinearization (Ql) method, which I will use later as a reference method for axisymmetric skyrmion solutions. This Section also describes the implementation of a high order accuracy finite difference scheme in Mumax – the open-source software for micromagnetic simulations. These high accuracy codes are parts of my research. The details of the methods and their implementation are provided in the Appendices.

1.1 Model

In this Section, I describe atomistic and micromagnetic models of the chiral magnet. I provide the general form of the model Hamiltonian and a brief description of different energy terms. Since the two models are equally often used throughout this thesis, I discuss the criteria for the transition between the models and approach, allowing a comparison of the results obtained in both models.

1.1.1 Atomistic model

A classical spin lattice model of the chiral magnet, to which I refer to as an *atomistic model*, is described by the Hamiltonian consisting of the Heisenberg exchange interaction, DMI, the magnetic anisotropy, and the Zeeman interaction:

$$H_{\mathrm{tot}} = H_{\mathrm{ex}} + H_{\mathrm{dmi}} + H_{\mathrm{anis}} + H_{\mathrm{Zeeman}}. \tag{1.1}$$

In most magnetic systems, the leading term is the Heisenberg exchange interaction,

$$H_{\mathrm{ex}} = \sum_{i,j} J_{i,j} \boldsymbol{S}_i \cdot \boldsymbol{S}_j, \tag{1.2}$$

where $\boldsymbol{S}_i$ and $\boldsymbol{S}_j$ are the unit vectors of the magnetic moments on the neighbouring lattice sites i and j. In the simplest model only the nearest neighbour spins i, j are taken into account. In general the lattice spins may have an arbitrary symmetry. For definiteness, everywhere below I consider the case of simple cubic lattice only with the lattice constant a. In isotropic magnets, the Heisenberg exchange coupling constant is identical for any interacting pair of spins, $J_{i,j} = J$. The second term in (1.1) corresponding to the DMI interaction

$$H_{\mathrm{dmi}} = \sum_{i,j} \boldsymbol{D}_{i,j} \cdot \boldsymbol{S}_i \times \boldsymbol{S}_j, \tag{1.3}$$

where $\boldsymbol{D}_{i,j} = D_{i,j} \hat{\boldsymbol{r}}_{ij}$ is the Dzyaloshinskii-Moriya vectors, $\hat{\boldsymbol{r}}_{ij}$ is the unit vector between sites i and j. In the case of isotropic DMI, $D_{i,j} = D$.

The general form for easy-plane/easy-axis anisotropy term in the Hamiltonian (1.1) is

$$H_{\mathrm{anis}} = -\sum_{i} K \left(\boldsymbol{S}_i \cdot \boldsymbol{e}_{\mathrm{z}}\right)^2. \tag{1.4}$$

For $K > 0$, it corresponds to easy-axis anisotropy, and for $K < 0$, it represents the easy-plane anisotropy.

The interaction with an external magnetic field $\boldsymbol{B}$ is presented by the Zeeman energy term,

$$H_{\mathrm{Zeeman}} = -\sum_{i} \mu_{\mathrm{s}} \boldsymbol{B} \cdot \boldsymbol{S}_i, \tag{1.5}$$

where μ_{s} is the absolute value of the magnetic moment assumed to be identical for each site of the lattice.

Since the dipole-dipole interaction (DDI) affects the effects discussed in this thesis on a quantitative level only, I have chosen to ignore it in the following consideration.

1.1.2 Micromagnetic model

When the magnetic moments in the crystal varies slowly between the lattice sites, $\arccos(\boldsymbol{S}_i \cdot \boldsymbol{S}_j) \ll 1$, in many cases it might be useful to use a continuum approximation of a discrete vector field in (1.1). The energy functional for the continuous vector field $\boldsymbol{n} = \boldsymbol{n}(\boldsymbol{r})$ defined in any point of the space inside the sample can be derived from Hamiltonian (1.1) as follows. When the angle between nearest neighbour spins is small, one can expand the discrete Hamiltonian in a Taylor series with respect to a small parameter a. This approach is described quite well in the literature [29, 30]. The corresponding micromagnetic functional containing the first nonzero terms in the expansion can be written as follows,

$$\mathcal{H}_{\mathrm{tot}} = \int_{\Omega} \mathrm{d}\Omega \left(\mathcal{A} \left(\nabla \boldsymbol{n} \right)^2 + w_{\mathrm{dmi}}\left(\boldsymbol{n}\right) - \mathcal{K} n_{\mathrm{z}}^2 - M_{\mathrm{s}} \boldsymbol{B} \cdot \boldsymbol{n} \right), \tag{1.6}$$

where the integration is taken over the whole volume of the sample, Ω. The micromagnetic constant $\mathcal{A}$ represents the Heisenberg exchange, and $\mathcal{K}$ is the micromagnetic anisotropy constant. The saturation magnetization, M_{s} is the averaged magnetic moment per unit volume of the sample. The second integrand in (1.6) is the DMI energy density. Depending on the crystal symmetry, the term $w_{\mathrm{dmi}}(\mathbf{n})$ has different representations in terms of the so-called Lifshitz invariants

$$\Lambda_{i,j}^{k} = n_i \partial_k n_j - n_j \partial_k n_i, \;\; (i,j,k) \in (\mathrm{x}, \mathrm{y}, \mathrm{z}). \tag{1.7}$$

Below I consider three main types of DMI corresponding to C_{nv}, D_n and D_{2d} ($n = 3, 4, 6$) crystallographic point groups [2]. In the case of the 2D model, the micromagnetic DMI energy term in (1.6) is described by the following combination of Lifshitz invariants. For the C_{nv} symmetry favouring Neel-type modulations of magnetization [31, 32, 33], the DMI reads:

$$w_{\mathrm{dmi}}^{\mathrm{N}}\left(\boldsymbol{n}\right) = \mathcal{D}\left(\Lambda_{\mathrm{xz}}^{\mathrm{x}} + \Lambda_{\mathrm{yz}}^{\mathrm{y}}\right). \tag{1.8}$$

For D_n symmetry favouring Bloch-type modulations [24, 27, 34], the DMI term is

$$w_{\mathrm{dmi}}^{\mathrm{B}}\left(\boldsymbol{n}\right) = \mathcal{D}\left(\Lambda_{\mathrm{zy}}^{\mathrm{x}} + \Lambda_{\mathrm{xz}}^{\mathrm{y}}\right). \tag{1.9}$$

For D_{2d} favouring opposite chirality of magnetization in orthogonal directions [35], the DMI term reads,

$$w_{\mathrm{dmi}}^{\mathrm{D}}\left(\boldsymbol{n}\right) = \mathcal{D}\left(\Lambda_{\mathrm{zy}}^{\mathrm{x}} + \Lambda_{\mathrm{zx}}^{\mathrm{y}}\right). \tag{1.10}$$

Depending on the handedness of the crystal, the micromagnetic DMI constant $\mathcal{D}$ can be positive or negative. By default I consider the case of $\mathcal{D} > 0$ and $w_{\mathrm{dmi}}(\boldsymbol{n}) = w_{\mathrm{dmi}}^{\mathrm{B}}(\boldsymbol{n})$, which in the most general case of 3D systems can be written in more compact form:

$$w_{\mathrm{dmi}}^{\mathrm{B}}(\boldsymbol{n}) = \mathcal{D}\left(\Lambda_{\mathrm{zy}}^{\mathrm{x}} + \Lambda_{\mathrm{xz}}^{\mathrm{y}} + \Lambda_{\mathrm{yx}}^{\mathrm{z}}\right) = \mathcal{D}\boldsymbol{n} \cdot \nabla \times \boldsymbol{n}. \tag{1.11}$$

Note, the results presented in the thesis remain valid for DMI of type (1.8) and (1.10) after performing the corresponding transformation of $\boldsymbol{n}$ and $\boldsymbol{r}$. Moreover, some of the results are valid for the crystals of C_n and S_4 symmetries [2].

While atomistic model (1.1) is used mainly for numerical simulation, the micromagnetic functional (1.6) is more suited for analytical study. When the aim is to find statically stable solutions, the strategy is to find such a distribution of the discrete vector field $\boldsymbol{S}_i$ or continuous vector field $\boldsymbol{n}(\boldsymbol{r})$ that corresponds to a local or the global energy minima – minimize the corresponding Hamiltonian. The comparison of the results requires an appropriate unit conversion, first of all, for the coupling constants. Since one can derive the micromagnetic model from the atomistic model, the ratio between coupling constants depends on the number of neighbouring spins taken into account in the atomistic parent model. In the case of nearest neighbours, only the micromagnetic and atomistic model constants are related by the expressions provided in Table (1.1).

Table 1.1: Coefficients in atomistic and micromagnetic models

Space	**Exchange stiffnes**	**DMI coefficient**	**Magnetization saturation**
1D	$\mathcal{A} = Ja/2$	$\mathcal{D} = D$	$M_{\mathrm{s}} = \mu_{\mathrm{s}}/a$
2D	$\mathcal{A} = J/2$	$\mathcal{D} = D/a$	$M_{\mathrm{s}} = \mu_{\mathrm{s}}/a^2$
3D	$\mathcal{A} = J/2a$	$\mathcal{D} = D/a^2$	$M_{\mathrm{s}} = \mu_{\mathrm{s}}/a^3$

1.2 Energy minimization and equations of motion

1.2.1 Euler-Lagrange equations

The advantage of the micromagnetic continuum model is that one can use the powerful and well-established calculus of variations theory and obtain analytical solutions. According to the calculus of variations, the sufficient condition for the distribution $\boldsymbol{n}$ to be a local minimum of the micromagnetic energy functional can be written as variational equation $\delta\mathcal{H}_{\mathrm{tot}} = 0$. To fulfill the normalization condition $|\boldsymbol{n}| = 1$, it is convenient to parametrize magnetization $\boldsymbol{n}$ by the polar, Θ, and azimuthal, Φ angles in a spherical coordinate system:

$$\boldsymbol{n} = (\sin\Theta\cos\Phi, \sin\Theta\sin\Phi, \cos\Theta)^{\mathrm{T}}. \tag{1.12}$$

In this case, for the Hamiltonian (1.6) with the DMI term as in (1.11) one gets the following EL equations, [36]

$$\begin{cases}\mathcal{A}\left((\nabla\Phi)^2\sin 2\Theta-2\triangle\Theta\right)-2\mathcal{D}\left(\boldsymbol{n}\cdot\nabla\Phi\right)\sin\Theta+\mathcal{K}\sin 2\Theta\\ +M_{\mathrm{s}}\left(B_{\mathrm{z}}\sin\Theta-n_{\mathrm{z}}B_{\mathrm{y}}\sin\Phi-n_{\mathrm{z}}B_{\mathrm{x}}\cos\Phi\right)=0,\\ -\mathcal{A}\left(2\left(\nabla\Theta\cdot\nabla\Phi\right)\cos\Theta+\sin\Theta\triangle\Phi\right)\sin\Theta+\mathcal{D}\left(\boldsymbol{n}\cdot\nabla\Theta\right)\sin\Theta\\ +M_{\mathrm{s}}\left(B_{\mathrm{y}}n_{\mathrm{x}}-B_{\mathrm{x}}n_{\mathrm{y}}\right)=0.\end{cases}\tag{1.13}$$

In the case of a geometrically confined system, for instance, the plate of finite thickness, the solution also should satisfy the following boundary conditions,

$$\begin{cases}\left.\dfrac{\partial\left(w_{\mathrm{ex}}+w_{\mathrm{dmi}}\right)}{\partial\left(\partial_{\perp}\Theta\right)}\right|_{\boldsymbol{r}\in\partial\Omega}=0,\\ \left.\dfrac{\partial\left(w_{\mathrm{ex}}+w_{\mathrm{dmi}}\right)}{\partial\left(\partial_{\perp}\Phi\right)}\right|_{\boldsymbol{r}\in\partial\Omega}=0,\end{cases}\tag{1.14}$$

where $\partial_{\perp}$ denotes the derivative taken in the direction of outer normal to the sample boundary, $\partial\Omega$.

For arbitrary $\mathcal{A}$, $\mathcal{D}$, $\mathcal{K}$, and $\boldsymbol{B}$, the system of EL equations (1.13) can be solved analytically only in a few exceptional cases. One of them is the conical spin spiral solution, representing the global energy minima for bulk crystal at a nonzero external magnetic field. For $B_{\mathrm{x}}=B_{\mathrm{y}}=0$ it can be written as following

$$\Theta=\Theta_{\mathrm{c}}=\arccos\left(\frac{M_{\mathrm{s}}B_{\mathrm{z}}}{\dfrac{\mathcal{D}^2}{2\mathcal{A}}-2\mathcal{K}}\right),\Phi=\phi_0+z\frac{\mathcal{D}}{2\mathcal{A}},\tag{1.15}$$

where ϕ_0 is an arbitrary cone phase shift angle. At $M_{\mathrm{s}}B_{\mathrm{z}}\geq\dfrac{\mathcal{D}^2}{2\mathcal{A}}-2\mathcal{K}$ this solution transforms into FM state, $\Theta=0$. In the case of $\mathcal{K}=0$, one can introduce the critical field, B_{D}, and equilibrium period of chiral modulations L_{D} defined as follows,

$$B_{\mathrm{D}}=\frac{\mathcal{D}^2}{2M_{\mathrm{s}}\mathcal{A}},\quad L_{\mathrm{D}}=\frac{4\pi\mathcal{A}}{\mathcal{D}}.\tag{1.16}$$

It is useful to introduce the reduced parameters of the magnetic field $\boldsymbol{h}=\boldsymbol{B}/B_{\mathrm{D}}$, the anisotropy, $u=\mathcal{K}/M_{\mathrm{s}}B_{\mathrm{D}}$ and the length $\boldsymbol{r}'=\boldsymbol{r}/L_{\mathrm{D}}$.

In reduced parameters, the micromagnetic Hamiltonian takes the following form,

$$\mathcal{E}=\frac{\mathcal{H}_{\mathrm{tot}}}{2\mathcal{A}}=\int_{\Omega}\mathrm{d}\Omega\left(\frac{1}{2}\left(\nabla\boldsymbol{n}\right)^2+2\pi\boldsymbol{n}\cdot\nabla\times\boldsymbol{n}+4\pi^2u\left(1-n_{\mathrm{z}}^2\right)+4\pi^2\left(h-\boldsymbol{h}\cdot\boldsymbol{n}\right)\right),\tag{1.17}$$

where spatial coordinates and the integration volume Ω are given in dimensionless units.

The energy functional (1.17) and the corresponding EL equations $\delta\mathcal{E} = 0$ are the basic formulas that will be used below.

1.2.2 Landau-Lifshitz equation

The near-equilibrium dynamics of magnetic Sks can be described using the LLG equation [37]. Having the magnetization distribution $\boldsymbol{n}(\boldsymbol{r}, t_0)$ at time, t_0 one can find $\boldsymbol{n}(\boldsymbol{r}, t)$ at any other time, t, by solving the LLG equation

$$\frac{\partial \boldsymbol{n}}{\partial t} = -\gamma \boldsymbol{n} \times \boldsymbol{B}_{\text{eff}} + \alpha \boldsymbol{n} \times \frac{\partial \boldsymbol{n}}{\partial t} - \boldsymbol{T}, \tag{1.18}$$

where γ, α are gyromagnetic ratio and Gilbert damping parameter correspondingly, $\boldsymbol{T}$ denotes additional torques that can be included and $\boldsymbol{B}_{\text{eff}}$ is a so-called effective field,

$$\boldsymbol{B}_{\text{eff}} = -\frac{1}{M_{\text{s}}} \frac{\delta \mathcal{H}_{\text{tot}}}{\delta \boldsymbol{n}}. \tag{1.19}$$

At $\boldsymbol{T} = 0$, it allows one to obtain equilibrium magnetic texture taking the limit $t \to \infty$, in this case, (1.18) takes the form of EL equations (1.13). The case $\boldsymbol{T} \neq 0$ corresponds to the presence of external stimuli caused, e.g., by the electric current. There are different types of current-induced spin-transfer torques, for instance, Slonczewski torque and Zhang-Li torque [38]. Here I consider only the case of Zhang-Li torque, which has the form $\boldsymbol{T}_{\text{ZL}} = \boldsymbol{n} \times (\boldsymbol{n} \times (\boldsymbol{I} \cdot \nabla) \boldsymbol{n}) + \xi \boldsymbol{n} \times (\boldsymbol{I} \cdot \nabla) \boldsymbol{n}$, electrical current $\boldsymbol{I} = \dfrac{P \mu_{\text{B}}}{e M_{\text{s}} (1 + \xi^2)} \mathbf{j}$ is proportional to the current density $\mathbf{j}$, P is polarization, ξ is the degree of non-adiabaticity, μ_{B} the Bohr magneton and e is the electron charge.

The presence of additional torques always complicates the analytical study of the LLG equation. The number of cases allowing exact analytical solutions is limited. Nevertheless, for the rotation of the cone phase induced by Zhang-Li torque, I found the exact solution, see **Section** 7.1.

In insulating magnets the magnetization dynamics can also be induced by spatial variation and/or time variation of micromagnetic parameters $\mathcal{A}, \mathcal{D}, \mathcal{K}, \boldsymbol{B}$. In particular, the gradient magnetic fields were widely used for controllable motion of the bubble domains [39]. The same approach can be used to manipulate Sk dynamics.

1.2.3 Thiele equation

An approach for solving the LLG equation in a particular case of the rigid soliton motion has been suggested by Thiele [40]. The Thiele approach is applicable when the soliton motion can be approximated as $\boldsymbol{n}(\boldsymbol{r}, t) = \boldsymbol{n}(\boldsymbol{r} - \boldsymbol{v}t)$ where $\boldsymbol{v}$ is a constant velocity vector. In this case, one can derive an algebraic equation for velocity called the Thiele equation.

In the absence of driving forces, when $\boldsymbol{T}=0$ and all micromagnetic parameters are fixed, the Thiele equation has a simple form:

$$\boldsymbol{G}\times\boldsymbol{v}-\alpha\boldsymbol{v}\hat{\Gamma}=0, \tag{1.20}$$

where gyro-vector $\boldsymbol{G}$ and dissipation tensor $\hat{\Gamma}$ with entries Γ_{ij} defined as

$$\boldsymbol{G}=-\frac{1}{4\pi}\int_{\Omega}\mathrm{d}\Omega\sin\Theta\nabla\Theta\times\nabla\Phi, \tag{1.21}$$

and

$$\Gamma_{ij}=\frac{1}{4\pi}\int_{\Omega}\mathrm{d}\Omega\left(\partial_i\Theta\partial_j\Theta+\sin^2\Theta\partial_i\Phi\partial_j\Phi\right), i,j\in(\mathrm{x},\mathrm{y},\mathrm{z}). \tag{1.22}$$

The presence of nonzero torques slightly modifies the Thiele equation (1.20). For instance, in the case of the Zhang-Li torque, it takes the following form:

$$\boldsymbol{G}\times(\boldsymbol{v}+\boldsymbol{I})-(\alpha\boldsymbol{v}+\xi\boldsymbol{I})\,\hat{\Gamma}=0. \tag{1.23}$$

Solutions of the Thiele equation (1.23) are an excellent approximation to magnetization dynamics described by LLG in the so-called long-time limit, $t\gg 0$. Because of that, the Thiele approach represents the primary tool for analyzing the magnetic textures dynamics. Additionally, it can be used to explain experimental observations without referring to the LLG equation [41].

1.2.4 Topology in chiral magnets

When the order parameter of the system represents a smooth unit vector field $\boldsymbol{n}(\boldsymbol{r})$ which is defined at any point of 2D space, $\boldsymbol{r}\in\boldsymbol{R}^2$, the field configurations corresponding to localized solutions ($\boldsymbol{n}(\boldsymbol{r})\to\boldsymbol{n}_0$ for $|\boldsymbol{r}|\to\infty$) can be classified using the topological concept of homotopy. In particular, the domain of definition of the order parameter can be mapped to a sphere, or in other words, there is a stereographic projection: $\mathbb{R}^2\cup\{\infty\}\leftrightarrow\mathbb{S}^2$. The space of the order parameter $\boldsymbol{n}$ is also a sphere, $\mathbb{S}^2_{\mathrm{M}}$. The map $\mathbb{S}^2\to\mathbb{S}^2_{\mathrm{M}}$ leads to a homotopy classification of localized solutions by the integer index defined by the following topological invariant:

$$Q=\frac{1}{4\pi}\int_{\Omega}\mathrm{d}\Omega q\left(\boldsymbol{r}\right)=\frac{1}{4\pi}\int_{\Omega}\mathrm{d}\Omega\left(\nabla\Theta\times\nabla\Phi\right)_{\mathrm{z}}\sin\Theta, \tag{1.24}$$

where Ω is $\mathbb{R}_2$ and $\mathrm{d}\Omega=\mathrm{d}x\mathrm{d}y$, the function $q\left(\boldsymbol{r}\right)$ is topological charge density. Note, the gyro-vector $\boldsymbol{G}$ (1.21) and the topological charge (1.24) are connected. When two different spin textures have identical Q, we say that they belong to the same homotopy class, i.e. there are smooth transformations of the magnetization $\boldsymbol{n}\left(\boldsymbol{r}\right)$ that allows transforming one spin texture into another. It is worth noting that one can compare the topological charge of different Sks only if the vacuum for both magnetic textures is the same, for instance, $\boldsymbol{n}(\boldsymbol{r}) \to \boldsymbol{n}_0$ at $|\boldsymbol{r}| \to \infty$ for both spin configurations. The homotopic transformation can be thought of as some path on the energy landscape. As I show below, such a homotopy path can be found, for instance, using the geodesic nudged elastic band method (GNEB) [42, 43]. In general, GNEB is used for finding minimum energy path (MEP), which connects two energy minima separated by the saddle point. The energy difference between the energy minimum and the saddle point is called the energy barrier. From the point of view of the continued Hamiltonian (1.6), the energy barrier between two textures with different Q is infinite. Because of this, such non-homotopic transitions [44] can be correctly described only by discrete model (1.1). A remarkable example of such transition is the temperature-induced nucleation of Sks [45].

For some Sks, the topological charge can be alternatively defined as a product of two scalar quantities: polarity, p, and vorticity, ν,

$$Q = p\nu. \tag{1.25}$$

The polarity is defined by the direction of the magnetization in the center of Sk $\boldsymbol{r}_0$: $p = +1$ if $\boldsymbol{n}(\boldsymbol{r}_0) \cdot \boldsymbol{e}_\mathrm{z} = 1$ and $p = -1$ if $\boldsymbol{n}(\boldsymbol{r}_0) \cdot \boldsymbol{e}_\mathrm{z} = -1$. The vorticity can be calculated as the following line integral

$$\nu = \frac{1}{2\pi} \oint \mathrm{d}\boldsymbol{r} \cdot \nabla\Phi(\boldsymbol{r}). \tag{1.26}$$

According to this definition, the vorticity, ν, is an integer number that, in general, depends on the chosen integration path. In principle, the integration path can be chosen arbitrary but it is essential to avoid the points where $\Phi(\boldsymbol{r})$ is undefined. In all the cases when expression (1.25) can be used for the calculation of the topological charge, it gives an identical result to that of equation (1.24). I follow this approach for the definition of the topological charge in **Sections** 2.3.

1.2.5 Skyrmions at Bogomol'nyi point

In the model of chiral magnets (1.17), there is a special point in the field-anisotropy parameter space, $h = -2u = 1$, which is called Bogomol'nyi point. At this point, the EL equations become analytically solvable and can be reduced to the Bogomol'nyi equations [46, 47, 48] which can be derived as follows. By means of covariant derivative $D_i\boldsymbol{n} = \partial_i\boldsymbol{n} + \boldsymbol{A}_i \times \boldsymbol{n}$, where $\boldsymbol{A}_i = -2\pi\boldsymbol{e}_i$ is the gauge field, one can write the energy functional (1.17) in the following form:

$$\mathcal{E} = \int_\Omega \mathrm{d}\Omega \left(\frac{1}{2}(D_x\boldsymbol{n})^2 + \frac{1}{2}(D_y\boldsymbol{n})^2 - \boldsymbol{n} \cdot \boldsymbol{F}_{xy} \right), \tag{1.27}$$

where the field strength $\boldsymbol{F}_{xy} = \partial_x \boldsymbol{A}_y - \partial_y \boldsymbol{A}_x + \boldsymbol{A}_x \times \boldsymbol{A}_y = 4\pi^2 \boldsymbol{e}_{\mathrm{z}}$. Up to summands that will not contribute to EL equations, the energy (1.27) can be written as

$$\mathcal{E}^* = \frac{1}{2}\int_\Omega \mathrm{d}\Omega \left(D_x \boldsymbol{n} + \boldsymbol{n} \times D_y\right)^2 + 4\pi Q. \tag{1.28}$$

The Bogomol'nyi equation followed from $\delta\mathcal{E}^* = 0$ has the form:

$$D_x \boldsymbol{n} + \boldsymbol{n} \times D_y = 0. \tag{1.29}$$

The solution for Bogomol'nyi equation (1.29) can be written as

$$\frac{1}{\eta} = -i\pi\bar{\zeta} + f(\zeta), \tag{1.30}$$

where $\zeta = x + iy$, $\bar{\zeta}$ is conjugate complex number of ζ and η is a complex value function,

$$\eta = \frac{n_x + i n_y}{1 - n_z}, \tag{1.31}$$

that is related to stereographic projection of magnetization vector $\boldsymbol{n}$ on the complex plane. In (1.30), f is an arbitrary holomorphic function of the spatial coordinate, ζ. Using the equation (1.31) one can derive the solution for Bogomol'nyi equation (1.29) in terms of $\boldsymbol{n}$,

$$\boldsymbol{n} = \frac{1}{1 + |\eta|^2}\left(\eta + \bar{\eta}, i(\bar{\eta} - \eta), 1 - |\eta|^2\right)^{\mathrm{T}}. \tag{1.32}$$

An important consequence of the above solution is that by choosing the function $f(\zeta)$, one can construct a large diversity of different magnetic textures, which can be used as an initial guess for the numerical solutions outside Bogomol'nyi point. This approach is discussed in detail in **Chapter** 3.

It is worth noting that there is an interesting connection between the model of chiral magnets at the Bogomol'nyi point and the 2D model of FM with exchange interaction only:

$$\mathcal{E}_{\mathrm{ex}} = \frac{1}{2}\int_\Omega \mathrm{d}\Omega \left(\nabla \boldsymbol{n}\right)^2. \tag{1.33}$$

The localized solutions of this model are known as Belavin-Polyakov solitons [49]. The common feature of the Belavin-Polyakov solitons and chiral Sks at the Bogomol'nyi point is that their energies are proportional to the topological charge, $\mathcal{E}_{\mathrm{ex}} = -4\pi Q$. Everywhere outside the Bogomol'nyi point, this relation can be used as reference energy for different Sk solutions. In particular, in **Section** 2.1 I use this property to prove π-skyrmion stability at $h \to \infty$.

1.3 Methods

1.3.1 Energy minimizations

In the case of the micromagnetic model, the numerical approach is usually based on the finite-difference scheme to represent the derivatives in the energy functional. In this case, one deals with the vector field on a discrete mesh or lattice. Because of that, the numerical energy minimization methods used for finding stable Sk solutions in atomistic and micromagnetic models are pretty similar. In both cases, the strategy is the same. One has to find $3N$ numbers – three Cartesian components of each of N vectors, that optimize the functional (1.1) under the constraint on the norm of the vectors. The constraint can be achieved in many different ways, e.g., by using Lagrange multipliers or fee-functions. One of the best approaches is the method of the stereographic projections, where instead of three Cartesian components of the vector $\boldsymbol{S}$ defined at every lattice site i one can introduce three numbers $\{\gamma_1, \gamma_2, p\}$

$$\gamma_1 = \frac{S_\mathrm{x}}{1+pS_\mathrm{z}}, \quad \gamma_2 = \frac{S_\mathrm{y}}{1+pS_\mathrm{z}}, \quad p = \begin{cases} +1, S_\mathrm{z} \geq 0, \\ -1, S_\mathrm{z} < 0. \end{cases} \tag{1.34}$$

The parameters γ_1, γ_2 are stereographic projections of vector unit vector $\boldsymbol{S}$ projected from the north or south pole of the corresponding unit sphere, which is defined by the sign of the parameter p. Two different poles, $p = \pm 1$, are used depending on the sign S_z to prevent approaching γ_1, γ_2 to infinity that appears if one uses the fixed projection from one pole for all spins.

I use the nonlinear conjugate gradient (NCG) algorithm implemented in the Excalibur software [50] developed by Filipp. N. Rybakov. The details of the implementation of the NCG with the stereographic projections can be found in supplementary materials of Ref. [36].

The agreement of the solutions obtained with micromagnetic (1.6) and atomistic (1.1) models can be improved with higher-order discretization scheme employing multiple neighbours beyond the nearest ones. For instance, the nearest neighbour model corresponds to the finite central difference scheme of the second-order accuracy for calculation derivatives in micromagnetic Hamiltonian (1.6). By default, in Mumax software [51] the second-order finite difference scheme (or first nearest spins model) is implemented. However, via build-in Mumax custom interactions and effective fields, one can implement the fourth-order finite difference scheme in (1.6). The listing of the Mumax script with the implemented fourth-order finite difference scheme [52] is provided in Appendix A1 .

1.3.2 Numerical solving of the Lagrange-Euler equations

In the general case, the system of EL equations (1.13) is a system of two nonlinear partial differential equations (PDEs), and its numerical investigation can meet some typical problems related to convergence and stability of the corresponding methods. On the other hand, in some cases, when the magnetic texture has a high symmetry, it might be possible to reduce the problem of PDEs to ordinary differential equations. A classic example is the $2D$ axial symmetrical π-skyrmion in a perpendicular magnetic field. In cylindrical coordinate system, (r, ϕ) the solution of such Sk has the form $\Phi = \phi + \pi/2$ and $\Theta = \Theta(r)$ and the equation for $\Theta(r)$ is [53]

$$r\Theta'' + \Theta' = \frac{\sin 2\Theta}{2r} - 4\pi \sin^2\Theta + 4\pi^2 r\left(h\sin\Theta + u\sin 2\Theta\right), \tag{1.35}$$

with the boundary conditions $\Theta(0) = \pi$ and $\Theta(r \to \infty) = 0$. One can solve (1.35) using the shooting method. This method is known to work well for periodic solutions, but also it can be used for isolated solitonic solutions. Another alternative approach is based on the relaxation method applied to linearized near solution $\Theta_0(r)$ equation (1.35). The method is called quasilinearization (Ql), [54] and it demonstrates both fast and accurate results. By this method, the π-skyrmion equation can be written as

$$r\Theta'' + \Theta' + f_1(r)\Theta = f_2(r), \tag{1.36}$$

where $f_1(r) = -\frac{\cos 2\Theta_0}{r} + 4\pi\sin 2\Theta_0 - 4\pi^2 r\left(h\cos\Theta_0 + 2u\cos 2\Theta_0\right)$, $f_2(r) = \frac{\sin 2\Theta_0}{2r} - 4\pi\sin^2\Theta_0 + 4\pi^2 r\left(h\sin\Theta_0 + u\sin 2\Theta_0\right) + f_1(r)\Theta_0$. Starting with trial function $\Theta_0(r)$ one can solve numerically linear equation (1.36) and then use the obtained function $\Theta(r)$ as a new guess $\Theta_0(r)$ in the next step. This procedure is repeated until the difference between $\Theta(r)$ and $\Theta_0(r)$ becomes lower than the chosen tolerance. The listing of the corresponding program for the π-skyrmion solution is provided in Appendix A2 . However, with an appropriate choice of the boundary conditions, the code can provide the solutions of other $k\pi$-skyrmions. In this case, it is enough to modify the boundary condition and set $\Theta(0) = k\pi$, $k \in \mathbb{N}$.

In **Table** 1.2, I provide the comparing of the energies of π-skyrmion at different values of the magnetic field, h, and anisotropy, u, which were obtained with Excalibur, Mumax3 and my implementation of the Ql method. For the generality of the results, all energies are provided in dimensionless units (see (1.17)). The energies obtained with Excalibur code are taken from [17].

It is worth emphasizing that the general theory of the Ql [54] does not forbid using this method also for PDEs. However, in the case of magnetic solitons and other systems where the order parameter is the unit vector field, there is no optimal parametrization

Table 1.2: The energy of the π-skyrmion calculated by different methods

Parameters	Mumax (2nd)	Mumax (4th)	Excalibur	Ql
$h=0.65, u=0.00$	-3.522	-3.565	-3.565	-3.5649707
$h=0.30, u=0.65$	0.673	0.6219	0.6220	0.6217628
$h=0.40, u=0.65$	2.666	2.6165	2.617	2.61621205

of the order parameter for which the linearized system of equations can be written. A summary of the problems arising when the Ql method is applied with the different methods discussed above is provided in **Table** 1.3. The approach based on the Ql method for general system (1.13) may overcome these problems and looks very promising for future study, which, however, is out of scope of this thesis.

Table 1.3: Problems that the Ql method meets for different magnetization parametrization

Parametrization	Problem
$\{n_x, n_y, n_z\}$ with the Lagrange multiplier	Slow convergence because of linearization the Lagrange multiplier.
$\{n_x, n_y, n_z\}$ with the penalty function	Slow convergence because of linearization the penalty function.
Spherical coordinates: $\{\Theta, \Phi\}$	Since corresponding angle functions are not smooth, it is impossible to use them in the finite differences scheme.
$\{\gamma_1, \gamma_2, p\}$ with fixed p	Problem with infinity of γ_1, γ_2 either at $\Theta=0$ or $\Theta=\pi$.
$\{\gamma_1, \gamma_2, p\}$, with not fixed p	It is impossible to write a linear system when different nodes in finite-difference scheme are projected from different poles p.

1.3.3 Numerical solving of the Landau-Lifshitz equation

The LLG equation in form (1.18) is suited well for analytical analysis. For the numerical simulations, however, the form of LLG equation with the time derivative of magnetization appearing only on the left-hand side of the equation is more suitable,

$$\frac{\partial \boldsymbol{S}_i}{\partial t} = -\frac{\gamma}{1+\alpha^2}\left(\boldsymbol{S}_i \times (\boldsymbol{B}_{\mathrm{eff},i} + \boldsymbol{T}_i) + \alpha \boldsymbol{S}_i \times \boldsymbol{S}_i \times (\boldsymbol{B}_{\mathrm{eff},i} + \boldsymbol{T}_i)\right), \tag{1.37}$$

here the effective field is

$$\boldsymbol{B}_{\mathrm{eff},i} = -\frac{1}{\mu_{\mathrm{s}}}\frac{\partial H_{\mathrm{tot}}}{\partial \boldsymbol{S}_i}. \tag{1.38}$$

When the external driving stimuli $\boldsymbol{T}_i \neq 0$ the equation (1.37) with (1.38) describes the magnetization dynamics. On the other hand, when additional torques $\boldsymbol{T}_i = 0$, the equation (1.37) can be used for energy minimization and the search of local energy minima close to the initial magnetic configuration at $t = 0$. There are different methods for solving LLG equation (1.37) available in Mumax [51], and self-implemented software Magnoom [55]. In most cases, I use the fourth-order Runge-Kutta method, which provides sufficient accuracy for the problems I study. For instance, this scheme was used for studying Sk dynamics induced by the Zhang-Li torque **Section** 5.1. In addition to the Zhang-Li and the Slonczewski torques, one can include in the LLG equation (1.37) the thermal fluctuation, $\boldsymbol{T}_{\mathrm{noise},i}$. The fluctuation-dissipation theorem connects the parameters of the white noise used in this torque with the temperature, T. The detailed description of the numerical scheme for the corresponding stochastic LLG equation solution, which I used in my study, can be found in Ref. [56].

1.3.4 Monte-Carlo method

In addition to the simulations with the stochastic LLG equation, one can calculate different properties of the magnetic system at finite temperatures utilizing the Monte-Carlo (MC) method [57]. Each MC iteration includes a few steps known as the Metropolis algorithm. First, one has to set a new randomly chosen direction for the vector, $\boldsymbol{S}_i$ for arbitrary chosen spin i. Then, one has to calculate the energy difference between the states at the previous and the current iteration, $\Delta E = H_{\mathrm{tot}}(\boldsymbol{S}_i) - H_{\mathrm{tot}}(\boldsymbol{S}_i)$. If $\Delta E < 0$, the new spin direction is accepted. Otherwise, it is accepted with probability $\exp(-\Delta E/k_{\mathrm{B}}T)$. This procedure repeats for all spins $i = \overline{1, N}$ in the system and is called one MC iteration. The actual sequence of the spins during each MC iteration does not play a significant role. In practice, for the increase of efficiency in the case of parallel calculations, the most efficient approach is splitting the square lattice of spins into chess-board-like subdomains. Note, the random choice for the direction of the spin, $\boldsymbol{S}_i$, has to be uniformly distributed over the unit sphere. One can obtain such uniform distribution, for instance, with the method suggested by Marsaglia [58]. I use the above MC algorithm for comparison with the results of the stochastic LLG simulations in **Section** 6.2. Implementing the MC method and stochastic LLG simulations can be checked by comparing the obtained results with analytical solutions based on the Fokker-Plank equation. This can be done only in a few simple cases, for instance, for the system of non-interacting spins. In this case, the system Hamiltonian includes only Zeeman energy term, and probability density function at finite temperature is, [59] y term, and probability density function at finite temperature writes, [59]

$$\varrho(\Theta, \Phi) = \frac{\varrho_0}{2\pi} \exp\left(\frac{\mu_{\mathrm{s}} B_{\mathrm{z}}}{k_{\mathrm{B}} T} \cos\Theta\right) \sin\Theta, \tag{1.39}$$

where ϱ_0 can be found from the normalization condition $\int_0^{2\pi}\int_0^{\pi}\varrho(\Theta,\Phi)\,\mathrm{d}\Theta\mathrm{d}\Phi = 1$. The exact result (1.39) has been used to test the implementation of MC and stochastic LLG methods in our software [55].

1.3.5 Vector field visualization

Across the whole theses, for the visualization of various spin textures I use a special color code [17], see, e.g., Fig. 1.1 **a**. Nowadays, this colour code has become the standard approach implemented, for instance, in Mumax, Excalibur, and other software. By this magnetization directions $(1,0,0)^{\mathrm{T}}$, $\left(-\sqrt{3}/2, 1/2, 0\right)^{\mathrm{T}}$ and $\left(-\sqrt{3}/2, -1/2, 0\right)^{\mathrm{T}}$ corresponds to red, green and blue colors, respectively. The directions $(0,0,1)^{\mathrm{T}}$ are marked in black color and $(0,0,-1)^{\mathrm{T}}$ are marked in white color, see Fig. 1.1 **b** or vice versa, see Fig. 1.1 **c**. Appendix A3 provides the details of the colour code in the most general case when it can also be used for not unit vector fields.

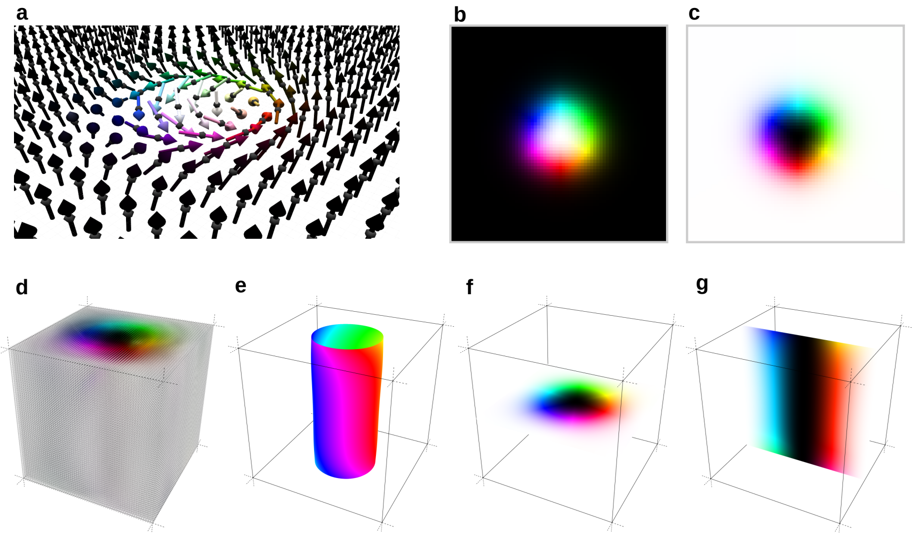

Figure 1.1: **Vector field visualization**. **a** the π-skyrmion, **b** and **c** correspond to its representation in different color codes described in the text, the direction of magnetization in the core of the πskyrmion $(0,0,-1)$ is shown in white **b** and black **c** colors. **d** vector field of 3D Sk tube, **e** its surface of constant angle $\Theta = \pi/2$, **f** and **g** sections of the tube by z- and y-planes, respectively.

For magnetic textures in a 3D case, see, e.g., Fig. 1.1 **d**, one can visualize the magnetic textures using different isosurfaces defined by the geometrical position of the points with constant values of Θ or Φ angles of the spins. The example of $\Theta = \pi/2$ surface for the π-skyrmion tube is shown in Fig. 1.1 **e**. Besides that, one can use 2D sections of the simulated domain, see the sections by z- and y-planes in **f** and **g**, respectively. In most of the cases, I used the Spirit code [60] for visualization of the spin textures.

2 Skyrmions in the tilted magnetic field

In this Chapter, I discuss π-skyrmion and antiskyrmion in the tilted external magnetic field. I present the stability diagram and inter-skyrmion interactions calculated with numerical and analytical methods. I provide the recipe and criteria for turning π-skyrmion inside out by tilting the external magnetic field in a quasi-static regime. One of the main achievements is finding a stable solution for antiskyrmion in a perpendicular magnetic field. Here I also discuss the effect of Sks splitting into vortex-antivortex pairs in the case of easy-plane anisotropy. Some of the presented results are published, see Ref. [61]. As it turned out, the findings presented in this Chapter may go far beyond the initially formulated problem and open perspective for further study of diverse solutions of 2D Sks.

2.1 Skyrmions stability diagram

2.1.1 Formulation of the problem

The solution for axially symmetric π-skyrmion (1.35) exists only in the FM background supported by the perpendicular magnetic field $\boldsymbol{h} = (0, 0, h_z)$ and/or uniaxial anisotropy $u > 0$. The axial symmetry of π-skyrmion can be broken due to different reasons, for instance, when the FM vacuum, $\boldsymbol{n}_0$ at $\boldsymbol{r} \to \infty$ is not homogeneous or $\boldsymbol{n}_0 \neq (0, 0, \pm 1)$. The above statements are valid irrespective of the dimensionality of the problem and remain true not only for 2D Sks but also for 3D Sk tubes. Let me consider the 3D Sk tube embedded into the conical phase (1.15) with $\boldsymbol{k}$-vector along the z-axis. In this case, every xy-section of such a Sk tube represents the 2D π-skyrmion in the tilted FM phase [62, 63]. Thus, it is reasonable to consider first a simple case of the 2D model in the presence of an inclined magnetic field [64]. Strictly speaking, such simplification does not reflect the actual structure of the 3D Sk tube but can be helpful in further studies.

First of all, it is convenient to parameterize the magnetic field as follows,

$$\boldsymbol{h} = (h_\mathrm{x}, 0, h_\mathrm{z})^\mathrm{T} = h\,(\sin\theta_\mathrm{h}, 0, \cos\theta_\mathrm{h})^\mathrm{T}\,, \tag{2.1}$$

where h_x and h_z are magnetic field in-plane and out-of-plane components. Because of the isotropic nature of the model, the h_y component of the field can be excluded from consideration. Below, where it is more suitable, I use the representation of the field via its magnitude, $h = \sqrt{h_\mathrm{x}^2 + h_\mathrm{z}^2}$, and the tilt angle, $\theta_\mathrm{h} = \arctan(h_\mathrm{x}/h_\mathrm{z})$. The tilted FM vacuum then can be written in terms of spherical angles as $\Theta = \Theta_\mathrm{h}, \Phi = 0$, where equilibrium angle value Θ_h can be found from the condition $\mathrm{d}\mathcal{E}/\mathrm{d}\Theta_\mathrm{h} = 0$ that is equivalent to the equation

$$u\sin 2\Theta_\mathrm{h} + h\sin(\Theta_\mathrm{h} - \theta_\mathrm{h}) = 0. \tag{2.2}$$

Knowing the value of Θ_h from (2.2) one can write down the energy functional (1.17) in the form where the energy is calculated with respect to the energy of tilted FM state,

$$\mathcal{E} = \int_\Omega \mathrm{d}\Omega\left(\frac{(\nabla\boldsymbol{n})^2}{2} + 2\pi\boldsymbol{n}\cdot\nabla\times\boldsymbol{n} + 4\pi^2 u\left(\cos^2\Theta_\mathrm{h} - n_\mathrm{z}^2\right) + 4\pi^2\left(h\cos(\theta_\mathrm{h} - \Theta_\mathrm{h}) - \boldsymbol{h}\cdot\boldsymbol{n}\right)\right). \tag{2.3}$$

The energy (2.3) is the starting point for the study of Sk solutions and their stability presented in this Chapter.

2.1.2 Analytical approach

The EL equations (1.13) are complicated enough, and there is no hope to solve them analytically in the most general case. On the other hand, for the particular case of zero anisotropy, $u = 0$, when $\Theta_\mathrm{h} = \theta_\mathrm{h}$, one can obtain the asymptotic expansions for Sk solutions at infinity $r \to \infty$. The magnetization vector $\boldsymbol{n}$ is parameterized in the following way that explicitly includes, the tilt angle of the FM vacuum,

$$\boldsymbol{n} = \begin{pmatrix} \cos\theta_\mathrm{h} & 0 & \sin\theta_\mathrm{h} \\ 0 & 1 & 0 \\ -\sin\theta_\mathrm{h} & 0 & \cos\theta_\mathrm{h} \end{pmatrix}\begin{pmatrix} \sin\Theta\cos\Phi \\ \sin\Theta\sin\Phi \\ \cos\Theta \end{pmatrix} = \begin{pmatrix} \cos\theta_\mathrm{h}\sin\Theta\cos\Phi + \sin\theta_\mathrm{h}\cos\Theta \\ \sin\Theta\sin\Phi \\ -\sin\theta_\mathrm{h}\sin\Theta\cos\Phi + \cos\theta_\mathrm{h}\cos\Theta \end{pmatrix}. \tag{2.4}$$

The corresponding EL equations for Θ, Φ and boundary condition for Θ in this case take the form,

$$\begin{cases} \triangle\Theta + 4\pi\sin\Theta\,(\boldsymbol{n}\cdot\nabla\Phi - \pi h) - \dfrac{\sin 2\Theta}{2}(\nabla\Phi)^2 = 0, \\ \triangle\Phi\sin^2\Theta - 4\pi\boldsymbol{n}\cdot\nabla\Theta\sin\Theta + \nabla\Theta\cdot\nabla\Phi\sin 2\Theta = 0, \\ \Theta(x, \pm\infty) = \Theta(\pm\infty, y) = 0. \end{cases} \tag{2.5}$$

Assuming that at infinity $|\Theta| \ll 1$ and $|\partial\Theta| \ll 1$ one can neglect the high order terms in the second equation in (2.5) and write it as

$$\Theta\triangle\Phi + 2\left(\nabla\Theta\cdot\nabla\Phi - 2\pi\frac{\partial\Theta}{\partial x}\sin\theta_\mathrm{h}\right) = 0. \tag{2.6}$$

With the change of variables, $\Phi(x, y) = 2\pi x \sin\theta_\mathrm{h} + \Psi(x, y)$, equation (2.6) simplifies to

$$\Theta\triangle\Psi + 2\nabla\Theta\cdot\nabla\Psi = 0. \tag{2.7}$$

Next, I make an assumption that the unknown functions Θ and Ψ are $\Theta = \Theta(r)$, $\Psi = \Psi(\phi)$, where r and ϕ are polar coordinates. Under this assumption the equation (2.7) becomes

$$\triangle\Psi = 0. \tag{2.8}$$

The solution of (2.8) can be written as $\Psi = \pm(\phi + \pi/2)$. The solution for Θ can be found from the first equation in (2.5), that with the above assumptions simplifies to

$$\frac{\mathrm{d}^2\Theta}{\mathrm{d}r^2} + \frac{1}{r}\frac{\mathrm{d}\Theta}{\mathrm{d}r} - 4\pi^2 h\Theta + \left(4\pi^2\sin^2\theta_\mathrm{h} - \frac{1}{r^2}\right)\Theta = 0. \tag{2.9}$$

At $h > \sin^2\theta_\mathrm{h}$ the solution of (2.9) can be expressed in terms of the modified Bessel function of the second kind, $\Theta = c^2 K_1\left(2\pi\sqrt{h - \sin^2\theta_\mathrm{h}}r\right)$, where c is arbitrary constant which, generally speaking, can be different for π-skyrmion and antiskyrmion. Therefore in the leading terms in expansion solutions for the π-skyrmion (+) and the antiskyrmion (−) have the form,

$$\begin{cases} \Theta \to \dfrac{c^2}{\sqrt{r}}\exp\left(-2\pi\sqrt{h - \sin^2\theta_\mathrm{h}}r\right), \\ \Phi \to \pm\left(\phi + \dfrac{\pi}{2}\right) + 2\pi\sin\theta_\mathrm{h} r\cos\phi, \end{cases} \quad r \to \infty. \tag{2.10}$$

In the case of zero tilt of the external magnetic field, $\theta_\mathrm{h} = 0$, the asymptotic behaviour of the π-skyrmion solution transforms into the earlier found form [65]. In the case of anti-skyrmion, remaining the asymptotic for $\Theta(r)$ unchanged (2.10), the function Φ modifies to $\Phi \to -\phi + \pi/2 + \mathcal{F}(\phi)$, where $\mathcal{F}(\phi)$ is arbitrary 2π-periodic function (for details, see Ref. [61]). The solutions for the π-skyrmion and the antiskyrmion profile (2.10) are valid only at a large distance from the center of the soliton. Nevertheless, equations (2.10) show a good agreement with the numerical solutions. For details, see Appendix A4 .

In the case of non-zero tilt, the asymptotic solutions (2.10) provide an estimate for the stability region for the π-skyrmion and the antiskyrmion only under the condition $h > \sin^2\theta_\mathrm{h}$. The numerical analysis of the solutions presented in the next Section provides the stability of these solutions in a broader range of fields.

2.1.3 Numerical results

The energy functional (2.3) can be approximated by the corresponding atomistic Hamiltonian (1.1). The results of direct energy minimization of that Hamiltonian for the π-skyrmion solution are shown in Fig. 2.1 **a**, **b**. The number of lattice sites per L_{D}, the so-called discretization length, Δl, is varied to see a convergence of the results to the limit of the micromagnetic model. In particular, the collapse field for π-skyrmion has been calculated for different Δl. Here, I use two approaches: I) with nearest neighbours only, and ii) a higher-order procession scheme with the nearest and next after nearest neighbours, see **Section** 1.3. The asterisk symbol marks the critical lines calculated with the nearest neighbour approximation.

The red region on the stability diagram corresponds to the area inside which the π-skyrmion is unstable with respect to elliptic deformations. The case of a perpendicular field, $h_{\mathrm{x}} = 0$, was considered earlier in Ref. [53]). Outside the red region, the π-skyrmion stability is bounded from above by a collapse field that depends on the Δl. The collapse corresponds to the π-skyrmion shrinking with increasing field magnitude h and happens when the π-skyrmion size becomes comparable with inter-atomic distance a in the atomistic model. h^{e} and h^{c} denote critical magnetic fields of elliptic instability and collapse, respectively. In the case of the in-plane magnetic field $\theta_{\mathrm{h}} = \pi/2$, the elliptic instability field goes through the point $h_{\mathrm{x}} = 1, h_{\mathrm{z}} = 0$, which agrees with the predicted from the asymptotic expansion (2.10). For all other parameters of the magnetic field, the curve $h = \sin^2\theta_{\mathrm{h}}$ lies inside the instability region. The stability region for π-skyrmion extends with an increase of Δl. In the limit $\Delta l \to \infty$, it seems that the π-skyrmion solution remains stable even at $h \to \infty$. The exception is the case of high tilt angles when one approaches the case of a fully inverted field, $\theta_{\mathrm{h}} \sim \pi$.

As follows from the stability diagram for π-skyrmion starting with the π-skyrmion in the perpendicular magnetic field $\theta_{\mathrm{h}} = 0$ by changing the tilt angle and the magnitude of the external magnetic field, it is possible to reach the stable solution at $\theta_{\mathrm{h}} = \pi$. Example of such a path is shown on Fig. 2.1 **a**, **b** as dashed blue curve. The corresponding magnitude of the external field $h(\theta_{\mathrm{h}})$ is given in **c**, see the blue curve. Note that without varying the absolute value h but varying only the tilt angle θ_{h} one cannot reach the inverted field state without crossing the elliptic instability area, see, for instance, the red curves in **a** and **c**. The dependencies of the self-energy of the π-skyrmion as a function of the tilt angle for both paths are shown on **d**. The variation of the magnetic texture at different stages of the blue path is depicted in figures **e**-**i**. We called this process *turning skyrmion inside out* [61]. The π-skyrmion obtained by this way at $\theta_{\mathrm{h}} = \pi$, Fig. 2.1**i**

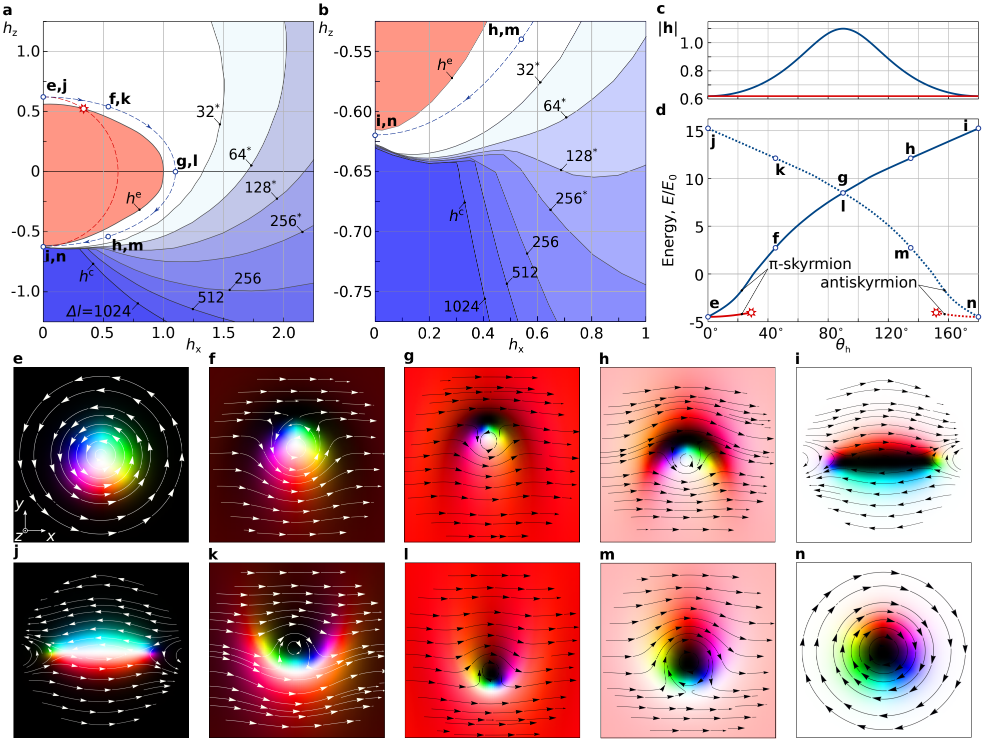

Figure 2.1: π**-skyrmion in the tilted magnetic field**. **a**, **b** Stability diagram for an isolated π-skyrmion in a tilted magnetic field, $\boldsymbol{h} = (h_{\mathrm{x}}, 0, h_{\mathrm{z}})^{\mathrm{T}}$ at $u = 0$. h^{e} and h^{c} are critical fields corresponding to the elliptical instability and the collapse of the π-skyrmion, respectively. With increasing mesh density Δl the region for stability extends. For Δl with an asterisk, the atomistic model with only first nearest spins is used. For all others Δl, the atomistic model with second nearest spins is considered. The dashed red line in **a** corresponds to the case when $h = 0.62$ and does not change with the tilt angle θ_{h} (see the red line in **c**). This leads to π-skyrmion instability at the point marked by a star symbol in **a** and **d**. The dashed blue line in **a** and **d** is the path along which the value of h changes with θ_{h} (see the blue line in **c**). At any point $(h_{\mathrm{x}}, h_{\mathrm{z}})$ along this path there are two stable Sk solutions with opposite topological charge Q. The energies of both solutions as functions of θ_{h} are given in **d**. Blue lines: Solid line for $Q = -1$, dotted line for $Q = +1$. The red lines in **d** correspond to the fixed $h = 0.62$. The spin textures in **e**-**i** and **j**-**n** represent the transient states of two Sk solutions with $Q = -1$ and $Q = 1$, respectively. The images in each row from left to right correspond to $\theta_{\mathrm{h}} = 0, \pi/4, \pi/2, 3\pi/4$, and π, respectively. In **e**-**n** the standard color scheme is used, the lines and arrows in **e**-**n** denote the streamlines of the in-plane component of the magnetization. This figure has been published in [61].

differs from the axial symmetric solution Fig. 2.1**n**. Using the soliton **n** as the initial point on the path, one can obtain elongated Sk shown in **j**. This Sk has $Q = +1$, and it is reasonable to refer to it as *antiskyrmion*. Thus the presented magnetic textures on **e**-**i** and **j**-**n** relate to π-skyrmion and antiskyrmion, respectively. The energy plot **d** indicates that both π-skyrmion and antiskyrmion have the same energy at the in-plane magnetic field. In the literature, such solutions at the in-plane magnetic field are called bimerons [66]. The stability region of antiskyrmion can be obtained from the region for the π-skyrmion by inversion of the out-of-plane component of the magnetic field $h_{\mathrm{z}} \to -h_{\mathrm{z}}$.

2.1.4 Analysis for π-skyrmion stability

From the numerical study presented in the previous Section, one can see that the increase of Δl leads to the extension of the stability region of the π-skyrmion. But the saturation rate significantly depends on the tilt angle θ_{h}, for instance, in the case $\theta_{\mathrm{h}} \sim \pi$ the considered values Δl did not allow the extension of the stability region as much as for smaller tilt angles, $\theta_{\mathrm{h}} \geq 0$. Earlier, Melcher has derived the energy bound for the π-skyrmion in the perpendicular magnetic field [67]. The proof provided by Melcher is based on a comparison of the energy of the π-skyrmion with the energy of the Belavin-Polyakov soliton. It shows that the π-skyrmion remains stable even at $h \to \infty$. Here I generalized the approach used by Melcher for the case of the tilted magnetic field.

By this, without loss of generality, the functional (1.17) can be written in the following reduced form,

$$\begin{gathered}\mathcal{E}\left(\boldsymbol{n}\right) = \mathcal{E}_{\mathrm{ex}}\left(\boldsymbol{n}\right) + \mathcal{E}_{\mathrm{DMI}}\left(\boldsymbol{n}\right) + \mathcal{E}_{\mathrm{Z}}\left(\boldsymbol{n}\right) = \\ \int_{\Omega} \mathrm{d}\Omega \left[\frac{1}{2}\left(\nabla \boldsymbol{n}\right)^2 + 2\epsilon\left(n_{\mathrm{x}}\frac{\partial n_{\mathrm{z}}}{\partial y} - n_{\mathrm{y}}\frac{\partial n_{\mathrm{z}}}{\partial x}\right) + \frac{\epsilon}{4}\left|\boldsymbol{n} - \boldsymbol{e}_{\mathrm{z}}\right|^2\right],\end{gathered} \tag{2.11}$$

where $\epsilon = 1/(2h)$. Here and below, I follow the notation used by Melcher [67]. The axially symmetric soliton is chosen as an ansatz for the π-skyrmion profile to which the rotation matrix about y-axis is applied,

$$\boldsymbol{n} = \begin{pmatrix} \cos\theta_{\mathrm{h}} & 0 & \sin\theta_{\mathrm{h}} \\ 0 & 1 & 0 \\ -\sin\theta_{\mathrm{h}} & 0 & \cos\theta_{\mathrm{h}} \end{pmatrix} \begin{pmatrix} -f_R'\left(r\right)\sin\phi \\ f_R'\left(r\right)\cos\phi \\ \operatorname{sgn}\left(r-1\right)\sqrt{1-\left(f_R'\left(r\right)\right)^2} \end{pmatrix}, \tag{2.12}$$

with the following function f_R

$$f_R\left(r\right) = \begin{cases} \ln\left(1+r^2\right), & \text{for } 0 \leq r \leq R, \\ c, & \text{for } r \geq 2R, \end{cases} \tag{2.13}$$

where c is a positive constant. The following conditions are applied to the first and second derivatives of the function f_R:

$$0 \leq f_R'(r) \leq \frac{2r}{1+r^2}, \quad 0 \leq -f_R''(r) \leq \frac{c}{1+r^2}, \text{for } \ r \geq R \gg 1. \tag{2.14}$$

In case of the high magnetic field, $\epsilon \ll 1$, exchange and Zeeman energy terms are bounded from above,

$$\mathcal{E}_{\mathrm{ex}}(\boldsymbol{n}) + \mathcal{E}_{\mathrm{Z}}(\boldsymbol{n}) \leq 4\pi + \pi\epsilon \ln\left(1+R^2\right) + c\left(\frac{1}{R^2}+\epsilon\right). \tag{2.15}$$

The DMI energy term splits into two parts – inside and outside the circle of radius R. In the region $r \leq R$, the DMI energy is

$$\mathcal{E}^{*}_{\mathrm{DMI}}(\boldsymbol{n}) = -8\pi\epsilon \frac{R^2\left(1+(R^2-1)\cos\theta_{\mathrm{h}}\right)\cos^2(\theta_{\mathrm{h}}/2)}{\left(1+R^2\right)^2}. \tag{2.16}$$

In the region $R < r \leq 2R$, the DMI energy density is bounded:

$$\begin{aligned}\mathcal{E}^{**}_{\mathrm{DMI}}(\boldsymbol{n}) &= 2\pi\epsilon \int_R^{2R} \frac{\sin^2\theta_{\mathrm{h}}\, f'(1-f'^2) + r\left(\sin^2\theta_{\mathrm{h}} + f'^2(\cos\theta_{\mathrm{h}} + \cos 2\theta_{\mathrm{h}})\right) f''}{\sqrt{1-f'^2}} \mathrm{d}r \\ &\leq \int_R^{2R} \frac{2\pi\epsilon\, r \sin^2\theta_{\mathrm{h}}}{1+r^2} \mathrm{d}r,\end{aligned} \tag{2.17}$$

at least when $\cos\theta_{\mathrm{h}} + \cos 2\theta_{\mathrm{h}} \geq 0$ (meaning $\theta_{\mathrm{h}} \leq \pi/3$). Taking into account (2.16) and (2.18) the upper bound DMI energy, $\mathcal{E}_{\mathrm{DMI}} = \mathcal{E}^{*}_{\mathrm{DMI}} + \mathcal{E}^{**}_{\mathrm{DMI}}$ is

$$\mathcal{E}_{\mathrm{DMI}}(\boldsymbol{n}) \leq -8\pi\epsilon \frac{R^2\left(1+(R^2-1)\cos\theta_{\mathrm{h}}\right)\cos^2(\theta_{\mathrm{h}}/2)}{\left(1+R^2\right)^2} + 2\pi\epsilon \sin^2\theta_{\mathrm{h}} \ln\frac{1+4R^2}{1+R^2}. \tag{2.18}$$

Defining $\tilde{\boldsymbol{n}} = \boldsymbol{n}(\lambda r)$, where λ is the rescaling parameter, the total energy bound can be written

$$\begin{aligned}\mathcal{E}(\tilde{\boldsymbol{n}}) &\leq 4\pi + \frac{\pi\epsilon}{\lambda^2}\ln\left(1+R^2\right) + c\left(\frac{1}{R^2}+\frac{\epsilon}{\lambda^2}\right) \\ &-\frac{8\pi\epsilon}{\lambda}\frac{R^2\left(1+(R^2-1)\cos\theta_{\mathrm{h}}\right)\cos^2\dfrac{\theta_{\mathrm{h}}}{2}}{\left(1+R^2\right)^2} + \frac{2\pi\epsilon\sin^2\theta_{\mathrm{h}}}{\lambda}\ln\frac{1+4R^2}{1+R^2}.\end{aligned} \tag{2.19}$$

Similarly to [67], by choosing $R = \dfrac{|\ln\epsilon|}{\sqrt{\epsilon}}$ and $\lambda = L\,|\ln\epsilon|$ one can write the following inequality for the total energy:

$$\mathcal{E}\left(\tilde{\boldsymbol{n}}\right) \leq 4\pi + \frac{\epsilon}{|\ln \epsilon|}\left(-\frac{8\pi}{L}\cos\theta_{\mathrm{h}}\cos^{2}(\theta_{\mathrm{h}}/2) + \frac{\pi}{L^{2}} + \frac{2\pi\left(\ln 4\right)\sin^{2}\theta_{\mathrm{h}}}{L} + \mathcal{O}\left(1\right)\right), \quad (2.20)$$

minimizing this expression for $L > 0$ gives

$$L = \left(4\cos\theta_{\mathrm{h}}\cos^{2}\frac{\theta_{\mathrm{h}}}{2} - (\ln 4)\sin^{2}\theta_{\mathrm{h}}\right)^{-1}. \quad (2.21)$$

Note that L in (2.21) remains positive only for angle $\theta_{\mathrm{h}} \leq \pi/3$. This critical angle defines the limit of applicability of the ansatz (2.12). Therefore, the energy of π-skyrmion in external magnetic field tilted by the angle $0 \leq \theta_{\mathrm{h}} \leq \pi/3$ to the plane normal is bounded,

$$\mathcal{E}\left(\tilde{\boldsymbol{n}}\right) \leq 4\pi + \frac{\epsilon\pi}{|\ln \epsilon|}\left[-\left(4\cos\theta_{\mathrm{h}}\cos^{2}\frac{\theta_{\mathrm{h}}}{2} - (\ln 4)\sin^{2}\theta_{\mathrm{h}}\right)^{2} + \mathcal{O}\left(1\right)\right]. \quad (2.22)$$

Therefore, the energy of the π-skyrmion is less than 4π (the energy of Belavin-Polyakov soliton) even at $h \to \infty$ ($\epsilon \to 0$).

With the simplified ansatz (2.12) and (2.13) which does not take into account an asymmetry of the π-skyrmion in the tilted magnetic field, the above remains true only for $\theta_{\mathrm{h}} \leq 60°$. The numerical analysis shows an even bigger critical angle value, which one can probably confirm analytically by using a more advanced ansatz for the π-skyrmion profile.

2.2 Inter-skyrmion interactions

2.2.1 The case of non-zero field tilt

Possibility of stabilization π-skyrmion and antiskyrmion together for specific parameters h, θ_{h} allows asking an obvious question about their interactions. There are three possible combinations of these two solitons: Sk-Sk, Sk-Ask, Ask-Ask. As an example, I chose the parameters of the field $h = 0.8, \theta_{\mathrm{h}} = \pi/3$ to decrease the exponential tail in asymptotic expressions (2.10) and enforce solitons interaction. Fixing these parameters, now one has to include into consideration the in-plane phase, ϕ_{h}, of the tilted magnetic field that now can be written as

$$\boldsymbol{h} = h\left(\sin\theta_{\mathrm{h}}\cos\phi_{\mathrm{h}}, \sin\theta_{\mathrm{h}}\sin\phi_{\mathrm{h}}, \cos\theta_{\mathrm{h}}\right)^{\mathrm{T}} = \left(h_{\mathrm{xy}}, h_{\mathrm{z}}\right), \quad (2.23)$$

where $h_{\mathrm{xy}} = h\left(\sin\theta_{\mathrm{h}}\cos\phi_{\mathrm{h}}, \sin\theta_{\mathrm{h}}\sin\phi_{\mathrm{h}}\right)^{\mathrm{T}}$ is in-plane component of the field $\boldsymbol{h}$. By pinning the spins with $n_{\mathrm{z}} = -1$ at points $(0, 0)$ and $(R, 0)$ which corresponds to the centers of two Sks and varying ϕ_{h} one can calculate the energy of the system as a function of only two parameters (R, ϕ_{h}). These two parameters, inter-soliton distance, R, and field phase, ϕ_{h}, can be interpreted as some polar coordinates that define the corresponding Cartesian local coordinates $(x', y') = (R\cos\phi_{\mathrm{h}}, -R\sin\phi_{\mathrm{h}})$ (see Fig. 2.2 **a**).

The interaction energy can be calculated as the total energy minus the self energies of two isolated solitons. In Figure 2.2 **b**, **c** and **d** I show representative example for the inter-skyrmion interaction potential for the cases of Sk-Sk, Sk-Ask, and Ask-Ask, respectively. The distinctive feature of the interactions is their oscillatory behaviour that is absent in the case of the perpendicular magnetic field. The minima of the energy corresponds to stable configurations that are shown on Fig. 2.2 **e**-**g**,**h**, **i**, **k**, **l**. The numerical analysis shows only the nearest metastable states, but from the asymptotic expansion, one can conclude that there are infinitely many of such local minima, strictly speaking.

At the short distances, Sk-Sk interaction is always repulsive, Fig. 2.2 **b**, that is not the case for Sk-Ask and Ask-Ask pairs. At a certain displacement of the π-skyrmion and the antiskyrmion, they can annihilate Fig. 2.2 **j**, as real particle and antiparticle. On the other hand, they can create *a chiral droplet* (CD) – a topologically trivial soliton [68], which I will discuss in **Section** 4.2. The corresponding annihilation channels are seen in the energy plot Fig. 2.2 **c**. At point **j** there is not a barrier that prevents moving the π-skyrmion and the antiskyrmion towards each other. A similar situation happens with the Ask-Ask pair, but instead of annihilation, there are fusion channels Fig. 2.2 **m**. They correspond to the displacements of two antiskyrmions that lead to their attraction and formation of the stable solitons with $Q = +2$. For details of such solitons, see **Chapter** 3.

2.2.2 The case of perpendicular field

The existence of stable antiskyrmion Fig. 2.1 **j** in the perpendicular magnetic field inside a small range of h allows studying the inter-skyrmion interactions also in the absence of the field tilt. Since, in this case, the phase of the magnetic field ϕ_{h} is not defined, I use another approach in the numerical experiment. In particular, the interaction strength between Sks is calculated at intermediate point R, equidistant from two skyrmions, see Fig. 2.3 **a**. The first soliton is placed at the origin, while the position of the second one is defined by distance to the origin, $2R$, and polar angle, ϕ.

To calculate the interaction between solitons, I use the semi-analytic approach based on the asymptotic expansions (2.10). The functional dependence of the polar angle Φ differs for skyrmion and antiskyrmion: for the π-skyrmion, $\Phi = \phi + \pi/2$ while for the

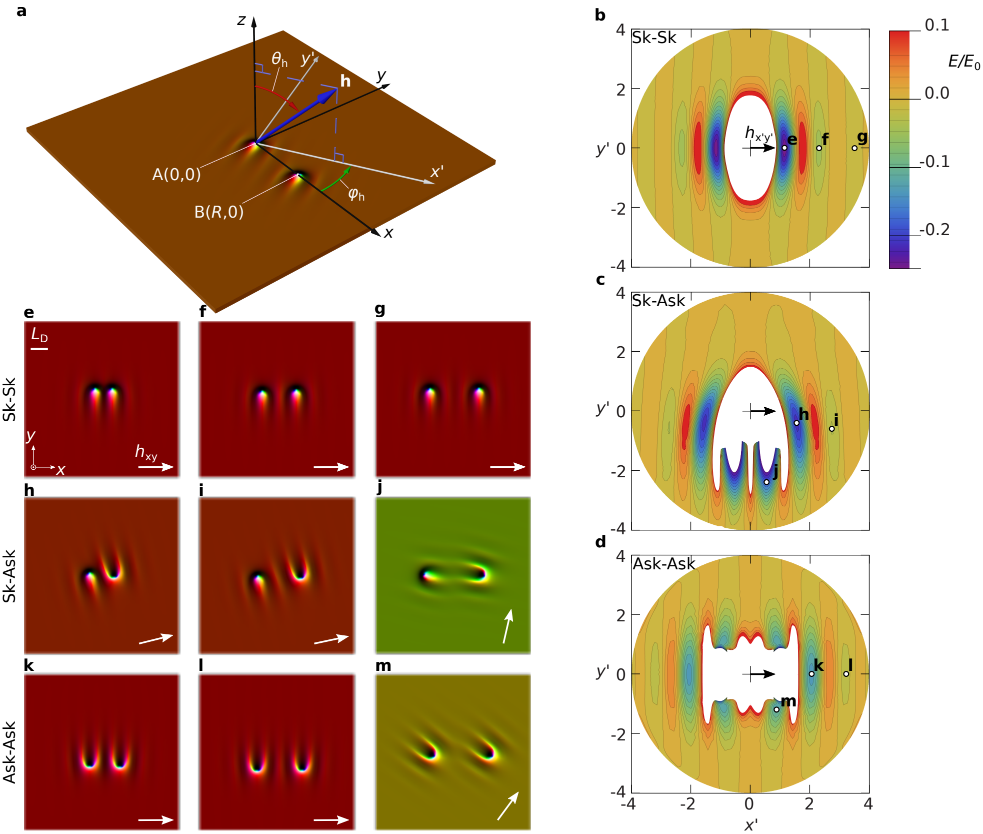

Figure 2.2: **Skyrmion interactions in the tilted magnetic field**. **a** Simulated domain of size $L_\mathrm{x} = L_\mathrm{y} = 20L_\mathrm{D}$, $L_\mathrm{D} = 52a$. The points A and B are the positions of two pinned spins with $\mathbf{n} = (0, 0, -1)$ at the center of two interacting Sks. **b**-**d** are the potential energies of two interacting Sks calculated for $\theta_\mathrm{h} = \pi/3$, $h = 0.8$, $u = 0$ and given in the local coordinate frame $(x', y') = (R\cos\phi_\mathrm{h}, -R\sin\phi_\mathrm{h})$, in which the in-plane component of the field is always pointing along x'-axis. **b**,**c** and **d** correspond to Sk-Sk, Sk-Ask and Ask-Ask interactions, respectively. The spin textures in **e**-**i**, **k**, **l** illustrate equilibrium states obtained by energy minimization without spins pinning. These states correspond to the local energy minima marked accordingly in **b**-**d**. The spin textures in **j** and **m** have been obtained with pinned spins and illustrate the states that are precursory for the fusion of two solitons. All images in **e**-**m** have identical sizes and show only the central part of the simulated domain. The white arrows in the bottom left corner indicate the direction of the in-plane component of the applied magnetic field, h_xy. This figure has been published in [61].

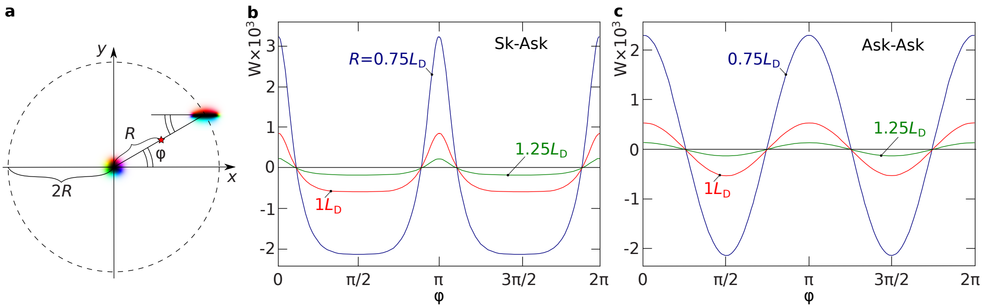

Figure 2.3: **Skyrmion interactions in the perpendicular magnetic field.** **a** Schematic representation of two interacting solitons (π-skyrmion and antiskyrmion) at the distance $2R$ at parameters $h = 0.62$, $u = 0$. The mutual orientation of the solitons is defined by azimuthal angle ϕ. **b** and **c** are the potential w calculated at the middle point between particles (star symbol in **a**) as functions of angle ϕ, for Sk-Ask in **b** and Ask-Ask in **c**. Note, $w < 0$ and $w > 0$ correspond to repulsion and attraction, respectively. This figure has been published in [61].

antiskyrmion $\Phi = -\phi - \pi/2 + \mathcal{F}(\phi)$. Function $\mathcal{F}(\phi)$ can be written in the form of Fourier series due to its periodicity. The corresponding amplitudes of the harmonics are found by fitting the solution for the antiskyrmion obtained by direct energy minimization. The exponential prefactors in functions Θ are calculated from the fit to the solutions found with numerical methods. Rewriting the asymptotics for two solitons in the form of magnetization vectors $\boldsymbol{n}_1(R,\phi)$ and $\boldsymbol{n}_2(R,\phi)$, one can consider the energy density assuming the linear adding of the vector fields, i.e. $w([\boldsymbol{n}_1(R,\phi) + \boldsymbol{n}_2(R,\phi)]/2)$. These plots are presented in Fig. 2.3 **b**, **c** for the cases of Sk-Ask and Ask-Ask interactions, respectively. In this approach, the sign of w defines the character of inter-soliton interaction: $w < 0$ repulsion, $w > 0$ attraction.

As it is shown on Fig.(2.3) **b**, **c**, there are regions with $w > 0$ in both cases of interactions Sk-Ask and Ask-Ask. That means at such displacement of solitons, they tend to move towards each other and either form a new coupled state or annihilate. Asymptotically that is true for big inter-solitonic distances because all curves $w(R,\phi)$ intersect at common points and region with $w > 0$ conserves up to infinity $R \to \infty$. Geometric place of points $w(R,\phi) = 0$ represents straight lines and corresponds to such displacements of the Sks at which they do not interact with each other. For instance, in such a case, the EL equations (1.13) can be solved to obtain the stable non-interacting pairs Sk-Ask and Ask-Ask. Note, in the case of two π-skyrmions, it does not seem to be possible due to the repelling interaction. Although the exponential localization of Sks leads to the exponential decay of their interaction energies, the numerical calculations often cannot catch such a tiny effect.

As follows from above, the presence of antiskyrmion in the system makes interactions between solitons more nontrivial compared to π-skyrmions. At the same time, the short stability range of the antiskyrmion brings in certain complications for its numerical and analytical study. Thereby it is natural to study the antiskyrmion more deeply and find the conditions allowing one to expand its stability range.

2.2.3 The role of magnetic anisotropy

The results discussed in the previous sections obtained at $u = 0$ remain true also at some non-zero anisotropy. The existence of the antiskyrmion at $\theta_\mathrm{h} = 0$, $h \neq 0$, $u \neq 0$ can prove the existence of the antiskyrmion at any tilt of the magnetic field because of continuity of the transformations Fig. 2.1 **e-i** and **j-n**. The corresponding stability range of the antiskyrmion at different u is given in Fig. 2.4.

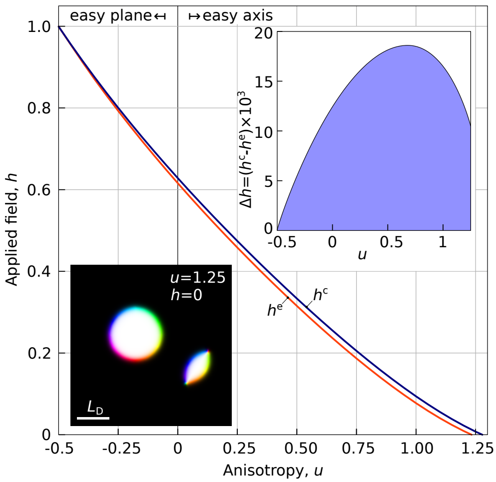

Figure 2.4: **Antiskyrmion stability diagram**. The range of existence for the antiskyrmion in the perpendicular magnetic field, h, is bounded by the fields of elliptic instability h^e and collapse, h^c. The field range Δh (right top inset) converges to zero at Bogomol'nyi point, $u = -0.5$ and $h = 1$. The bottom left inset illustrates the coexistence of the π-skyrmion and the antiskyrmion without fusion at large distances for zero magnetic field and strong perpendicular anisotropy. This figure has been published in [61].

The stability range of antiskyrmion is bounded by the elliptical instability and collapse fields. The corresponding field range, Δh, is shown in the top inset as a function of u. The maximal value of Δh corresponds to easy-axis anisotropy $u \simeq 0.65$. The instability curves intersect at so-called Bogomol'nyi point $(h = 1, u = -0.5)$ [47], where the model become explicitly solvable, see **Section** 1.2. Remarkably, at the strong easy-axis anisotropy, the antiskyrmion can be stabilized even without a magnetic field, see bottom inset in Fig. 2.4. At these conditions, the antiskyrmion is more compact than the π-skyrmion. The antiskyrmion solution's stability confirms that one can realize the effect of turning skyrmion inside out in a wide range of parameters (h, u). Therefore, the model's presence of anisotropy in the range $-1 \leq u \lesssim -1.24$ does not lead to any qualitatively new physical phenomena absent in $u = 0$ case discussed at the beginning of this Chapter. However, for completeness of the study $u \neq 0$ case, I derive the EL equations and provide some of their analysis below.

2.2.4 Lagrange-Euler equations in the general case

By generalizing the analytic approach for $u = 0$, (2.4), (2.5), one can parameterize the $\boldsymbol{n}$ field as follows

$$\boldsymbol{n} = \begin{pmatrix} \cos\Theta_{\mathrm{h}}\sin\Theta\cos\Phi + \sin\Theta_{\mathrm{h}}\cos\Theta \\ \sin\Theta\sin\Phi \\ -\sin\Theta_{\mathrm{h}}\sin\Theta\cos\Phi + \cos\Theta_{\mathrm{h}}\cos\Theta \end{pmatrix}, \tag{2.24}$$

and obtain the following EL equations for Θ, Φ and boundary condition for Θ in the most general case of non-zero anisotropy

$$\begin{cases} \triangle\Theta + 4\pi\sin\Theta\left(\boldsymbol{n}\cdot\nabla\Phi - \pi h\cos\left(\theta_{\mathrm{h}} - \Theta_{\mathrm{h}}\right)\right) - \dfrac{\sin 2\Theta}{2}\left(\nabla\Phi\right)^2 \\ +4\pi^2 h\sin\left(\theta_{\mathrm{h}} - \Theta_{\mathrm{h}}\right)\cos\Theta\cos\Phi - 4\pi^2 u\sin 2\Theta_{\mathrm{h}}\cos 2\Theta\cos\Phi \\ -4\pi^2 u\left(\cos^2\Theta_{\mathrm{h}} - \sin^2\Theta_{\mathrm{h}}\cos^2\Phi\right)\sin 2\Theta = 0, \\ \triangle\Phi\sin^2\Theta - 4\pi\boldsymbol{n}\cdot\nabla\Theta\sin\Theta + \nabla\Theta\cdot\nabla\Phi\sin 2\Theta \\ -4\pi^2 h\sin\left(\theta_{\mathrm{h}} - \Theta_{\mathrm{h}}\right)\sin\Theta\sin\Phi + 2\pi^2 u\sin 2\Theta_{\mathrm{h}}\sin 2\Theta\sin\Phi \\ -4\pi^2 u\sin^2\Theta_{\mathrm{h}}\sin^2\Theta\sin 2\Phi = 0, \\ \Theta\left(x, \pm\infty\right) = \Theta\left(\pm\infty, y\right) = 0, \end{cases} \tag{2.25}$$

It is easy to see that for $u = 0$ and $\Theta_{\mathrm{h}} = \theta_{\mathrm{h}}$, equations (2.25) transform into (2.5). Taking into account (2.2) and that at the spatial infinity $|\Theta| \ll 1$, $|\partial\Theta| \ll 1$, the system (2.25) becomes

$$\begin{cases} \triangle\Theta + 4\pi\Theta\left(\dfrac{\partial\Phi}{\partial x}\sin\Theta_{\mathrm{h}} - \pi h\cos\left(\theta_{\mathrm{h}} - \Theta_{\mathrm{h}}\right)\right) - \Theta\left(\nabla\Phi\right)^2 \\ -8\pi^2 u\Theta\left(\cos^2\Theta_{\mathrm{h}} - \sin^2\Theta_{\mathrm{h}}\cos^2\Phi\right) = 0, \\ \Theta\triangle\Phi - 4\pi\dfrac{\partial\Theta}{\partial x}\sin\Theta_{\mathrm{h}} + 2\nabla\Theta\cdot\nabla\Phi - 4\pi^2 u\Theta\sin^2\Theta_{\mathrm{h}}\sin 2\Phi = 0. \end{cases} \tag{2.26}$$

To simplify the above equation I introduce the notations $\Phi(x, y) = \Psi(x, y) + 2\pi x\sin\Theta_{\mathrm{h}}$ and $\lambda^2 = h\cos\left(\theta_{\mathrm{h}} - \Theta_{\mathrm{h}}\right) - \sin^2\Theta_{\mathrm{h}} + u\left(2 - 3\sin^2\Theta_{\mathrm{h}}\right)$. With that, the system (2.26) can be written as

$$\begin{cases} \triangle\Theta - 4\pi^2\lambda^2\Theta - \Theta\left(\nabla\Psi\right)^2 = -4\pi^2 u\Theta\sin^2\Theta_{\mathrm{h}}\cos 2\Phi, \\ \Theta\triangle\Psi + 2\nabla\Theta\cdot\nabla\Psi = 4\pi^2 u\Theta\sin^2\Theta_{\mathrm{h}}\sin 2\Phi. \end{cases} \tag{2.27}$$

The expressions on the right-hand side of the equations in (2.27) is a fast-oscillating function at $|x| \to \infty$. Although the exact form of solutions satisfying (2.27) has not been found the function $\Phi_{\pm} = \pm\left(\phi + \dfrac{\pi}{2}\right) + 2\pi x\sin\Theta_{\mathrm{h}} + c_1\cos\phi$ provides a good fit for numerical data. The latter I prove by numerical analysis of the solutions provided in Appendix A4 . At the same time, naively choosing the expression for Θ in the form of Bessel function $K_1(2\pi\lambda r)$ did not lead to a positive result. Thereby, further analysis of (2.27) is required.

2.3 Skyrmions at strong easy-plane anisotropy

As follows from above, the presence of a tilted magnetic field reveals new Sk properties. The reason for that is the tilt of the FM background. The presence of strong easy-plane anisotropy can cause the non-zero tilt Θ_{h} of the vacuum even in the case of the perpendicular magnetic field. This can be seen from the condition (2.2), where setting $\theta_{\mathrm{h}} = 0$ one gets two possible solutions: $\Theta_{\mathrm{h}} = 0$ (FM state) and $\cos\Theta_{\mathrm{h}} = -h/2u$ (tilted FM state). The energies of both solutions are invariant under rotation about the z-axis by an arbitrary phase angle Φ_{n}. From the analysis of the second-order derivative $\mathrm{d}^2\mathcal{E}/\mathrm{d}\Theta_{\mathrm{h}}^2$ we conclude that at $u > -h/2$ the minimum corresponds to the state with $\Theta_{\mathrm{h}} = 0$, while at $u < -h/2$ the minimum corresponds to $\cos\Theta_{\mathrm{h}} = -h/2u$. Strictly speaking, both solutions are not global minima of the functional (2.3) because we exclude from consideration other phases, e.g., helical spin spiral. In this Section, I ignore this fact and consider the properties of Sks imposed in the tilted FM state at $u < -h/2$. Some representative examples of π-skyrmion and antiskyrmion solutions obtained at $u = -2$ by direct energy minimization are shown in Fig. 2.5.

In the case of $h = 0$, from positiveness of the expression for λ^2 in (2.27) it follows that $u < -1$. Note that this estimation provides only the upper bound for the anisotropy, below which one can find stable well-localized solitons.

Strictly speaking, these magnetic textures have more in common with pairs of vortices and pairs of antivortices rather than with magnetic solitons. One can easily distinguish two regions around up and down cores (white and black spots) with a certain chirality of the vector field. In total, there are 2 vortices (see Fig. 2.5 **e**, **f**) and 2 antivortices (see Fig. 2.5 **g**, **h**). They can be characterized by the following values of polarity, p, and vorticity, ν: **e** $p = -1$ and $\nu = -1$, **f** $p = 1$ and $\nu = 1$, **g** $p = -1$ and $\nu = 1$, **h** $p = 1$ and

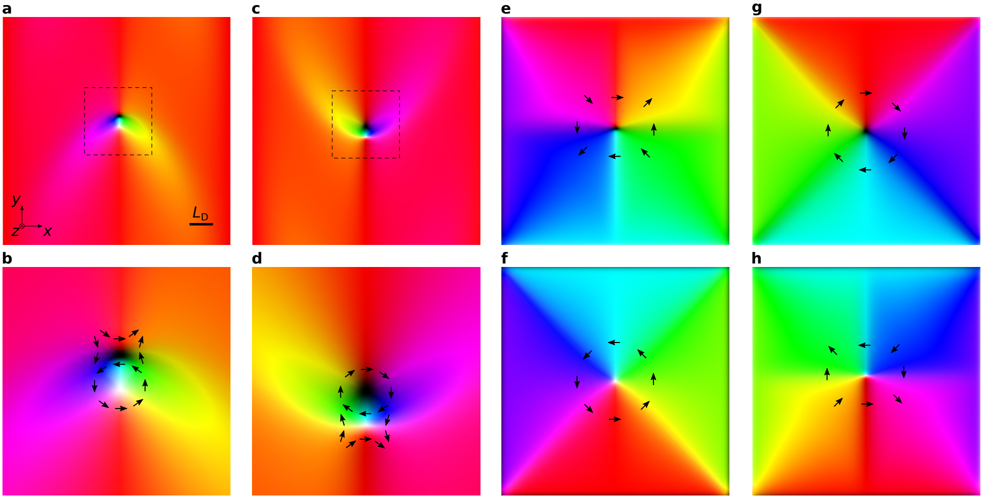

Figure 2.5: **Vortices, antivortices and their pairs**. The equilibrium spin textures obtained by direct energy minimization of functional (2.3) for zero magnetic field, $h = 0$, and strong easy-plane anisotropy $u = 2$. The simulation domain of size $L_\mathrm{x} = L_\mathrm{y} = 10L_\mathrm{D}$ is used with $L_\mathrm{D} = 52a$ (see the scale bar on **a**). The π-skyrmion and the antiskyrmion that represent pairs of vortices and antivortices with a total topological charge $Q = 1$ in **a** and $Q = +1$ in **c**. Their zoomed textures are shown in **b** and **d**, respectively. The isolated vortices and antivortices are shown on **e**, **f** and **g**, **h**, respectively. The simulations have been performed with PBCs for **a**-**d**, and with open in xy boundaries for **e**-**h**. This figure has been published in [61]

$\nu = -1$. The pair of vortices **e**, **f** form the π-skyrmion shown on **a** and **b**, while a pair of antivortices **g**, **h** form the antiskyrmion shown on **c** and **d**. Any vortex-antivortex pair annihilates. The stability of vortex (or antivortex) pairs can be achieved in the domain with PBC because of the pair localization.

On the contrary, a single vortex or single antivortex can be stabilized in the domain with open boundary conditions only. That is because vortices are non-localized in the 2D and require the presence of additional "defects" in the system, for instance, free boundaries.

Vortices and antivortices serve as elementary building blocks not only for the π-skyrmion and the antiskyrmion but for more complicated textures. Some examples of such complex textures are shown in Fig. 2.6 **a**-**h**. Vortex with $p = 1$, $\nu = 1$ and additional modulation around the core is shown in Fig. 2.6 **a**. Noticeably, it remains stable even with the presence of another vortex pair **b**. Configurations with three vortices are shown in **c** and **d**. Any even number of vortices and antivortices that form a coupled state can interact with a single vortex (see **e** and **f**). These coupled states may resemble a skyrmion chain **f**-**h**. The result of energy minimization starting from the randomly

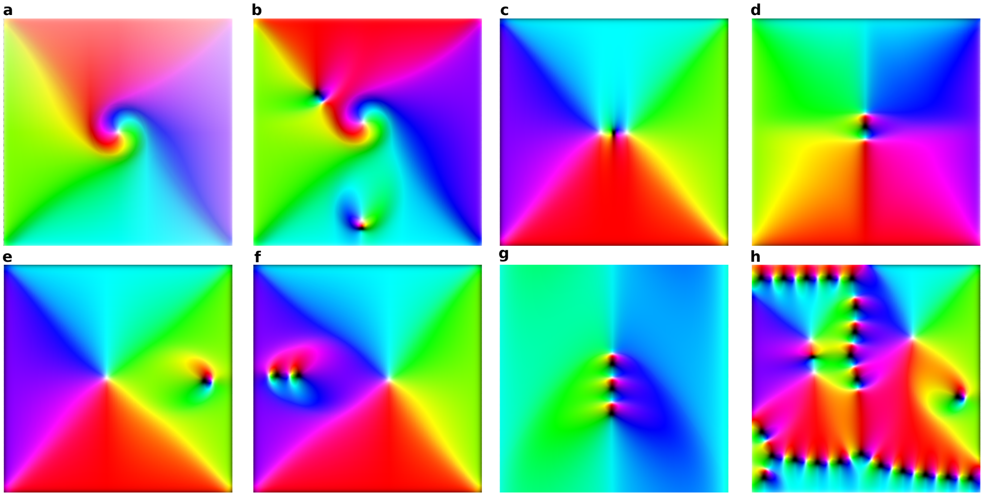

Figure 2.6: **Multi-vortex configurations**. **a** A vortex with $p = 1$, $\nu = 1$. **b** The same vortex as in **a** with two different vortex-antivortex pairs. **c** A vortex triplet state is composed of two vortices and one antivortex. **d** A vortex triplet state is composed of two antivortices and one vortex. **e** A state composed of three different types of vortices, where a mutually attractive vortex and antivortex form a localized pair on the right with a topological charge of the pair $Q = +1$. That pair repel the vortex on the left. **f** Another example of the state composed of three different types of vortices. Two vortices and two antivortices form a chain on the left with a topological charge $Q = 2$. **g** A chain of alternating vortices and antivortices. **h** An example of a complex state obtained after full energy minimization starting from a random spin distribution. The state contains all four types of vortices and antivortices. All simulations have been performed on the domain with open boundaries. This figure has been published in [61].

distributed spins can lead to the magnetic texture containing all four types of vortices (see **h**).

Therefore, 2D chiral magnets at strong easy-plane anisotropy can host various magnetic textures composed of four basic vortices. The inter-vortex interactions are characterized by slowly decreasing potentials, which give rise to a rich diversity of states. In many cases, easy-plane anisotropy effectively describes the presence of demagnetized fields. These fields slowly decrease with the distance that causes similar behaviour in vortex interaction potentials. The detailed study of magnetic textures at the presence of strong easy-plane anisotropy is beyond the scope of the present study. In the following chapters, I mainly concentrate on the situations when the anisotropy is either zero or its presence does not lead to qualitatively new physical phenomena.

2.4 Conclusions

In this Chapter, I have presented the main results related to the properties of the π-skyrmion and the antiskyrmion in the tilted FM vacuum, caused by either the tilted magnetic field or easy-plane anisotropy. For the first case, the stability diagram for the π-skyrmion has been calculated numerically and approaching the limit of the micromagnetic model. Analytical study of single π-skyrmion in micromagnetic model shows that its energy is bounded by Belavin-Poliakov soliton energy in some range of magnetic field tilt values and due to this prevents the π-skyrmion from the collapse even at $h \to \infty$. The analysis based on the numerical methods shows that statically stable π-skyrmion exists in the whole range of magnetic field tilts if its amplitude is tuned. Moreover, I presented the effect of turning π-skyrmion inside out, induced by changing the tilt angle of the external magnetic field between 0 to π. The new soliton obtained by this method represents the mirror version of the antiskyrmion, which is also stable in the whole range of magnetic field tilts. Thereby, the model of the chiral magnet is an example of a system where both particle and antiparticle can coexist and interact non-trivially.

The problem of interactions between these solitons is studied in detail numerically and analytically. The analytical study utilizes the found asymptotic expansions for the π-skyrmion and the antiskyrmion solutions. I presented the numerical calculations of the inter-soliton interactions for the pairs of Sk-Sk, Sk-Ask, and Ask-Ask. The common feature of all interaction potentials is their oscillatory behaviour, which is absent in the case of the perpendicular magnetic field. In particular, the presence of the non-zero tilt of the magnetic field can lead to the formation of coupled states with different equilibrium distances between the particles. For the Sk-Ask pair, the interaction potential is characterized by the presence of the annihilation channels corresponding to such solitons displacements that lead to their disappearing. On the contrary, for the Ask-Ask pair, such channels correspond to a fusion of antiskyrmions and lead to the appearance of a new soliton.

For the case of strong easy-axis anisotropy, both π-skyrmion and antiskyrmion do not seem to be elementary objects and decay into vortex-antivortex pairs. These vortices represent building blocks for other diverse magnetic textures that can be stabilized, for instance, Sk chains.

3 Diversity of chiral skyrmions

In this Chapter, I discuss the variety of Sks in the 2D chiral magnets [19]. The first **Section** 3.1 reveals the interconnection between the notion of Bloch lines in bubble material and CKs in chiral magnets. **Section** 3.2 systematically describes different classes of Sks in terms of solutions of the Bogomol'nyi equation. The last **Section** 3.3 provides information about interactions between CKs hosted by the isolated stripe.

3.1 Domain walls and chiral kinks

3.1.1 Domain walls

In this Section, I describe an alternative approach for the classification of Sk solutions based on the concept of the oriented DW contours – the lines that separate the magnetic vector field into domains according to particular rules. In particular, in the case of the perpendicular magnetic field, it is reasonable to use the contours, C_i, that separate regions with $n_z > 0$ and $n_z < 0$. The corresponding contour lines $n_z(x, y) = 0$, or $\Theta(x, y) = \pi/2$, can be either closed in the case of localized objects (solitons) or infinitely long in the case of extended objects, e.g., infinite DWs. Generally speaking, the choice of such contours is arbitrary and, for instance, in the presence of a tilted magnetic field, the definition of a contour might be different. In this Chapter, the magnetic field is considered to be applied in the positive direction of z-axis, and values of anisotropy are so to keep the vacuum as $\boldsymbol{n} = \mathbf{e}_z$, i.e. $h + 2u > 0$. The orientation of the contour, $\mathrm{d}\boldsymbol{r}$, is chosen so that the positive domain, $n_\mathrm{z} > 0$, is on the left and the negative domain, $n_\mathrm{z} > 0$, is on the right as illustrated in Fig. 3.1. The magnetization along such a contour is exclusively defined by the function $\Phi(\boldsymbol{r})$. Its gradient, $\nabla\Phi$, carries essential information and defines the geometrical properties of the contour.

The contour may contain special points at which $\nabla\Phi$ has maximum. In the case of a Bloch-type domain wall as in Fig. ,3.1 the magnetization in these pints is perpendicular to the tangent of the contour, $\boldsymbol{n} \perp \mathrm{d}\boldsymbol{r}$. In the theory of bubble domains, such points of the DW are called *Bloch lines*. In the case of finite thickness film, Bloch lines represent the

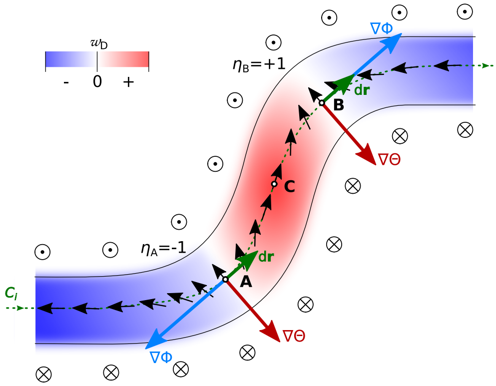

Figure 3.1: **Schematic representation of a section of the domain wall**. The black arrows are magnetization vector $\mathbf{n}$ along the oriented contour C_i (green dotted line), which divides the plane between the positive domain, $n_z > 0$ (on top) and negative domain $n_z < 0$ (at the bottom). The orientation of the contour $\mathrm{d}\boldsymbol{r}$ is chosen so that the positive domain is on the left and the negative domain is on the right. The red-white-blue colours represent the variation of the chiral energy density, which is vanishing at Bloch lines marked as A and B. The handedness index of the Bloch lines is defined as $\eta = \mathrm{sign}(\nabla\Phi\cdot\mathrm{d}\boldsymbol{r})$. Along the path between A and B, the vector $\nabla\Phi$ changes the direction with respect to $\mathrm{d}\boldsymbol{r}$ and vanishes at point C while w_{D} at this point reaches the maximal value. This figure has been published in [19].

lines, while in the 2D case, they degenerate into points. Bloch lines differ by handedness, defined as $\eta = \mathrm{sign}(\nabla\Phi \cdot \mathrm{d}\boldsymbol{r})$. On the closed domain walls, Bloch lines always emerge in pairs. The pair shown in Fig. 3.1 corresponds to opposite handedness, η. Such a pair can smoothly unwind and represents the configuration that is typically unstable. In the case of a nonchiral FM, the two possible magnetization directions between Bloch lines are energetically equivalent, which is not the case in chiral magnets. The DMI favours the fixed chirality of magnetic modulations. Fig. 3.1 schematically shows the DMI energy density distribution (1.11) for the particular case of the DW with two Bloch lines. In the following Section, I show how the presence of DMI affects the shape of the contours containing Bloch lines.

3.2 Skyrmions diversity

3.2.1 Closed domain walls

This Section considers the simplest case of localized magnetic texture, which a single closed contour can describe. The first two columns of images in Fig. 3.2 show a schematic representation of magnetic skyrmion or bubble domain. The bubble domains depicted in Fig. 3.2 **a** and **b** are stable and energetically equivalent. On the contrary, in the case of the chiral magnet with the positive constant of bulk DMI, soliton depicted in **b** can exist while π-skyrmion depicted in **a** will be unstable. The magnetization vector field for the skyrmion schematically shown in **b** is given in **c**. This configuration is obtained by direct energy minimization. The DMI energy density corresponding to this case is presented in **d**. Noticeably, the DMI energy density is negative in the whole xy space around the skyrmion and converges to zero at a large distance from the soliton. The same behaviour of the DMI energy density holds for $k\pi$-skyrmions and skyrmion bags [17, 18]. The situation changes with the presence of Bloch lines.

Let us consider the bubble domain depicted in **a**. One can add to it different number of Bloch line pairs as indicated in **e**, **i**, and **m**. The textures in **e** and **m** contain only one pair of Bloch lines, while configuration in **i** has two pairs. A characteristic feature of Bloch lines in the bubble domains is their equidistant distribution over the corresponding contour of the DW. This remains true if the DMI is absent in the system. It is shown schematically with red and blue colour how DMI density would be distributed if chiral interactions were present. To increase the energy gain of DMI contribution, the system will reshape the regions of different chiralities in between Bloch lines as shown in **f**, **j**, **n**. To reduce the area with positive DMI energy, the Bloch lines approach each other and form a so-called *chiral kink* (CK). The topological charge of the CK depends on the sign of the handedness index of the Bloch lines. For instance, in the case of $\eta = +1$, the CK itself is characterized by charge $Q = +1$. Because of that, the total topological index of the skyrmion in **f** has a total topological index $Q = 0$. When the Bloch lines have handedness index, $\eta = -1$, the CK has $Q = -1$ and can be called *chiral antikink* (CA). Because of that the skyrmion in **n** has total topological index, $Q = -2$. The topological charge for CK (and CA) can be understood as a change in the topological charge of the host soliton with and without the kink. For instance, by adding one CK to the π-skyrmion depicted in **c** one gets a new soliton shown in **g** of topological charge $Q = 0$. Despite its triviality, this soliton has a lot of interesting properties, which I will discuss in the following chapters. It has been called in literature *chiral droplet* and seems to be the simplest and most compact soliton with CK. π-skyrmion with two CKs depicted in **k** represents the antiskyrmion, $Q = +1$, which had been discussed in the previous Chapter. π-skyrmion with single CA depicted in **o** has topological charge $Q = -2$. The configurations **g**, **k** and **o** correspond to relaxed states or local minima of the energy functional (1.17). The corresponding distributions of DMI energy density are given in **h**, **l** and **p**, respectively. As one can see, the regions of positive energy are present in all cases when soliton contains CK or CA. In the previous Chapter, I showed the attraction between the π-skyrmion and the antiskyrmion. Such interaction between the particles can be explained by the positiveness of DMI energy density caused by the presence of CKs. From general considerations, all solitons containing CKs (or CAs) should have

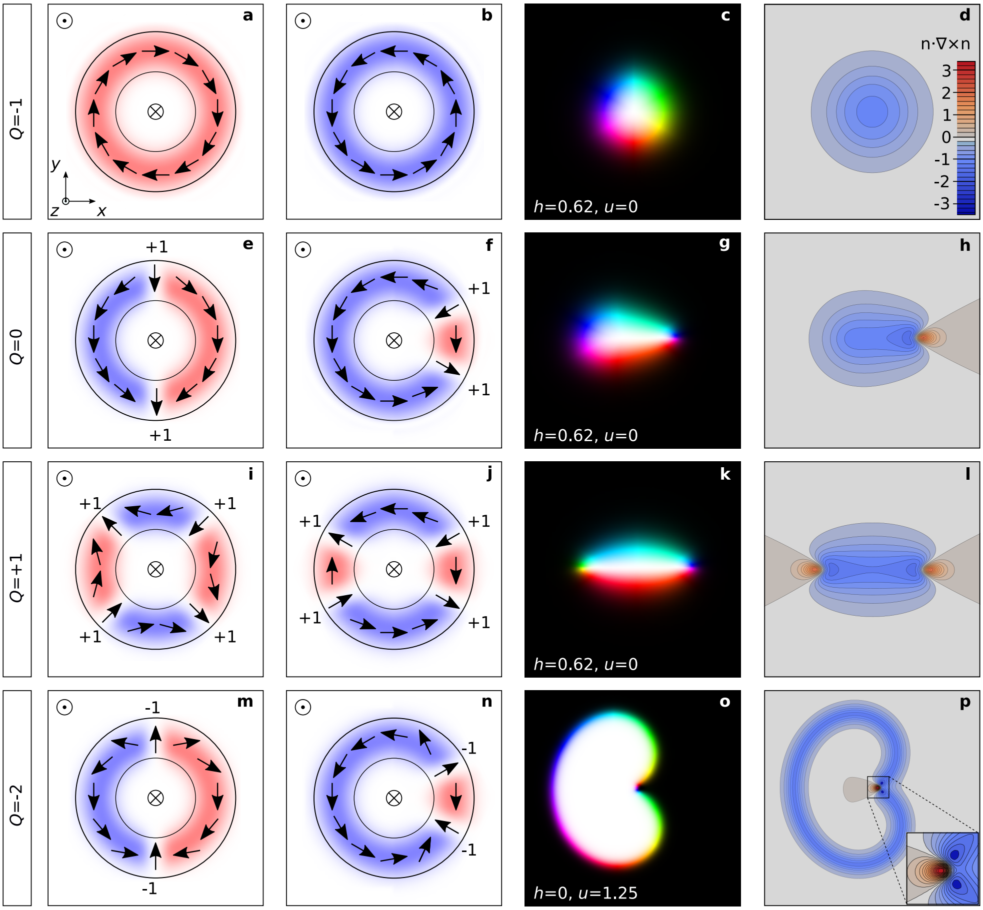

Figure 3.2: **Bloch lines and chiral kinks**. Magnetic Sks with CKs in 2D magnet with DMI supporting right-handed Bloch-type modulations. Each row illustrates the Sks of a particular topological charge, as indicated on the left. The first and the second columns schematically illustrate the orientation of the spins around the bubble domain core or Sk at $D \to 0$ and $D \neq 0$, respectively. The bluish and reddish regions in the schematic images indicate the negative and positive energy density of DMI, respectively. The third column represents the spin texture of the corresponding Sk obtained by direct energy minimization. All images are given on the same scale. The values of the external field, h, and uniaxial anisotropy, u, are indicated at the bottom of each image. The rightmost column contains the contour plots illustrating the distribution of scalar quantity $\boldsymbol{n}\cdot\nabla\times\boldsymbol{n}$ corresponding to the equilibrium spin texture shown in the third column. This scalar field up to a positively defined constant corresponds to the energy density of DMI. This figure has been published in [19].

similar interaction properties. The shown solutions with CKs are only some examples of solitons existing in chiral magnets. In the next Section, I discuss some other solitons and their properties.

The concept of closed contours provides an alternative approach for the classification of the skyrmions solutions. For closed contour, C_i, one can assign the winding number:

$$w\left(C_i\right)=\frac{1}{2\pi}\int_{C_i}\mathrm{d}\boldsymbol{r}\cdot\nabla\Phi, \tag{3.1}$$

where the direction of integration is determined by the orientation of the DW contour, C_i. These numbers may be noninteger or even infinite for curves going off to infinity, but they are necessarily integers for closed curves. In the case of the presence of the multiple DWs in the magnetic texture, e.g. skyrmion bags, one needs to add all corresponding winding numbers to get the total topological charge of the related spin texture,

$$Q=\sum_i w\left(C_i\right), \tag{3.2}$$

The topological charge definitions (1.24) and (3.2) give identical results in all the cases when Q is a well-defined quantity. The presence of CKs and CAs on the contour requires a generalization of the definition (3.2). To do this, one can introduce the kink number N_{kink}

$$N_{\text{kink}}\left(C_i\right)=w\left(C_i\right)-\iota(C_i), \tag{3.3}$$

where $\iota(C)$ is the geometrical winding number of the DW. By Hopf's Umlaufsatz [69], $\iota(C)=\pm1$ for closed walls, the sign coincides with the DW sign. In the case of positive (negative) wall it gives $N_{\text{kink}}(C_i)=w(C_i)-1$ ($N_{\text{kink}}(C_i)=w(C_i)+1$). The kink number depends on the handedness index η of the Bloch line and can be of an arbitrary sign. It is reasonable to distinguish positive and negative contours for solitons with a few domain walls, e.g., skyrmion bags. One can split the set of contours into a disjoint union and write,

$$Q=\sum_{i\in l^+}(N_{\text{kink}}(C_i)+1)+\sum_{i\in l^-}(N_{\text{kink}}(C_i)-1), \tag{3.4}$$

where l^+ and l^- are numbers of positive and negative contours. Expression (3.4) allows alternative classification of topological solitons in chiral magnets in terms of CKs on closed DWs.

A representative set of stable Sks with a different number of CKs is given in Fig. 3.3. The first column represents the host Sks without CKs: π-skyrmion **a**, skyrmionium **g** and skyrmion bag of $Q=+1$ **m**. These host Sks represent the solitons with 1, 2 and 3 closed DWs, respectively. The solitons on the right in each raw differ by the number and the position of CKs on the parent texture.

In the case of π-skyrmion, magnetic solitons **b-f** can be easily classified by the number of CKs. On the contrary, for the case of skyrmionium as a parent texture, **h-l**, it is more difficult because one needs to distinguish CKs on the inner and outer contour of the host

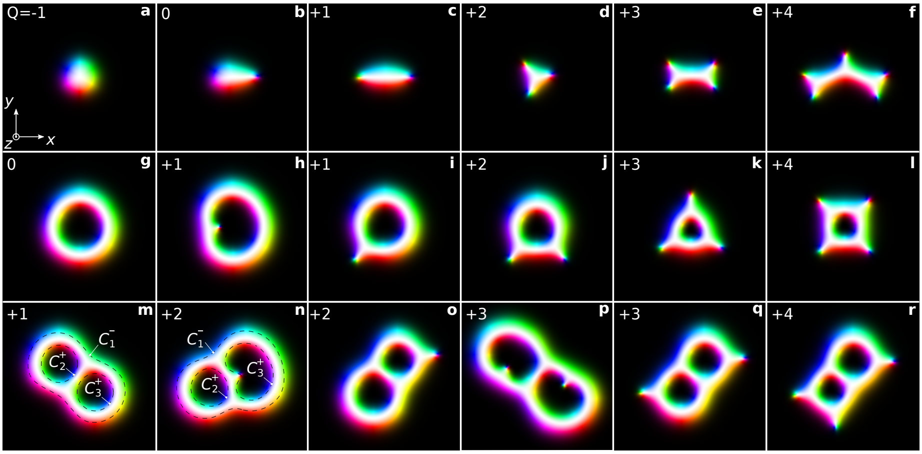

Figure 3.3: **Skyrmions with chiral kinks**. The images **a**, **g**, and **m** in the first column show the host Sks with $Q = -1$, 0, and +1. Other images in each row show the Sks with a different number of kinks at different places of the host spin texture. The solutions are obtained by direct energy minimization on the domain with the size of $L_\mathrm{x} = L_\mathrm{y} = 10L_\mathrm{D}$ and the mesh density $\Delta l = 64$. For all cases, the anisotropy is zero, $u = 0$. For Sk in **d** the external field $h = 0.61$, for Sks in **a**-**c** and **e**-**f** $h = 0.62$, and for Sks in **g**-**r** $h = 0.64$. In images **m** and **n**, the DWs of the spin-texture enter the expression for Q in Eq. (3.2) are highlighted. The superscript $\pm$ indicates the sign of the closed DW, see Eq. (3.4). This figure has been published in [19].

soliton. For instance, Sks shown on **h** and **i** are different in this sense, but have identical topological index, $Q = +1$. The situation becomes even more complicated when one deals with skyrmion bags, **n**-**r**, with a big number of inner and outer contours. Therefore, the classification of Sks can not be based just on morphological features, as the presence or absence of CKs and their numbers only, but should rely on more fundamental and mathematically strict arguments. In the following Section, I analyze skyrmion solutions based on studying analytical solutions of EL equations at the Bogomol'nyi point.

3.2.2 Holomorphic functions and skyrmions

In the **Section** 1.2 I provided basic concepts of the Bogomol'nyi equation derived for the 2D model of the chiral magnet at the external magnetic field $h = 1$ and easy-plane anisotropy of $u = -0.5$. Starting with the solutions of the latter equation (1.30) in **Section** 1.2 one can construct the following generalized ansatz function,

$$\frac{1}{\nu} = -\frac{i\pi\bar{\zeta}}{l_1} + f\left(\frac{\zeta}{l_2}\right), \tag{3.5}$$

where l_1 and l_2 are arbitrary scaling parameters. Note that in the exact solution at the Bogomol'nyi point, the parameter $l_1 = 1$ and parameter l_2 can be set arbitrary. The parameters l_1 and l_2 in (3.5) define the size of Sk and should be chosen taking into account the size of the simulated domain and the mesh density of the finite difference scheme. The function $f(\zeta)$ is holomorphic [70]. One can consider different classes of holomorphic functions that differ by the number of zeros and poles in the complex plane. Although the expression (3.5) is not a solution of EL equations outside the Bogomol'nyi point, it conserves the structure of Sk, and due to this, it still represents a good initial state – ansatz, for the subsequent energy minimization. As I show below, different classes of function $f(\zeta)$ provide the corresponding classification of Sk solutions.

The first class of $f(\zeta)$ function is a polynomial function that has no poles but has zeros,

$$f(\zeta) = 2\zeta^p, \tag{3.6}$$

where $p \in \mathbb{Z}^+$ – positive integer number. The function (3.6) has zero at $\zeta = 0$. This ansatz describes the soliton profiles with $p+1$ CKs distributed equidistantly along the contour.

The corresponding configurations for skyrmions obtained with ansatz (3.6) for p varying between 1 and 10 are presented in Fig. 3.4. The results of numerical energy minimization for these textures are given to the right from the initial configurations. The topological charge of obtained Sk solutions, in this case, coincides with the parameter p.

There are a few interesting aspects of these solutions. First of all, some morphologically similar Sks can be stabilized at different external magnetic fields, and the ranges of the fields may not overlap. The solitons depicted in Fig. 3.4 **a** and **b** are representative examples of such solutions. This feature distinguishes these solutions from skyrmion bags discussed earlier [17]. Another interesting aspect of the solutions depicted in Fig. 3.4 is the broken axial symmetry of the solutions with $p \geq 1$. It is worth noting that the initial configurations have rotational symmetry of order $p+1$ for any p. The equilibrium configurations obtained with the ansatz (3.6) differ from initial configurations. Note, for $p > 10$, the function (3.6) does not represent a good ansatz while the solutions of the same class but a larger number of CKs still exist as stable solutions. To obtain such solutions with direct energy minimization, one has to modify the ansatz function. This can be done by using more general polynomials $f(\zeta) = \prod_{j=1}^{p}(\zeta - a_j)$ with adjustable position of zeros a_j at the complex plane.

The second class of the Sk solutions can be obtained using trigonometric and exponential functions. They have an infinite number of zeros, but in any bounded region, the number of such zeros is finite, and hence these functions can describe some localized spin

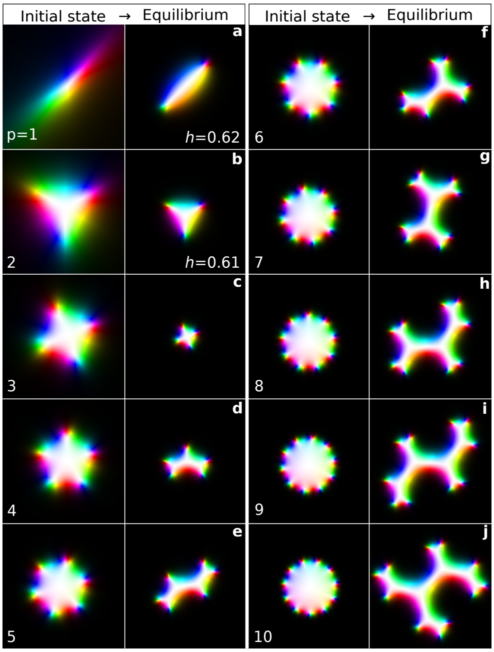

Figure 3.4: **Class of skyrmions** $f(\zeta) = 2\zeta^p$. The left image in each figure **a-j** is the initial magnetic textures which are described by (3.5) where $f(\zeta) = 2\zeta^p$ and the scaling parameters are $l_2 = 0.5$ and $l_1 = 1$. The right image is the equilibrium magnetization corresponding to a local minimum obtained after numerical energy minimization. The parameters of the system: $h = 0.62$ **f**, $h = 0.61$ **g** and $h = 0.65$ for all others, $u = 0$ in all cases. The size of simulated domain $8L_\mathrm{D} \times 8L_\mathrm{D}$ with $L_\mathrm{D} = 128a$. This figure has been published in [19].

textures. Below I will consider the ansatz based on sin function,

$$f(\zeta) = \alpha \sin(p\zeta), \tag{3.7}$$

where α is an arbitrary non-zero constant, and p is an integer number. The equilibrium Sks obtained with (3.7) are shown in Fig. 3.5.

The significant feature of these Sks is their stretched shape caused by the shape of the initial configuration. Interestingly, the solutions of this type with higher Q require a stronger magnetic field for their stabilization. The external field maintains the elongated shape of Sks and prevents the branched structure formation similar to that in Fig. 3.4. Such stretched Sks can have arbitrary high positive topological charges and sometimes exist at magnetic fields higher than the collapse field for skyrmion bags of the same Q.

Now instead of considering functions with zeros, let me take a look at functions with

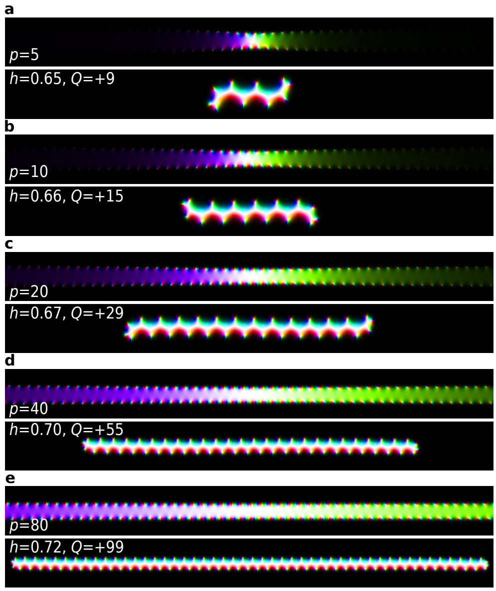

Figure 3.5: **Class of skyrmions** $f(\zeta) = \alpha \sin(p\zeta)$. The top image in each figure **a-e** is the initial magnetic textures which are described by (3.5) where $f(\zeta) = 0.025 \sin(p\zeta)$ and the scaling parameters $2l_2 = l_1 = p/20$. The bottom image is the equilibrium magnetization corresponding to a local minimum obtained after numerical energy minimization. The parameters of the system: domain size $16L_\mathrm{D} \times 2L_\mathrm{D}$, mesh density $\Delta l = 128$, $u = 0$, the values of external magnetic field h and topological charge Q after full energy minimization are indicated in the images. This figure has been published in [19].

poles. For instance, the choice of $f(\zeta)$ in the form,

$$f(\zeta) = \frac{1}{2\zeta^p}, \tag{3.8}$$

where p is positive integer defining the order of pole $\zeta = 0$, leads to the Sk solutions shown in Fig. 3.6. Although the function (3.8) is just an inverted version of (3.6), the magnetic textures look completely different. Ansatz with $p = 1$ converges to the skyrmionum, Fig. 3.6 **a**, while all textures with $p > 1$ converge to the skyrmionium with $p - 1$ CKs which equidistantly distributed over the inner contour, see **b-j**. The connection between parameter p and topological charge, Q, writes as $Q = p - 1$. Interestingly, function (3.8) is a suitable ansatz for any values of $p > 0$ that seems to be caused by a good matching of shapes of the initial and equilibrium states.

The last class of Sks, which I will consider here, is described by the function $f(\zeta)$, which has zeros and poles. An example of such functions can be written as

$$f(\zeta) = \frac{\zeta^{p-1}}{\zeta^p - 1}, \tag{3.9}$$

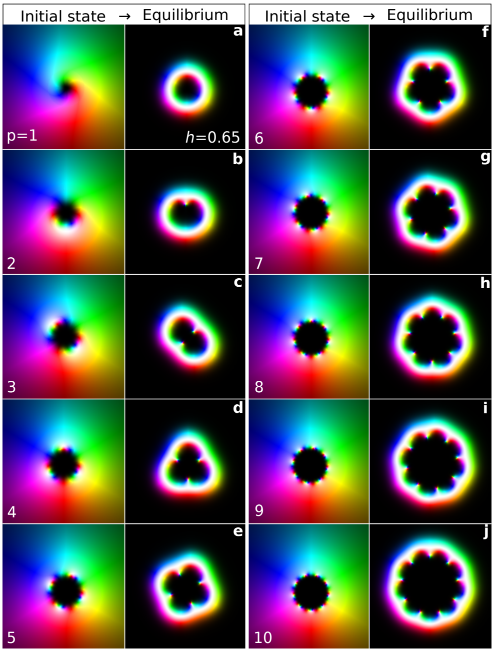

Figure 3.6: **Class of skyrmions** $f(\zeta) = 1/(2\zeta^p)$ The left image in each figure **a-j** is the initial magnetic textures which are described by (3.5) where $f(\zeta) = 1/(2\zeta^p)$ and the topological charge of the solution is $Q = p-1$. The right image is the equilibrium magnetization corresponding to a local minimum obtained after numerical energy minimization. The parameters of the system: $h = 0.65$, the size of simulated domain $8L_\mathrm{D} \times 8L_\mathrm{D}$ with $L_\mathrm{D} = 128a$. This figure has been published in [19].

where positive integer p defines the order of zero $\zeta = 0$ of $f(\zeta)$ which equals $p-1$. The number of poles, in this case, equals p. The initial states defined by (3.9) for $1 \leq p \leq 10$ and the corresponding relaxed configurations are given in Fig. 3.7.

The equilibrium texture in Fig. 3.7 **a** represents the CD soliton while the rest of solitons in **b-j** are skyrmion bags of positive topological charge, $Q = p-1$. The ansatz (3.9) works well for small p, but it fails for $p > 10$, which is caused by a significant difference in the structure of the initial and equilibrium configurations. In particular, the equilibrium texture of skyrmion bags might have very different shapes, while the initial ansatz always has rotational symmetry of order p. One can improve the ansatz (3.9) by fixing the positions of zeros a_j and poles b_j manually, $f(\zeta) = \dfrac{1}{\zeta - b_p}\displaystyle\prod_{j=1}^{p-1}\dfrac{\zeta - a_j}{\zeta - b_j}$. This function describes the shape of Sk bags much better and thus provides a good initial configuration for Sk bags with $Q > 10$.

Even though the presented above approach allows constructing very diverse Sks, it has some limitations. First of all, there is no one-to-one correspondence between the

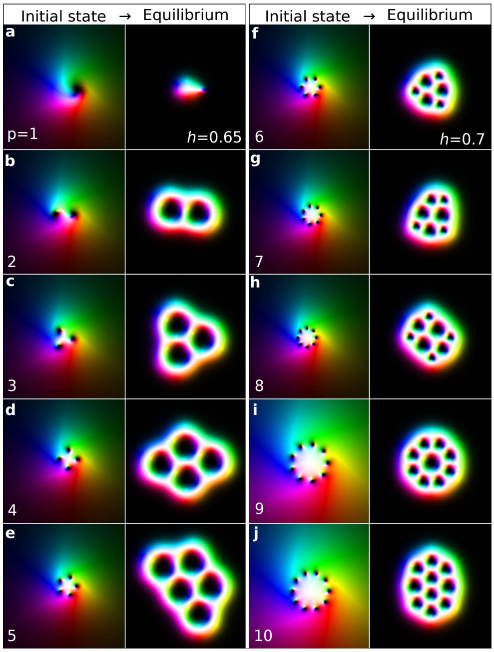

Figure 3.7: **Class of skyrmions** $f(\zeta) = \zeta^{p-1}/(\zeta^p - 1)$. The left image in each figure **a-j** is the initial magnetic textures which are described by (3.5), (3.9). The right image is the equilibrium magnetization corresponding to a local minimum obtained after numerical energy minimization. The parameters of the system: the size of simulated domain $8L_{\mathrm{D}} \times 8L_{\mathrm{D}}$ with $L_{\mathrm{D}} = 128a$, $u = 0$. For Sks in **a-e** the external field $h = 0.65$, for **f-j** $h = 0.7$. This figure has been published in [19].

whole diversity of the skyrmion solutions which exists in and outside the Bogomol'nyi point. It means that some solutions which do exist in a wide range of parameters may become unstable at the Bogomol'nyi point or simply cannot be obtained using the ansatz (3.5). The most representative example is 3π-skyrmion (the π-skyrmion imposed into the skyrmionium). It does not exist among solutions of the Bogomol'nyi equation. The reason for that is an absence of tension from the outer shell of the skyrmion bag. Nothing prevents skyrmionium from expanding to infinity when putting the π-skyrmion inside the skyrmionium. Because of that, the stable 3π-skyrmion does not exist at the Bogomol'nyi point. The same is true for Sk bags with $Q < -2$. It is because, on the one hand, all solutions at the Bogomol'nyi point are bounded from below by the energy of π-skyrmion, -4π, and on the other hand, all solitons at this point must have energy $4\pi Q$.

Therefore, to construct some magnetic solitons, one must use alternative approaches. The most straightforward approach is the construction of initial configurations for the Sks with piecewise functions [17]. In practice, I use both approaches, based on the holomorphic functions and piecewise functions, nearly equally often.

3.2.3 Energies of skyrmions with CKs

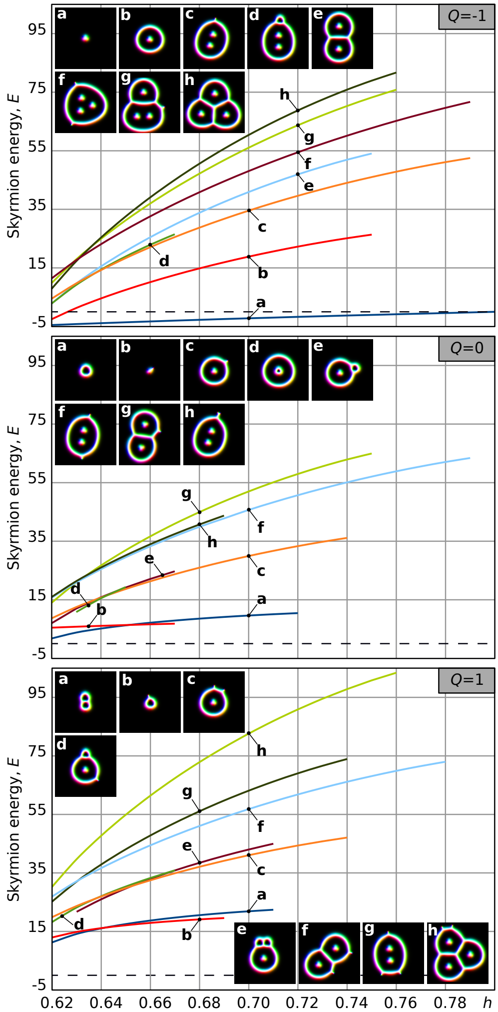

Figure 3.8: **Energies comparing for various skyrmions**. The energies of Sks are shown at various external magnetic fields, h, for the case of zero anisotropy, $u = 0$. The top, middle, and bottom plots correspond to the Sks with $Q = -1$, 0, and +1, as indicated in the right top corner. The horizontal dashed line corresponds to $E = 0$ – the energy of the field saturated state. The parameters of the system: the size of simulated domain $8L_\mathrm{D} \times 8L_\mathrm{D}$, and $L_\mathrm{D} = 64a$. This figure has been published in [19].

The energy of Sks with CK with respect to the energy of ordinary π-skyrmion is an important aspect of the problem. The analysis of the DMI energy density Fig. 3.2 suggests that Sks with CKs should have energies higher than that for Sk bags. However, a more detailed study shows that at certain magnetic fields, Sks with CKs can be energetically more favourable than the Sk free of CKs.

It is reasonable to compare the energies for the Sks of the same topological charge. The energy dependencies on the external magnetic field for some Sks with topological charges $Q = -1$, 0 and 1 are presented in Fig. 3.8. Here I consider the case of the isotropic system, $u = 0$. Since, in this case, most solutions become elliptically unstable at $h \leq 0.62$, I consider the field range above that characteristic field. On the other hand, the upper bound limit – the Sk collapse field, varies extensively for different Sks. The estimation of the collapse field can be improved and evaluated more precisely by increasing the mesh density of the finite difference scheme. However, it is not the case for all Sks [71, 72]. In particular, it has been shown that in the micromagnetic limit, π-skyrmion remains stable at any sufficiently strong magnetic field, $h \to \infty$. Moreover, in the topological sector $Q = -1$, π-skyrmion has the lowest energy, or in other words, is the global minimizer at any h. That is not surprising since in the range of fields, $0.2 < h < 0.82$, the lattice of π-skyrmions is the system's ground state. In this range of fields, the isolated π-skyrmion has energy lower than the FM state, which is marked by the dashed horizontal line.

For solutions with $Q = -1$, the second-lowest energy solution is 3π-skyrmion **b**, which collapses at $h \gtrsim 0.75$ and then the Sk with a CK **c** takes the place of the second lowest energy state. Moreover, the solution depicted in **c** competes in energy with many other structures including skyrmion bags **d**, **e** and **h**, and skyrmion bags with CKs **f**, **g**.

In other topological sectors, the situation is less trivial – there is no global minimizer, and at different ranges of fields, different Sks become the lowest energy state. For the case $Q = 0$, the energy of skyrmionium **a** can become higher than the energy of CD **b** at $h \gtrsim 0.65$. However, CD collapses at $h \gtrsim 0.67$, and skyrmionium becomes again the most energetically favourable soliton in this topological sector. At $h \gtrsim 0.0.72$, the skyrmionium collapses, and a solution that represents the 3π-skyrmion with a CK depicted in **c** takes its place. At $h \gtrsim 0.74$ soliton shown in **f** becomes the minimizer in this topological sector. Remarkably, 3π-skyrmion with a CK is significantly more stable than 4π-skyrmion **d**, which is free of CKs. Similar behaviour is rather generic and can be observed for different Sks **e**-**h**.

Now I consider the topological sector $Q = 1$. Skyrmion bag **a** has the lowest energy at $0.62 \lesssim h \lesssim 0.64$ and at $0.69 \lesssim h \lesssim 0.71$. In between these ranges, Sk with a CK **b** is more energetically favourable. At $0.71 \lesssim h \lesssim 0.74$, another Sk with two CKs **c** becomes the minimizer in this topological sector. The solution depicted in **f** takes its place at $h \approx 0.74$. Noticeably, the Sks with quite complicated structures (see, e.g., Sks in **f** and **h**) remain stable in a remarkably wide range of fields.

As follows from the above dependencies, the Sks containing CKs must be considered when one needs to find the lowest energy solutions in a particular topological sector. There are no doubts that the situation with solutions of $|Q| > 1$ is no less diverse than for $Q = -1$, 0, and 1. A more detailed study of the lowest energy states in each topological sector can be a subject of further research.

3.2.4 Skyrmions with chiral antikinks

Up to now, I have considered solutions with CKs only; however, as has been mentioned above, the model also allows the solutions with CAs. As it turned out, for their stability, the presence of a strong easy-axis anisotropy in the Hamiltonian (1.6) is required.

As a representative example, I consider the π-skyrmion with a CA. The stability range of this Sk is shown in Fig. 3.9. The spin texture of this Sk at different parameters (h, u) are given in insets **a**, **c**, and **e**. Note, due to the presence of a CA, the topological charge of this Sk is -2. Three critical curves bound the stability range. On the right, it is bound by the transition to a pair of π-skyrmions (red curve). On the left, it is bound by the transition to a single π-skyrmion (blue curve), and from below, it is bounded by the so-called bursting field (green curve). The curves are denoted by h_d, h_t and h_b, respectively. The duplication **b**, or transformation to a pair of π-skyrmions, is an example of homotopic transition because it occurs with conservation of the total topological charge. On the contrary, the transformation to a single π-skyrmion **d** represents a topological transition because Q changes from -2 to -1. In the calculations with fixed $L_{\mathrm{D}} = 64a$, the critical curves $h_{\mathrm{d}}(u)$ and $h_{\mathrm{t}}(u)$ intersect at $u \simeq 1.287$. Strictly speaking, the value of the crossing point may change for more dense meshes. Moreover, the blue curve, corresponding to the topological transition, is shifted to the right – towards higher anisotropies with increasing mesh densities. It is reasonable to expect that such topological transition does not exist at all in the micromagnetic limit. On the other hand, the curve corresponding to the bursting field, $h_b(u)$, is not very sensitive to the mesh density in the numerical calculations and stays nearly the same even when one approaches the micromagnetic limit.

The discussed above Sks with CKs can also be stabilized in the presence of anisotropy. It is useful for further research to know the parameters at which most of the presented Sks can coexist. The region in the close vicinity to the point marked by a star symbol, see Fig. 3.9 **g** seems to be most optimal for these purposes. Most of the Sk solutions presented above are stable at this point. Besides that, at this point, I found one of the most exotic Sk solutions, which contains both CK and CA and has the shape of a heart, see inset **g**. Note that such a configuration with Bloch lines of different handedness is always unstable in the model of magnetic bubbles. On the contrary, in the model of the chiral magnet, it represents a statically stable solution. Although Sks with CAs are stable only in a pretty small range of parameters (h, u), they possess some unique properties and thus represent interesting objects to future research.

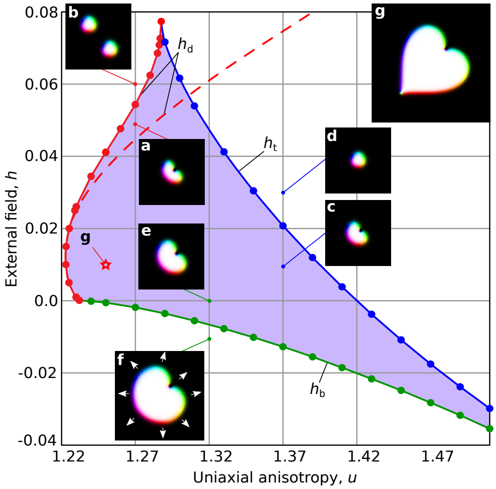

Figure 3.9: **Skyrmion with antikink stability diagram**. h-u diagram of stability of the Sk with negative CK and $Q = -2$ **a**, **c**, **e**. Below the blow-up-field, h_b (green line), the Sk starts to expand abruptly **f**. The Sk with one negative CK may abruptly split into two π-skyrmions **b** with increasing field. This Sk duplication transition is marked as h_d (solid red line). Above the critical field, h_t the Sk with $Q = -2$ transforms into a single π-skyrmion **d**. The inset **g** illustrate the solution, which is the most exotic and least stable Sk among other presented here. The Sk in **g** is stable in the narrow range near $h = 0.01$, $u = 1.25$ and contains one CK and one CA, $Q = -1$. The parameters of the system: domain size $5L_\mathrm{D} \times 5L_\mathrm{D}$,with $L_\mathrm{D} = 64a$. With increasing L_D the critical field h_d tends to dashed (red) line, while h_t shifts towards $u \to \infty$. This figure has been published in [19].

3.3 Chiral kinks on 2π-domain wall

2π-domain wall is an example of 1D solitons intensively studied in the literature due to their simplicity and the opportunity to derive analytical solutions. In the scope of this thesis, the interest in such objects is conditioned by the fact that 2π-DW can host single or multiple CKs. Thereby, 2π-DW with a CK seems to be a promising platform for studying the properties of CKs, e.g., their stability and Interaction with each other. Moreover, 2π-DW with a CK can be stabilized in a wide range of fields and anisotropy values that make it a promising object for experimental observations [73, 74].

3.3.1 Stability range of the domain wall with a CK

Let me consider a large skyrmion bag with negative Q containing a single CK on the outer contour, as depicted in Fig. 3.10 **a**. Such Sk may provide a good estimation for the upper bound limit for the stability of skyrmions with CKs in general. The collapse of such skyrmion bag occurs through a rupture of its shell at the CK position as illustrated in Fig. 3.10 **b-d**. Note that this transition occurs with the conservation of the topological charge. The larger the Sk bag, the higher its collapse field. The blue line, h_c, represent the critical field for the rupture of an isolated 2π-DW containing CK, see Fig. 3.10 **e-f**. This critical field can be considered an upper bound limit for the stability of an extremely large skyrmion bag with a radius tending to infinity.

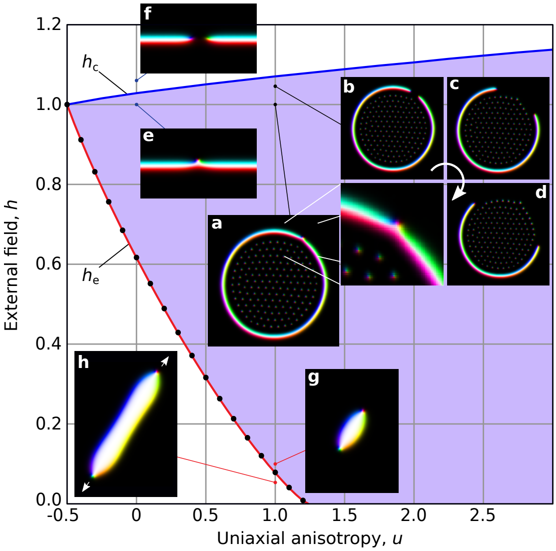

Figure 3.10: **Upper bound for stability diagram of various Sks with CKs**. h-u diagram of stability of magnetic skyrmions with CKs. **a** is an example of a large skyrmion bag with the negative CK on the outer side of the shell at $h = 1$, $u = 1$. **b-d** are the snapshots of the system after performing different number of energy minimization iterations with NCG method at $h = 1.05$. The collapse field, h_c (blue solid line) corresponds to the field at which 2π-DW with a CK **e** is ruptured **f**. The elliptic instability field, h_e, (solid red line) is defined by the criteria that the energy of 2π-DW in (3.11) equals zero, $\mathcal{E}_\mathrm{DW} = 0$. The black dots lying very close to the red line correspond to numerically estimated elliptic instability of the antiskyrmion **g**. For $h < h_\mathrm{e}$ the antiskyrmion starts to elongate abruptly as indicated by wight arrows **h**. This figure has been published in [19].

The critical field h_c has been estimated numerically. However, some analysis can also be done analytically using ansatz describing the profile of the 2π-DW with a CK. The solution for 2π-DW without CKs can be written as [75, 76]

$$\Theta(x) = 2\,\mathrm{arccot}\left(\frac{\sqrt{h}|\sinh(2\pi\sqrt{h+2u}x)|}{\sqrt{h+2u}}\right), \quad \Phi(x) = \frac{\pi}{2}\mathrm{sign}(x). \tag{3.10}$$

Using (3.10) one can find the expression for the energy density of 2π-DW per unit length,

[53]

$$\mathcal{E}_{\rm DW} = -4\pi^2 + 8\pi\sqrt{h+2u} + \frac{2\pi\sqrt{2}h}{\sqrt{u}}\ln\frac{\sqrt{h+2u}+\sqrt{2u}}{\sqrt{h+2u}-\sqrt{2u}}. \tag{3.11}$$

The energy (3.11) increases with increasing h and u. The asymptotic behaviour of the energy density (3.11) has the following form:

$$\mathcal{E}_{\rm DW}(u) = 16\pi^2 u - 4\sqrt{2}\pi^3\sqrt{u} + \mathcal{O}\left(\sqrt{u}\right),\ u \gg 1, \tag{3.12}$$

for fixed $h \geq 0$, and

$$\mathcal{E}_{\rm DW}(h) = 16\pi^2 h - 4\pi^3\sqrt{h} + \mathcal{O}\left(\sqrt{h}\right),\ h \gg 1, \tag{3.13}$$

for fixed values of u.

By modifying function Φ in (3.10) one can get ansatz for the 2π-DW with a CK,

$$\Phi_{\rm a}\left(x,y\right) = \begin{cases} -\dfrac{\pi}{2} & x<0, \\ 4\arctan(e^{my}) + \dfrac{\pi}{2} & x>0, \end{cases} \tag{3.14}$$

where m is a parameter that has to be found by minimizing the energy from the condition $\delta\mathcal{E} = 0$. The solution to this problem is discussed in detail in Appendix A5 . The primary outcome of this solution is that one can show that the energy of CK decreases with increasing u for fixed h. One can write the CK energy as

$$\mathcal{E}_{\rm CK} = \mathcal{E}_{\rm DW+CK} - \mathcal{E}_{\rm DW}, \tag{3.15}$$

where $\mathcal{E}_{\rm DW+CK}$ is the energy of configuration described by the ansatz function (3.14). The expression for $\mathcal{E}_{\rm CK}$ which follows from (3.15) reads

$$\mathcal{E}_{\rm CK} = \sqrt{\frac{\sqrt{h+2u}\pi}{u} - \frac{h\pi}{2\sqrt{2}u^{3/2}}\ln\frac{\sqrt{h+2u}+\sqrt{2u}}{\sqrt{h+2u}-\sqrt{2u}}} \tag{3.16}$$

In the limit $u \to \infty$ for any fixed h, the energy of CK in (3.16) is $\mathcal{E}_{\rm CK} \to u^{-1/4}$. Therefore, in the micromagnetic limit, 2π-DW with CK remains stable at any sufficiently high value of anisotropy.

While the 2π-DW with a CK is a good upper bound for Sks with CKs, $h_{\rm c}$, the Ask stretching instability provides a good estimation of the lower bound for the stability range, $h_{\rm e}$. Remarkably, the critical field h_e, with a high precision coincides with curve $\mathcal{E}_{\rm DW}(h,u) = 0$. For magnetic field below h_e, the antiskyrmion expands in the directions where CKs are placed, see Fig. 3.10 **g** and **h**. It is worth noting that in a strict mathematical sense, the critical field h_e in Fig. 3.10 does not represent the lower bound for all skyrmions with CKs. Nevertheless, it represents a good approximation of the lower bound limit – most of the Sks with CK are not stable below the line h_e. The critical fields h_e and h_c, intersect at the Bogomol'nyi point $h = 1$, $u = -0.5$. Thereby, below the anisotropy value $u = -0.5$, Sks with CKs do not exist in the sense of exponentially localized in space solutions. At the same time, at any point in the shaded region in Fig.,3.10 one can always find the solution for some exponentially localized Sk with CK. Only a few Sks with CKs can be found outside of this region. The π-skyrmion with CA, for example, can be stabilized at $h < 0$ (see Fig. 3.9).

3.3.2 Interaction of CKs

There is no unique approach for the estimation of soliton size. Even for well-studied π-skyrmion, there is not a common definition of its size. The same problem occurs with the definition of the size of CK. The additional complexity of this problem is related to the fact that CK does not exist as an isolated object and is only as a part of another host soliton. Nevertheless, following the approach widely used in nuclear physics, the characteristic size of CKs can be estimated from their interactions. The interaction energy, $\mathcal{E}_{\text{int}}$, for a pair of CKs hosted by one 2π-DW, see Fig. 3.11 **a**-**d**, can be calculated as

$$\mathcal{E}_{\text{int}}(R) = \mathcal{E}_{\text{tot}}(R) - 2\mathcal{E}_{\text{CK}} - \mathcal{E}_{\text{DW}}, \tag{3.17}$$

where R is the distance between two CKs, $\mathcal{E}_{\text{tot}}(R)$ is the total energy of 2π-DW with two CKs, $\mathcal{E}_{\text{CK}} = \mathcal{E}_{\text{DW+CK}} - \mathcal{E}_{\text{DW}}$ is the energy of an isolated CK, while $\mathcal{E}_{\text{DW+CK}}$ and $\mathcal{E}_{\text{DW}}$ are the energies of 2π-DW with and without CK, respectively, see Fig. 3.11 **e** and **f**.

The red points in Fig. 3.11 correspond to two equilibrium configurations. Note, the third equilibrium point corresponds to $R \to \infty$. To estimate the energies of CKs pair out of these equilibrium positions, I fixed two spins that define the distance between CKs and numerically minimized the system's energy. The distance $R = |\mathbf{r}_{\text{A}} - \mathbf{r}_{\text{B}}|$ is the distance between points A and B with the spins pinned in the directions $\mathbf{n}(\mathbf{r}_{\text{A}}) = (-1/\sqrt{2}, 1/\sqrt{2}, 0)$ and $\mathbf{n}(\mathbf{r}_{\text{B}}) = (1/\sqrt{2}, 1/\sqrt{2}, 0)$, respectively. The coordinates of these points on the plane are $\mathbf{r}_{\text{A}} = (x_0, -R/2)$ and $\mathbf{r}_{\text{B}} = (x_0, R/2)$. In the numerical experiment, we change the parameter x_0 to change the distance between CKs, R. Performing the direct energy minimization for various values of R, one can calculate the energies in (3.17) with any sufficient accuracy. As I mentioned above, the interaction energy between two CKs in Fig. 3.11 has two local minima at $R \approx 0.2L_{\text{D}}$ and $R \approx 0.9L_{\text{D}}$ and one global minimum at $R \to \infty$. The presence of the second local minima at $R \approx 0.2L_{\text{D}}$ is an intriguing feature of CKs interaction. The states corresponding to the local minima have been

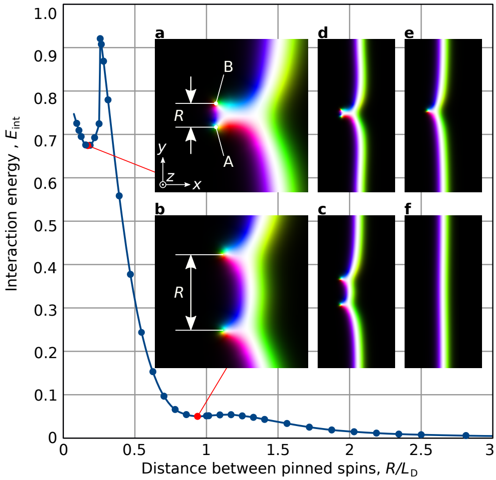

Figure 3.11: **Interaction of chiral kinks on the 2π-domain wall**. The interaction energy between two CKs as a function of the distance between them is shown. The points A and B indicate the position of pinned spins with $\Theta = \pi/2$ and $\Phi_A = 3\pi/4$ and $\Phi_B = \pi/4$, respectively. **a** and **b** are zoomed images of **c** and **d**, respectively. **e** and **f** are 2π-DWs with one CK and 2π-DW without kinks, respectively. The parameters of the system: $h = 0.65$, $u = 0$, domain size is $3L_D \times 6L_D$, and $L_D = 128a$. This figure has been published in [19].

obtained without pinned spins **a** and **b**. The distance $R \approx 0.9L_D$ represents the standard characteristic length of spiral modulation in the chiral magnet. The distance $R \approx 0.2L_D$ corresponding to the first minima is a good estimation for the CK size. The presence of two characteristic scales of inhomogeneity is not typical for magnetic systems and represents a distinct property of chiral magnets.

Additionally, different inhomogeneity scales allow one to classify magnetic textures in chiral magnets by the lowest scale of inhomogeneity present in the corresponding textures. For instance, solutions without CKs represent the first group, while those possessing CKs and CAs belong to the second group. In conclusion, it is worth noting that the numerical scheme applied to such solutions requires using more dense meshes in the finite difference scheme.

3.4 Conclusions

In this Chapter, I presented a diverse variety of Sk solutions in the model of the chiral magnets. I showed that such diversity could be well understood and classified using the earlier concepts for magnetic bubbles. In particular, the concept of DWs contours allows one to introduce the notion of CK – a coupled pair of Bloch lines that other Sks can host. Combining CKs with previously known solitons results in a large diversity of new magnetic configurations. Some of them are shown in this Chapter. Exact analytical solutions for skyrmions at Bogomol'nyi point provide analytical ansatz configuration for many Sks with and without CKs that can be used as reliable initial configurations in the following numerical energy minimization. I have shown that despite the relatively high energy of the CK, at certain external magnetic fields, some Sks with CKs can have energy lower than that of Sks of the same Q but free of CKs. In particular, this suggests that Sks with CKs can be good candidates for global minimizers in some topological sectors. With this, excluding such solutions from consideration may give a wrong picture of Sk diversity.

The structure of CK attached to the 2π-DW has been analyzed in detail. Since this magnetic texture has a wide stability range at different magnetic fields and anisotropy values, it provides essential information on the properties of the CK itself. The size of CK has been estimated from the Interaction between a pair of CKs on the 2π-DW and turned out to be one order smaller than characteristic length L_{D}. The interaction energy of two CKs has two local minima – the first is of the order of L_{D} while the second is related to the CK size. Therefore, it allows the introduction of two scales of inhomogeneity in chiral magnets.

The fact that in the experiment in 2D chiral magnets, only the particles (π-skyrmion) have been reported and the antiparticles (antiskyrmion) have not been observed so far can be easily explained by the large energy difference between particles and antiparticles. Interestingly, the energies of CKs and CAs are comparable. However, the stability region for Sks with CAs does not coincide with those for Sks with CKs. Such symmetry breaking is akin to the similar problem in high-energy physics related to inequality between matter and antimatter in the observable world. Studying similar problems in totally different physical systems is sometimes helpful. Developed mathematical tools can help solve the problem in related areas. This is an additional argument favouring the fact that studying the chiral magnets model can benefit or inspire research in contiguous branches of science.

4 2D skyrmion homotopies

In this Chapter, I consider the homotopies of some 2D magnetic textures. This study is motivated by discovering a wide diversity of solitons discussed in the previous Chapter. My aim here is to show how one can transform two distinct Sks of identical topological charge into each other. I start with the most stable configuration hosting CK – 2π-DW with CK, in **Section** 4.1. In particular, I show how to move the CK from one side of the wall onto another one. Then in **Section** 4.2, I consider the tilted field-induced decay of skyrmion bags into skyrmions and antiskyrmions. In both cases, the appearance of CKs at a particular stage of transformation is a crucial feature of such homotopic transformations. Next, I consider the transformations free of CKs, which are presented in **Section** 4.3. Starting with the π-skyrmion, I show its 'trivial' transformations into so-called Sks with tails. Some of the presented Sks have been discussed in the literature as dynamically excited states of the π-skyrmion [77]. On the contrary, I show that these Sks become statically stable solutions at some parameters.

4.1 Homotopy transition of the domain wall with CK

In many cases, the search for a homotopy transition between two states consists of two steps. In the first step, one has to guess a set of intermediate configurations and optimize this path in the second step. The first step relies on some ingenuity, while the second is rather technical. I found that studying Sks at different external parameters, such as the tilted magnetic field and anisotropy, can already provide hints for the initial homotopy path. The tilted magnetic field can give a suitable ansatz for the shape of the homotopy path containing configurations with CKs. In the case of anisotropy, the same is true for CAs.

To find the homotopy transformation of the 2π-DW with a CK, it is useful to study 2π-DW attached to the skyrmionium. Below I show the stability range of this texture in the presence of the tilted magnetic field.

4.1.1 2π-domain wall with skyrmionium

Varying the in-plane and out-of-plane components of the magnetic field, one can find that the stability of the 2π-DW with a skyrmionium can be broken in three different ways Fig. 4.1 **a**. The stable texture **b** collapses into a single 2π-DW **c** at fields higher than h_c. At

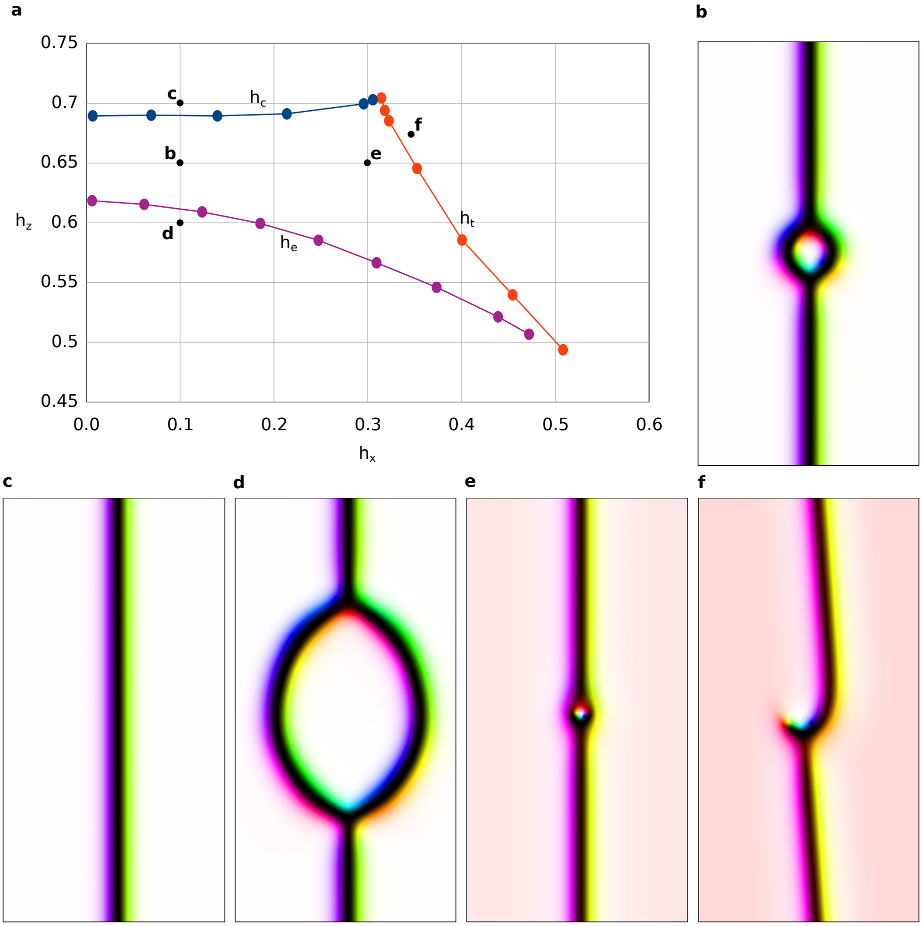

Figure 4.1: **Stability range of the 2π-domain wall with a skyrmionium**. **a** shows the stability diagram of the 2π-DW with skyrmionium depicted in **b**. The diagram provided in terms of in-plane, h_x, and out-of-plane, h_z, components of the magnetic field. Note the system is assumed to be isotropic, $u = 0$. The blue line corresponds to the collapse field, h_c, above which, the configuration **b** transforms into **c**. The purple line corresponds to the elliptic instability field, h_e, the magnetic texture at magnetic field below this line is given in **d**. The red line corresponds to the transition field, h_t. Representative examples of the equilibrium spin textures below and above the critical field h_t are shown in **e** and **f**. The simulations have been performed for the system of size $L_x = L_y = 8L_D$, $L_D = 64a$.

the reduced magnetic field, below h_d, the 2π-DW with a skyrmionium becomes unstable with respect to the stretching (elliptical instability) **d**. When both tilt and amplitude of the field increase, 2π-DW with skyrmionium **e** transforms into the 2π-DW with a CK **f**, the corresponding magnetic field is denoted as h_{t}. The latter transformation is of higher interest because it represents the homotopy transformation. It is worth noting that breaking left and right of two skyrmionium half-shells can happen with equal probability, which means the final 2π-DW state can have a CK on its left or right side.

A precise estimation of the field h_{t} is challenging and requires a slow variation of the parameters when one is approaching this curve. It is because approaching the field h_{t} from below, the energy barrier protecting the equilibrium configuration depicted in **e** becomes very small. At $h = h_{\mathrm{t}}$, the minima for this configuration, strictly speaking, degenerates into a saddle point on the energy landscape. I found that changing the magnetic field amplitude with a step $\Delta h = 0.001$ at every fixed tilt angle is enough to determine the transition point accurately. Using the larger steps for the magnetic field can lead to artifacts such as simultaneous breaking the skyrmionium shell in two or more points at once.

4.1.2 Homotopy path for the 2π-domain wall with a CK

I rely on the previous section's results to identify the homotopy path between the states, which represent 2π-DW with CK on the left side and the right side. In particular, knowing that the 2π-DW with a skyrmionium can smoothly transform into 2π-DW with a CK state at some field, I use this transition as the initial guess for searching the MEP. Performing MEP calculations with the GNEB method implemented in Spirit code [60], I found such transformation, which is shown in Fig. 4.2 **a**-**e**. In addition to the two local minima corresponding to the initial state **a** and final state **e**, the homotopy path contains an additional intermediate minimum – the 2π-DW with a skyrmionium, **c**. There are also two maxima **b** and **d** which represent saddle points on the energy landscape. The MEP shown in **f** justifies the identification of these points as minima and saddle points. The reaction coordinate is usually chosen to be positive; however, in this particular case, due to the presence of 'mirror' symmetry of states **a** and **e**, it is more convenient to distinguish the symmetrical parts of the path by the reaction coordinate of the opposite signs.

It is worth noting that without a good initial guess for MEP, the GNEB algorithm cannot find the homotopy path with topological charge conserved in most cases. In particular, an attempt to find the homotopy path between states **a** and **e** without including the intermediate state **c** fails. The MEP provided by the algorithm, in this case, passes through the isolated 2π-DW without CK – first, CK disappears on one side and then appears on another one. The topological charge along such MEP is not conserved. The corresponding MEP is shown in Fig. 4.2 **g**. The intermediate state, in this case, is the

2π-DW, which is a topologically trivial texture, while initial and final states are characterized by charge $+1$. The micromagnetic Hamiltonian of the 2D chiral magnet forbids the appearance of singularities because they have infinite energy. However, since I use a finite difference scheme in my numerical calculations, the singular points have finite energy. Because of the above, a search of a homotopy path requires high accuracy of the finite difference scheme in numerical simulations.

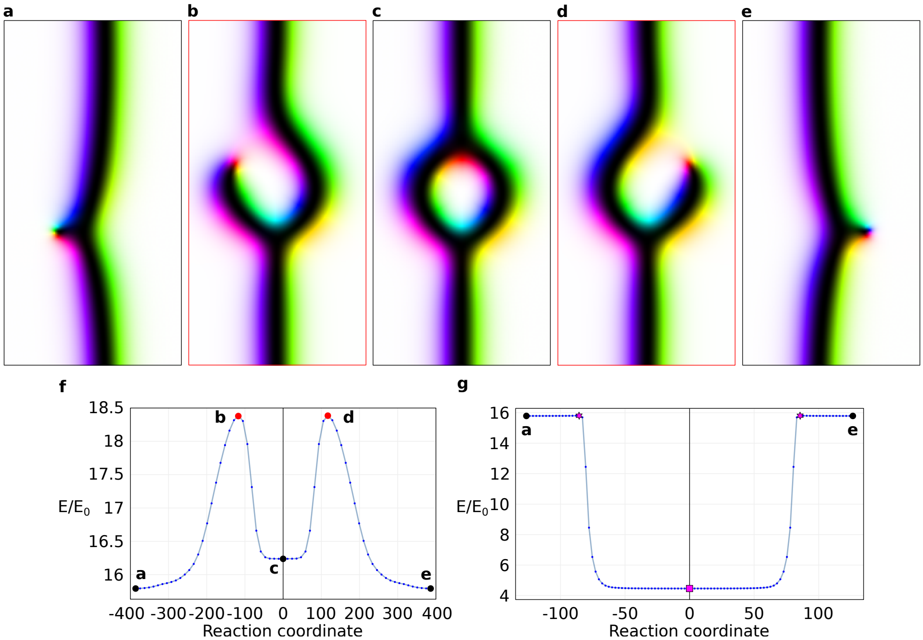

Figure 4.2: **Homotopy path of 2π-domain wall with a CK**. **a**-**e** show magnetic textures corresponding to the homotopy path connecting 2π-DW with a CK on left side **a** and 2π-DW with a CK on the right side **e**. States **b** and **d** represent saddle points, state **b** is an intermediate local minimum corresponding to the 2π-DW with with skyrmionium. The homotopic MEP is shown in **f**. A non-homotopic MEP connecting states **a** and **e** is shown in **g**. The intermediate square point corresponds to the single 2π-DW Fig. 4.1 **c**. Star symbols denote saddle points. The simulations have been performed for the system of size $L_\mathrm{x} = L_\mathrm{y} = 4L_\mathrm{D}$, $L_\mathrm{D} = 64a$ at magnetic field $h = 0.65$ and $u = 0$.

Although the presented above method for homotopy path searching has been applied to the not-fully-localized magnetic texture, one can use this method for solitons that are fully localized in all spatial directions. In the next Section, I consider this case.

4.2 The role of CK in homotopy transitions of Sks

Below I apply the analysis of the Sks stability in the tilted magnetic field to predict possible homotopy transformations of these Sks. Then the corresponding homotopy paths are optimized using the GNEB method and, thus, represent MEPs.

4.2.1 Skyrmion bags in the tilted magnetic field

The skyrmionium is a topologically trivial skyrmion bag and the simplest object among solitons of such a type. The stability diagram of skyrmionium in a tilted magnetic field is shown in Fig. 4.3 **a**. Similar to the case of 2π-DW with skyrmionium, the diagram is bound by three instability curves: collapse, h_{c}, elliptic instability, h_{e}, and transformation into the FM state, h_{t}. At the magnetic field higher than h_{c}, the skyrmionium core shrinks, and it transforms into the π-skyrmion **c**. This transition is not a homotopic one – the corresponding topological charge changes from 0 to -1 abruptly. Since the topological charge of the system is not conserved, this type of transition can be called a *topological transition.* At magnetic fields below h_{e}, the skyrmionium becomes unstable with respect to the stretching. The energy barrier preventing its deformation is absent in this case. After crossing the curve h_{t}, stable configuration **d** transforms into the FM state **g** going through states **e** and **f** which are unstable. The states depicted in **e**-**f** are the snapshots of the system taken at different stages during direct energy minimization. The magnetic texture on **e** represents the Sk-Ask pair. The mutual orientation of Sk and Ask corresponds to the annihilation channel discussed in **Section** 2.2. The texture shown in **f** can be thought of as another topologically trivial soliton – the CD which is embedded into the tilted FM. As I show further, the appearance of the CD is not an accident, and this soliton is an important part of the skyrmionium homotopy path.

As the next example of a skyrmion bag, I consider the soliton with the topological charge +1, see Fig. 4.4 **b**. The stability diagram in **a** looks similar to that of the skyrmionium; however, there are some differences. The curve h_{c} lies lower than that for skyrmionium and as a result, for the field above h_{c}, the stable configuration **b** transforms into the skyrmionium **c**. With further field increasing, skyrmionium transforms into π-skyrmion. With this, the topological charge changes from +1 to 0 and then to -1. This type of topological transition is not a homotopy. The elliptic instability curve, h_{e}, coincides with good precision with the corresponding curve for skyrmionium. Above the critical field h_{t} the state depicted in **d** undergoes a homotopic transition into Ask depicted in **g**. The transient states during this transformation are shown in **e** and **f**. The configuration in **e** represents a pair of Sk-Ask (above) and single Ask (below). The pair of Sk-Ask is unstable and annihilates, going through the droplet state seen in **f** (above). The single Ask in **f** (below) remains stable. Therefore, the curve h_{t} separates states of an identical topological charge $Q = +1$, and the textures in **d**-**g** provide a good hint for the homotopy path.

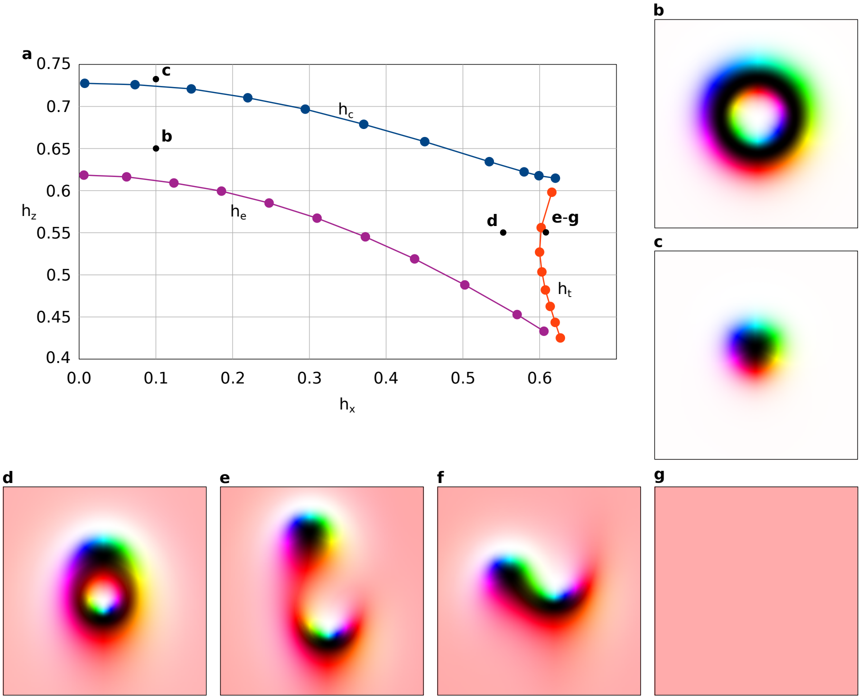

Figure 4.3: **Skyrmionium stability diagram in the tilted magnetic field**. **a** The stability diagram of the skyrmionium **b** is given in terms of in-plane, h_{x}, and out-of-plane, h_{z}, components of the magnetic field at $u = 0$. The blue line corresponds to the collapse field, h_{c}, above which the configuration **b** transforms into **c** (π-skyrmion). The purple line corresponds to the elliptic instability field, h_{e}. The red line corresponds to the transition field, h_{t}. Above this critical field the state depicted in **d** becomes unstable with respect to the transition in FM state in **g** via transient unstable configurations depicted in **e** and **f**. The simulations have been performed for the system of size $L_{\mathrm{x}} = L_{\mathrm{y}} = 8L_{\mathrm{D}}$, with $L_{\mathrm{D}} = 64a$. This figure has been published in [78].

4.2.2 Homotopy paths for the skyrmion bags

The homotopy path corresponding to the annihilation of the skyrmionium is shown in Fig. 4.5. Following this path, stable skyrmionium **a** goes through the saddle point **b** and transforms into the CD **b** which represents another local minima on the MEP. The minimum for the CD is separated from the FM state by another barrier with the saddle point **d** (see details in Appendix A6). As it follows from the MEP shown in **e**, the energies of the skyrmionium and the CD are comparable at the magnetic field $h \simeq 0.65$. At the same time, the corresponding energy barriers are of different heights. The latter explains why skyrmionium is more stable than the CD.

In the following chapters, I will discuss an interesting phenomena, the discovery of which was inspired by the homotopic transformation of CD revealed during the calcula-

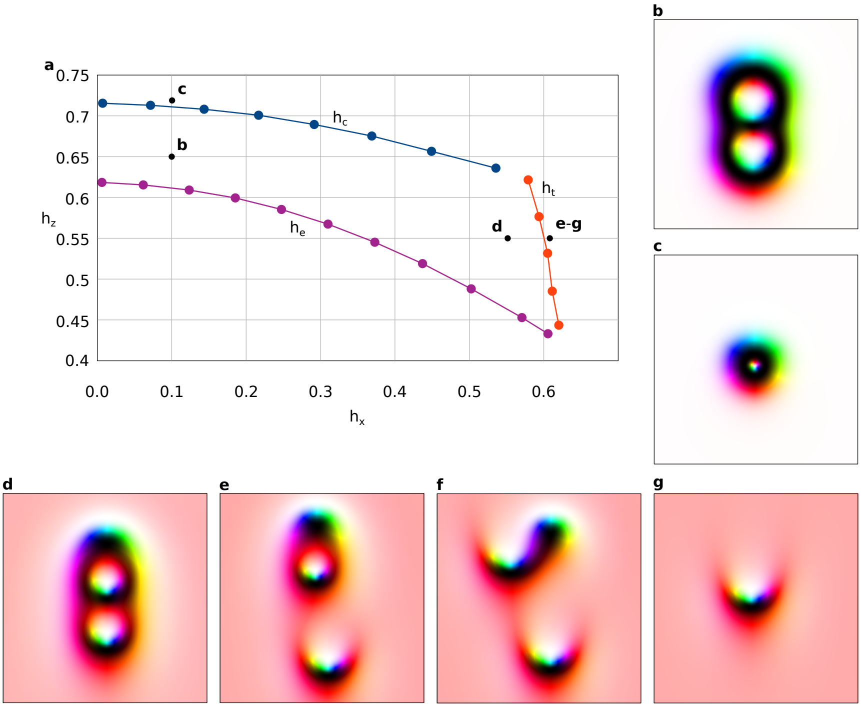

Figure 4.4: **Skyrmion $Q = +1$ stability diagram in the tilted magnetic field**. **a** The stability diagram of Sk with topological charge +1 **b** is shown in terms of in-plane, h_{x}, and out-of-plane, h_{z}, components of the magnetic field at $u = 0$. The blue line corresponds to the collapse field, h_{c}, after crossing it, the configuration **b** transforms into **c** (skyrmionium). The purple line corresponds to the elliptic instability field, h_{e}. The red line corresponds to the transition field, h_{t}, separating states **d** and **e**-**g**. Magnetic textures **e**, **f** are unstable and transform into Ask in **g**. The simulations have been performed for the system of size $L_{\mathrm{x}} = L_{\mathrm{y}} = 8L_{\mathrm{D}}$, $L_{\mathrm{D}} = 64a$. This figure has been published in [78].

tions of the skyrmionium homotopy. In particular, in **Chapter** 6 I consider the thermal generation of CDs, and in **Section** 8.3 I study the stability of CD in 3D.

Now let me consider the homotopy for the skyrmion bag of $Q = +1$, stability of which has been discussed above. This skyrmion bag can be smoothly transformed into the antiskyrmion, as shown in Fig. 4.6. The transformation path between minima **a** and **f** contains two saddle points **b** and **d** and an intermediate local minimum **c**. The initial configuration of this skyrmion bag has two loops. Its transformation into the antiskyrmion can be thought of as a sequential rupture of each loop. The intermediate local minimum corresponds to Sk depicted in **c** that can be considered as a skyrmionium with a CK on the outer contour. Note that two simultaneous ruptures can also happen. In this case, the homotopy path has only one saddle point. I consider both situations in constructing 3D hybridized Sk tubes, which will be discussed in **Section** 8.2.

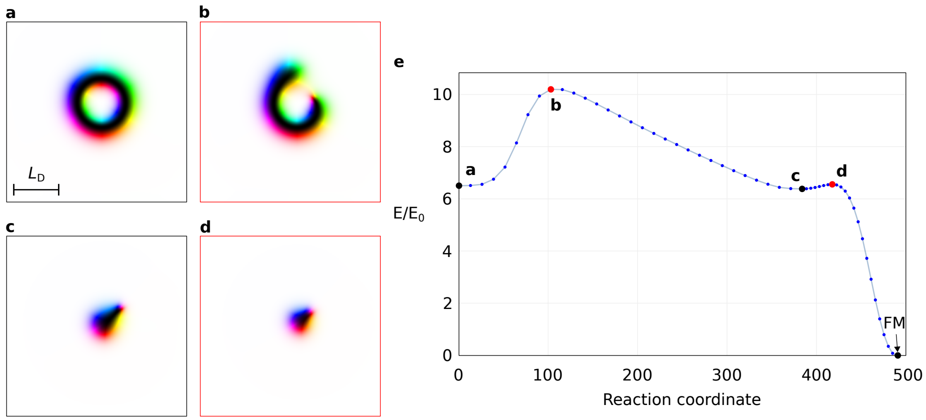

Figure 4.5: **Homotopy path between skyrmionium and the FM**. The snapshots of the system in **a-d** show magnetic textures corresponding to the homotopy path connecting skyrmionium **a** with the FM state. The states in **b** and **d** correspond to the saddle points. The state shown in **c** is an intermediate local minimum corresponding to the CD. The calculated MEP is given in **e**. The simulations have been performed for the system of size $L_\mathrm{x} = L_\mathrm{y} = 4L_\mathrm{D}$, $L_\mathrm{D} = 64a$ at the magnetic field $h = 0.65$ and zero anisotropy, $u = 0$. This figure has been adapted from [79].

Additionally to the minima and saddle points, the MEP shown in **g** has an inflection point corresponding to magnetic texture **e**. Although the texture is not stable (it is not a local minimum), it has an interesting structure. Two CKs are displaced quite close to each other (in comparison to the antiskyrmion **f**), which is in agreement with the prediction of their interaction potential studied in **Section** 3.3. Another interesting feature of this configuration is the elongated part on the left, which has the proper Bloch chirality but tends to have an elongated shape. Note, such elongation is not due to the CKs' presence but reflects an additional degree of freedom of the skyrmions, which was not known before. In the following, I refer to such elongations as *skyrmion tails*. The Sks with tails are considered in the following Section. However, to make the content of this Section complete, first, I want to discuss the homotopy of the skyrmion containing CA.

4.2.3 Homotopy paths for skyrmions with chiral antikinks

Sks with CA can be stabilized at strong easy-axis anisotropies. The stability range for π-skyrmion with a CA has been presented in the previous Chapter, see Fig. 3.9. One of the instability curves corresponds to the transformation of such Sk into a pair of π-skyrmions. This type of instability coincides with the homotopy path shown in Fig. 4.7 **a-c**. The corresponding MEP is given in **d**. As one can notice, the magnetic texture related to the saddle point **b** looks very similar to the initial equilibrium configuration

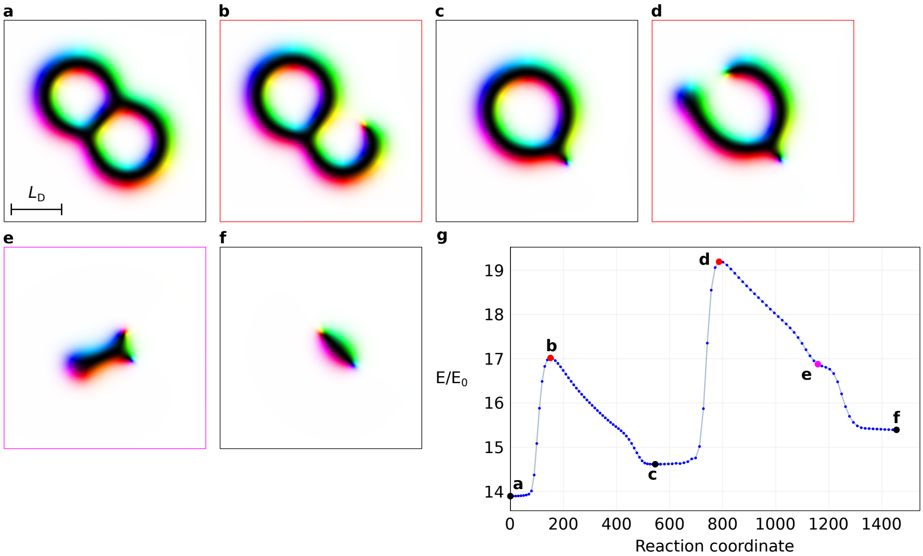

Figure 4.6: **Homotopy path between $Q = +1$ skyrmion bag and the anti-skyrmion**. **a-f** Magnetic textures corresponding to the homotopy path connecting Sk bag **a** and the antiskyrmion **f**. The states depicted in **b** and **d** represent saddle points. The state in **c** is an intermediate local minimum corresponding to the skyrmionium with one CK. The spin texture in **e** corresponds to the inflection point on the MEP. The simulations have been performed for the system of size $L_\mathrm{x} = L_\mathrm{y} = 4L_\mathrm{D}$, $L_\mathrm{D} = 64a$ at the magnetic field $h = 0.627$. This figure has been adapted from [79].

in **a**. Additional details regarding the saddle point analysis are given in Appendix A6 . On the other hand, the final state significantly differs from the initial configuration and represents a pair of π-skyrmions. These π-skyrmions are repelling and tend to run away from each other to infinity. However, due to the exponential localization of solitons and limited precision in the numerical calculations, it is possible to stabilize such a pair at a finite distance. The flattening of the MEP near point **c** illustrates the convergence of repulsive interaction between skyrmions to zero with increasing distance. Note, in the micromagnetic limit, the position of the point **c** tends to infinity.

Another example of Sk with a CA is the solution presented in Fig. 4.7 **e**, it represents the π-skyrmion with one CK and one CA. Due to the compensation of contribution to the topological charge of both kinks, the charge remains unchanged, $Q = -1$. The transformation path for this Sk follows a similar scenario – the CA splits the Sk apart, see **f**, **g**. Two parts represent the π-skyrmion and the CD **h**. These two solitons also repel each other. From the corresponding MEP shown in **i**, it is hard to estimate the exact position of the saddle point, which has to be displaced close to the point **e**.

The shown in this Section Sks are the simplest textures containing CA. The other

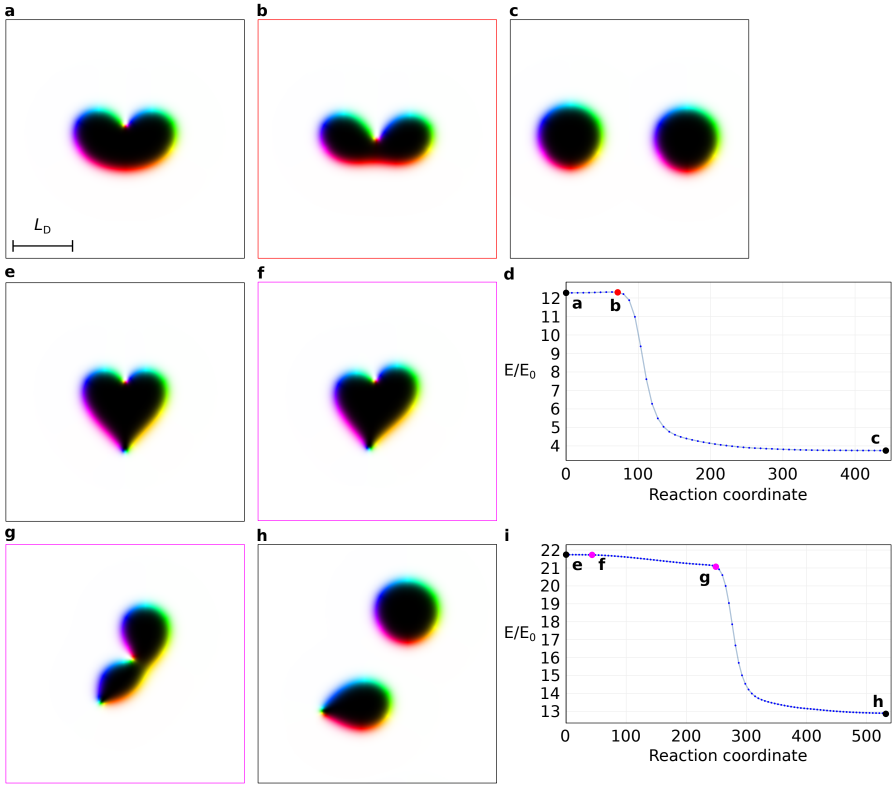

Figure 4.7: **Homotopy paths for skyrmions with antikinks**. **a-c** show magnetic textures corresponding to the homotopy path connecting π-skyrmion with a CA, an intermediate saddle point and a pair of π-skyrmions, respectively. The MEP is shown on **d**. A similar transformation for the π-skyrmion with one CK and one CA is illustrated by snapshots **e-h**. The initial **a** and final **h** states represent minima on the MEP. States **f** and **g** correspond to representative intermediate states. The final state comprises two solitons: the π-skyrmion and the CD. The simulations have been performed for the system of size $L_\mathrm{x} = L_\mathrm{y} = 4L_\mathrm{D}$, $L_\mathrm{D} = 64a$ at the magnetic field $h = 0.01$ and anisotropy $u = 1.23$.

more complicated solitons can also be stabilized at some easy-axis anisotropies, but they all seem to have similar properties from the point of view of homotopy transitions. As follows from all examples shown above, a common feature of the homotopy paths is the emergence of CK or CA, at least at specific transformation steps. At the same time, there are homotopy transformations that are free of CK or CA. Such transitions are discussed below.

4.3 Skyrmions with tails

4.3.1 Transformation of the π-skyrmion

It is well known that at low magnetic field π-skyrmion becomes unstable with respect to elliptic deformation of its shape [53]. I found that just above the elliptic instability field, there is another solution for elongated but still stable Sk with $Q = -1$. The axially symmetric π-skyrmion is homotopic to these new stable states, and the transition between them occurs without the appearance of CKs or CAs. As before, I use the GNEB method to calculate the MEP to illustrate the above statement, see Fig. 4.8.

According to the terminology I used above, the axially symmetric π-skyrmion depicted in Fig. 4.8 **a** is a Sk free of tails, while the states depicted in **c**, **e** and **g** are Sks with 2, 3 and 4 tails, respectively. The presence of tails does not change the topological charge but only the shape of solitons and their energy. The skyrmions with tails are always higher in energy than the solutions free of tails, see local minima at the MEP shown in **h**. Nevertheless, the Sks with tails can not be excluded from consideration for studying the diversity of the solution in a particular topological sector. The soliton with 2 tails **c** has the second-lowest energy among Sks with $Q = -1$. The solutions with different number of tails are separated by saddle points **b**, **d** and **f**. Since the energy barriers between different states are reasonably large, one may expect that Sk with tails can be observed in experiments performed at low temperatures.

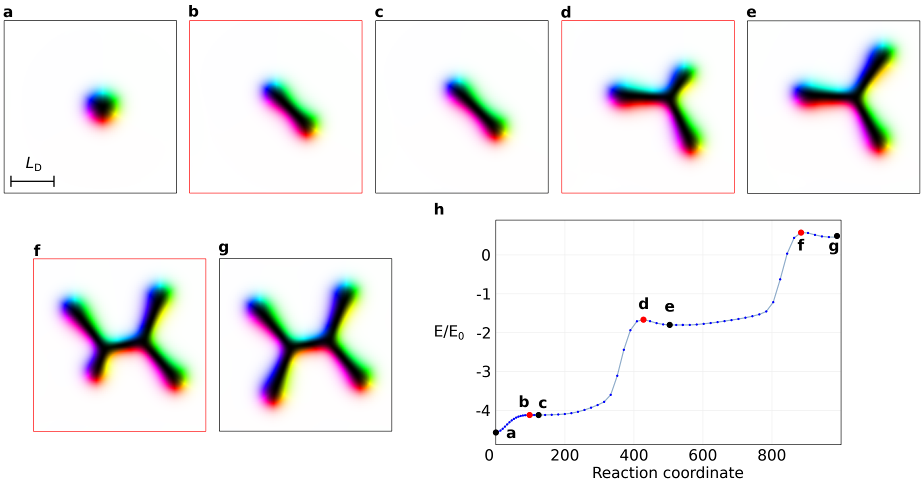

Figure 4.8: **Homotopy path for skyrmion with tails**. **a**, **c**, **e**, **g** Equilibrium magnetic textures corresponding to the π-skyrmion with different number of tails. These 4 minima configurations are separated by 3 maxima points **b**, **d** and **f**. All images **a**-**g** belong to the minimum energy path shown in **h**. The simulations have been performed for the system of the size $L_\mathrm{x} = L_\mathrm{y} = 4L_\mathrm{D}$, $L_\mathrm{D} = 64a$ at magnetic field $h = 0.617$.

An intriguing feature of Sks with tails is that the stability of these solutions always requires a nonzero magnetic field. The π-skyrmion can be stabilized at zero magnetic field and strong easy-axis anisotropy, but it is not the case for Sks with the tails. In principle, one can add tails to any magnetic soliton discussed above. Below, I show how one can extend the diversity of solitons discussed in the previous Chapter by means of tails.

4.3.2 Extension of the skyrmion 'zoo'

Representative examples of stable solutions which represent the skyrmions with tails are given in Fig. 4.9. The first row of images illustrates that tails can appear at inner contours **a**-**d**, outer contours **f**-**o** or both **e**. The shape and size of the host skyrmionium change respectively. In the case of a small number of tails, **f**-**h**, the size of the inner contour of the skyrmionium changes insignificantly. However, when the number of tails increases, the inner contour first notably shrinks, **i**- **j**, but then increases gradually with the rise of the number of tails, **l**- **o**. The solutions with a small number of tails are quite flexible and can have a few equilibrium configurations, compare **i** and **j**. On the other hand, the solutions with four or more tails tend to keep the fixed shape, see bottom row of images, **k**-**o**. An interesting feature of these solutions is their rotational symmetry. As I show further in **Section** 5.3, the symmetry of Sks plays an important role in their dynamics. It is worth noting that the interactions between the solitons depicted in Fig. 4.8 and 4.9 have a repelling character. This is not the case for soliton with CKs. Below I consider such solutions.

The simplest soliton with a CK is the CD. Figure 4.10 **a** and **b** illustrate CD with two and three tails, respectively. The solution shown on **c** looks very similar to the texture at the inflection point on the homotopy path Fig. 4.6 **e**, but at the magnetic field of $h = 0.623$, it turns out to be local minima – represents a statically stable state. It has one tail, but textures with more tails are also stable, see **d** and **e**.

Tails and CKs can also be added to skyrmion bags. The case of skyrmionium with tails and CKs is shown in **f**, **g** while **h** illustrates the bag of $Q = +1$ with two loops.

The presence of CKs and tails makes the diversity of the Sks even richer. At the same time, the classification of possible solutions in the model becomes more complicated because the tails can be branched, see **b**, **d** and **e**, while CKs can form coupled pairs, see **c**-**e**. It is worth emphasizing the impressive diversity of the solitons in the model of the chiral magnet, which is not inherent to other physical systems.

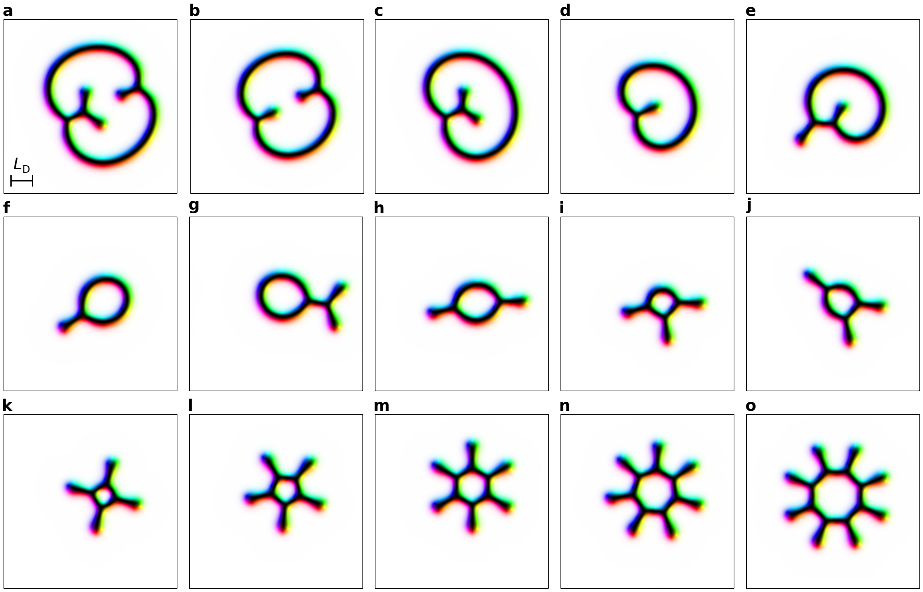

Figure 4.9: **Skyrmionium with tails.** **a-o** show skyrmionium, $Q = 0$, with different number of tails. Configurations **a-d** correspond to the skyrmionium with tails only on its inner contour while the texture in **e** has tails on both inner and outer contours. The skyrmionium in **f-o** has tails only on the outer side. Additionally, these textures have rotational symmetry proportional to the number of tails. The simulations have been performed for the system of size $L_\mathrm{x} = L_\mathrm{y} = 8L_\mathrm{D}$, $L_\mathrm{D} = 64a$ at the magnetic field $h = 0.623$ and zero anisotropy $u = 0$.

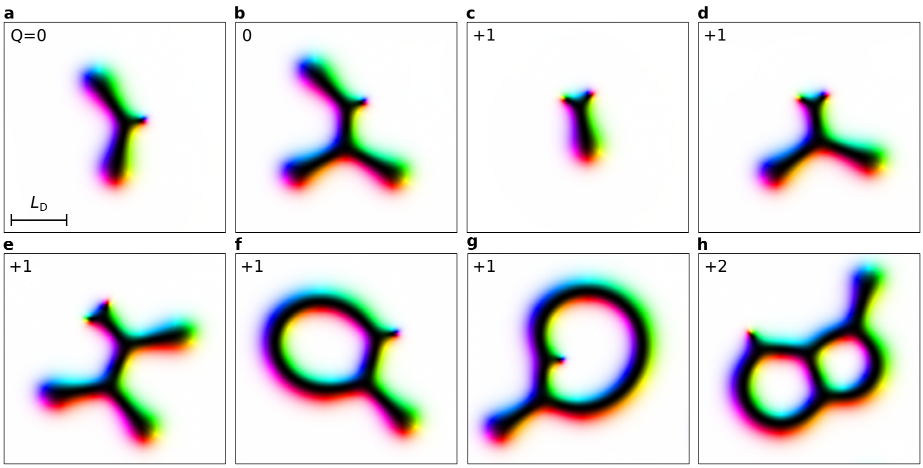

Figure 4.10: **Skyrmions with tails and CKs.** **a-h** show magnetic solitons containing both tails and CKs. The topological charge of each texture is indicated in the left upper corner. The simulations have been performed for the system of size $L_\mathrm{x} = L_\mathrm{y} = 4L_\mathrm{D}$, $L_\mathrm{D} = 64a$ at the magnetic field $h = 0.623$ and zero anisotropy $u = 0$.

4.4 Conclusions

In this Chapter, I have studied homotopy transitions of different chiral magnetic solitons. As an example of a not-fully-localized object, I considered the 2π-DW with a CK, while other examples relate to well-localized Sk solutions. In many cases, CKs play an important role – they appear on a certain stage of homotopy transformations, even if the original texture is free of CKs. The main reason for the appearance of a CK is the conservation of the topological charge for all intermediate magnetic textures which belong to the homotopy path. The latter is the only option that allows going from one Sk to another in a micromagnetic model. At the same time, it is not necessarily true for the discrete model due to the breaking of the topology concept in such models. As I show in various examples, the homotopy paths can be obtained by the GNEB method, calculating the MEPs. This holds even in discrete models when the discretization density is high enough and an initial path is accurately chosen. The task of finding the ansatz for the initial path is beyond the scope of the present study and is more of a mathematical problem. Nevertheless, I found the solution to this problem. By studying the behaviour of certain solitons in the tilted magnetic field, I found the instabilities of these solutions, which are very close to homotopy transition. The snapshots of the system at the instability point turned out to be a good initial guess for the following optimization of the homotopy transition with the GNEB method.

In the last Section, I have studied homotopy transformations that happen without the emergence of CKs. The detailed investigation of this case has led to the discovery of a new type of Sk solutions – Sks with tails. These solutions can be stabilized in the relatively narrow range of parameters above the elliptic instability of the host soliton. Many examples of such solutions are provided. Sks with both tails and CKs can also exist and significantly extend the solitons' diversity in the model of chiral magnets.

5 Current induced dynamics of skyrmions

This chapter is devoted to the dynamic properties of chiral Sks. In **Section** 5.1 I will discuss the dynamics of the 2D Sks induced by Zhang-Li torque. The results obtained in numerical simulations with the LLG equation are supported by analytical solutions obtained with the Thiele equation. The complete analysis provided in **Sections** 5.2, 5.3 leads to the classification of magnetic Sks according to their symmetry. I show that the symmetry of Sks defines their dynamic properties. Some of the results presented below have been published in Ref. [80].

5.1 LLG equation with the Zhang-Li torque

As I have shown in the previous chapters, the model of the chiral magnet contains a rich diversity of very different Sks. The natural question that arises relates to the dynamical properties of these Sks [81, 82, 83, 84]. I consider the case when the Sk motion is induced by electric current [85] and additional torques appearing in the LLG equations are described by the Zhang-Li torque. For this case, the numerical simulations based on the LLG equation and analytical analysis based on the Thiele equation are done. It is worth noting that as long as the Sk moves as a rigid object, the obtained results, to a certain extent, can be applied not only to the Zhang-Li torque but also to the Sk dynamics induced by other external stimuli [86].

The LLG equation (1.18) with the Zhang-Li torque writes,

$$\frac{\partial \boldsymbol{n}}{\partial t} = -\gamma \boldsymbol{n} \times \boldsymbol{B}_{\text{eff}} + \alpha \boldsymbol{n} \times \frac{\partial \boldsymbol{n}}{\partial t} - \boldsymbol{n} \times \left(\boldsymbol{n} \times \left(\boldsymbol{I} \cdot \nabla\right) \boldsymbol{n}\right) - \xi \boldsymbol{n} \times \left(\boldsymbol{I} \cdot \nabla\right) \boldsymbol{n}. \tag{5.1}$$

Without loss of generality, the direction of the electric current flow is chosen to be opposite to the positive direction of x-axis, i.e. $\boldsymbol{I} = -I\boldsymbol{e}_{\mathrm{x}}$, as it is shown in Fig.5.1 **a**. I work in a regime of low currents, the case of high current strength was studied in Ref. [87].

The switching on of the current at the moment $t = 0$, strictly speaking, can be done

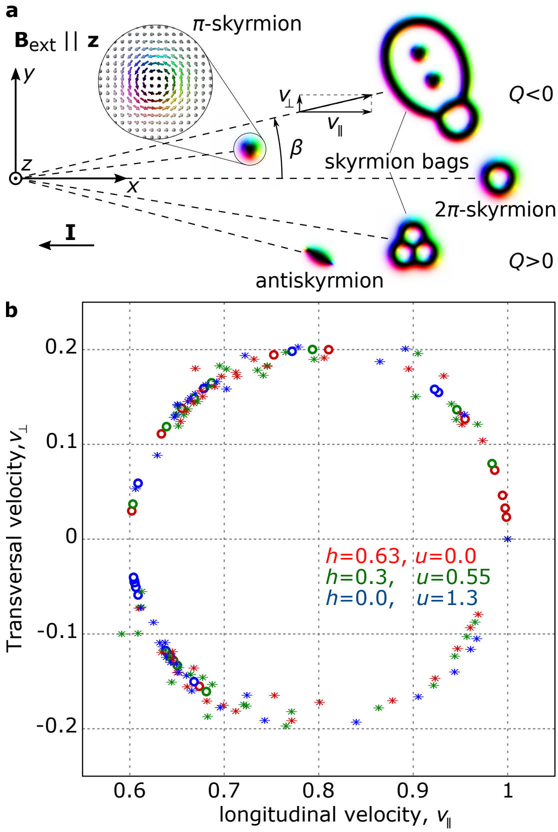

Figure 5.1: **Representative example for skyrmions velocity distribution**. **a** Schematic representation for the trajectories of Sks moving under electric current $\boldsymbol{I}$. β is the Sk deflection angle. The inset shows the spin texture for the π-skyrmion. **b** The velocity distribution for a wide diversity of skyrmions obtained in micromagnetic simulations at different values of the external magnetic field h and anisotropy u. The velocities represented by the circle symbols lie on a perfect circle with the centre at $v_\parallel = 0.8$, $v_\perp = 0$ irrespective of h and u. The velocities marked by the stretched star symbols lie close to that circle. The velocities are given in reduced units concerning the velocity of the skyrmionium. The simulations are performed at realistic values of the Gilbert damping $\alpha = 0.06$ and the degree of non-adiabaticity, $\xi = 0.1$. This figure has been published in [80].

in different ways. For instance, one can apply the time-dependent function $I(t)$ for the current continuously changing from zero to a constant value. Instead, here I consider the case when the current is abruptly switched from zero to constant at $t > 0$, which makes the following analysis simpler and reflects the critical physics of the process. The arguments supporting the latter are the following. The Sk dynamics can be split into two types: steady-state motion corresponding to rigid translations of the magnetic texture and transition state, which precedes the uniform motion. The duration of the transient state is usually short in time, and the system exponentially fast tends to come to the uniform motion regime. The latter agrees well with the observations in the numerical simulations of Sks dynamics based on the equation (5.1). It also agrees with the results of analytical solutions for the case of the current induced rotation of the cone phase, which I provide in **Section** 7.1. De facto, the exact way the current function changes at $t > 0$ does not affect the dynamics at the steady motion regime and only influences the duration of the transient state. In addition, from the general point of view, the tendency of the system of magnetic spins to move coherenly is a common feature of different dynamical systems, also known as synchronization.

The uniform motion of Sks corresponds to its translation with the constant velocity, $\boldsymbol{V}$, which is nothing but the time derivative of the collective coordinate $\boldsymbol{r}_s = (x_s, y_s)$. As soon as the use of collective coordinates is possible, they can be defined in various ways. In the case of an infinite $2D$-plane with a single soliton, one can use the following formula, [88]

$$\boldsymbol{r}_s = \frac{\int \mathrm{d}\Omega(1 - n_\mathrm{z})\boldsymbol{r}}{\int \mathrm{d}\Omega(1 - n_\mathrm{z})}. \tag{5.2}$$

Substituting the magnetic texture, $\boldsymbol{n}(\boldsymbol{r}, t)$, obtained from the numerical solution of the LLG equation (5.1) into (5.2), one can obtain the Sk position at a particular moment in time, $\boldsymbol{r}_s(t)$. In practice, however, the LLG simulations are performed with PBCs. When the soliton approaches the boundary of the simulated box, formula (5.2) fails. To fix this problem, I use the modified formula for the calculation of the Sk position:

$$\begin{aligned} x_s &= \frac{L_\mathrm{x}}{2\pi} \arctan \frac{\int \mathrm{d}\Omega(1 - n_\mathrm{z}) \sin 2\pi x/L_\mathrm{x}}{\int \mathrm{d}\Omega(1 - n_\mathrm{z}) \cos 2\pi x/L_\mathrm{x}} + l_\mathrm{x} L_\mathrm{x}, \\ y_s &= \frac{L_\mathrm{y}}{2\pi} \arctan \frac{\int \mathrm{d}\Omega(1 - n_\mathrm{z}) \sin 2\pi y/L_\mathrm{y}}{\int \mathrm{d}\Omega(1 - n_\mathrm{z}) \cos 2\pi y/L_\mathrm{y}} + l_\mathrm{y} L_\mathrm{y}, \end{aligned} \tag{5.3}$$

where $L_\mathrm{x}, L_\mathrm{y}$ correspond to the size of the rectangular shape domain and integer numbers $l_\mathrm{x}, l_\mathrm{y}$ account how many times the Sk crossed the x and y boundaries, respectively. This approach for the calculation of a center of mass of a many-particle system [89] provides a formula very similar to (5.3).

Knowing the Sk position, the velocity of its uniform motion can be easily found $\boldsymbol{V} = \dot{\boldsymbol{r}}_s(t)$. The velocities of different Sks have been calculated and are shown in Fig. 5.1 **b** in dimensionless units $\boldsymbol{V}/V_0 = (v_\parallel, v_\perp)$, where $V_0 = -I\xi/\alpha$ is the speed of topologically trivial Sk [88]. The Sk deflection angle, β is another important dynamical characteristic, which is defined as

$$\beta = \arctan \frac{v_\perp}{v_\parallel}. \tag{5.4}$$

The sign of β correlates with the sign of the topological charge Q and for topologically trivial Sks $\beta = 0$. The distribution of Sk velocities Fig. 5.1 **b** is calculated at fixed dynamical parameters I, α, ξ and for three different sets of parameters h, u. The obtained distribution indicates some correlations between velocities of different Sks appearing in a clearly seen ring-shaped pattern. Remarkably, this phenomenon remains for different values of an external magnetic field and anisotropy. As I show below, the study of this intriguing property of chiral magnetic Sks does not require time-consuming LLG simulations but can be performed entirely within a semi-analytical approach based on the Thiele equation.

5.2 The geometry of the Thiele equation

The Thiele equation (1.23) is nothing but the system of linear equations for the Sk velocity $\boldsymbol{V}$. The solution of this system of linear equations can be easily obtained and written as follows,

$$v_{\parallel} = \frac{\alpha}{\xi}\left(1 + \frac{\left(\alpha \det \hat{\Gamma} + Q\Gamma_{\mathrm{xy}}\right)(\xi - \alpha)}{Q^2 + \alpha^2 \det \hat{\Gamma}}\right), v_{\perp} = -\frac{\alpha}{\xi}\frac{(\xi - \alpha)\, Q}{Q^2 + \alpha^2 \det \hat{\Gamma}}\Gamma_{\mathrm{xx}}, \tag{5.5}$$

where $\det \hat{\Gamma} = \Gamma_{\mathrm{xx}}\Gamma_{\mathrm{yy}} - \Gamma_{\mathrm{xy}}^2$ is the determinant of dissipation tensor, $\hat{\Gamma}$, defined in (1.22). It is easy to show that the formula (5.5) can be presented in an alternative form containing the equation of a circle explicitly. The goal behind this is to reveal the velocity distribution observed in the numerical experiment, Fig. 5.1 **b**. Interestingly, the numerically found velocity distribution can provide some hints. For instance, as follows from Fig. 5.1 **b** the radius and the center of the circle do not depend on the spin texture of the Sk but may depend on dynamical parameters α and ξ. In view of the above I introduce the following parameters of the circle $R_c = \dfrac{\xi - \alpha}{2\xi}$, $v_c = \dfrac{\xi + \alpha}{2\xi}$ and rewrite (5.5) as

$$v_{\parallel} - v_c = R_c \frac{\alpha^2 \det \hat{\Gamma} - Q^2 + 2\alpha Q \Gamma_{\mathrm{xy}}}{\alpha^2 \det \hat{\Gamma} + Q^2}, v_{\perp} = -R_c \frac{2\alpha Q \Gamma_{\mathrm{xx}}}{\alpha^2 \det \hat{\Gamma} + Q^2}. \tag{5.6}$$

My next step is based on the observation that (5.6) has parts similar to the double-angle formulae for *sin* and *cos* functions

$$\sin \rho = \frac{2 \tan \rho/2}{1 + \tan^2 \rho/2}, \ \cos \rho = \frac{1 - \tan^2 \rho/2}{1 + \tan^2 \rho/2}. \tag{5.7}$$

To employ (5.7) one needs to define the angle ρ, which can be chosen as $\rho = 2 \arctan \dfrac{-Q}{\alpha\sqrt{\det \hat{\Gamma}}}$, and then (5.6) takes the form

$$v_{\parallel} - v_c = R_c \left(\cos \rho - \frac{\Gamma_{\mathrm{xy}}}{\sqrt{\det \hat{\Gamma}}} \sin \rho\right), v_{\perp} = R_c \frac{\Gamma_{\mathrm{xx}}}{\sqrt{\det \hat{\Gamma}}} \sin \rho. \tag{5.8}$$

As it follows from (5.8), to get the circle equation, one needs to require fulfilling the two conditions: $\Gamma_{\rm xy} = 0$ and $\Gamma_{\rm xx} = \Gamma_{\rm yy}$, or in other words, dissipation tensor must be proportional to the identity matrix. Only in this case, (5.8) is the parametric equation of the circle with the radius $|R_c|$ and the center at $(v_c, 0)$ in the velocity plane. In the next Section, I discuss a particular case when $\hat{\Gamma}$ is proportional to the identity matrix, but first, I want to consider the most general case. The quantity that can be thought of as the deviation measure for the tensor from the identity matrix must be proportional to both the difference of diagonal terms $\Gamma_{\rm xx} - \Gamma_{\rm yy}$ and to non-diagonal term $\Gamma_{\rm xy}$. Moreover, it is convenient to choose this quantity in such a way that it contains the determinant and a trace of tensor Γ. Taking the above into account, I define this quantity as follows,

$$S^2 = (\Gamma_{\rm xx} - \Gamma_{\rm yy})^2 + 4\Gamma_{\rm xy}^2 = \left(\mathrm{Tr}\hat{\Gamma}\right)^2 - 4\det\hat{\Gamma}, \tag{5.9}$$

where $\mathrm{Tr}\hat{\Gamma} = \Gamma_{\rm xx} + \Gamma_{\rm yy}$ is the trace of tensor Γ. The expression (5.9) is nothing but a square of the modulus of the complex number $S = \Gamma_{\rm xx} - \Gamma_{\rm yy} + 2i\Gamma_{\rm xy}$, which in polar coordinates can be written as

$$S = |S|\left(\cos\psi + i\sin\psi\right), \psi = \arctan\frac{2\Gamma_{\rm xy}}{\Gamma_{\rm xx} - \Gamma_{\rm yy}}, \tag{5.10}$$

The latter provides the useful expressions $\Gamma_{\rm xx} - \Gamma_{\rm yy} = |S|\cos\psi$ and $2\Gamma_{\rm xy} = |S|\sin\psi$ which can be employed into velocity formula (5.8). The formula for the longitudinal component of the velocity becomes

$$v_{\parallel} = v_c + R_c\cos\rho - R_c\frac{|S|\sin\rho}{2\sqrt{\det\hat{\Gamma}}}\sin\psi, \tag{5.11}$$

and the transversal component of the velocity takes the form

$$v_{\perp} = R_c\frac{\mathrm{Tr}\hat{\Gamma}}{2\sqrt{\det\hat{\Gamma}}}\sin\rho + R_c\frac{|S|\sin\rho}{2\sqrt{\det\hat{\Gamma}}}\cos\psi. \tag{5.12}$$

As I will show below, the angle ψ reflects the rotation of Sks about z-axis.

5.3 Skyrmion symmetry

5.3.1 Dissipation tensor transformations

In cylindrical coordinates $r = \sqrt{x^2+y^2}$, $\phi = \arctan(y/x)$, $z = z$ the dissipation tensor (1.22) can be written as

$$\hat{\Gamma} = \frac{\mathrm{Tr}\hat{\Gamma}}{2}\begin{pmatrix} 1 & 0 \\ 0 & 1 \end{pmatrix} + \frac{1}{2}\begin{pmatrix} F & G \\ G & -F \end{pmatrix}, \tag{5.13}$$

Interestingly, the trace of the tensor Γ can be written as $\mathrm{Tr}\hat{\Gamma} = \mathcal{E}_{\mathrm{ex}}/(4\pi)$ where $\mathcal{E}_{\mathrm{ex}}$ is exchange energy (1.33). The values of components F and G are defined through the integrals:

$$\begin{aligned} F &= \frac{1}{4\pi}\int_0^\infty\int_0^{2\pi} r\mathrm{d}\phi\mathrm{d}r\left(f\cos 2\phi - g\sin 2\phi\right), \\ G &= \frac{1}{4\pi}\int_0^\infty\int_0^{2\pi} r\mathrm{d}\phi\mathrm{d}r\left(f\sin 2\phi + g\cos 2\phi\right), \end{aligned} \tag{5.14}$$

where $f(r,\phi) = \left(\dfrac{\partial \boldsymbol{n}}{\partial r}\right)^2 - \dfrac{1}{r^2}\left(\dfrac{\partial \boldsymbol{n}}{\partial \phi}\right)^2$, $g(r,\phi) = \dfrac{2}{r}\dfrac{\partial \boldsymbol{n}}{\partial r}\cdot\dfrac{\partial \boldsymbol{n}}{\partial \phi}$ and $\boldsymbol{n} = (n_{\mathrm{x}}, n_{\mathrm{y}}, n_{\mathrm{z}})^{\mathrm{T}}$. Note that functions f and g are scalar functions, meaning they do not depend on the magnetic vector rotations about z-axis by arbitrary angle χ. The corresponding transformation of the magnetization field is given by $(n_{\mathrm{x}}, n_{\mathrm{y}}, n_{\mathrm{z}}) \to (n_{\mathrm{x}}\cos\chi - n_{\mathrm{y}}\sin\chi, n_{\mathrm{x}}\sin\chi + n_{\mathrm{y}}\cos\chi, n_{\mathrm{z}})$. To keep the Hamiltonian (1.6) unchanged, the latter transformation requires performing an additional spatial rotation $\phi \to \phi \pm \chi$ (sign depends on the DMI form). Performing both rotations in (5.14), one obtains that functions F, G transform according to $(F, G) \to (F\cos 2\chi \pm G\sin 2\chi, \mp F\sin 2\chi + G\cos 2\chi)$. For simplicity, hereinafter, I will refer to these two rotations – spin rotation and spatial rotation, as just rotation of Sk. Noticing from (5.13) that $F = \Gamma_{\mathrm{xx}} - \Gamma_{\mathrm{yy}}$ and $G = 2\Gamma_{\mathrm{xy}}$, leads to an equivalent form of the transformation of the complex number S, $S \to Se^{\pm 2i\chi}$. Therefore, angle ψ in (5.10) is connected to the rotation angle χ by the simple rule: rotating of the Sk by angle χ leads to the change of angle ψ by 2χ. In particular, from this follows that the rotation of every Sk by angle π does not change its velocity components (5.11), (5.12). All above makes sense only in the most general case when F and G can take arbitrary values. Now, I will consider a particular case $F = G = 0$ and identify the conditions when it takes place.

For the following analysis it is convenient to consider the magnetization vector $\boldsymbol{n}$, in the cylindrical coordinate system,

$$\boldsymbol{n} = n_{\rm r}\boldsymbol{e}_{\rm r} + n_{\phi}\boldsymbol{e}_{\phi} + n_{\rm z}\boldsymbol{e}_{\rm z}, \tag{5.15}$$

where cylindrical basis vectors $\boldsymbol{e}_{\rm r}$, $\boldsymbol{e}_{\phi}$, $\boldsymbol{e}_{\rm z}$ are connected to Cartesian coordinates $\boldsymbol{e}_{\rm x}$, $\boldsymbol{e}_{\rm y}$, $\boldsymbol{e}_{\rm z}$ as follows

$$\boldsymbol{e}_{\rm r} = \boldsymbol{e}_{\rm x}\cos\phi + \boldsymbol{e}_{\rm y}\sin\phi,\ \boldsymbol{e}_{\phi} = -\boldsymbol{e}_{\rm x}\sin\phi + \boldsymbol{e}_{\rm y}\cos\phi,\ \boldsymbol{e}_{\rm z} = \boldsymbol{e}_{\rm z}. \tag{5.16}$$

By substituting (5.16) into (5.15) one can find connection between the projections $n_{\rm x}, n_{\rm y}$ and $n_{\rm r}, n_{\phi}$, note that $n_{\rm z}$ coincides in both systems

$$n_{\rm x} = n_{\rm r}\cos\phi - n_{\phi}\sin\phi,\ n_{\rm y} = n_{\rm r}\sin\phi + n_{\phi}\cos\phi. \tag{5.17}$$

Substituting (5.17) into the formula for $f\,(r,\phi)$ and $g\,(r,\phi)$ I get

$$\begin{aligned} f\,(r,\phi) &= \left(\frac{\partial\boldsymbol{n}}{\partial r}\right)^2 - \frac{1}{r^2}\left(\frac{\partial\boldsymbol{n}}{\partial\phi}\right)^2 - \frac{2}{r^2}\left[n_{\rm r}\frac{\partial n_{\phi}}{\partial\phi} - n_{\phi}\frac{\partial n_{\rm r}}{\partial\phi}\right] - \frac{1}{r^2}\left[n_{\rm r}^2 + n_{\phi}^2\right], \\ g\,(r,\phi) &= \frac{2}{r}\frac{\partial\boldsymbol{n}}{\partial r}\cdot\frac{\partial\boldsymbol{n}}{\partial\phi} + \frac{1}{r}\left[n_{\rm r}\frac{\partial n_{\phi}}{\partial r} - n_{\phi}\frac{\partial n_{\rm r}}{\partial r}\right], \end{aligned} \tag{5.18}$$

where $\boldsymbol{n}$ is assumed to be in cylindrical coordinates (5.15). In the next step, I write the magnetization components as the generalized Fourier series,

$$n_i(r,\phi) = a_i^0(r) + \sum_{q=1}^{\infty}\left(a_i^q(r)\cos qk_s\phi + b_i^q(r)\sin qk_s\phi\right),\ i \in (r,\phi,z). \tag{5.19}$$

where functions $a_i^0(r), a_i^q(r), b_i^q(r)$ are not independent and constrained due to $|\boldsymbol{n}| = 1$. The positive integer number k_s accounts for the Sk symmetry corresponding to the transformation $n_i(r,\phi) = n_i(r,\phi + 2\pi l/k_s)$ with $l = \overline{1,k_s}$. Substituting (5.19) into (5.18) one gets the similar Fourier series for functions f and g, taking into account they appear in (5.14) as multipliers with $\sin 2\phi$ and $\cos 2\phi$, it is enough to present them in the restricted form

$$\begin{aligned} f\,(r,\phi) &= \tilde{f}\,(r,\phi) + a_1(r)\cos 2\phi + b_1(r)\sin 2\phi, \\ g\,(r,\phi) &= \tilde{g}\,(r,\phi) + a_2(r)\cos 2\phi + b_2(r)\sin 2\phi \end{aligned} \tag{5.20}$$

The functions $\tilde{f}\,(r,\phi)$ and $\tilde{g}\,(r,\phi)$ in (5.20) are linearly independent on functions $\cos 2\phi$ and $\sin 2\phi$. Because of that, after integration in (5.14) they give zero contribution to F and G. Functions $a_1(r)$, $b_1(r)$, $a_2(r)$, and $b_2(r)$ are connected to the Fourier series coefficients in (5.19) and depend on the value of k_s. For instance, if $k_s \geq 3$ one has

$$a_1(r) = b_1(r) = a_2(r) = b_2(r) = 0. \tag{5.21}$$

This can be proven as follows. The substitution of (5.19) into (5.18) leads to the appearance of the terms which are proportional to $[f_1(qk_s\phi)\, f_2(pk_s\phi)]$, where functions f_1, f_2 can be either sin or cos, while q, p are non-negative integers. Using the product-to-sum identity formulae, one can get $\cos(qk_s\phi)\cos(pk_s\phi) = [\cos(p-q)k_s\phi + \cos(p+q)k_s\phi]/2$, and similarly for other products of trigonometric functions. From this follows that at $k_s \geq 3$, for all integers q and p one never get $(p-q)k_s = 2$ or $(p+q)k_s = 2$ due to the fact that $2/k_s$ is non-integer. However, if $k_s = 1$ or $k_s = 2$, strictly speaking, functions $a_1(r)$, $b_1(r)$, $a_2(r)$, $b_2(r)$ can take non-zero values.

$k\pi$-skyrmions in the model with D_{2d} type of DMI (1.10) can be thought of as an example for the class of solutions with $k_s = 2$ and $F = G = 0$. With parametrization of the magnetization with spherical angles Θ and Φ, these Sks are described by functions $\Theta = \Theta(r)$, $\Phi = -\phi$, with boundary conditions $\Theta(0) = k\pi$, $\Theta(r \to \infty) = 0$. As one can get by direct calculations $n_\mathrm{r} = \sin\Theta\cos 2\phi$, $n_\phi = -\sin\Theta\sin 2\phi, n_\mathrm{z} = \cos\Theta$, so indeed, according to (5.19), $k_s = 2$. On the other hand, the functions f and g write:

$$f(r,\phi) = \left(\frac{\mathrm{d}\Theta}{\mathrm{d}r}\right)^2 - \frac{\sin^2\Theta}{r^2},\ g(r,\phi) = 0. \tag{5.22}$$

Using (5.22) for calculation the integrals (5.14) gives $F = G = 0$.

The connection between the Sks rotation symmetry and transformations $n_i(r,\phi) = n_i(r,\phi+2\pi l/k_s)$ with $l = \overline{1,k_s}$ can be seen from (5.17). In terms of Cartesian components, it can be written as

$$\begin{aligned} n_\mathrm{x}(r,\phi+\phi_s) &= n_\mathrm{r}\cos(\phi+\phi_s) - n_\phi\sin(\phi+\phi_s) = n_\mathrm{x}(r,\phi)\cos\phi_s - n_\mathrm{y}(r,\phi)\sin\phi_s,\\ n_\mathrm{y}(r,\phi+\phi_s) &= n_\mathrm{r}\sin(\phi+\phi_s) + n_\phi\cos(\phi+\phi_s) = n_\mathrm{x}(r,\phi)\sin\phi_s + n_\mathrm{y}(r,\phi)\cos\phi_s, \end{aligned} \tag{5.23}$$

where $\phi_s = 2\pi l/k_s$. In the case of D_{2d} type of DMI, the above remains true if one uses a left-hand-side cylindrical coordinate system. In this case ϕ changes it sign, $\phi \to -\phi$ in (5.16), (5.17) and, as a result, in (5.23). Thereby, the $k\pi$-skyrmions in the case of D_{2d} type of DMI, in fact, correspond to $k_s = \infty$ and not $k_s = 2$.

Thus, based on the symmetry of the dissipation tensor, all Sks can be split into two classes: high-symmetry ($S = 0$) and low-symmetry ($S \neq 0$) Sks. Sks of different symmetry possess different dynamics according to the solutions of the Thiele equation (5.11), (5.12). As follows from above, Sks with $k_s \geq 3$ belong to the high-symmetry class, while those with $k_s = 2$ or $k_s = 1$ are not necessarily characterized by $S \neq 0$.

5.3.2 High- and low-symmetry skyrmions

The examples of high-symmetry Sks with $S = 0$ and different k_s are given in Fig. 5.2 **a** for three different sets of parameters (h, u): $(0.63, 0)$, $(0.3, 0.55)$ and $(0, 1.3)$. At these parameters, the shown solutions have the rotational symmetry of the order k_s. However, that may not be the case for other values of parameters (h, u).

The changing of Sk shapes at these parameters mimics the behaviour of the 2π-DW, the solution of which is known. That means that at the higher magnetic field and lower anisotropy, the distance between contours $n_{\mathrm{z}} = 0$ becomes smaller. From the point of view of the dynamics, it is crucial how the dissipation tensor of Sk changes.

At a fixed value of α and ξ, only this quantity defines the Sk velocity distribution along the circle Fig. 5.2 **b**. As follows from the solution of the Thiele equation (5.11), (5.12), the point on the circle is entirely defined by angle ρ, the varying of which at different α is shown in Fig. 5.2 **c**. Note, the parameters of the circle v_c and R_c are depends on α and ξ only.

The connection between ρ and deflection angle β follows from the law of sines,

$$\tan\beta = \frac{\sin\rho\sin\beta_{\max}}{1+\cos\rho\sin\beta_{\max}}, \tag{5.24}$$

where $\beta_{\max} = \arcsin(R_{\mathrm{c}}/v_{\mathrm{c}})$ is the maximal deflection angle that high-symmetry Sk can have. This formula is useful because it allows one to obtain values of α and ξ from experimental fit for deflection angle as function of an external magnetic field, for instance. To see this clearly, I write (5.24) explicitly as

$$\tan\beta = \frac{8\pi Q\mathcal{E}_{\mathrm{ex}}(\xi-\alpha)}{(8\pi Q)^2 + (\mathcal{E}_{\mathrm{ex}})^2\alpha\xi}, \tag{5.25}$$

where exchange energy can be calculated in equilibrium for any Sk at given value of the magnetic field. Formula (5.25) also works well for low-symmetry Sks as long as the modulus of complex number S is small.

As follows from the formulas for Sk velocity and connection between Sk rotations and phases ψ, the velocity space for any low-symmetry Sk ($S \neq 0$) is nothing but a circle defined accordingly to (5.11), (5.12). Each point on this circle corresponds to two Sks orientations that differ by angle π. The center of that circle $(v_\parallel^0, v_\perp^0)$ and its radius $|R_0|$ are defined as following

$$v_\parallel^0 = v_{\mathrm{c}} + R_{\mathrm{c}}\cos\rho,\ v_\perp^0 = -R_c\frac{\mathrm{Tr}\hat{\Gamma}}{2\sqrt{\det\hat{\Gamma}}}\sin\rho,\ R_0 = R_c\frac{|S|\sin\rho}{2\sqrt{\det\hat{\Gamma}}}. \tag{5.26}$$

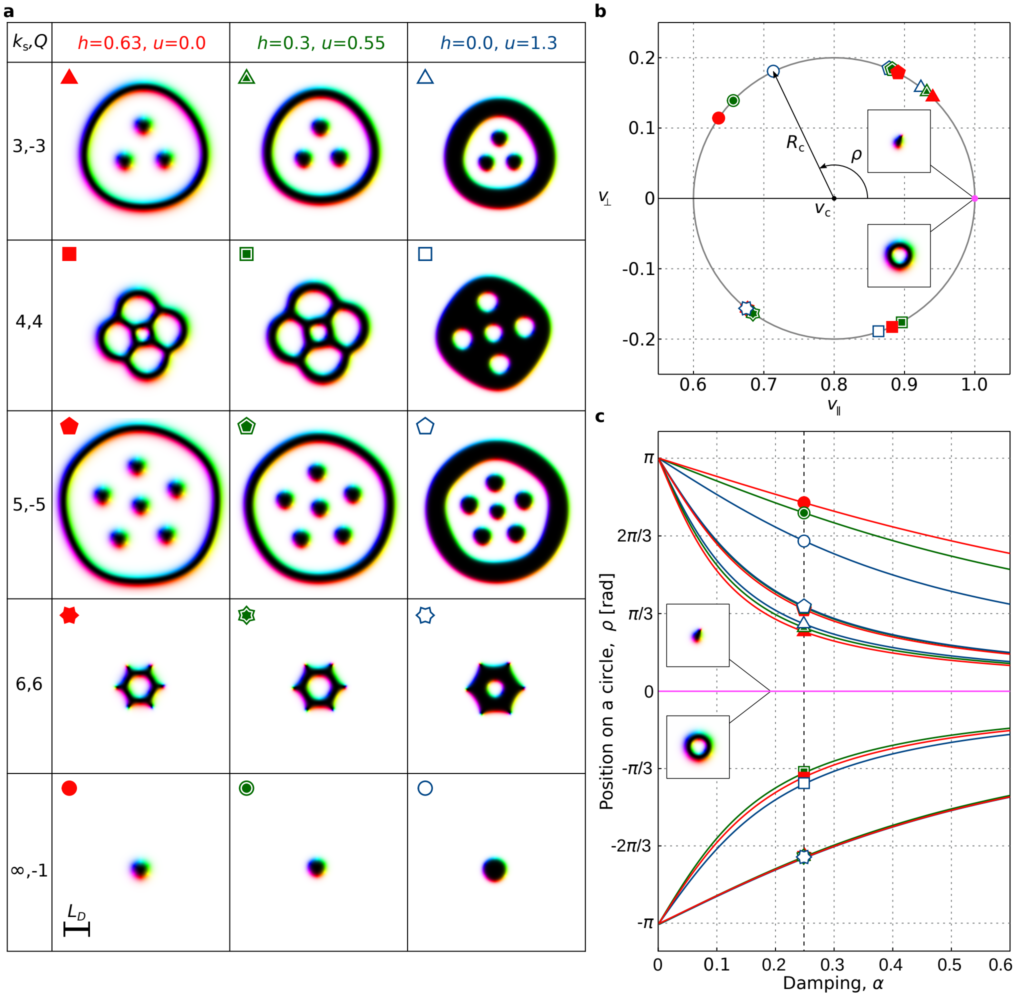

Figure 5.2: **The velocity circle for high-symmetry skyrmions**. **a** shows the set of high-symmetry Sks at different external magnetic fields, h and anisotropies, u. The parameter k_s in the first column stands for the order of the rotational symmetry of the Sk, and Q is the topological charge. The π-skyrmion in the last row has axial symmetry, $k_s = \infty$. **b** shows the distribution of velocities of skyrmions for particular symmetry, and the corresponding symbols depict particular values of h and u. The velocity of topologically trivial solutions, e.g. the skyrmionium and the CD (see insets), is marked with a magenta circle, $v_\parallel = 1$, $v_\perp = 0$. The calculations based on a semi-analytical approach are performed for $\alpha = 1/4$, $\xi/\alpha = 5/3$. The grey circle corresponds to (5.8). **c** shows the change of angle ρ for the solitons depicted in **a** as a function of $\alpha \in (0, 0.6]$, for fixed $\xi/\alpha = 5/3$. The dashed line corresponds to damping parameter $\alpha = 1/4$ as in **b**. This figure is adapted from [80].

Consequently, the velocity space for a set of low-symmetry Sks represents a set of such circles, see Fig. 5.3 **a-c**. The plotted velocities correspond to the same Sks as on Fig. (5.1)

b. Additionally to three different sets of (h, u) I consider three different sets of parameters (α, ξ) with fixed ratio $\alpha/\xi = 3/5$ that is needed to keep the values of v_c and R_c unchanged. Since the radii of these circles usually are smaller than the radius of the high-symmetry Sks circle, $|R_0| < |R_c|$, I refer to them as small and big circles, respectively.

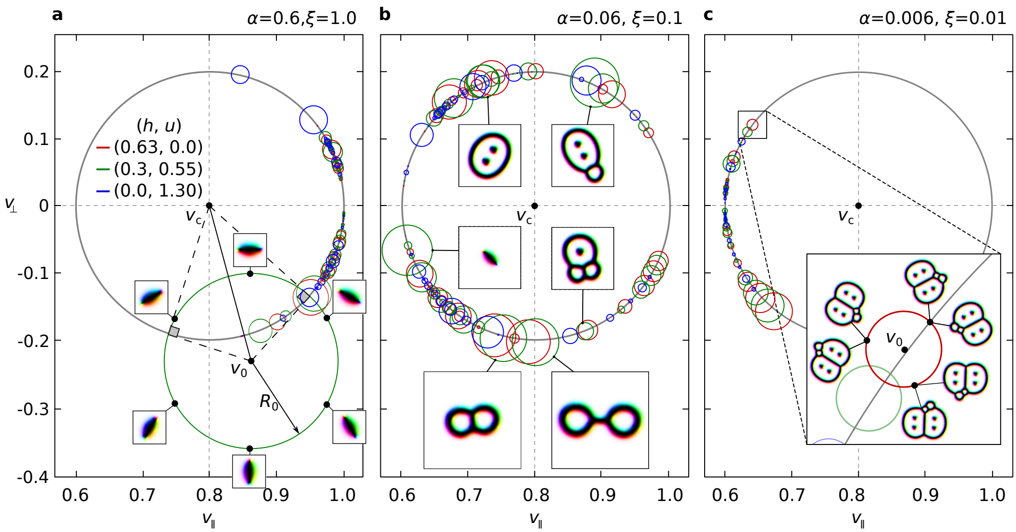

Figure 5.3: **Velocity circles for low-symmetry skyrmions**. **a-c** show the velocity distribution for various low-symmetry Sks at different α and ξ. Some Sks are depicted in the insets. The grey velocity circle for high-symmetry Sks (5.8) is provided for comparison. The velocities of low-symmetry Sks depend on the Sk orientation to the current direction and are bound by a unique circle for each such Sk as illustrated for the antiskyrmion with $k_s = 2$ in **a** and another low-symmetry Sk with $k_s = 1$ in **c**. This figure has been published in [80].

As shown in Fig. 5.3, the center of the small circles is always near the big circle. Taking into account (5.9), the formula (5.26) provides the connection between the parameters of the big circle and small circles:

$$\left(v_\parallel^0 - v_c\right)^2 + \left(v_\perp^0\right)^2 = R_c^2 + R_0^2. \tag{5.27}$$

In particular, as follows from (5.27), the Sks characterized by smaller $|R_0|$ lie closer to the big circle. Besides the value of $|S|$, the radius of the small circle depends on the angle ρ (5.26) as $R_0 \sim \sin\rho$. Thereby, smaller circles generally correspond to ρ near 0 and π while bigger circles are characterized by $\rho \sim \pm\pi/2$. That is seen in Fig. 5.3 **a** and **c** where most of the small circles are located near to the right and the left sides of the big circle, respectively.

5.3.3 Interesting mathematical aspects

The geometry of the velocity space of low-symmetry Sks has many interesting aspects distinguishing this type of solitons from high-symmetry Sks. First of all, it was found that the small circles always intersect the big circle at the right angles. For a particular case of the antiskyrmion, it is shown in Fig. 5.3 **a**. In the set theory [90], the set with a such property is known as the Poincaré disk model. All small circles of low-symmetry Sks have another constraint – they always belong to only one half-plane in the velocity space ($v_\perp > 0$ or $v_\perp < 0$), irrespective of the external parameters. The exception is when all small circles degenerate into one point on the velocity plane. The velocity distribution of both low-symmetry and high-symmetry solutions strongly depends on α and ξ parameters. For instance, for $\alpha < \xi$ and $\alpha > \xi$ (both can be realized in real magnetic systems), the deflection angle β (Sk Hall angle) changes its sign. Figure. 5.4 illustrates this effect.

In particular, under the assumption that α and ξ are independent parameters, figures **a** and **b** show how the big circle for high-symmetry Sks changes with α at fixed ξ and vice versa. In both cases, one can see a set of circles with one common point. For $\alpha = \xi = 0.5$ the velocity circle degenerate into the point, $v_\parallel = 1, v_\perp = 0$ which is the common point for all circles. The changing of the velocity of the π-skyrmion is shown as a black curve. It represents a straight line in the case $\alpha =$ const and a part of a circle in the case $\xi =$ const. The equation of that circle can be obtained from (5.11), (5.12) by eliminating the dependence on α,

$$\left(v_\parallel - \frac{1}{2}\right)^2 + \left(v_\perp - \frac{Q}{\xi \mathrm{Tr}\hat{\Gamma}}\right)^2 = \frac{1}{4} + \frac{Q^2}{\xi^2 \mathrm{Tr}\hat{\Gamma}^2}. \tag{5.28}$$

This is a general formula valid for all high-symmetry Sks. Remarkably, in the case of low-symmetry Sks, this curve represents an ellipse (see Appendix A7). For instance, Fig. 5.4 **c** illustrates this for Ask. Note, the blue curves are parts of the ellipses. The region they swept can be obtained as a set of red circles, each of them is a small circle corresponding to a fixed value of α. The family of complete ellipses is shown in **d**. The corresponding area obtained by varying both α and ψ looks like a set $\mathcal{B}_1 \cup \mathcal{B}_2/(\mathcal{B}_1 \cap \mathcal{B}_2)$ where $\mathcal{B}_k = \left\{ (v_\parallel, v_\perp) : \left(v_\parallel - \frac{1}{2}\right)^2 + (v_\perp - v_k)^2 \leq v_k^2 \right\}, k = 1, 2$, parameters v_1, v_2 are functions of ξ. Varying additionally parameter ξ, one can cover the whole velocity space except the points $v_\parallel \in \mathbb{R}/\left\{0, 1\right\}, v_\perp = 0$.

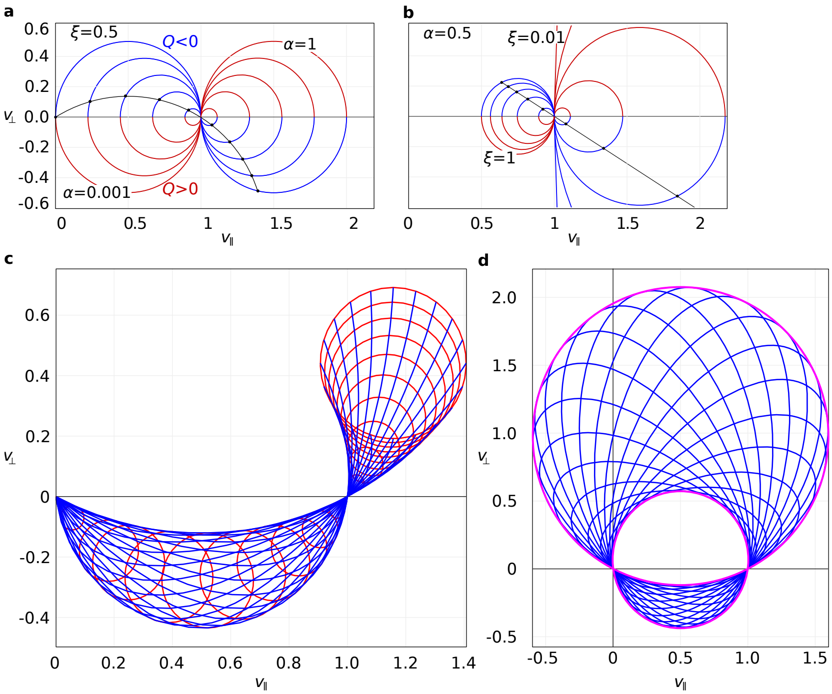

Figure 5.4: **Velocity circles transformations at various α, ξ.** **a** shows the transformation of the circle (5.8) under varying the Gilbert damping, α, at fixed degree of non-adiabaticity $\xi = 0.5$. The circles correspond to α in the interval $[0.001, 1]$ with equidistant step of 0.111. **b** shows the transformation of the big circle under varying degree of non-adiabaticity, ξ, at fixed $\alpha = 0.5$. The circles correspond to ξ in the interval $[0.01, 1]$ with equidistant step 0.11. Black dots in **a** and **b** denote the velocities of π-skyrmion at corresponding parameters α and ξ. Black curve in **a** is given by (5.28). The red and blue colours of the half-circles correspond to $Q > 0$ and $Q < 0$, respectively. **c** shows the velocity space for the antiskyrmion at a fixed $\xi = 0.5$. Each red circle corresponds to velocities of the antiskyrmion at a fixed value of α and different orientation angles $\psi \in [0, \pi)$. Each blue curve corresponds to the antiskyrmion velocity at a fixed value of the orientation angle ψ and different damping parameters of finite range, $\alpha \in [0.001, 1]$. Each blue curve belongs to some ellipse. The complete set of such ellipses is shown in **d**. **a** and **b** have been published in [80].

5.4 Conclusions

In this chapter, I have studied the dynamical properties of Sks induced by the Zhang-Li torque. The obtained results are general for all Sks that move as rigid objects – preserving their shapes and velocities.

The numerical simulations have revealed an intriguing geometric phenomenon that manifests itself by the distribution of velocities of different Sks. The velocities form a ring-shaped pattern that preserves at various parameters (h, u) and depends only on dynamical parameters: the current density, the Gilbert damping, and the coefficient of non-adiabaticity. The analysis based on the Thiele equation allowed explaining this observation establishing the connection between the symmetry of Sks and their dynamics. Note, under the symmetry, I mean the rotational symmetry of magnetic texture that includes the transformation of both spatial and magnetization coordinates. Sks characterized by the rotational axis of order $k_s > 2$ belong to the class of high-symmetry solutions, while all others belong to the class of low-symmetry solutions. The high-symmetry Sks move so that their velocities are bound to a single, big circle. The dynamical properties of low-symmetry Sks depend on the Sk orientation with respect to the current direction. Considering all possible orientations leads to the appearance of a small circle in the velocity plane, which is unique for every Sk but, in a certain sense, is connected to the big one. Thereby, the total velocity space for the studied Sks represents a set of circles, the radii and centers of which are somehow distributed for given external parameters. Topologically trivial Sks, irrespective of their symmetry, move with the same velocity and, thereby, represent only a point on the velocity plane.

The velocity space of Sks has many beautiful geometrical properties that have been deduced from the solution of the Thiele equation. The most interesting properties are i) the intersection of small and big circles at right angles and ii) the region in the velocity plane that under varying the damping parameter in the case of low-symmetry Sks takes the shape of two circles union.

The first one follows from the distribution of the centres for small circles (5.27). The second one has not strict mathematical proof for now, but the first steps in this direction have been done in Appendix A7 . In particular, I have shown that for a fixed orientation of low-symmetry Sk, its velocity belongs to some ellipse, while the exact position on this ellipse depends on the damping value. Including different orientations of the Sk into consideration sweeps a region on the velocity plane with the mentioned property.

6 Thermal generation of chiral droplets

In this Chapter, I study the effect of the spontaneous nucleation of CDs induced by thermal fluctuation at the tilted magnetic field. In **Section** 6.1, I estimate the stability range of the CD and provide some arguments in favour of the possibility to generate these solitons from the FM vacuum at finite temperatures. The analysis of asymptotic behaviour of the CD solution is based on the analysis of 2π-DW in the tilted magnetic field. This analysis provides an estimate for the size of CD in the configuration space. Then in **Section** 6.2 I present the results of the numerical experiment based on Monte-Carlo and stochastic LLG simulations. Both approaches give nearly identical results and independently prove the reality of the observable phenomenon.

6.1 Chiral droplet in the tilted magnetic field

Some of the static properties of the CD, which are typical for all Sks with CKs, have been considered in two previous chapters where I consider the case of the perpendicular magnetic field only. Below I focus on the stability of the CD in the presence of a tilted magnetic field. As I show later, the presence of the tilted magnetic field plays a crucial role in the thermal generation of CDs. The general reasons for that are the following. From the topology point of view, the CD is a trivial soliton, $Q = 0$, so one can expect its appearance in the system without the appearance of singularities. Magnetic singularities usually appear at a high-temperature regime where π-skyrmions and their lattice are generated. Therefore, at low temperatures, one should expect the appearance of solitons whose nucleation does not require the creation of singularities. Because of the reasons which I discussed in detail in **Chapter** 4, the solitons with $Q = 0$ satisfy this criterion. Moreover, the CD is the most compact soliton in this model, and due to this, it is the most promising topologically trivial soliton which can be generated by thermal fluctuation. Before discussing the stochastic dynamics, it is important to estimate the stability of CD at zero temperature, $T = 0$.

6.1.1 Stability range

The stability region of the CD is shown in Fig. 6.1 **a** in terms of the amplitude of the magnetic field, h and its tilt angle, θ_{h}. The phase angle, ϕ_{h} which determines the direction of the field in the plane, is set to $-\pi/4$. The region at which the CD is stable is bounded by the collapse field (from above) and the elliptic instability field (from below). It is worth noting that the elliptic instability field also represents the phase transition line between the lattice of π-skyrmions and the state of the periodic spin spirals. Thereby, the region of stability of the CD is entirely inside the area where the ground state of the system is the lattice of π-skyrmions while the FM state is a metastable state at these parameters. With the increase of the tilt of the magnetic field, the stability range for CD decreases and disappears at $\theta_{\mathrm{h}} \simeq 1.1$. The corresponding point on the stability diagram represents the triple point at which the FM state, the π- skyrmion lattice and periodic spin spiral have identical energies [64].

The presence of the tilted magnetic field slightly changes the shape of the CD (see lower panel on **a**). The energy difference between CD and FM sate decreases with an increase of the tilt angle, see Fig. 6.1 **b**.

Let me compare the magnetic textures of CD and π-skyrmion in the presence of the tilted magnetic field. The π-skyrmion, the CD and the 2π-DW in the tilted magnetic field are shown in Fig. 6.1 **c**. The projections of their corresponding vector fields on the unit sphere are presented in **d** and on the plane (Θ, Φ) in **e**. These projections differ by shape and the area they occupy in the parameter space. In the case of π-skyrmion, the $\mathbb{S}^2$ sphere is entirely covered. From the conservation of the topological charge for this solution, it follows that the π-skyrmion vector field can not be continuously transformed into a single point on the sphere – configuration space of the FM state. On the contrary, in the case of CD, the $\mathbb{S}^2$ sphere is only partially covered. Therefore, there is a mapping of such a region into a single point. Note, such mapping exists for any topologically trivial soliton. The 2π-DW corresponds to a closed curve on the $\mathbb{S}^2$ sphere. That also agrees with the topological triviality of this magnetic texture.

From general considerations, the probability of spontaneous nucleation of the localized magnetic texture of particular distribution $\boldsymbol{n}(\boldsymbol{r})$ is proportional to the area its configuration space occupies on a $\mathbb{S}^2$ sphere. It is reasonable to compare only localized states, such as the π-skyrmion and the CD. For the case of the π-skyrmion, this area equals 4π, while it is sufficiently smaller for the CD. Moreover, the area of the CD decreases at a bigger tilts angle of the magnetic field that is not the case for the π-skyrmion. As one can conclude from Fig. 6.1 **e**, the area corresponding to the CD can be roughly estimated from the configuration space occupied by 2π-DW. In the following section, I study the 2π-DW in the presence of a tilted magnetic field based on the solutions of EL equations.

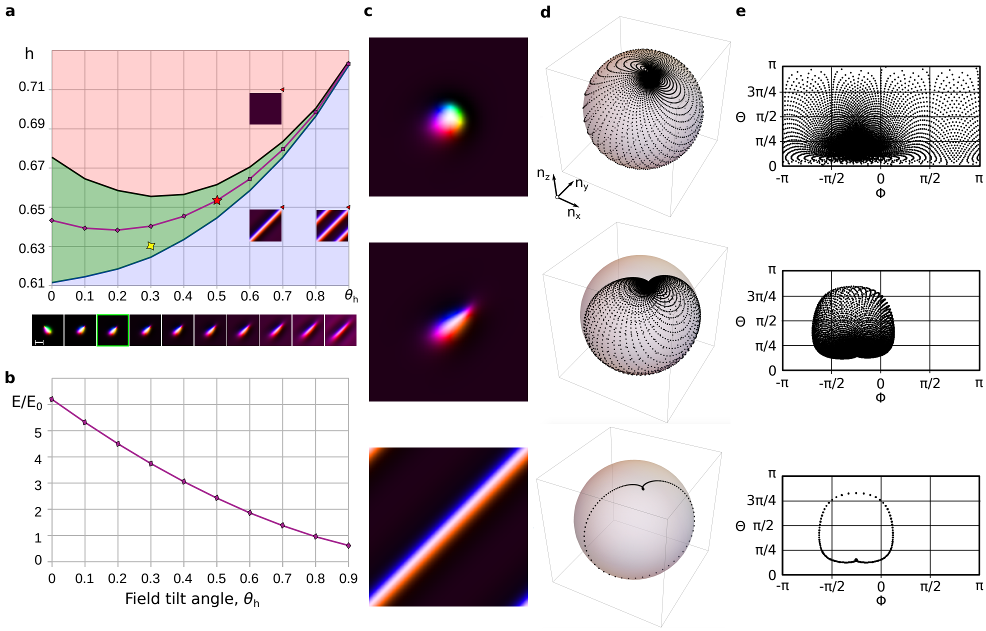

Figure 6.1: **Chiral droplet in the tilted magnetic field.** **a** Stability range of the chiral droplet in terms of the amplitude of the external magnetic field, h, and its tilt angle, θ_{h}, in-plane phase of the field is fixed, $\phi_{\mathrm{h}} = -\pi/4$. The CD is stable inside the green area. Above the critical field denoted by the black line, the CD collapses into the FM state (red region). Below the critical field denoted by the blue line, the CD becomes unstable with respect to stretching (blue region). These states are shown in inserts. Inside the blue region, both states isolated 2π-DW and periodical spin spirals can exist in certain conditions. The purple curve corresponds to the middle of the stability range in terms of h. The panel with the images below contains the magnetic textures of the CD along this curve. The energy of these configurations with respect to the energy of tilted FM state is shown in **b**. **c** shows the magnetic textures of the π-skyrmion, the CD and the 2π-DW obtained by energy minimization at $h = 0.653$ and $\theta_{\mathrm{h}} = 0.5$ (see red star symbol in **a**). The corresponding occupation of the configuration spaces for each of three states is given in the projections of the spins n on $\mathbb{S}^2$ sphere in **d** and in terms of the angles (Θ, Φ) in **e**. **a** is adapted from Ref. [91].

6.1.2 The 2π-DW in the tilted magnetic field

In the presence of the tilted magnetic field, the $\boldsymbol{k}$-vector of the spin spiral is always parallel to the in-plane projection of the magnetic field, see Fig. 6.1 **c**. This state corresponds to the energy minimum of the system. Because of that, one can always choose the coordinate system in which the isolated 2π-DW is described by functions of one variable $\boldsymbol{n} = \boldsymbol{n}(x)$. For analytical study of the corresponding EL equations, I parametrize the magnetization as $\boldsymbol{n} = (\sin\Upsilon\cos\Theta, \sin\Theta, \cos\Upsilon\cos\Theta)$. The functions $\Upsilon(x)$ and $\Theta(x)$ have the following boundary conditions,

$$\Upsilon(x \to \pm\infty) = \Theta_{\mathrm{h}},\ \Theta(x \to \pm\infty) = 0. \tag{6.1}$$

Note, that the value of Θ_{h} is given by the solution of equation (2.2) in the most general case when $u \neq 0$. In the absence of anisotropy, one has $\Theta_{\mathrm{h}} = \theta_{\mathrm{h}}$.

Accordingly to (1.17), the energy density of isolated 2π-DW can be written as,

$$\begin{aligned} w(x) = \frac{1}{2}\left((\Theta')^2 + (\Upsilon')^2\cos^2\Theta\right) + 2\pi\left(\Theta'\cos\Upsilon + \Upsilon'\frac{\sin 2\Theta}{2}\sin\Upsilon\right) \\ +4\pi^2 h(\cos(\Theta_{\mathrm{h}} - \theta_{\mathrm{h}}) - \cos\Theta\cos(\theta_{\mathrm{h}} - \Upsilon)) + 4\pi^2 u(\cos^2\Theta_{\mathrm{h}} - \cos^2\Upsilon\cos^2\Theta). \end{aligned} \tag{6.2}$$

The corresponding EL equations that follow from (6.2) are,

$$\begin{aligned} \Theta'' + (\Upsilon')^2\frac{\sin 2\Theta}{2} - 4\pi\Upsilon'\sin\Upsilon\cos^2\Theta - 4\pi^2\left(h\cos(\theta_{\mathrm{h}}-\Upsilon)\sin\Theta + u\cos^2\Upsilon\sin 2\Theta\right) = 0, \\ \Upsilon''\cos\Theta - 2\Upsilon'\Theta'\sin\Theta + 4\pi\Theta'\sin\Upsilon\cos\Theta + 4\pi^2\left(h\sin(\theta_{\mathrm{h}}-\Upsilon) - u\sin 2\Upsilon\cos\Theta\right) = 0. \end{aligned} \tag{6.3}$$

The system of nonlinear equations (6.3) can be used to analyze the asymptotic of solutions at $x \to \pm\infty$. Taking into account boundary conditions (6.1), substituting the variables, $\Upsilon = \Psi + \Theta_{\mathrm{h}}$, and assuming that functions Θ and Ψ are small, one has the following equations

$$\begin{aligned} \Theta'' - 4\pi\Psi'\sin\Theta_{\mathrm{h}} - 4\pi^2\Theta\left(h\cos(\theta_{\mathrm{h}}-\Theta_{\mathrm{h}}) + 2u\cos^2\Theta_{\mathrm{h}}\right) = 0, \\ \Psi'' + 4\pi\Theta'\sin\Theta_{\mathrm{h}} - 4\pi^2\Psi\left(h\cos(\theta_{\mathrm{h}} - \Theta_{\mathrm{h}}) + 2u\cos 2\Theta_{\mathrm{h}}\right) = 0. \end{aligned} \tag{6.4}$$

The solutions of (6.4) at zero anisotropy are obtained in Appendix A8 and can be written as

$$\begin{aligned} \Theta = c_1\exp\left(-2\pi\sqrt{h - \sin^2\theta_{\mathrm{h}}}|x|\right)\sin\left(2\pi x\sin\theta_{\mathrm{h}} + \phi_{\pm}\right), \\ \Psi = -c_1\exp\left(-2\pi\sqrt{h - \sin^2\theta_{\mathrm{h}}}|x|\right)\cos\left(2\pi x\sin\theta_{\mathrm{h}} + \phi_{\pm}\right), \end{aligned} \tag{6.5}$$

where $c_1, \phi_{\pm}$ are arbitrary constants, ϕ_+ and ϕ_- correspond to the cases $x > 0$ and $x < 0$, respectively. Solving the minimization problem for such a case numerically I obtained the profile of the solution that is shown on Fig. 6.2 **a**.

To compare the profile obtained numerically with asymptotic solutions (6.5) one can notice that at $|x| \to \pm\infty$, the functions Θ and Ψ are connected to magnetization components as $\Theta = n_{\mathrm{y}}$ and $\Psi\cos\Theta_{\mathrm{h}} = n_{\mathrm{x}} - \sin\Theta_{\mathrm{h}}$. Calculating the logarithm of the absolute value of these functions allows getting the factor of exponential decay, $2\pi\sqrt{h - \sin^2\theta_{\mathrm{h}}}$, and checking that the period of oscillations of Θ, Ψ is equal to $(2\sin\theta_{\mathrm{h}})^{-1}$ (see Fig.6.2

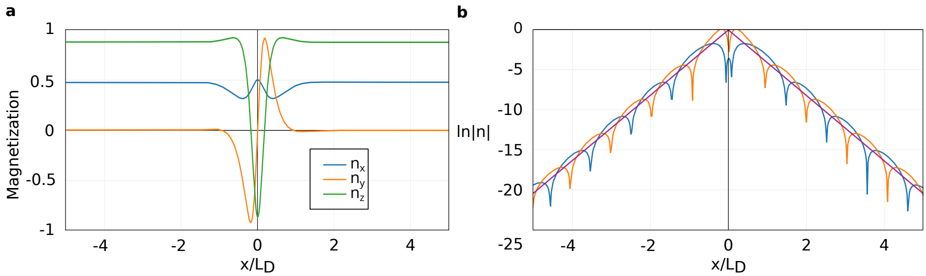

Figure 6.2: **The 2π-DW in the tilted magnetic field**. **a** Components of the magnetization $\boldsymbol{n}$ as function of x obtained at parameters $h = 0.653$ and $\theta_\mathrm{h} = 0.5$. **b** Dependence of $\ln|n_\mathrm{x} - \sin\theta_\mathrm{h}|$ (blue curve) and $\ln|n_\mathrm{y}|$ (orange curve) on x , linear function $y = -2\pi\sqrt{h - \sin^2\theta_\mathrm{h}}\,|x|$ obtained from (6.5) (red line). Period of peaks is $(2\sin\theta_\mathrm{h})^{-1}$.

b). These results agree with those obtained for the π-skyrmion and the antiskyrmion in the tilted magnetic field in **Section** 2.1.

As it follows from the stripe profile near its center $x = 0$, the asymptotic solutions (6.5) differ from the actual functional dependence. Therefore they can not be used to calculate the area in the configuration space bounded by the corresponding curve on the sphere trustfully, see Fig. 6.1 **d**, **e**. Due to this, one has to use alternative approaches to determine the 2π-DW profile more accurately. In particular, numerical solving of the problem is an easy and promising way of doing this.

6.2 Numerical simulations

The presence of thermal fluctuations in the spin system can be effectively modelled by the stochastic LLG (**Section** 1.3.3) and MC (**Section** 1.3.4) simulations. These approaches have different physical backgrounds but should be in a good agreement when the system reaches thermal equilibrium. These approaches can be verified by calculating critical temperature, which corresponds to the transition between different phases. In the case of the 2D magnet, one can consider the transition between the π-skyrmion lattice and the paramagnetic phase. Energy is a reasonable order parameter, which defines the system's state at thermal equilibrium.

The numerical experiment setup is shown in Fig. 6.3 **a**. I assume that thermal fluctuations are uniformly distributed in the 2D plate with PBCs in x and y directions. For definiteness I chose the following magnetic field parameters $h = 0.645$, $\theta_\mathrm{h} = 0.4$ and $\phi_\mathrm{h} = -\pi/4$ that corresponds to the point on the middle line of CD stability range (see Fig. 6.1 **a**). I use the simulated domain of size $L_\mathrm{x} = L_\mathrm{y} = 8L_\mathrm{D}$ with $L_\mathrm{D} = 64a$. In calculations with the stochastic LLG equation, the time step equals to $\Delta t = 0.01\gamma J\mu_\mathrm{s}^{-1}$ and the damping parameter is $\alpha = 0.3$.

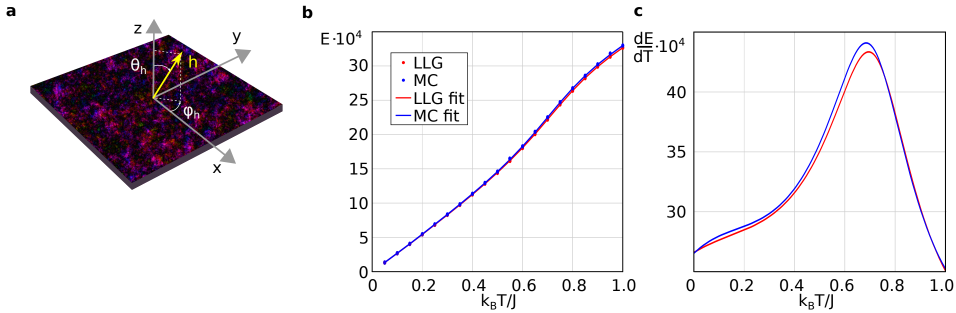

Figure 6.3: **Calculation of the Curie temperature**. **a** show the scheme of the numerical experiment. The domain size is $L_\mathrm{x} = L_\mathrm{y} = 8L_\mathrm{D}$ with $L_\mathrm{D} = 64a$, PBCs in xy-plane are assumed. The amplitude h and the angles θ_h, ϕ_h are parameters of the tilted magnetic field. In simulations, I use $h = 0.645$, $\theta_\mathrm{h} = 0.4$ and $\phi_\mathrm{h} = -\pi/4$. **b** shows the averaged energies corresponding to an equilibrium state at a given temperature which have been obtained in stochastic LLG simulations (red points) and MC simulations (blue points). The curves correspond to their approximation by polynomial functions. **c** shows the derivatives of the energy, $\mathrm{d}E/\mathrm{d}T$, calculated from the fit functions. The peak for both curves coincides at Curie temperature $T_\mathrm{c} \simeq 0.7J/k_\mathrm{B}$. **b** and **c** are adapted from Ref. [91].

Calculating the averaged energy of the system at different temperatures, one can see that the values obtained in LLG and MC simulations are in good agreement, see Fig. 6.3 **b**. To estimate the transition temperature for this system, one can analyze the dependence of the energy derivative on the temperature. The corresponding functions obtained with both methods have a peak at $T_\mathrm{c} \simeq 0.7$.

The next step is to study the system dynamics at smaller temperatures $T < T_\mathrm{c}$ to suppress the appearance of π-skyrmions in the system. While the appearance of topologically non-trivial Sks in the system can be easily identified by the change of total topological charge, detecting Sks with $Q = 0$ requires an alternative approach. The method I use here is based on calculating the net magnetization of the system. This method is akin to the maximum likelihood method [92]. Following this method, I divide the whole system into N overlapping domains Ω_i, $i = \overline{1, N}$ of size $L_\mathrm{D} \times L_\mathrm{D}$. At each iteration, I calculate the z-component of the net magnetization, of these domains

$$\mathcal{N}_i = \sum_{\boldsymbol{n} \in \Omega_i} \left(\cos\theta_\mathrm{h} - n_\mathrm{z}\right), \tag{6.6}$$

and find the domain corresponding the maximal value of $\mathcal{N}_i$ which is denoted as $\mathcal{N}^*$. This procedure is repeated at each moment and can provide the region's position in the simulation box at which the CD can appear with a high probability.

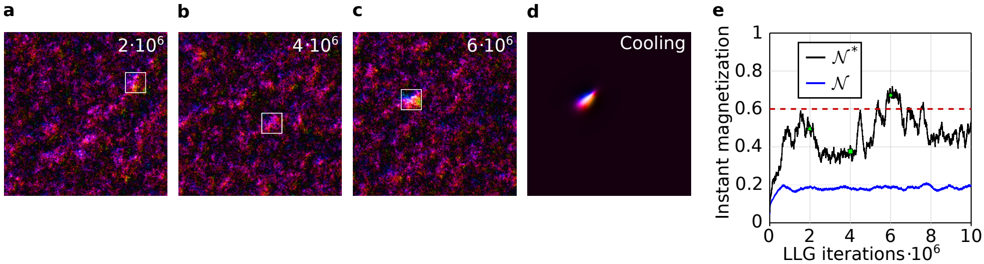

Figure 6.4: **Generation of the CD in the stochastic LLG equation simulations**. **a**-**c** show magnetic textures obtained in simulations based on the stochastic LLG equation at $T = 0.18J/k_{\mathrm{B}}$ after $2 \cdot 10^6$, $4 \cdot 10^6$ and $6 \cdot 10^6$ iterations, respectively. The white square of size $L_{\mathrm{D}} \times L_{\mathrm{D}}$ corresponds to an area with maximal instant magnetization, $\mathcal{N}^*$. The magnetic texture obtained after performing relaxation at zero temperature with the LLG equation starting with texture **c** is shown in **d**. The changing of total (blue) and maximal (black) instant magnetizations are shown on **e**, the red dashed line corresponds to the threshold value $\mathcal{N} = 0.6$. This figure is adapted from Ref. [91].

6.2.1 Stochastic LLG

The simulations with the stochastic LLG equations are performed for the temperature $T = 0.18J/k_{\mathrm{B}}$, and other parameters have the same values which have been used for calculation T_{c}. The snapshots of the system after $2 \cdot 10^6$, $4 \cdot 10^6$ and $6 \cdot 10^6$ iterations are shown in Fig. 6.4 **a**, **b** and **c**, respectively.

The positions of the white square correspond to the region with maximal value of instant magnetization, $\mathcal{N}^*$. The dependence of $\mathcal{N}^*$ on time is given in **e**. As one can notice, the value of $\mathcal{N}^*(t)$ (black curve) is more non-deterministic than the value of total net magnetization $\mathcal{N}(t)$ (blue curve). This reflects the fact that even though the system has reached the thermal equilibrium ($\mathcal{N}(t)$ oscillates around constant value), the fluctuations on the smaller scale $L_{\mathrm{D}} \times L_{\mathrm{D}}$ is still present. An empirically estimated threshold for these fluctuations, $\mathcal{N} = 0.6$, has been used as the criterion indicating the event of CD nucleation. For instance, textures shown in **a** and **d** are characterised by $\mathcal{N}^* < 0.6$ and hence do not contain the CD soliton. The texture shown in **c** has $\mathcal{N}^* > 0.6$ and therefore contains the CD state. Another necessary condition relates to the time the system spends with $\mathcal{N}^* > 0.6$, from numerical estimations, it follows that if the criterion holds during at least $5 \cdot 10^5$ iterations, one can say the system hosts the CD solution. To some extent, this time can be thought of as the CD lifetime. Cooling down the texture depicted in **c** with LLG simulations at $T = 0$, one ends up with the stable CD soliton **d**.

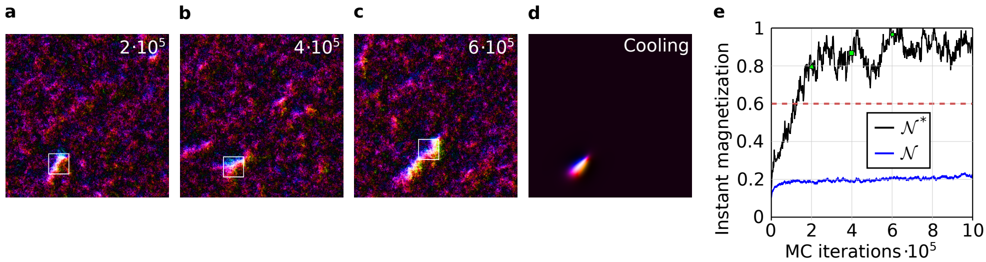

Figure 6.5: **Generation of the CD in stochastic the Monte-Carlo simulations.** **a**-**c** show magnetic textures obtained in Monte-Carlo simulations at $T = 0.18J/k_\mathrm{B}$ after $2 \cdot 10^5$, $4 \cdot 10^5$ and $6 \cdot 10^5$ steps, respectively. The white square of size $L_\mathrm{D} \times L_\mathrm{D}$ corresponds to an area with maximal instant magnetization, $\mathcal{N}^*$. The magnetic texture obtained after performing the LLG relaxation at zero temperature starting with **c** is shown on **d**. The changing of total (blue) and maximal (black) instant magnetizations are shown on **e**, the red dashed line corresponds to the threshold value $\mathcal{N} = 0.6$. This figure is adapted from Ref. [91].

6.2.2 Monte-Carlo simulations

Performing the MC simulations, one can obtain results similar to those obtained in stochastic LLG simulations. The magnetic textures obtained after $2 \cdot 10^5$, $4 \cdot 10^5$ and $6 \cdot 10^5$ MC time steps are shown in Fig. 6.5 **a**, **b** and **c**, respectively. The white square indicates the position of the CD, in all three cases, $\mathcal{N}^* > 0.6$ that satisfies the criterion.

The changing of the total and maximal instant magnetization during the whole simulation process is given in **e**. As in the case of LLG simulations, one can see slightly different functional behaviour of both curves. It is interesting to compare this plot with one obtained in simulations based on the LLG equation. While the behaviour of $\mathcal{N}(t)$ looks very similar in both cases, the dependencies of $\mathcal{N}^*(t)$ seem to describe different stochastic processes. At the same time, the physical reality has to coincide in both methods, which can be seen in a more general Fokker-Plank equation [59] that unites the MC and the LLG approaches. So, the seemed inconsistency is rather visual and is absent on the level of stochastic processes.

After cooling (temperature set to zero), the state depicted in **c** converges to the state shown in **d**. The final state contains the CD solution and thus illustrates the validity of the criterion I introduce for the threshold value of $\mathcal{N}^*$. The interesting point relates to the shape of the CD on **c**. The elongation of the soliton seems to be caused by the presence of an easily excited mode corresponding to stretching of the CD, which has been excited in the MC simulations. In contrast, in the stochastic LLG simulations, this mode seems to be not excited. However, it might appear at longer simulation times.

6.3 Conclusions

In this Chapter, I have studied the CD soliton and the possibility of its thermal generation in the tilted magnetic field. The presence of the tilted field plays a crucial role in this process because it modifies the area which CD occupies in the configuration space. In the first approximation, this area is proportional to the probability of the nucleation of this state by thermal fluctuations.

I have shown the connection between 2π-DW and the CD in the tilted magnetic field, which manifests itself in the shape of the configuration space and the functional behaviour of asymptotic expansions of the solutions. Both solutions demonstrate oscillatory behaviour, similar to the case of the π-skyrmion and the antiskyrmion in the tilted magnetic field. Some of the CD properties calculated at zero temperature remain true for low temperatures. In particular, the stability range in the tilted magnetic field seems to be weakly dependent on the temperature when $T \ll T_c$.

Simulations based on the stochastic LLG and the MC simulations prove the possibility CDs generation. This process takes place at small temperatures comparable to T_c, which corresponds to the transition between the lattice of π-skyrmions and the paramagnetic phase. Both methods have led to the same result and are in good agreement. To summarize, I provide three criteria that have to be fulfilled to generate the CD

- presence of the tilted magnetic field corresponding to the stability range of the CD at $T = 0$;
- presence of the small temperatures, $T < T_\mathrm{c}$, at which the π-skyrmion can not be generated for a reasonable time;
- materials with sufficiently big values of L_D (due to the presence of the CK).

7 Dynamics in a 3D chiral magnet

This Chapter is dedicated to the spin dynamics in 3D chiral magnets. Starting with the analytically solvable problem – the current-induced rotation of the cone phase, I show that the system's dynamics converge to the Thiele regime motion exponentially fast. In **Section** 7.2 I study the dynamics of the Sk tubes and the chiral bobber in a thin film of chiral magnet and compare the results with the Thiele approach. In **Section** 7.3, I discuss the open boundary problem in chiral magnet systems and show how the system's ground state modifies with an example of the exactly solvable problem.

7.1 Rotation of the cone phase

7.1.1 Basic equation

It is well known that the ground state of a bulk crystal of chiral magnet is the cone phase(1.15). Applying the electric current allows one to obtain an analytic solution describing the dynamics of the cone phase. I will assume that the presence of the eclectic current give rise to the Zhang-Li torque,

$$\boldsymbol{T}_{\mathrm{ZL}} = \boldsymbol{n} \times (\boldsymbol{n} \times (\boldsymbol{I} \cdot \nabla) \, \boldsymbol{n}) + \xi \boldsymbol{n} \times (\boldsymbol{I} \cdot \nabla) \, \boldsymbol{n}. \tag{7.1}$$

Assuming that the current is applied in z-axis $\boldsymbol{I} = I\boldsymbol{e}_{\mathrm{z}}$ and along the $\boldsymbol{k}$-vector of the cone, the equation (7.1) takes the form,

$$\boldsymbol{T}_{\mathrm{ZL}} = -I\frac{\partial \boldsymbol{n}}{\partial z} + I\xi \boldsymbol{n} \times \frac{\partial \boldsymbol{n}}{\partial z}. \tag{7.2}$$

I also assume that the external magnetic field is also applied along z-axis $\boldsymbol{B} = B\boldsymbol{e}_{\mathrm{z}}$ and its absolute value $B < |B_{\mathrm{D}} - 2\mathcal{K}|$, that represents necessary condition for existence of the cone phase, $0 < \Theta_{\mathrm{c}} < \pi$. Assuming $\Theta = \Theta\,(t, z)$ and $\Phi = \Phi\,(t, z)$, the corresponding

LLG equation (1.18) can be written as

$$\begin{cases} -\gamma \dfrac{\mathcal{A}}{M_\mathrm{s}} \left(\left(\dfrac{\partial \Phi}{\partial z} \right)^2 \sin 2\Theta - 2 \dfrac{\partial^2 \Theta}{\partial z^2} \right) + \gamma \dfrac{\mathcal{D}}{M_\mathrm{s}} \dfrac{\partial \Phi}{\partial z} \sin 2\Theta - \gamma \mathcal{K} \sin 2\Theta \\ -\gamma B \sin \Theta + I\xi \dfrac{\partial \Theta}{\partial z} - \alpha \dfrac{\partial \Theta}{\partial t} + \left(-I \dfrac{\partial \Phi}{\partial z} + \dfrac{\partial \Phi}{\partial t} \right) \sin \Theta = 0, \\ -2\gamma \dfrac{\mathcal{A}}{M_\mathrm{s}} \left(2 \dfrac{\partial \Theta}{\partial z} \dfrac{\partial \Phi}{\partial z} \cos \Theta + \dfrac{\partial^2 \Phi}{\partial z^2} \sin \Theta \right) + 2\gamma \dfrac{\mathcal{D}}{M_\mathrm{s}} \dfrac{\partial \Theta}{\partial z} \cos \Theta \\ -I \dfrac{\partial \Theta}{\partial z} + \dfrac{\partial \Theta}{\partial t} + \left(-I\xi \dfrac{\partial \Phi}{\partial z} + \alpha \dfrac{\partial \Phi}{\partial t} \right) \sin \Theta = 0. \end{cases} \tag{7.3}$$

The constant Θ function describes the static equilibrium solution for the cone phase. After applying the direct current along z-axis, the uniformity of Θ must conserve and hence one can let $\Theta(t,z) = \Theta(t)$ in (7.3). The latter leads to the following system of equations:

$$\begin{cases} -\gamma \dfrac{\mathcal{A}}{M_\mathrm{s}} \left(\dfrac{\partial \Phi}{\partial z} \right)^2 \sin 2\Theta + \gamma \dfrac{\mathcal{D}}{M_\mathrm{s}} \dfrac{\partial \Phi}{\partial z} \sin 2\Theta - \gamma \mathcal{K} \sin 2\Theta \\ -\gamma B \sin \Theta - \alpha \dfrac{\mathrm{d}\Theta}{\mathrm{d}t} + \left(-I \dfrac{\partial \Phi}{\partial z} + \dfrac{\partial \Phi}{\partial t} \right) \sin \Theta = 0, \\ -2\gamma \dfrac{\mathcal{A}}{M_\mathrm{s}} \dfrac{\partial^2 \Phi}{\partial z^2} \sin \Theta + \dfrac{\mathrm{d}\Theta}{\mathrm{d}t} + \left(-I\xi \dfrac{\partial \Phi}{\partial z} + \alpha \dfrac{\partial \Phi}{\partial t} \right) \sin \Theta = 0. \end{cases} \tag{7.4}$$

The next assumption relates to the change of function $\Phi(t,z)$ in the presence of the current. I presume that this function can be written in the form $\Phi(t,z) = \phi_0 + kz - \Psi(t)$, where $k = 2\pi/L_\mathrm{D}$, ϕ_0 is initial phase of the cone phase, and $\Psi(t)$ is some unknown function on time only. Substituting this ansatz into (7.4) one can get the following equations:

$$\begin{cases} -\gamma \left(-\dfrac{1}{2} B_\mathrm{D} + \mathcal{K} \right) \sin 2\Theta - \gamma B \sin \Theta - \alpha \dfrac{\mathrm{d}\Theta}{\mathrm{d}t} - \left(Ik + \dfrac{\mathrm{d}\Psi}{\mathrm{d}t} \right) \sin \Theta = 0, \\ \dfrac{\mathrm{d}\Theta}{\mathrm{d}t} - \left(I\xi k + \alpha \dfrac{\mathrm{d}\Psi}{\mathrm{d}t} \right) \sin \Theta = 0. \end{cases} \tag{7.5}$$

As follows from the static solution for the cone phase (1.15), the initial conditions for unknown functions are $\Theta(0) = \Theta_c$ and $\Psi(0) = 0$.

7.1.2 Undamped dynamics

In the simplest case of $\alpha = 0$ the equation (7.5) has the following solutions for $\Theta(t)$ and $\Psi(t)$,

$$\tan \frac{\Theta}{2} = \tan \frac{\Theta_\mathrm{c}}{2} e^{I\xi kt}, \tag{7.6}$$

$$\Psi = (\gamma(B_{\mathrm{D}} - 2\mathcal{K}) - Ik - \gamma B)t - \frac{\gamma(B_{\mathrm{D}} - 2\mathcal{K})}{I\xi k} \ln \frac{1 + \tan^2 \dfrac{\Theta_{\mathrm{c}}}{2} e^{I\xi kt}}{1 + \tan^2 \dfrac{\Theta_{\mathrm{c}}}{2}}. \tag{7.7}$$

Equation (7.6) describes the transition process from cone phase state to the FM state with $\Theta = 0$ if $I < 0$ and $\Theta = \pi$ if $I > 0$. The rotation of the cone phase in the transient regime is given by equation (7.7). Using (7.7) one can show that

$$\Phi(t, z) \to \phi_0 + kz - (\gamma B - Ik - \gamma \operatorname{sign}(I)(B_{\mathrm{D}} - 2\mathcal{K}))\, t,\ t \to \infty. \tag{7.8}$$

Therefore, in the long time limit, the rotation of the cone phase is characterized by rotation with a constant angular velocity. Generally speaking, the dynamics in the case of zero damping is always characterized by a certain instability process because of the constant energy pumping into the system. The absence of energy dissipation, in the case of the Zhang-Li torque, breaks the cone phase state.

7.1.3 General case, $\alpha \neq 0$

By the elimination derivative of Ψ from both equations in (7.5) one gets the ordinary differential equation for Θ that is valid at any $\alpha > 0$:

$$\frac{\mathrm{d}\Theta}{\mathrm{d}t} + \frac{\gamma\alpha}{1+\alpha^2}\left(a_1 \sin\Theta - a_2 \frac{\sin 2\Theta}{2}\right) = 0, \tag{7.9}$$

where $a_1 = B - \dfrac{Ik}{\gamma}\left(\dfrac{\xi}{\alpha} - 1\right)$ and $a_2 = B_{\mathrm{D}} - 2\mathcal{K}$ are the constants defined by physical parameters of the system. The solution of (7.9) is presented in Appendix A9 (see Eq. (A9 .4)). The primary outcome of this analysis is the *critical current*, $I_{\mathrm{c}}^{\pm}$ that induces the transition from the cone phase state to the FM state with $n_{\mathrm{z}} = \mp 1$,

$$I_{\mathrm{c}}^{\pm} = \frac{\gamma\alpha(B_{\mathrm{D}} - 2\mathcal{K})L_{\mathrm{D}}}{2\pi(\xi - \alpha)}(\pm 1 - \cos\Theta_{\mathrm{c}}). \tag{7.10}$$

The formula (7.10) has sense only at $\xi \neq \alpha$. In the case $\xi = \alpha$, the solution of (7.9) is a constant, $\Theta(t) = \Theta_{\mathrm{c}}$. Below the critical regime, i.e. $|I| < |I_{\mathrm{c}}^{\pm}|$, $\Theta(t)$ monotonically changes from Θ_{c} to Θ_I, the latter can be found in the limit $\Theta(t \to \infty)$

$$\cos\Theta_I = \frac{a_1}{a_2} = \frac{B + \dfrac{Ik}{\gamma}\left(\dfrac{\xi}{\alpha} - 1\right)}{B_{\mathrm{D}} - 2\mathcal{K}}. \tag{7.11}$$

For $|I| \geq |I_{\mathrm{c}}^{\pm}|$ the angle Θ_I equals to 0 or π depending on the sign of the current, I.

The differential equation for Ψ can be obtained using (7.9) and (7.5)

$$\frac{\mathrm{d}\Psi}{\mathrm{d}t} = \frac{I\xi}{\alpha}k - \frac{\gamma}{1+\alpha^2}\left(a_1 - a_2\cos\Theta\right). \tag{7.12}$$

Its soliton is given by integral equation,

$$\Psi(t) = \frac{I\xi}{\alpha}kt - \frac{\gamma}{1+\alpha^2}\int_0^t \mathrm{d}\tau\left(a_1 - a_2\cos\Theta(\tau)\right). \tag{7.13}$$

As I mentioned above, the solution to $\Theta(t)$ is provided in Appendix A9 and is written in implicit form. Because of that, the integration in (7.13), in the general case, can be done only numerically. Nevertheless, in the non-critical regime, and in the long time limit, one has

$$\Phi(t,z) \to \phi_0 + k\left(z - \frac{I\xi}{\alpha}t\right), t \to \infty. \tag{7.14}$$

The expression (7.14) describes the clockwise (anticlockwise) rotation of the cone phase if $I > 0$ ($I < 0$), with a constant angular velocity. This velocity $V_0 = -I\xi/\alpha$, has already appeared in the **Chapter** 5, where I discussed Sk dynamics in 2D, and it has a sense of the velocity of topologically trivial Sks.

7.1.4 Numerical verification

To check the obtained analytical solutions, which describe the rotation of the cone phase, I performed the simulations based on the LLG equation (1.37). For this simulations I used the following parameters: saturation magnetization $M_\mathrm{s} = 384 \cdot 10^3$A/m, exchange stiffness $A = 3.25 \cdot 10^{-12}$J/m, characteristic length $L_\mathrm{D} = 70$nm, anisotropy $\mathcal{K} = 0$, non-adiabaticity constant $\xi = 0.05$, current polarization $P = 0.3$. I consider different sets of the damping parameters, magnetic fields and current densities to estimate their influence on the magnetization dynamics. The later is shown on Fig. 7.1 **a**, **b** and **c** for three cases of $(\alpha, h, I) = (0, 0.65, -13.53)$, $(0.01, 0.65, 13.53)$ and $(0.01, 0.8, -13.53)$, respectively. The system size is 1nm $\times$ 1nm $\times$ 70nm with PBCs in all spatial directions, the number of cuboids in z-direction is 128. For these simulations, I used Mumax [51] with default settings. For numerical integration of the LLG, I used the fourth-order Runge-Kutta method with adaptive time step control.

In Figure 7.1 **a** the undamped dynamics for the first 10ns after switching on the current is shown. The analytic solutions are given by (7.6), (7.7). At 9ns, the numerical scheme becomes unstable. Different other schemes were tested and have led to the same or even worse result. It seems that the particular case of $\alpha = 0$ demands developing another numerical algorithm for solving the LLG equation.

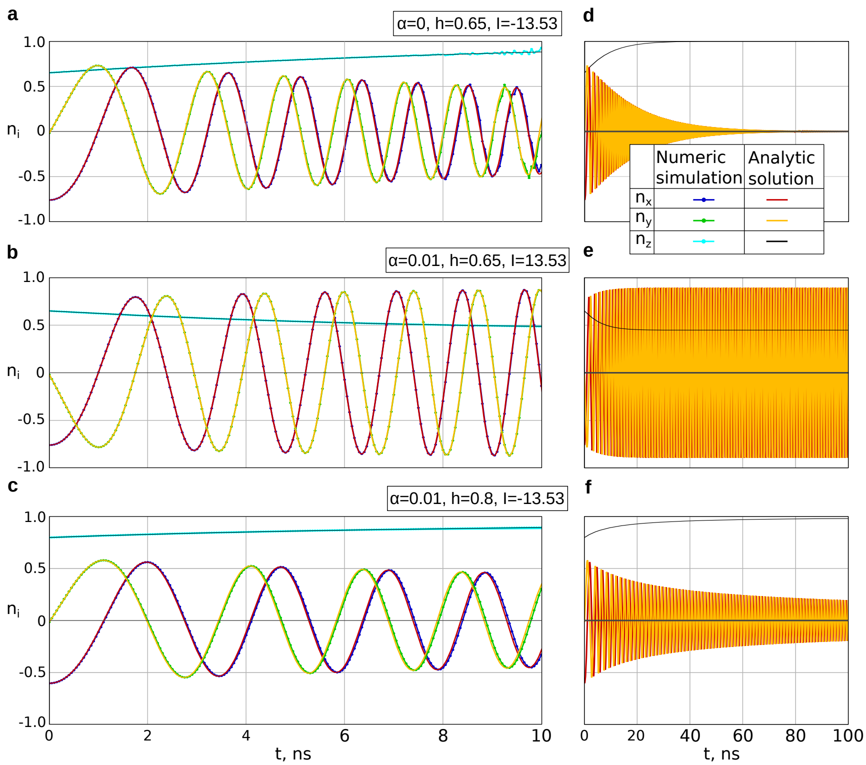

Figure 7.1: **Rotation of the cone phase induced by Zhang-Li torque**. Comparison of the numerical and analytical solutions for magnetization vector is shown in **a-c** for the first 10 ns for different parameters: damping, α, magnetic field, h, and current, I. In **d-f** analytical solutions are shown for a longer time range. The external parameters for **a** and **d**, **b** and **e**, **c** and **f** are the same. Undamped dynamics, $\alpha = 0$ is shown in **a** and **d**. Dynamics with a non-zero damping is presented on **b**,**e** (case $|a_1| \neq |a_2|$) and on **c**, **f** (case $a_1 = a_2$).

The damped dynamics is shown in Fig. 7.1 **b** and **c**, the parameters h, I are chosen in such a way to have $|a_1| \neq |a_2|$ (in **b**) and $a_1 = a_2$ (in **c**). These two cases correspond to functionally different but qualitatively similar time-dependent behaviour of the magnetization (see also Appendix A9). The agreement between numerical simulations and analytical solutions is good in all three cases. The numerical noise caused by the finite-difference discretization of spatial and temporal derivatives in the LLG equation can affect their long-time behaviour. In **d**-**f** only analytic solutions for magnetization vector components for a longer time range are shown . In the cases of the zero damping parameter and $a_1 = a_2$, the cone phase state degenerates into the FM state. The case $|a_1| \neq |a_2|$ corresponds to transition from one cone state to another that differ by Θ_c angle. Besides fundamental interest, the presented analytical results can be useful for testing the accuracy of numerical algorithms solving the LLG equation.

The analytic solutions for current-driven dynamics of the cone phase are also applicable to the system with open boundary conditions along the z-axis as long as the cone phase state is stable. The numerical solving of the minimization problem for obtaining the stable cone phase requires using more dense meshes for discretization along the spiral propagation direction. As it is shown in Fig. 7.2 **a** the boundary effect leading to deviation from the cone state persists even at sufficiently dense meshes. Interestingly, these deviation effects are characterized by the opposite signs in Mumax [51] and Magnoom [55] codes. The corresponding discrepancy, d, from the analytical solution can be defined by the following integral:

$$d = \frac{1}{L_\mathrm{z}} \int_0^{L_z} \mathrm{d}z |n_\mathrm{z}^\mathrm{theory} - n_\mathrm{z}^\mathrm{num}|, \tag{7.15}$$

As it follows from Fig. 7.2 **b**, this quantity becomes smaller as discretization increases. After choosing the proper axis scale, one can deduce the following formula for d in both codes,

$$d = cL_z^q, \tag{7.16}$$

where c and q are constants that define how fast the discrepancy between numerical and analytical solutions converges to zero.

Implementation of a numerical scheme for more accurate boundary treatment is essential. In particular, such numerical errors might affect the interpretation of results for solitons that are stabilized near the surface, for instance, in the case of chiral bobbers.

The most straightforward approach to improve the numerical scheme is to correct the Zeeman term at the free boundary of the simulated domain,

$$H_\mathrm{correction} = \frac{1}{2}\mu_\mathrm{s}\boldsymbol{B}\cdot\left(\boldsymbol{S}_0 + \boldsymbol{S}_{N_\mathrm{z}-1}\right), \tag{7.17}$$

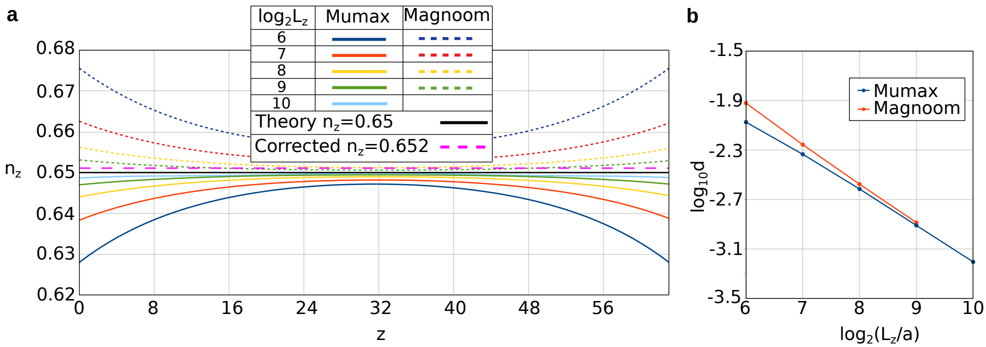

Figure 7.2: **Numerical artifact caused by open boundary**. **a** At zero anisotropy $u = 0$ and magnetic field $h = 0.65$ the theoretical solution for cone state is $n_z = 0.65$ (black line). All other curves correspond to different discretizations along film thickness $L_z = L_D$ obtained in Mumax (solid lines) and Magnoom (dashed lines) codes. The correction (7.17) corresponds to $L_z = 64a$ (dashed magenta line).

The term (7.17) corresponds to the case when open boundaries are along the z-axis. The spins $\boldsymbol{S}_0$ and $\boldsymbol{S}_{N_z-1}$ denote the endmost spins in the z-direction. As it follows from the comparison of solutions, even at $L_D = 64a$, this correction leads to a much smaller discrepancy for the solution of the cone phase (see the magenta dashed line on Fig. 7.2 **a**). Everywhere below, if I do not specify the opposite, the correction (7.17) is used by default for the systems of finite thickness along z-axis.

7.2 Zhang-Li torque in thin film

Strictly speaking, the transition between the case of 2D magnet discussed previously and 3D systems of finite thickness can not be accomplished continuously, simply assuming that $L_z \to 0$. The 3D system has some qualitative differences in terms of the ground state and types of solitons that can be stabilized there. For instance, additionally to the π-skyrmion tube (Fig. 7.3 **a**), in this geometry, one can obtain a stable antiskyrmion tube and the chiral bobber (see **b**, **c**). Both π-skyrmion and antiskyrmion tubes are characterized by a fixed topological charge $Q = -1$ and $Q = +1$, respectively, in each cross-section $z = \text{const}$. The chiral bobber has a non-zero topological charge only in a certain range of its z cross-sections near the surface. The distance to the surface at which the topological charge changes from -1 to 0 corresponds to the Bloch point (BP) position. The BP is a micromagnetic singularity – a point close to which all magnetization directions are present. In particular, the latter breaks the assumption about the smoothness of the magnetic vector field required by the micromagnetic model. Nevertheless, it has been shown that exchange energy remains finite at any sufficiently small spherical region surrounding the BP [93, 94]. In other words, one may think of it as a removable

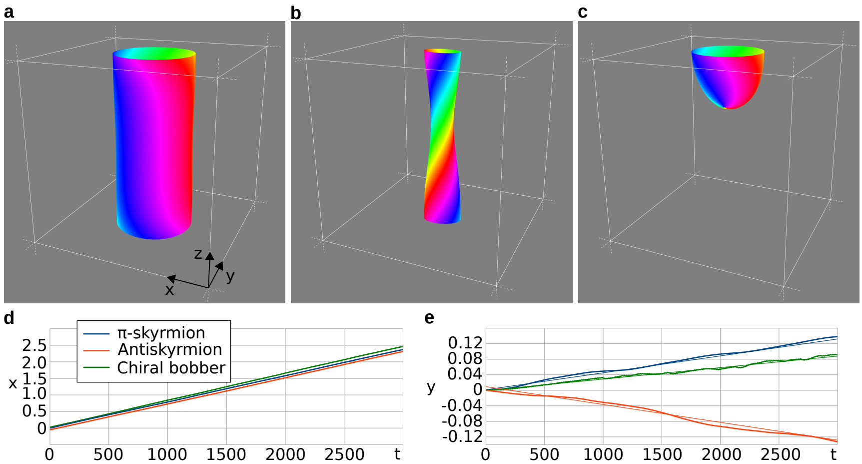

Figure 7.3: **Magnetic solitons in thin film**. Skyrmion **a**, antiskyrmion **b** and chiral bobber **c** are stabilized at $h = 0.78$ inside cubic domain, L_{D}^3, $L_{\mathrm{D}} = 64a$, with PBCs in x and y directions, and open in z direction. **d**, **e** show the change of x and y coordinates of the solitons center with a time.

singularity and still use the continuum Hamiltonian of chiral magnet (1.6) to study static properties of the chiral bobber. The study of BP dynamics is more complex because, strictly speaking, the derivation of the LLG equation requires the magnetic texture to be smooth and the corresponding effective field to be small at any moment. At the same time, if the region with high-noncolinear magnetization is small enough compared to the whole domain, one can expect that it provides negligible or at least feeble influence on the system's dynamics. Therefore, standard numerical schemes (Runge-Kutta, SIB) for solving the LLG equation can often be used.

While the study of dynamics of Sks in 2D has been done in **Chapter** 5, here I show the current-driven dynamics for solitons in the film of finite thickness. As an example, I compare the velocities of the chiral bobber, π-skyrmion and antiskyrmion tubes. Simulations of the current-induced motion of these solitons are performed at parameters $I_{\mathrm{x}} = -0.05\ m/sec$, $\xi = 0.05$, $\alpha = 0.01$, $L_{\mathrm{D}} = 64a$, $\Delta t = 0.01\gamma J \mu_{\mathrm{s}}^{-1}$ with Magnoom code [55]. As follows from the dependence of the positions of the solitons in time shown in Fig. 7.3 **d**, **e**, in all three cases these dependencies have nearly linear character. This allows one to deduce that they all move with constant velocities, $\boldsymbol{v} = (v_{\mathrm{x}}, v_{\mathrm{y}})^{\mathrm{T}}$. Following the Thiele approach, one can write such dynamics as $\boldsymbol{n}(\boldsymbol{r}, t) = \boldsymbol{n}(\boldsymbol{r} - \boldsymbol{v}t)$. In the assumption that all solitons, including the chiral bobber, move in the film plane, the Thiele equation has a standard form (1.23). The corresponding quantities that define the dynamics of the solitons are the z-component of the gyrovector $\boldsymbol{G}$ and the dissipation tensor components Γ_{xx}, Γ_{yy}, Γ_{xy} which are given in the **Table** 7.1.

Table 7.1: Results of soliton dynamics in the finite thickness sample

Type of soliton	$G_{\rm z}$	$\Gamma_{\rm xx}$	$\Gamma_{\rm yy}$	$\Gamma_{\rm xy}$	$v_{\rm x}^{\rm Thiele}$	$v_{\rm y}^{\rm Thiele}$	$v_{\rm x}^{\rm num}$	$v_{\rm y}^{\rm num}$
π-skyrmion	-64	83.29	83.29	-5.6×10^{-6}	78.2	4.07	78.0	4.06
Antiskyrmion	$+64$	85.81	80.09	0.249	78.2	-4.19	78.1	-4.59
Chiral bobber	-18	24.58	26.65	0.392	78.1	4.27	80.4	2.82

The value of $G_{\rm z}$ for the π-skyrmion and the antiskyrmion tubes differs by the sign due to their opposite topological charge. Note, in the case of film, one can write $G_{\rm z} = QL_{\rm z}/a$. Applying the latter to the chiral bobber, one can easily get the position of the BP corresponding to the distance $18a$ from the surface. Analyzing the dissipation tensor components, one can conclude that the π-skyrmion tube can be attributed to the class of high-symmetry Sks, while the antiskyrmion tube and the chiral bobber belong to the low-symmetry solutions. The corresponding velocity components obtained from the Thiele equation (1.23) are denoted as $v_{\rm x}^{\rm Thiele}$ and $v_{\rm y}^{\rm Thiele}$. The velocities obtained from the numerical solution of the LLG equation have superscript "num". As one can notice, the Thiele approach provides a reasonably good estimation for the velocity of both π-skyrmion and antiskyrmion tubes. For the chiral bobber, the x component of the velocity agrees with the theory, while y components are noticeably different. The reason for that seems to be in the presence of the BP. I found that using the more dense meshes, one can significantly decrease the discrepancy between numerical and analytical results [95]. Studying of the dynamics of other magnetic textures [96, 97] stabilized in thin films of a chiral magnet is the subject of future research.

7.3 Surface modulations at the strong tilted field

The presence of open boundaries in the samples of chiral magnets leads to appearing surface modulations [75, 76]. A good example is the surface spiral [36], which exists on the top of the cone phase. The analytic solutions for these spirals are still unknown. However, to get, at least a notion of how surface modulations can look I consider a simple problem that can be analytically solved.

7.3.1 Derivation of Euler-Lagrange equations

Applying an external magnetic field $h > 1$ perpendicular to the open boundary, one gets the saturated FM in which surface modulations are not energetically favourable. If the magnetic field is slightly tilted to the sample boundaries, the situation changes. Without loss of generality one can choose the in-plane component of the field to be along x-axis, so $\boldsymbol{h} = h(\sin\theta_{\rm h}, 0, \cos\theta_{\rm h})$. The magnetization can be parametrized in the following way

$\boldsymbol{n} = (\sin\Upsilon\cos\Theta, \sin\Theta, \cos\Upsilon\cos\Theta)$, where functions Υ and Θ depend only on z. In terms of these functions, the energy density writes:

$$w = \frac{1}{2}(\Theta')^2 + \frac{\cos^2\Theta}{2}(\Upsilon')^2 - 2\pi\Theta'\sin\Upsilon + \pi\Upsilon'\sin 2\Theta\cos\Upsilon \\ -4\pi^2 h\cos(\theta_\mathrm{h} - \Upsilon)\cos\Theta. \tag{7.18}$$

Using (7.18) one can derive EL equations:

$$\Theta'' - 4\pi\Upsilon'\cos^2\Theta\cos\Upsilon + \frac{\sin 2\Theta}{2}(\Upsilon')^2 - 4\pi^2 h\cos(\theta_\mathrm{h} - \Upsilon)\sin\Theta = 0, \\ \Upsilon''\cos^2\Theta - \Upsilon'\Theta'\sin 2\Theta + 4\pi\Theta'\cos^2\Theta\cos\Upsilon + 4\pi^2 h\sin(\theta_\mathrm{h} - \Upsilon)\cos\Theta = 0, \tag{7.19}$$

with the following boundary conditions:

$$(\Theta' - 2\pi\sin\Upsilon)\Big|_{z\in\mathrm{Boundary}} = 0, (\Upsilon'\cos^2\Theta + \pi\sin 2\Theta\cos\Upsilon)\Big|_{z\in\mathrm{Boundary}} = 0. \tag{7.20}$$

At a strong magnetic field, $h > 1$, and small tilt angle, $\theta_\mathrm{h} \ll 1$, the magnetization profile can be found as a small perturbation to the corresponding tilted FM, i.e. $\Theta \ll 1$. Taking the above into account, and introducing a new variable $\Upsilon - \theta_\mathrm{h} = \theta \ll 1$,the system of equations (7.19) can be linearized

$$\Theta'' - 4\pi\theta'\cos\theta_\mathrm{h} - 4\pi^2 h\Theta = 0, \\ \theta'' + 4\pi\Theta'\cos\theta_\mathrm{h} - 4\pi^2 h\theta = 0. \tag{7.21}$$

The same can be applied to the boundary conditions (7.20), and then one gets

$$(\Theta' - 2\pi\theta\cos\theta_\mathrm{h})\Big|_{z\in\mathrm{Boundary}} = 2\pi\sin\theta_\mathrm{h}, (\theta' + 2\pi\Theta\cos\theta_\mathrm{h})\Big|_{z\in\mathrm{Boundary}} = 0. \tag{7.22}$$

The system of equations identical to (7.21) has already been solved in Appendix A8 . In particular, introducing the complex function $\zeta = \Theta + i\theta$, one gets

$$\zeta'' + 4\pi i\zeta'\cos\theta_\mathrm{h} - 4\pi^2 h\zeta = 0. \tag{7.23}$$

In contrast to the equation solved in Appendix A8 , here one has in addition the boundary conditions (7.22) that in terms of new variables can be written as,

$$(\zeta' + 2\pi i\zeta\cos\theta_\mathrm{h})\Big|_{z\in\mathrm{Boundary}} = 2\pi\sin\theta_\mathrm{h}. \tag{7.24}$$

Now I consider different geometries of the sample for which one can apply different general forms for the solution of equation (7.23).

7.3.2 Semi-infinite sample

Choosing the origin $z = 0$ at the open surface, one can write a solution of (7.23) in the form,

$$\zeta = \left(ae^{kz} + be^{-kz}\right) \exp\left(-2\pi iz \cos\theta_{\mathrm{h}}\right), \tag{7.25}$$

where $k = 2\pi\sqrt{h - \cos^2\theta_{\mathrm{h}}}$, and a, b are arbitrary complex constants. Far away from the boundary, $z \to -\infty$, the magnetization is indistinguishable from the tilted FM solution, so one has to let $b = 0$. Constant a can be found by substituting (7.25) into (7.24),

$$a = \frac{2\pi}{k} \sin\theta_{\mathrm{h}}. \tag{7.26}$$

Then the solution of Eq. (7.21) writes

$$\begin{aligned} \Theta &= \frac{2\pi e^{kz}}{k} \sin\theta_{\mathrm{h}} \cos\left(2\pi z \cos\theta_{\mathrm{h}}\right), \\ \theta &= -\frac{2\pi e^{kz}}{k} \sin\theta_{\mathrm{h}} \sin\left(2\pi z \cos\theta_{\mathrm{h}}\right). \end{aligned} \tag{7.27}$$

The numerical verification of this result is shown in Fig. 7.4 **a**. The parameters I used for comparison of numerical and analytical results are as follows: $h = 1.4$, $\theta_{\mathrm{h}} = 5°$, $L_{\mathrm{D}} = 64$, the size of the system is $20L_{\mathrm{D}}$ in z direction, spins on the distance greater than $19L_{\mathrm{D}}$ from the open boundary are pinned in the direction of an external magnetic field. The analytical solution provides a good approximation for the numerical data as follows from the figure.

7.3.3 Sample of finite thickness

Now I consider the plate of finite thickness, L. I set the the origin $z = 0$ in the middle of the sample. In this case one can write the solution of (7.23) in the form,

$$\zeta = \left(a \sinh(kz) + b \cosh(kz)\right) \exp\left(-2\pi iz \cos\vartheta\right), \tag{7.28}$$

where a, b are arbitrary complex constants. The boundary condition (7.24) is true for $z = \pm L/2$. The substitution of (7.28) into (7.24) leads to the system of equations for coefficients a and b

$$\begin{aligned} a \cosh\frac{kL}{2} + b \sinh\frac{kL}{2} &= \frac{2\pi}{k} \sin\theta_{\mathrm{h}} \exp\left(\pi iL \cos\theta_{\mathrm{h}}\right), \\ a \cosh\frac{kL}{2} - b \sinh\frac{kL}{2} &= \frac{2\pi}{k} \sin\theta_{\mathrm{h}} \exp\left(-\pi iL \cos\theta_{\mathrm{h}}\right). \end{aligned} \tag{7.29}$$

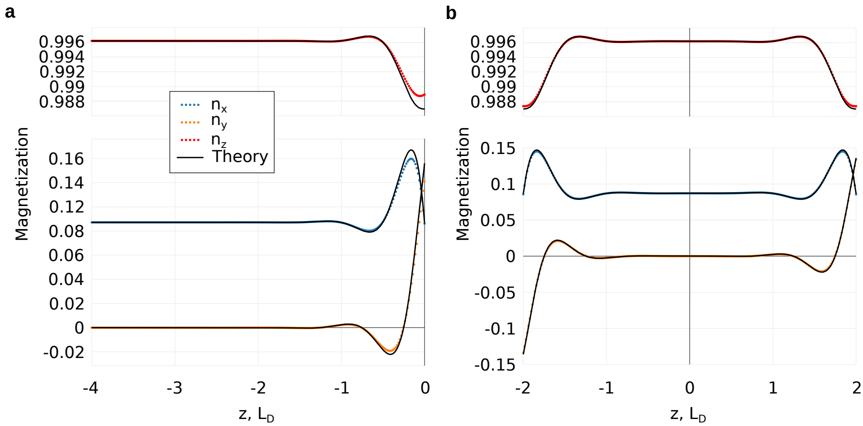

Figure 7.4: **Near surface modulations of magnetization**. For the semi-infinte crystal **a** and the sample of finite thickness **b**, it shows the change of magnetization components as a function on z. Numerical data are shown as points, while analytic results (7.27), (7.31) as black curves. The parameters are $h = 1.4$, $\vartheta = 5°$, $L_{\mathrm{D}} = 64a$.

The solution of (7.29) can be easily found

$$a = \frac{2\pi \sin\theta_{\mathrm{h}} \cos\left(\pi L \cos\theta_{\mathrm{h}}\right)}{k \cosh \dfrac{kL}{2}}, \; b = \frac{2\pi i \sin\theta_{\mathrm{h}} \sin\left(\pi L \cos\theta_{\mathrm{h}}\right)}{k \sinh \dfrac{kL}{2}}. \tag{7.30}$$

Substituting (7.30) into (7.28) and separating real and imaginary parts of ζ one obtains the solution of (7.21)

$$\begin{aligned} \Theta &= \frac{2\pi \sin\theta_{\mathrm{h}}}{k}\left(\frac{\cos\dfrac{qL}{2}}{\cosh\dfrac{kL}{2}} \sinh(kz)\cos(qz) + \frac{\sin\dfrac{qL}{2}}{\sinh\dfrac{kL}{2}}\cosh(kz)\sin(qz)\right), \\ \theta &= \frac{2\pi \sin\theta_{\mathrm{h}}}{k}\left(\frac{\sin\dfrac{qL}{2}}{\sinh\dfrac{kL}{2}} \cosh(kz)\cos(qz) - \frac{\cos\dfrac{qL}{2}}{\cosh\dfrac{kL}{2}}\sinh(kz)\sin(qz)\right), \end{aligned} \tag{7.31}$$

where $q = 2\pi \cos\theta_{\mathrm{h}}$.

For numerical verification of the analytic results, I have considered the sample of size $L = 4L_{\mathrm{D}}$ with $L_{\mathrm{D}} = 64a$, parameters of the magnetic field are $h = 1.4$, $\theta_{\mathrm{h}} = 5°$. As it follows from Fig. 7.4 **b**, the found solutions are in excellent agreement with the numerical calculations.

7.3.4 Surface modulations at larger tilts of the field

The surface modulations become stronger at smaller field amplitudes and/or larger tilts of the field. In this case, the exact solutions describing magnetization profile can not be found in the linear approximation. On Fig. 7.5 **a**-**c** the corresponding magnetization components are shown for magnetic field tilts 5°, 10°, 15° and 20°. For the tilt 5°, the obtained solutions (7.31) describe the surface modulations with reasonable accuracy. That is not the case for the tilt 10° (see the inset on **b**). The discrepancy between the analytical solution and numerical data becomes even more significant by further increasing the tilt angle. This demonstrates the fact of non-applicability of the linear theory for analysis of EL equations (7.19). So, to study the surface modulations of $\boldsymbol{n}$ in this regime analytically, other methods of analysis of the non-linear systems have to be used.

In a numerical study of the surface twist, it is important to use a scheme with high accuracy to describe the boundary effects. In particular, the used correction for Zeeman energy term (7.17) has allowed increasing the agreement between numerical and analytical results even at relatively small mesh density, $L_{\mathrm{D}} = 64a$. Many other promising methods can be implemented to increase the accuracy of numerical solving. One of them is the Ql technique discussed above, and it can be efficiently utilized for the system of ordinary differential equations (7.19).

From the point of view of solitons, the systems with open boundaries are of high interest because they better describe the reality. The presence of the surface modulations gives an additional energy gain [98] that sometimes can be crucial for the stability of some solutions, for instance, the chiral bobber [36] and the antiskyrmion tube, Fig. 7.3 **b**, **c**. Due to this, the surface twist can not be excluded from the considerations and has to be studied in all cases where the open boundary is present.

Additionally, to various new effects of static properties of chiral magnets, the presence of the free boundary also changes its dynamics. In particular, the excitation of magnetization by different oscillatory magnetic fields (in-plane, out-of-plane and circular) lead to the appearance of standing spin waves absent in the systems with PBCs. The considered model problem in the case of a strong magnetic field and the small tilt angle is also helpful for further study of spin dynamics in chiral magnets. The obtained solution (7.31) can be used to study the time-dependent magnetization dynamics by different perturbation methods. In the case when the dynamics of the magnetization is far from the static profile (7.31), the used ideas for solving the corresponding EL equations remain helpful for analysis of the LLG equation. The detailed analysis of the dynamics in linear and beyond linear regimes is the subject of further study.

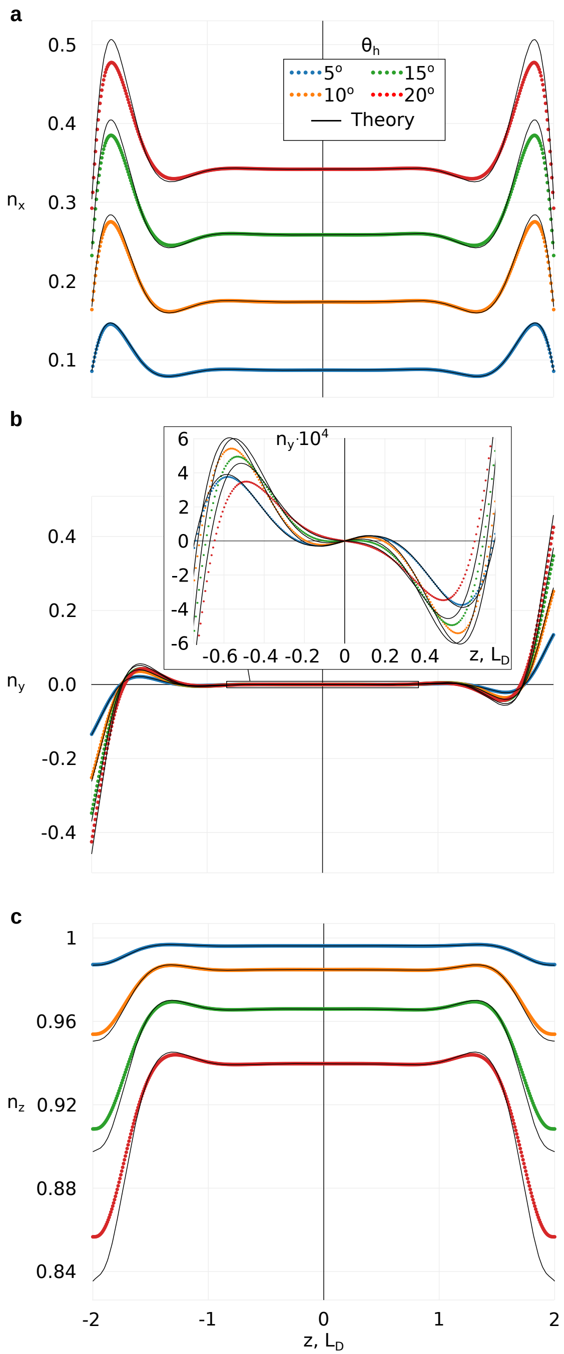

Figure 7.5: **Surface modulations of magnetization at bigger field tilts**. Modulations along the film thickness of magnetization components n_x, n_y and n_z are shown on **a**, **b** and **c**, respectively. Amplitude of the magnetic field is fixed $h = 1.4$, its tilts are varied: $\theta_\mathrm{h} = 5°$ (blue), $\theta_\mathrm{h} = 10°$ (orange), $\theta_\mathrm{h} = 15°$ (green) and $\theta_\mathrm{h} = 20°$ (red). The corresponding analytical curves (7.31) are shown in black colour. The inset on **b** shows the zoomed region of n_y at $z \in [-0.75L_\mathrm{D}, 0.75L_\mathrm{D}]$.

7.4 Conclusions

In this Chapter, I have studied some properties of bulk crystals and systems of finite thickness of the chiral magnets. From the analytical solution for the rotation of the cone phase, one can deduce that the corresponding transition regime ends up exponentially fast. Therefore, most of the time electric current is applied the system spends in the regime of rigid motion, which, with reasonable accuracy, is described by the corresponding Thiele equation. This situation seems to be generic for all cases when the torque in the Zhang-Li form is present in the LLG equation.

Under the in-plane electric current, the solitons in the film of finite thickness move similar to a 2D system. The corresponding dynamics of the π-skyrmion, the antiskyrmion tubes and the chiral bobber have been studied. The numerical (LLG equation) and semi-analytical (Thiele equation) approach agree well for all cases. The transverse velocity component of the chiral bobber has some discrepancy with the one predicted by the Thiele equation. When BPs are present in the system, one has to use very dense meshes to reach a reasonable agreement between numerical simulations and analytical solutions.

In the last Section, I have discussed the change of the static magnetization profile in the vicinity of the free boundary. I found that the surface modulations appear at any non-zero tilt of an external magnetic field, even above the saturation regime $h > 1$. I have shown that the corresponding EL equations can be solved in linear approximation and estimated the limit of applicability of the analytical solution. It is shown that when the assumptions of high field and slight tilt angle are satisfied, the analytical functions fit the numerical data with good accuracy.

8 3D solitons in chiral magnet

In this Chapter, I consider magnetic solitons in bulk crystals of the chiral magnet. In **Section** 8.1, I study π-skyrmion tube embedded in the conical phase and estimate the soliton asymptotic in the far-field by analyzing the effective 2D Hamiltonian. In **Section** 8.2, I show an example of a new type of solution representing a Sk tube constructed from the homotopy paths between 2D Sks of the same topological charge [79]. Applying this approach to topologically trivial 2D Sks – CD leads to obtaining a new soliton localized in all spatial directions, which I discuss in **Section** 8.3. Some of the static and dynamical properties of these new solitons are discussed in detail.

8.1 Skyrmion tube in the bulk crystal

8.1.1 Analytical description

In the bulk crystal of chiral magnets, the absence of the free boundaries leads to simpler functional behaviour for magnetization of corresponding textures. In particular, a single π-skyrmion tube does not have additional surface twist modulations. As it has been shown in Ref. [99], such a soliton can be described by an effective 2D Hamiltonian:

$$\mathcal{E} = \int_\Omega \mathrm{d}\Omega \left(\frac{(\nabla \boldsymbol{n})^2}{2} + 2\pi \boldsymbol{n} \cdot \nabla \times \boldsymbol{n} - 4\pi^2 h n_\mathrm{z} + 2\pi^2 n_\mathrm{z}^2 + 2\pi^2 \left(y \frac{\partial \boldsymbol{n}}{\partial x} - x \frac{\partial \boldsymbol{n}}{\partial y} \right)^2 \right), \quad (8.1)$$

where $\mathrm{d}\Omega = \mathrm{d}x\mathrm{d}y$. To find the 3D magnetization distribution, $\boldsymbol{m}$, one has to perform the following transformation

$$\boldsymbol{m}(x, y, z) = \begin{pmatrix} \cos 2\pi z & -\sin 2\pi z & 0 \\ \sin 2\pi z & \cos 2\pi z & 0 \\ 0 & 0 & 1 \end{pmatrix} \boldsymbol{n}(x', y'),$$
$$x' = x \cos 2\pi z + y \sin 2\pi z, \; y' = y \cos 2\pi z - x \sin 2\pi z. \quad (8.2)$$

In the case $-1 < h < 1$, the vacuum is is the cone phase with the cone angle $\Theta_\mathrm{c} = \arccos(h)$. Therefore, the corresponding boundary conditions for the isolated Sk are

$$\boldsymbol{n}\,(x \to \pm\infty, y) = \boldsymbol{n}\,(x, y \to \pm\infty) = (\sin\Theta_\mathrm{c}, 0, \cos\Theta_\mathrm{c})\,,\ \boldsymbol{n}\,(0,0) = -\boldsymbol{e}_\mathrm{z}. \tag{8.3}$$

As follows from (8.3), the Sk profile, $\boldsymbol{n}$, might be similar to the profile of the π-skyrmion in the tilted magnetic field that I have considered in **Section** 2.1. However, such similarity is rather visual, and it does not capture significant features of 3D Sk described by (8.1). The main difference is the presence in (8.1) the term explicitly containing spacial coordinates x and y. This term complicates the analysis even for the asymptotics of the Sk solution. On the other hand, some properties of these solutions qualitatively can be estimated using the approach of ansatz functions. Let the magnetization, $\boldsymbol{n}$, is parameterized as

$$\boldsymbol{n} = \begin{pmatrix} \cos\Lambda\sin\Theta\cos\Phi + \sin\Lambda\cos\Theta \\ \sin\Theta\sin\Phi \\ -\sin\Lambda\sin\Theta\cos\Phi + \cos\Lambda\cos\Theta \end{pmatrix}, \tag{8.4}$$

where Λ, Θ are functions only on $r = \sqrt{x^2+y^2}$ with boundary conditions $\Theta(0) = \pi$, $\Theta(r \to \infty) = 0$, $\Lambda(r \to \infty) = \Theta_\mathrm{c}$, and $\Phi = \phi + \pi/2$. One can perform an integration over ϕ after substitution (8.4) into (8.1). Then from variation principle $\delta\mathcal{E} = 0$, I derive the equations for Λ and Θ

$$\begin{gathered} r\left(-8\pi r\Lambda'\cos^2\Theta\sin\Lambda + r\left(\Lambda'\right)^2\sin 2\Theta + 4\Theta' + 4r\Theta''\right) - 2\left(1 + 6\pi^2 r^2\sin^2\Lambda\right)\sin 2\Theta \\ +8\pi r\sin\Theta\left(\sin\Theta + \cos\Lambda\left(-2\pi h r + \sin\Theta\right)\right) = 0, \\ r\left(3 + \cos 2\Theta\right)\Lambda'' + \Lambda'\left(3 + \cos 2\Theta - 2r\Theta'\sin 2\Theta\right) + 2\pi^2 r\left(1 + 3\cos 2\Theta\right)\sin 2\Lambda \\ +8\pi\cos\Theta\sin\Lambda\left(-2\pi h r + \sin\Theta + r\Theta'\cos\Theta\right) = 0. \end{gathered} \tag{8.5}$$

The system of coupled ordinary differential equations (8.5) is hard to solve due to the non-linearity of the equations. However, this system can be used to analyze the asymptotic behaviour of the solutions. After denoting $\Lambda = \Theta_\mathrm{c} + \theta$ and under the assumption that $\theta(r \to \infty) \ll 1$ and $\Theta(r \to \infty) \ll 1$, one obtains the linear system of equations

$$\begin{cases} r^2\Theta'' + r\Theta' - \left(\left(4\pi^2 + \dfrac{\kappa^2}{2}\right)r^2 + 1\right)\Theta - \kappa r^2\theta' = 0, \\ r^2\theta'' + r\theta' - \kappa^2 r^2\theta + \kappa r\Theta + \kappa r^2\Theta' = 0, \end{cases} \tag{8.6}$$

where $\kappa = 2\pi\sqrt{1-h^2}$. Equations (8.6) have a form of Bessel equations with an additional coupling between them. So, I assume that the solutions of these equations can be written in the following form:

$$\Theta(r) = C_1 K_1(\alpha r), \ \theta(r) = C_2 K_0(\beta r), \tag{8.7}$$

where $K(r)$ is modified Bessel function of the second kind, and C_1, C_2, α, β are constants. Substituting (8.7) into (8.6) gives

$$\begin{cases} \alpha^2 r^2 \Theta - \left(4\pi^2 + \dfrac{\kappa^2}{2}\right) r^2 \Theta - \kappa r^2 \theta' = 0, \\ \beta^2 r^2 \theta - \kappa^2 r^2 \theta + \kappa r \Theta + \kappa r^2 \Theta' = 0. \end{cases} \tag{8.8}$$

The first equation in (8.8) allows one to find

$$\Theta = \frac{\kappa}{\alpha^2 - 4\pi^2 - \kappa^2/2} \theta'. \tag{8.9}$$

Using (8.9), the second equation in (8.8) becomes

$$r^2 \theta'' + r\theta' - \frac{\beta^2 - \kappa^2}{\kappa^2} \left(4\pi^2 + \frac{\kappa^2}{2} - \alpha^2\right) r^2 \theta = 0. \tag{8.10}$$

In addition, as follows from (8.9)

$$C_1 K_1(\alpha r) = \frac{\kappa \beta}{4\pi^2 + \kappa^2/2 - \alpha^2} C_2 K_1(\beta r), \tag{8.11}$$

so $\alpha = \beta$ and $C_1 = \dfrac{\kappa \alpha C_2}{4\pi^2 + \kappa^2/2 - \alpha^2}$. Taking this into account, one can get from (8.10) the equation for α

$$\frac{\alpha^2 - \kappa^2}{\kappa^2} \left(4\pi^2 + \frac{\kappa^2}{2} - \alpha^2\right) = \alpha^2. \tag{8.12}$$

I write the solution for (8.12) through magnetic field parameter h

$$\alpha^2 = \pi^2 \left(3 - h^2\right) \left(1 \pm \sqrt{\frac{7h^2 - 5}{3 - h^2}}\right). \tag{8.13}$$

At $h = 1$ the π-skyrmion asymptotic is known, $\alpha = 2\pi$, so in (8.13) one has to take the solution with "$+$" sign. An interesting feature of the equation (8.13) is that at some h it can have non-zero imaginary part, that happens if $h^2 < 5/7$, and defines the critical magnetic field $h_{\mathrm{cr}} = \sqrt{5/7} \simeq 0.845$. For this case one can write (8.13) as a complex number in exponential form

$$\alpha^2 = 2\sqrt{2}\pi^2\sqrt{3-h^2}\sqrt{1-h^2}\exp\left(i\arctan\sqrt{\frac{5-7h^2}{3-h^2}}\right). \tag{8.14}$$

By taking the square root of (8.14), one gets the following expression for α

$$\alpha_{\pm} = \pi\sqrt{2\sqrt{2}\sqrt{3-h^2}\sqrt{1-h^2}}\left(\cos\psi \pm i\sin\psi\right), \tag{8.15}$$

where $\psi = \dfrac{1}{2}\arctan\sqrt{\dfrac{5-7h^2}{3-h^2}}$. In the case $h \geq \sqrt{5/7}$ the expression for α can be easily calculated from (8.13).

8.1.2 Numerical solving

I have implemented a scheme with exponential precision, the details are given in the Appendix A10 . The simulations have been performed in the domain of size $L_\mathrm{x} = L_\mathrm{y} = 16L_\mathrm{D}$, $L_\mathrm{z} = L_\mathrm{D}$ with $L_\mathrm{D} = 32$, so every spin interacts with 31 others, PBCs are assumed. Two values of the magnetic field are chosen to be smaller and bigger than the critical field h_cr, i.e. $h = 0.8$ and $h = 0.9$. The corresponding equilibrium profiles of the skyrmions are shown in Fig. 8.1 **a** and **d**, respectively.

The energies of π-skyrmion tubes counted from the energy of the cone phase are $\mathcal{E}_{h=0.8} = 2.1595941694$ and $\mathcal{E}_{h=0.9} = 2.4168933106$. As follows form (8.4), at $r \to \infty$ the magnetization component $n_\mathrm{y} \to \dfrac{x\Theta}{\sqrt{x^2+y^2}}$, so oscillations in n_y are directly connected with those in function Θ. The calculated above critical magnetic field agrees with the results shown in Fig. 8.1 **b** and **e**. Oscillations in Θ are present at $h = 0.8$ and absent at $h = 0.9$, at least on the domain of considered size. The integration of the energy density over the period of cone phase allows me to estimate how oscillations in magnetization influence the averaged energy density (see Fig. 8.1 **c** and **f**). In the case of $h = 0.8$, the oscillations appear in the energy density but do not appear at $h = 0.9$. In the latter case, $w(x, y)$ remains positive at $r \gg 0$. This indicates the attraction between two π-skyrmion tubes, while the oscillatory energy density behaviour leads to similar oscillatory interaction potential between the Sk pair.

The approach based on the ansatz functions method does not show the quantitative agreement with the numerical results. On the other hand, it gives a reasonable value for critical magnetic field h_cr which correlates with numerical observations. Therefore, more advanced methods have to be developed to analyze π-skyrmion tubes in the cone phase. In particular, it seem to be promising to consider the functions $\Theta(r, \phi)$ and $\Lambda(r, \phi)$.

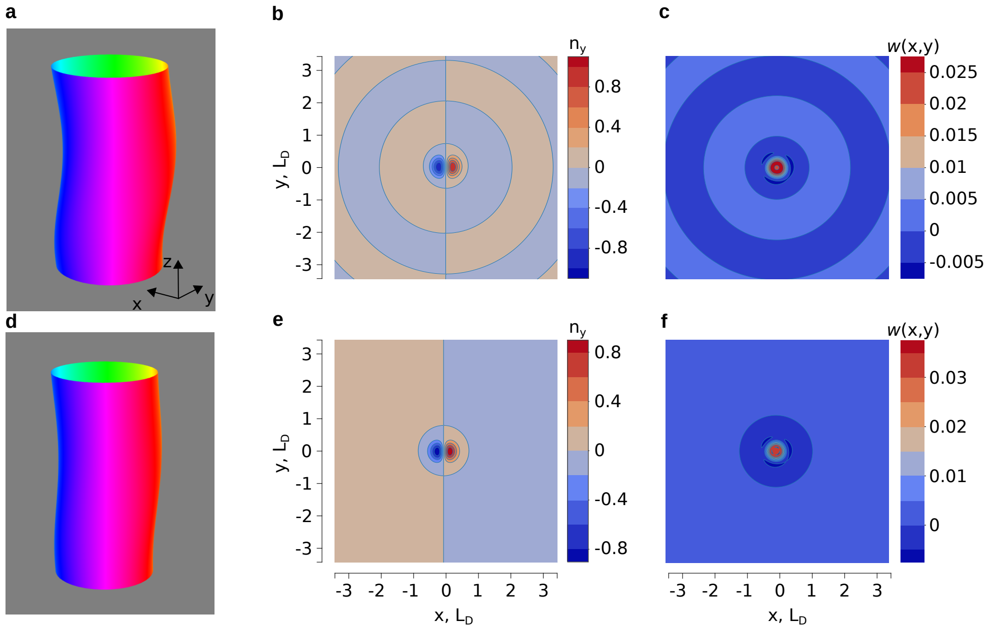

Figure 8.1: **Skyrmion tube in the cone phase**. Surfaces $n_z = 0$ relate to relaxed skyrmion tubes are shown in **a** and **d**. n_y components of magnetization in cross-section $z = 0$ are given as contour plots in **b** and **e**. The cone phase energy densities integrated over one period of the cone phase are shown in **c** and **f**. **a-c** and **d-f** correspond to magnetic fields $h = 0.8$ and $h = 0.9$, respectively.

The π-skyrmion tube is the simplest soliton in this model, but one can not do much analytically, even in this case. At the same time, a numerical investigation is a powerful tool that helps to go beyond a single skyrmion tube case and explore the diversity of other 3D solitons.

8.2 Skyrmion tubes and homotopy paths

The presence of the cone phase instead of the FM state influences the stability of solitons. To suppress the conical modulations, in the simplest case, one can add easy-axis anisotropy to the energy functional. Then, effectively, the 3D magnet can be thought of as a set of 2D cross-sections, and in each of them, the solitons are identical. Such Sk tubes are trivial constructions because they do not modulate along the third dimension. The situation changes if one considers different solitons of the same topological charge and tries to construct a tube with different Sks in different cross-sections. An example of such solitons is given in Fig. 8.2 **a**. The homotopy path connects these solutions, and the topological charge in any xy-plane is +1. Some aspects of the search method for such homotopies have been discussed earlier in **Chapter** 4, while here, I will focus on the stability of such 3D solitons.

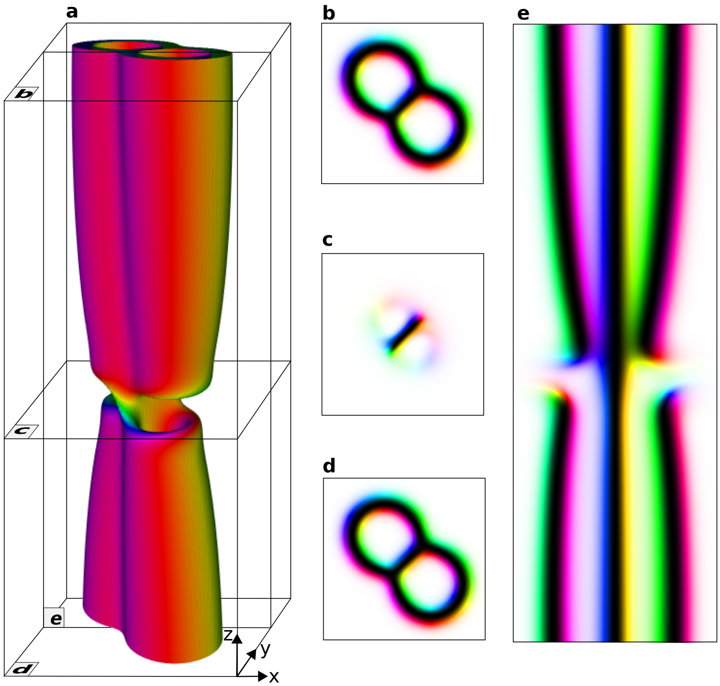

Figure 8.2: **Hybridized skyrmion tube in FM**. **a** Surface $n_z = 0$ corresponding to relaxed Sk tube which is constructed of two different 2D Sks. These Sks are shown in **b-d**, they correspond to different z cross-section of the tube. The section by plane $y = 0$ is depicted on **e**. For calculations it has been used as a system of size $L_x = L_y = L_z = 6L_D$ with $L_D = 32a$, PBCs are assumed, parameters are $h = 0.3$ and $u = 0.43$.

The top **b** and bottom **d** cross-sections of the tube coincide due to the PBCs and represent skyrmion bag constructing of two loops (three closed contours). In the middle cross-section **c**, the soliton profile is similar to the 2D antiskyrmion discussed above in **Chapter** 3. The magnetic texture as a whole is smooth and has no singularities. This can be easily understood from the topological reasons – there is always a homotopy path between two distinct 2D Sks of identical Q. The surrounding vacuum of such a tube is the FM state stabilized by the presence of both: magnetic field $h = 0.3$ and easy-axis anisotropy $u = 0.43$.

As it turned out, this hybridized Sk tube remains stable at a certain range of magnetic fields even in the isotropic case, $u = 0$, when the surrounding vacuum is the cone phase. An example of a stable Sk tube at $h = 0.4$ is shown in Fig. 8.3 **a**. Its cross-sections **b-f** now represent 2D Sks that exist at the corresponding tilted FM vacuum. In addition to the Sk bag **d**, **f** and Ask **e**, the magnetic textures in cross-sections **b**, **c** represents the skyrmionium with a CK. The latter has a topological charge of +1, and now the Sk tube

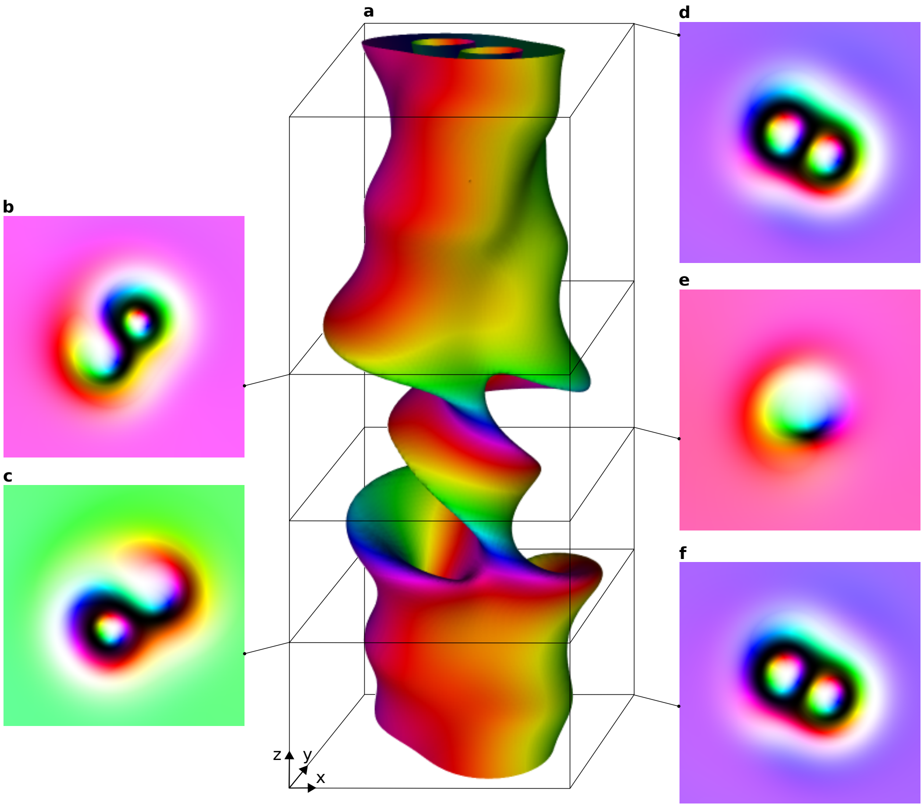

Figure 8.3: **Hybridized skyrmion tube in the cone phase**. **a** Surface $n_{\mathrm{z}} = 0$ corresponding to relaxed hybridized Sk tube which has different 2D Sks in its cross-sections. Some of them are shown in **b-f**. For calculations a system of size $L_{\mathrm{x}} = L_{\mathrm{y}} = L_{\mathrm{z}} = 6L_{\mathrm{D}}$ with $L_{\mathrm{D}} = 32a$ was used, PBCs are assumed, parameters are $h = 0.4$ and $u = 0$.

combines three types of different 2D Sks (see the homotopy path Fig. 4.6).

Alternatively, the hybridized Sk tubes can be considered as the host Sk tube with additional lengthwise modulations. This modulation is some soliton that is localized and can move under external stimuli, e.g., electric current or oscillatory magnetic field. The possibility of motion of such soliton follows from the fact that its translation in z-direction is a zero mode, i.e. the motion that leaves the energy unchanged. The latter is obvious for the tube embedded by the FM vacuum. However, it can be shown that the presence of the cone phase on the far-field does not destroy the corresponding translational symmetry of the Hamiltonian.

The existence of a smooth transformation of a hybridized tube into an ordinary one remains an open question. The analysis of this problem goes beyond the thesis research and requires additional study, which is a subject of future research.

The Sk tube discussed in this Section has the topological charge +1. However, in principle, considering 2D Sks of arbitrary topological charge can lead to many other hybridized Sk tubes. The general idea, nevertheless, remains the same. The case of trivial 2D skyrmions is of additional interest because they allow getting solitons localized in all three spatial directions. In the following Section, I discuss this particular type of solitons.

8.3 3D chiral droplet

8.3.1 Ansatz construction

Following the approach from the previous Section, instead of the path between two Sks, one can consider a topologically trivial Sk and its homotopy path into a FM state. As an example, I take the CD discussed above and write a smooth transformation from the FM into the droplet texture. The FM is given as $\boldsymbol{n}_{\mathrm{FM}} = (0,0,1)^{\mathrm{T}}$, Fig. 8.4 **a**. Applying to $\boldsymbol{n}_{\mathrm{FM}}$ the rotation about y axis creates the texture with $\boldsymbol{n}(r=0) = (0,0,-1)^{\mathrm{T}}$

$$\boldsymbol{n} = \begin{pmatrix} \cos\Theta(r) & 0 & \sin\Theta(r) \\ 0 & 1 & 0 \\ -\sin\Theta(r) & 0 & \cos\Theta(r) \end{pmatrix} \boldsymbol{n}_{\mathrm{FM}}, \tag{8.16}$$

where $\Theta(r)$ describes π-skyrmion-like profile, for instance, one can use $\Theta(r) = 2\arctan\left(e^{-r}/r\right)$. The next step is the rotation of the spins in the plane. This can be done by applying the rotation matrix about z axis to the result of (8.16),

$$\boldsymbol{n} = \begin{pmatrix} \cos\Phi(\phi) & \sin\Phi(\phi) & 0 \\ -\sin\Phi(\phi) & \cos\Phi(\phi) & 0 \\ 0 & 0 & 1 \end{pmatrix} \begin{pmatrix} \cos\Theta(r) & 0 & \sin\Theta(r) \\ 0 & 1 & 0 \\ -\sin\Theta(r) & 0 & \cos\Theta(r) \end{pmatrix} \boldsymbol{n}_{\mathrm{FM}}, \tag{8.17}$$

where $\Phi(\phi) = \frac{\pi}{2} - \frac{9}{8\pi^2}\phi^2(\phi-2\pi)$, $\phi \in [0, 2\pi)$. The resulting spin texture (8.17) can be used as the initial state for the numerical energy minimization. The magnetic textures obtained in (8.16), (8.17) and the relaxed state are shown in Fig. 8.4 **b**, **c** and **d**, respectively.

To write the homotopy path connecting FM and the droplet state as a function of a single parameter, z, one can include it explicitly into $\Theta(r)$ and $\Phi(\phi)$ as following,

$$\begin{aligned} \Theta(r,z) &= 2e^{-z^2}\arctan\frac{e^{-r}}{r}, \\ \Phi(\phi,z) &= \left(\frac{\pi}{2} - \frac{9}{8\pi^2}\phi^2(\phi-2\pi)\right)e^{-z^2}. \end{aligned} \tag{8.18}$$

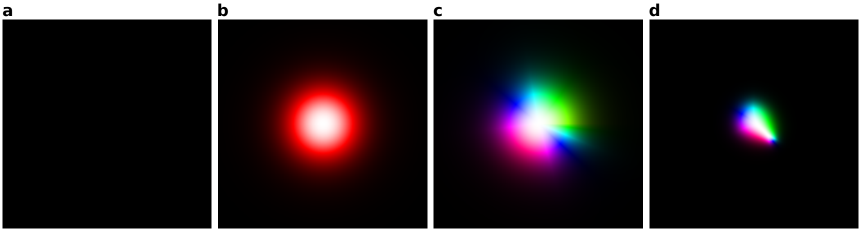

Figure 8.4: **Transformation from the FM to the CD**. **a** initial FM state, **b** and **c** magnetic textures obtained in (8.16), (8.17). The result of numerical minimization at $h = 0.65$ starting with the ansatz **c** is shown in **d**.

Then the 3D magnetic texture obtained from (8.17) and (8.18) is

$$\boldsymbol{n}(r, \phi, z) = (\sin\Theta(r, z)\cos\Phi(\phi, z), \sin\Theta(r, z)\sin\Phi(\phi, z), \cos\Theta(r, z))^{\mathrm{T}}, \tag{8.19}$$

It describes the mapping of the homotopy path into spatial z axis. From continuity of functions $\Theta(r, z)$ and $\Phi(\phi, z)$ in (8.18) follows the continuity of magnetic texture $\boldsymbol{n}(r, \phi, z)$. At $z = 0$, $\boldsymbol{n}(r, \phi, z)$ describes the droplet state (Fig. 8.17 **c**), which transforms into the FM at $z \to \pm\infty$. Using the configuration (8.19) as an initial guess (see Fig. 8.5 **a**) in the subsequent energy minimization allows one to obtain a stable 3D soliton (**b**, **c**).

Although the initial vacuum represents the FM state, the stabilization 3D droplet requires the presence of the cone phase corresponding to parameters $h = 0.34$ and $u = 0.26$. In each sections the spin texture of the 3D chiral droplet has the topological charge 0 but still represents well-localized 3D soliton. The sections by planes $x = 0$ and $y = 0$ are shown in Fig. 8.5 **d** and **e**. The cross-section by plane $z = 0$ is given in Fig. 8.5 **f**, and resembles the 2D CD imposed into the tilted FM vacuum.

It is worth noting that the 3D droplet is topologically trivial from the point of view of the Hopf invariant – Hopf index $H = 0$. That means such 3D droplets can be created from the FM (or cone phase) without the appearance of BPs. It has been shown recently [100] that 3D solitons of non-zero Hopf index can be stabilized in the model of chiral magnet. However, the problem of controllable creation of such solitons and the role of so-called topological protection of solitons with $H \neq 0$ is not well understood yet.

8.3.2 Droplet motion under circular magnetic field

An important feature of 3D solitons is their ability to move in all spatial directions. It is quite obvious that the dynamics of CD in xy-plane can be induced by the electric current, similar to the case of of Sk tubes and bobbers **Section** 7.2 and hopfions [101]. As I have shown in the previous Chapter, applying electrical current in the direction of the z axis leads to the rotation of the cone phase. So, by this driving force, one can not achieve the

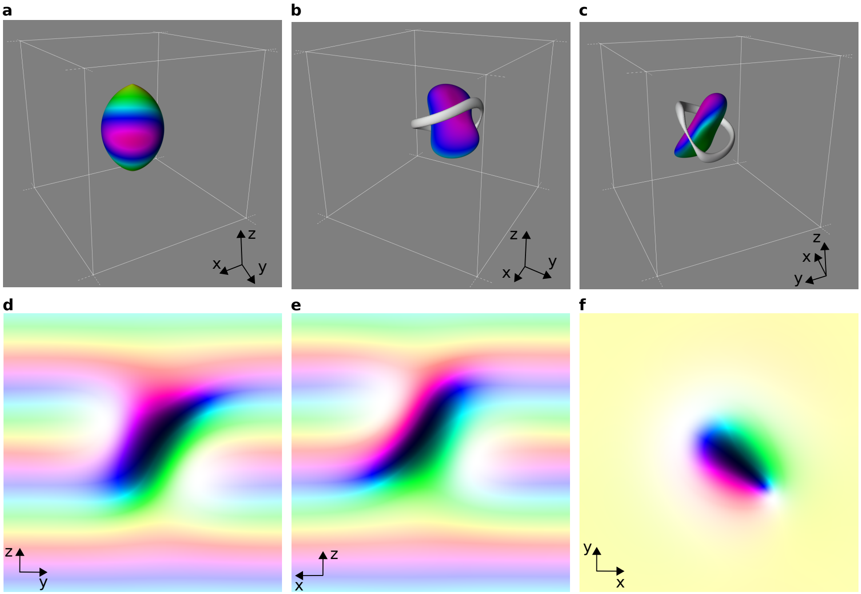

Figure 8.5: **Stable 3D chiral droplet**. **a** isosurface $n_z = 0$ corresponding to ansatz (8.19). The relaxed configurations corresponding to a local energy minimum are shown on **b**, **c**; the white loops correspond to $n_z = 1$. The sections of 3D droplet by planes $x = 0$, $y = 0$ and $z = 0$ are shown on **d**-**f**. Simulations have been performed at $h = 0.34$ and $u = 0.26$ with $L_\mathrm{D} = 64a$, the system size is $L_\mathrm{x} = L_\mathrm{y} = L_\mathrm{z} = 3L_\mathrm{D}$ and PBCs in all directions are assumed. This figure has been adapted from [79].

motion of soliton without the motion of the vacuum. However, it has been demonstrated in [100] that in the case of a bulk crystal, a circular magnetic field enforces hopfions to move in the z direction without rotation of the cone phase. I utilize this approach to show the motion of the 3D droplet. Applying the tilted field $\boldsymbol{h} = h(0.1\cos\phi_\mathrm{h}, 0.1\sin\phi_\mathrm{h}, 1)^T$ causes the droplet orientation change. Slowly changing phase ϕ_h enforces the droplet to rotate about z-axis. As it turned out, there is a coupling between the rotation of the 3D droplet and its translation in z direction Fig. 8.6 **a**-**f**. The numerical experiment indicates that a combination of rotation and translation along the z axis represents a zero mode. The fact that this motion happens even in a quasi-stationary regime when the frequency of changing the in-plane phase of the magnetic field tends to 0 also supports the statement above.

8.3.3 Homotopy path for the 3D droplet

The triviality of the 3D droplet from the point of the Hopf charge allows constructing a homotopy path describing annihilation of the droplet into the cone phase. Using the GNEB method implemented in Spirit software [60], I have calculated the corresponding

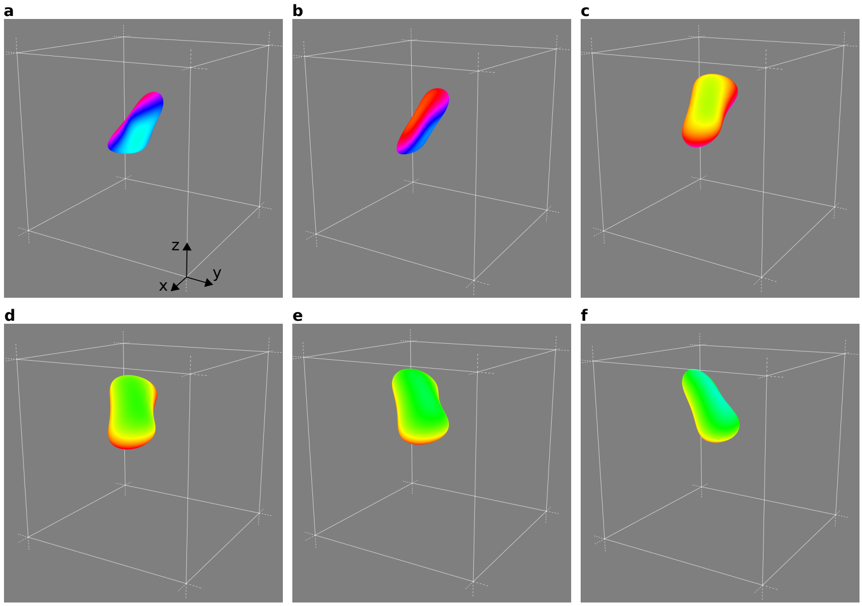

Figure 8.6: **Rotation and translation of the 3D droplet**. **a-f** the surfaces $n_z = 0$ corresponding to the 3D droplet are obtained for different phases of the in-plane magnetic field $\phi_h = 0°, 30°, 60°, 90°, 120°, 150°$, respectively.

MEP Fig. 8.7.

The local minima corresponding to the 3D droplet **a** and cone phase are separated by the saddle point **e**. The sections by planes $x = 0$, $y = 0$ and $z = 0$ are given for the first minimum **b-d** and for saddle point **f-h**, for the cone phase only section by plane $x = 0$ is shown **i**, it coincides with the section by plane $y = 0$. The transitions along the MEP can be easily seen from comparison snapshots **b**, **c**, **f**, **g**, and with the cone phase state **i**. The change of the texture in z-sections **d**, **h** is similar to the process of the collapse of the CD studied in **Chapter** 4. Despite using such a small mesh density of the lattice ($L_D = 22a$), the calculated transition still represents a homotopic path – all textures corresponding to each point on the MEP **j** free of singularities.

The new 3D solitons shown in the last two sections are only a few examples obtained by mapping the homotopy paths between 2D Sks into the spatial z-axis. No doubt, following the approach discussed here, one can find many other similar textures. The detailed study of the diversity of such 3D solutions and their physical properties is out of the scope of this thesis and will be a subject of future research.

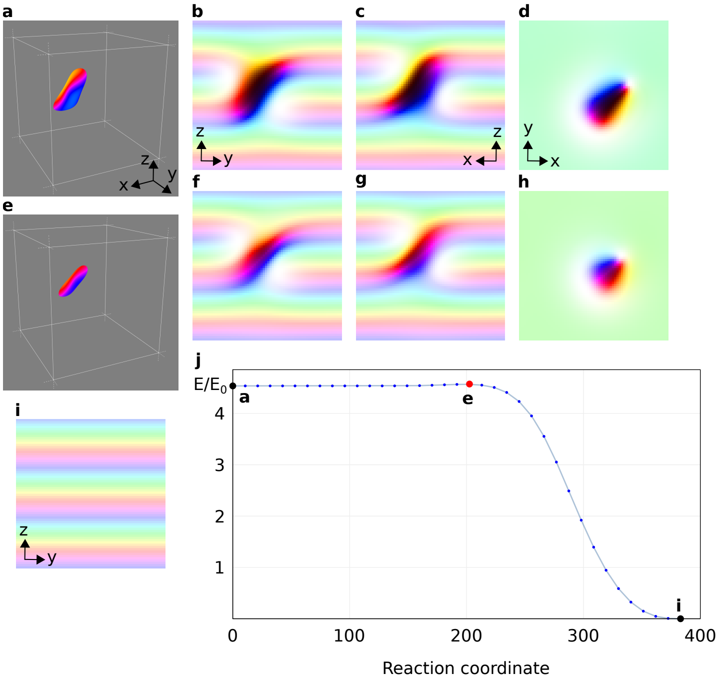

Figure 8.7: **Homotopy paths for the 3D droplet**. **a**, **e** show surfaces $n_z = 0$ for the 3D droplet and its saddle point before collapse to the cone phase. Sections by planes $x = 0$, $y = 0$ and $z = 0$ are shown on **b-d** for the droplet and on **f-h** for the saddle point. **i** Section by plane $x = 0$ for the cone phase. The MEP connecting droplet **a**, saddle point **e** and cone phase **i** is shown in **j**. The system of size $L_x = L_y = L_z = 3L_D$ with $L_D = 22a$ has been used for numerical simulations, physical parameters are $h = 0.34$, $u = 0.26$.

8.4 Conclusions

In this Chapter, I have studied π-skyrmion tube and a few new solutions, particularly the hybridized Sk tubes and the 3D droplet, which have not been reported in the literature before. Based on the ansatz method approach, I have shown that asymptotics of the solution for the π-skyrmion tube in the cone phase is described by oscillatory functions. Numerical simulations prove this finding and show similar oscillatory behaviour of interacting π-skyrmion tubes. In agreement with analytical results, such oscillations have been observed only below a particular critical field.

The results from **Chapter** 4 on homotopy transitions have inspired me to develop a new method for the construction of 3D magnetic solitons. The proposed method is based on the projection of the homotopy path into the spatial z-axis. Such mapping by default does not guaranty the stability of the spin texture constructed using this method. However, I show that optimal parameters for the stability of such solutions can be found by varying external or internal parameters of the system, such as magnetic field and anisotropy. I provide examples for two limiting cases when the parent 2D Sks has zero and non-zero topological charges. In the case of topologically nontrivial 2D Sks, I obtained the solution representing 3D tubes, which penetrate through the whole system and strictly speaking are not localized in all three spatial dimensions. I have shown that such tubes can be stable in the vacuum representing the cone phase and the FM state. On the other hand, mapping the homotopy path for topologically trivial 2D Sks provide a good initial state for statically stable solitons that are genuinely localized in 3D space. Numeric calculations proved the latter.

Similar to the CDs in 2D systems, the 3D droplet seems to be the most compact 3D soliton in chiral magnets. The 3D droplet has been constructed using a homotopy path describing the transition from the CD to the FM state. Interestingly the 3D droplet is stable in the cone phase and requires the presence of easy-axis anisotropy. However, one may expect this solution to become stable even in a pure isotropic system in the more realistic case of geometrical confinement and with demagnetizing fields. The numerical simulations of the 3D droplet show the possibility of its motion in the direction of z-axis with the help of a circular magnetic field. The Zhang-Li torque studied in the previous Chapter on Sk dynamics can induce its motion in the xy plane.

The calculation of the MEP corresponding to the 3D droplet annihilation shows that the energy barrier for its nucleation has a finite size, which agrees with the fact that the droplet has a zero Hopf index. The latter is an intriguing feature of such 3D soliton because, despite the topological triviality, it still represents a statically stable solution.

9 Conclusions

The results of this thesis are related to different aspects of chiral magnetic skyrmions in the model of chiral magnets. I presented a detailed study of the diversity of skyrmion solutions, their dynamics, homotopy transitions, and the processes of inter-soliton interaction. I also studied aspects of the applicability of the results to 3D magnets that represent a starting point for a more profound investigation of such systems. The work combines analytical and numerical techniques, which might be helpful in further research of similar models from a methodological point of view.

The first chapter contains a short overview of the used models and methods. The second chapter is devoted to the 2D π-skyrmion in a tilted magnetic field. I have shown the possibility of turning π-skyrmion inside out by applying a magnetic field with a changing tilt angle and amplitude. An essential outcome of this finding is the possibility of stabilizing the antiskyrmion in a perpendicular magnetic field. I found the parameters at which both particle (π-skyrmion) and antiparticle (antiskyrmion) can coexist. The exponential localization of the π-skyrmion and the antiskyrmion has been shown analytically. I obtained the asymptotic expansion of the solutions describing their profiles given by decreasing oscillatory functions. The inter-soliton interaction potential also demonstrates oscillatory behaviour, leading to the attraction/repulsion of solitons depending on their distance. The 2D solutions in the tilted magnetic field represent a reference solution for many 3D solutions embedded in the vacuum of the cone phase. Applying these results to thin films of chiral magnets has been successful, and a stable antiskyrmion has been observed in this type of material. The results presented in the second chapter, de facto, laid the groundwork and stimulated the subsequent studies. In particular, the discovery of antiskyrmion in a perpendicular magnetic field motivated the discovery of a wide variety of 2D skyrmions with chiral kinks.

In the third chapter, I discussed a variety of new 2D skyrmions. Based on the Bogomol'nyi equation, I showed that one could classify a wide diversity of skyrmion solutions in holomorphic functions. There I also discussed properties of the newly found skyrmions. In particular, I have shown that such solutions can become the global minimizers in the corresponding topological sector; therefore, they have to be taken into account. I show that well-known skyrmion bags solutions become energetically less favourable at specific parameters than skyrmions with chiral kinks. The properties of chiral kinks and antikinks have been studied. In particular, the interaction between chiral kinks hosted by a single domain wall revealed a second characteristic scale of magnetic inhomogeneities in chiral magnets. That, in particular, allows one to predict the materials where such skyrmions can be observed.

The presence of different skyrmions in the model raises the natural question of the possible transitions between them. This aspect of the problem is discussed in the fourth chapter, where I have concentrated on the homotopy transitions. It has been shown that they can be obtained as minimum energy paths (MEPs), which in turn can be numerically calculated by the so-called geodesic nudged elastic band (GNEB) method. Usually, the GNEB method converges to MEPs that do not necessarily coincide with the homotopy paths. I have improved on this method by choosing the initial paths taking into account possible instabilities of skyrmions solutions caused by a tilted magnetic field or anisotropy. The study of the stability range of these textures and calculations of their homotopy paths have allowed further exploration of the continual transformations of topological magnetic solitons. I show that chiral kinks play an essential role in these transitions. On the other hand, I show that there are also homotopy transitions that are free of chiral kinks. This case is mediated by the appearance of textures with so-called tails that can be thought of as the local elliptical deformations of the skyrmion shape. Adding the tails to solutions found earlier has allowed expanding the diversity of skyrmion solutions even further. Additionally, I showed that homotopy transformations could be used to construct 3D magnetic solitons, which are discussed in the following chapters.

The fifth chapter is dedicated to the study of the current-induced motion of different kinds of skyrmions. The additional torque in the LLG equation has been chosen in the Zhang-Li form. The numerical simulations have revealed an interesting feature of skyrmion solutions. In particular, it was found that irrespective of external parameters such as magnetic field and anisotropy, the velocities of different skyrmions form a specific ring-shaped pattern on the velocity plane. It has been shown that one can explain this geometric phenomenon within the Thiele approach. The interconnection between Sk rotational symmetry and its dynamical properties has been established. A rigorous mathematical analysis has shown that the dissipation tensor becomes proportional to the identity matrix when the skyrmion has a rotational axis of order > 2. In this case, the velocities of such so-called high-symmetry skyrmions are bound to the big circle irrespective of the skyrmion orientation with respect to the direction of the electric current. The case of low-symmetry skyrmions corresponding to solutions with a rotational axis of order 1 or 2 has a significant difference. The Sk orientation defines its velocity and deflection angle. The velocities corresponding to different skyrmion orientations are bound to another so-called small circle which is individual for each skyrmion. The structure of the low-symmetry skyrmion defines the size and position of this circle through its topological charge and components of the dissipation tensor. The general result for the relative distribution of small circles in the close vicinity to the big one has been obtained. Additional geometrical features of the Thiele equation have been discussed in detail.

One of the open questions that remains is how to generate different skyrmions in experiments. In the sixth chapter, I suggest the method to solve this problem. The method is based on applying small temperatures and a tilted magnetic field to the sample. In particular, the possibility of chiral droplet generation with this method has been shown through numerical Monte-Carlo and stochastic LLG equation simulations. Both methods provide similar results and agree on a quantitative level. Furthermore, static properties of the chiral droplets in a tilted magnetic field have been studied, and the arguments that justify the possibility of such a generation process are provided. The chiral droplet represents an interesting object to study because it is the most compact skyrmion hosting chiral kink, which can be used as a building block for more complicated solitons.

The findings presented in the seventh chapter are related to properties of chiral magnet systems with free boundaries. The analytically solved problems of current-induced rotation of the cone phase and appearance of the surface modulation at a strong, slightly tilted magnetic field have been provided. Besides fundamental value, these mathematically strict results can be used to test the accuracy of numerical LLG and energy minimization solvers. The seventh chapter also contains the simulation of the motion of skyrmion tubes and chiral bobbers induced by electric current. It has been shown that the Thiele equation describes the steady motion of 3D solitons quite well. The interesting point being the motion of the chiral bobber, which despite containing a Bloch point – a micromagnetic singularity – can nevertheless be effectively described by the above-mentioned micromagnetic equations.

In the eighth and last chapter, I study 3D solitons in the bulk crystal of chiral magnets. The analytical results, based on ansatz functions for the skyrmion tube in the cone phase and obtained by asymptotic expansion, have shown the oscillatory behaviour of the solutions. Furthermore, the numerical simulations exhibit similar energy density behaviour, which also serves as corroborating evidence for the oscillatory inter-soliton interactions, as was the case in the 2D system. Applying the concept of projecting the homotopy path between different 2D Sks onto the spatial z-axis, I have shown the possibility of constructing new 3D solitons: hybridized skyrmion tubes and 3D chiral droplets localized in all three spatial directions. These two cases are distinguished by non-trivial and trivial 2D Sks used in the homotopy transformations. As an example of a non-trivial solution, I have considered the antiskyrmion with $Q = +1$, which can be transformed into the skyrmion bag of the same topological index, $Q = +1$. I used the chiral droplet as an example of a trivial transformation with the homotopy path between a 2D soliton and collinear ferromagnetic state. The parameters at which both 3D textures can be stabilized are found and given in the text. It has been demonstrated that the magnetic field precessing about the z-axis causes the motion of 3D chiral droplets. The calculation of the MEP for the annihilation of the droplet has revealed a finite energy barrier, a promising feature for the experimental observation of the droplet.

Bibliography

[1] I. Dzyaloshinsky. A thermodynamic theory of "weak" ferromagnetism of antiferromagnetics. *Journal of Physics and Chemistry of Solids*, 4(4):241 – 255, 1958. ISSN 0022-3697. doi: https://doi.org/10.1016/0022-3697(58)90076-3. URL http://www.sciencedirect.com/science/article/pii/0022369758900763.

[2] A. N. Bogdanov and D. A. Yablonskii. Thermodynamically stable "vortices" in magnetically ordered crystals. the mixed state of magnets. *Sov. Phys. JETP*, 68 (101), 1989. URL http://www.jetp.ac.ru/cgi-bin/e/index/e/68/1/p101?a=list.

[3] Skyrme T. H. R. A non-linear field theory. *Proc. R. Soc. Lond. A260127–138*, 1961. URL https://doi.org/10.1098/rspa.1961.0018.

[4] J. Clerk Maxwell. A dynamical theory of the electromagnetic field. *Philosophical Transactions of the Royal Society of London*, 155:459–512, 1865. ISSN 02610523. URL http://www.jstor.org/stable/108892.

[5] Lev Davidovich Landau and E Lifshitz. On the theory of the dispersion of magnetic permeability in ferromagnetic bodies. *Phys. Z. Sowjet.*, 8:153, 1935. URL http://cds.cern.ch/record/437299.

[6] W. Kohn and L. J. Sham. Self-consistent equations including exchange and correlation effects. *Phys. Rev.*, 140:A1133–A1138, Nov 1965. doi: 10.1103/PhysRev.140.A1133. URL https://link.aps.org/doi/10.1103/PhysRev.140.A1133.

[7] Robert G. Parr and Weitao Yang. *Density-Functional Theory of Atoms and Molecules (International Series of Monographs on Chemistry)*. Oxford University Press, USA, 1994. ISBN 0195092767.

[8] Wu-Ki Tung. *Group theory in physics*. World Scientific Publishing Co., Philadelphia, PA, 1985. ISBN 9971-966-57-3. doi: 10.1142/0097. URL https://doi.org/10.1142/0097.

[9] James Parker Elliott and P. G. Dawber. Symmetry in physics. 1979.

[10] G. Binasch, P. Grünberg, F. Saurenbach, and W. Zinn. Enhanced magnetoresistance in layered magnetic structures with antiferromagnetic interlayer exchange. , 39(7):4828–4830, March 1989. doi: 10.1103/PhysRevB.39.4828.

[11] M. N. Baibich, J. M. Broto, A. Fert, F. Nguyen Van Dau, F. Petroff, P. Etienne, G. Creuzet, A. Friederich, and J. Chazelas. Giant magnetoresistance of (001)fe/(001)cr magnetic superlattices. *Phys. Rev. Lett.*, 61:2472–2475, Nov 1988. doi: 10.1103/PhysRevLett.61.2472. URL `https://link.aps.org/doi/10.1103/PhysRevLett.61.2472`.

[12] Tien Chi Chen and Hsu Chang. Magnetic bubble memory and logic. volume 17 of *Advances in Computers*, pages 223–282. Elsevier, 1978. doi: https://doi.org/10.1016/S0065-2458(08)60393-9. URL `https://www.sciencedirect.com/science/article/pii/S0065245808603939`.

[13] Wang Kang, Xing Chen, Daoqian Zhu, Sai Li, Yangqi Huang, Youguang Zhang, and Weisheng Zhao. Magnetic skyrmions for future potential memory and logic applications: Alternative information carriers. In *2018 Design, Automation Test in Europe Conference Exhibition (DATE)*, pages 119–124, 2018. doi: 10.23919/DATE.2018.8341990.

[14] Christian Back, Vincent Cros, Hubert Ebert, Karin Everschor-Sitte, Albert Fert, Markus Garst, Tianping Ma, Sergiy Mankovsky, TL Monchesky, Maxim Mostovoy, et al. The 2020 skyrmionics roadmap. *Journal of Physics D: Applied Physics*, 53 (36):363001, 2020.

[15] Kyung Mee Song, Jae-Seung Jeong, Sun Kyung Cha, Tae-Eon Park, Kwangsu Kim, Simone Finizio, Jörg Raabe, Joonyeon Chang, Hyunsu Ju, and Seonghoon Woo. Skyrmion-based artificial synapses for neuromorphic computing. *Nature Electronics*, 3:148–155, 2019.

[16] A. Bogdanov and A. Hubert. The stability of vortex-like structures in uniaxial ferromagnets. *Journal of Magnetism and Magnetic Materials*, 195(1):182–192, 1999. ISSN 0304-8853. doi: https://doi.org/10.1016/S0304-8853(98)01038-5. URL `https://www.sciencedirect.com/science/article/pii/S0304885398010385`.

[17] Filipp N. Rybakov and Nikolai S. Kiselev. Chiral magnetic skyrmions with arbitrary topological charge. *Phys. Rev. B*, 99:064437, Feb 2019. doi: 10.1103/PhysRevB.99.064437. URL `https://link.aps.org/doi/10.1103/PhysRevB.99.064437`.

[18] David Foster, Charles Kind, Paul J. Ackerman, Jung-Shen B. Tai, Mark R. Dennis, and Ivan I. Smalyukh. Two-dimensional skyrmion bags in liquid crystals and ferromagnets. *Nature Physics*, 15(7), 4 2019. doi: 10.1038/s41567-019-0476-x.

[19] Vladyslav M. Kuchkin, Bruno Barton-Singer, Filipp N. Rybakov, Stefan Blügel, Bernd J. Schroers, and Nikolai S. Kiselev. Magnetic skyrmions, chiral kinks, and holomorphic functions. *Phys. Rev. B*, 102:144422, Oct 2020. doi: 10.1103/PhysRevB.102.144422. URL `https://link.aps.org/doi/10.1103/PhysRevB.102.144422`.

[20] S. Mühlbauer, B. Binz, F. Jonietz, C. Pfleiderer, A. Rosch, A. Neubauer, R. Georgii, and P. Böni. Skyrmion lattice in a chiral magnet. *Science*, 323(5916):915–919, 2009. ISSN 0036-8075. doi: 10.1126/science.1166767. URL `https://science.sciencemag.org/content/323/5916/915`.

[21] Akira Tonomura, Xiuzhen Yu, Keiichi Yanagisawa, Tsuyoshi Matsuda, Yoshinori Onose, Naoya Kanazawa, Hyun Soon Park, and Yoshinori Tokura. Real-space observation of skyrmion lattice in helimagnet mnsi thin samples. *Nano Letters*, 12 (3):1673–1677, 2012. doi: 10.1021/nl300073m. URL `https://doi.org/10.1021/nl300073m`. PMID: 22360155.

[22] B Lebech, J Bernhard, and T Freltoft. Magnetic structures of cubic FeGe studied by small-angle neutron scattering. *Journal of Physics: Condensed Matter*, 1(35): 6105–6122, sep 1989. doi: 10.1088/0953-8984/1/35/010. URL `https://doi.org/10.1088/0953-8984/1/35/010`.

[23] H. Wilhelm, M. Baenitz, M. Schmidt, U. K. Rößler, A. A. Leonov, and A. N. Bogdanov. Precursor phenomena at the magnetic ordering of the cubic helimagnet fege. *Phys. Rev. Lett.*, 107:127203, Sep 2011. doi: 10.1103/PhysRevLett.107.127203. URL `https://link.aps.org/doi/10.1103/PhysRevLett.107.127203`.

[24] X. Z. Yu, N. Kanazawa, Y. Onose, K. Kimoto, W. Z. Zhang, S. Ishiwata, Y. Matsui, and Y. Tokura. Near room-temperature formation of a skyrmion crystal in thin-films of the helimagnet fege. *Nature Materials*, 10(2):106–109, February 2011. ISSN 1476-1122. doi: 10.1038/nmat2916.

[25] K Shibata, XZ Yu, T Hara, D Morikawa, N Kanazawa, K Kimoto, S Ishiwata, Y Matsui, and Y Tokura. Towards control of the size and helicity of skyrmions in helimagnetic alloys by spin-orbit coupling. *Nature nanotechnology*, 8(10):723—728, October 2013. ISSN 1748-3387. doi: 10.1038/nnano.2013.174. URL `https://doi.org/10.1038/nnano.2013.174`.

[26] T. Yokouchi, N. Kanazawa, A. Tsukazaki, Y. Kozuka, M. Kawasaki, M. Ichikawa, F. Kagawa, and Y. Tokura. Stability of two-dimensional skyrmions in thin films of $\mathrm{mn}_{1-x}\mathrm{fe}_x\mathrm{si}$ investigated by the topological hall effect. *Phys. Rev. B*, 89:064416, Feb 2014. doi: 10.1103/PhysRevB.89.064416. URL `https://link.aps.org/doi/10.1103/PhysRevB.89.064416`.

[27] X. Z. Yu, Y. Onose, N. Kanazawa, J. H. Park, J. H. Han, Y. Matsui, N. Nagaosa, and Y. Tokura. Real-space observation of a two-dimensional skyrmion crystal. *Nature*, 465(7300):901–904, June 2010. ISSN 0028-0836. doi: 10.1038/nature09124.

[28] Y. Onose, Y. Okamura, S. Seki, S. Ishiwata, and Y. Tokura. Observation of magnetic excitations of skyrmion crystal in a helimagnetic insulator cu_2oseo_3. *Phys. Rev. Lett.*, 109:037603, Jul 2012. doi: 10.1103/PhysRevLett.109.037603. URL `https://link.aps.org/doi/10.1103/PhysRevLett.109.037603`.

[29] A. Aharoni. *Introduction to the Theory of Ferromgnetism.* Claredon Press, 1965.

[30] T. Schäpers S. Blügel, Y. Mokrousov and Y. Ando. *Topological Matter: Topological Insulators, Skyrmions and Majoranas.* Forschungszentrum Jülich GmbH, 2017.

[31] Niklas Romming, Christian Hanneken, Matthias Menzel, Jessica E. Bickel, Boris Wolter, Kirsten von Bergmann, André Kubetzka, and Roland Wiesendanger. Writing and deleting single magnetic skyrmions. *Science*, 341(6146):636–639, 2013. doi: 10.1126/science.1240573.

[32] István Kézsmárki, Sándor Bordács, Peter Milde, E Neuber, LM Eng, JS White, Henrik M Rønnow, CD Dewhurst, M Mochizuki, K Yanai, et al. Néel-type skyrmion lattice with confined orientation in the polar magnetic semiconductor gav 4 s 8. *Nature materials*, 14(11):1116–1122, 2015.

[33] Niklas Romming, André Kubetzka, Christian Hanneken, Kirsten von Bergmann, and Roland Wiesendanger. Field-dependent size and shape of single magnetic skyrmions. *Physical review letters*, 114(17):177203, 2015.

[34] Xiuzhen Yu, Akiko Kikkawa, Daisuke Morikawa, Kiyou Shibata, Yusuke Tokunaga, Yasujiro Taguchi, and Yoshinori Tokura. Variation of skyrmion forms and their stability in mnsi thin plates. *Physical Review B*, 91(5):054411, 2015.

[35] Ajaya K Nayak, Vivek Kumar, Tianping Ma, Peter Werner, Eckhard Pippel, Roshnee Sahoo, Franoise Damay, Ulrich K Rößler, Claudia Felser, and Stuart SP Parkin. Magnetic antiskyrmions above room temperature in tetragonal heusler materials. *Nature*, 548(7669):561–566, 2017.

[36] Filipp N. Rybakov, Aleksandr B. Borisov, Stefan Blügel, and Nikolai S. Kiselev. New type of stable particlelike states in chiral magnets. *Phys. Rev. Lett.*, 115: 117201, Sep 2015. doi: 10.1103/PhysRevLett.115.117201. URL `https://link.aps.org/doi/10.1103/PhysRevLett.115.117201`.

[37] 18 - on the theory of the dispersion of magnetic permeability in ferromagnetic bodies. In D. TER HAAR, editor, *Collected Papers of L.D. Landau*, pages 101

– 114. Pergamon, 1965. ISBN 978-0-08-010586-4. doi: https://doi.org/10.1016/B978-0-08-010586-4.50023-7. URL `http://www.sciencedirect.com/science/article/pii/B9780080105864500237`.

[38] S. Zhang and Z. Li. Roles of nonequilibrium conduction electrons on the magnetization dynamics of ferromagnets. *Phys. Rev. Lett.*, 93:127204, Sep 2004. doi: 10.1103/PhysRevLett.93.127204. URL `https://link.aps.org/doi/10.1103/PhysRevLett.93.127204`.

[39] A. Malozemoff and J. Slonczewski. Magnetic domain walls in bubble materials. 1979.

[40] A. A. Thiele. Steady-state motion of magnetic domains. *Phys. Rev. Lett.*, 30:230–233, Feb 1973. doi: 10.1103/PhysRevLett.30.230. URL `https://link.aps.org/doi/10.1103/PhysRevLett.30.230`.

[41] TJ Beaulieu, BR Brown, BA Calhoun, T Hsu, and AP Malozemoff. Wall states in ion-implanted garnet films. In *AIP Conference Proceedings*, volume 34, pages 138–143. American Institute of Physics, 1976.

[42] Pavel F Bessarab, Valery M Uzdin, and Hannes Jónsson. Method for finding mechanism and activation energy of magnetic transitions, applied to skyrmion and antivortex annihilation. *Computer Physics Communications*, 196:335–347, 2015.

[43] PF Bessarab. Comment on "path to collapse for an isolated néel skyrmion". *Physical Review B*, 95(13):136401, 2017.

[44] MN Potkina, IS Lobanov, H Jónsson, and VM Uzdin. Lifetime of skyrmions in discrete systems with infinitesimal lattice constant. *arXiv preprint arXiv:2111.12014*, 2021.

[45] Johannes Wild, Thomas N. G. Meier, Simon Pöllath, Matthias Kronseder, Andreas Bauer, Alfonso Chacon, Marco Halder, Marco Schowalter, Andreas Rosenauer, Josef Zweck, Jan Müller, Achim Rosch, Christian Pfleiderer, and Christian H. Back. Entropy-limited topological protection of skyrmions. *Science Advances*, 3 (9):e1701704, 2017. doi: 10.1126/sciadv.1701704.

[46] Bernd Schroers. Gauged sigma models and magnetic skyrmions. *SciPost Physics*, 7(3):030, 2019.

[47] Bruno Barton-Singer, Calum Ross, and Bernd J. Schroers. Magnetic Skyrmions at Critical Coupling. *Commun. Math. Phys.*, 375(3):2259–2280, 2020. doi: 10.1007/s00220-019-03676-1.

[48] Bernd Schroers. Solvable models of magnetic skyrmions. In *Quantum Theory and Symmetries*, pages 535–544. Springer, 2021.

[49] Alexander M. Polyakov and A. A. Belavin. Metastable States of Two-Dimensional Isotropic Ferromagnets. *JETP Lett.*, 22:245–248, 1975.

[50] F. N. Rybakov and E. Babaev. Quantum and classical solutions, 2020. URL `http://quantumandclassical.com/excalibur/`.

[51] Arne Vansteenkiste, Jonathan Leliaert, Mykola Dvornik, Mathias Helsen, Felipe Garcia-Sanchez, and Bartel Van Waeyenberge. The design and verification of mumax3. *AIP Advances*, 4(10):107133, 2014. doi: 10.1063/1.4899186. URL `https://doi.org/10.1063/1.4899186`.

[52] MJ Donahue and RD McMichael. Exchange energy representations in computational micromagnetics. *Physica B: Condensed Matter*, 233(4):272–278, 1997.

[53] A. Bogdanov and A. Hubert. Thermodynamically stable magnetic vortex states in magnetic crystals. *Journal of Magnetism and Magnetic Materials*, 138(3):255 – 269, 1994. ISSN 0304-8853. doi: https://doi.org/10.1016/0304-8853(94)90046-9. URL `http://www.sciencedirect.com/science/article/pii/0304885394900469`.

[54] Richard Ernest Bellman and Robert E. Kalaba. *Quasilinearization and nonlinear boundary-value problems.* RAND Corporation, Santa Monica, CA, 1965.

[55] N. S. Kiselev. Magnoom, 2018. URL `https://github.com/n-s-kiselev/magnoom`.

[56] J H Mentink, M V Tretyakov, A Fasolino, M I Katsnelson, and Th Rasing. Stable and fast semi-implicit integration of the stochastic landau–lifshitz equation. *Journal of Physics: Condensed Matter*, 22(17):176001, apr 2010. doi: 10.1088/0953-8984/22/17/176001. URL `https://doi.org/10.1088/0953-8984/22/17/176001`.

[57] David P. Landau and Kurt Binder. *A Guide to Monte Carlo Simulations in Statistical Physics.* Cambridge University Press, 4 edition, 2014. doi: 10.1017/CBO9781139696463.

[58] George Marsaglia. Choosing a Point from the Surface of a Sphere. *The Annals of Mathematical Statistics*, 43(2):645 – 646, 1972. doi: 10.1214/aoms/1177692644. URL `https://doi.org/10.1214/aoms/1177692644`.

[59] William Fuller Brown. Thermal fluctuations of a single-domain particle. *Phys. Rev.*, 130:1677–1686, Jun 1963. doi: 10.1103/PhysRev.130.1677. URL `https://link.aps.org/doi/10.1103/PhysRev.130.1677`.

[60] Gideon P. Müller, Markus Hoffmann, Constantin Dißelkamp, Daniel Schürhoff, Stefanos Mavros, Moritz Sallermann, Nikolai S. Kiselev, Hannes Jónsson, and Stefan Blügel. Spirit: Multifunctional framework for atomistic spin simulations. *Phys. Rev. B*, 99:224414, Jun 2019. doi: 10.1103/PhysRevB.99.224414. URL `https://link.aps.org/doi/10.1103/PhysRevB.99.224414`.

[61] Vladyslav M. Kuchkin and Nikolai S. Kiselev. Turning a chiral skyrmion inside out. *Phys. Rev. B*, 101:064408, Feb 2020. doi: 10.1103/PhysRevB.101.064408. URL `https://link.aps.org/doi/10.1103/PhysRevB.101.064408`.

[62] Damien McGrouther, RJ Lamb, Matus Krajnak, Sam McFadzean, Stephen McVitie, RL Stamps, AO Leonov, AN Bogdanov, and Yoshihiko Togawa. Internal structure of hexagonal skyrmion lattices in cubic helimagnets. *New Journal of Physics*, 18(9):095004, 2016.

[63] András Kovács, Jan Caron, Andrii S Savchenko, Nikolai S Kiselev, Kiyou Shibata, Zi-An Li, Naoya Kanazawa, Yoshinori Tokura, Stefan Blügel, and Rafal E Dunin-Borkowski. Mapping the magnetization fine structure of a lattice of bloch-type skyrmions in an fege thin film. *Applied Physics Letters*, 111(19):192410, 2017.

[64] A. O. Leonov and I. Kézsmárki. Skyrmion robustness in noncentrosymmetric magnets with axial symmetry: The role of anisotropy and tilted magnetic fields. *Phys. Rev. B*, 96:214413, Dec 2017. doi: 10.1103/PhysRevB.96.214413. URL `https://link.aps.org/doi/10.1103/PhysRevB.96.214413`.

[65] A O Leonov, T L Monchesky, N Romming, A Kubetzka, A N Bogdanov, and R Wiesendanger. The properties of isolated chiral skyrmions in thin magnetic films. *New Journal of Physics*, 18(6):065003, may 2016. doi: 10.1088/1367-2630/18/6/065003. URL `https://doi.org/10.1088/1367-2630/18/6/065003`.

[66] Börge Göbel, Alexander Mook, Jürgen Henk, Ingrid Mertig, and Oleg A. Tretiakov. Magnetic bimerons as skyrmion analogues in in-plane magnets. *Phys. Rev. B*, 99:060407, Feb 2019. doi: 10.1103/PhysRevB.99.060407. URL `https://link.aps.org/doi/10.1103/PhysRevB.99.060407`.

[67] Lukas Döring and Christof Melcher. Compactness results for static and dynamic chiral skyrmions near the conformal limit. *Calculus of variations and partial differential equations*, 56(3):60, 2017. ISSN 1432-0835. doi: 10.1007/s00526-017-1172-2. URL `https://publications.rwth-aachen.de/record/690025`.

[68] Naveen Sisodia, Pranaba Kishor Muduli, Nikos Papanicolaou, and Stavros Komineas. Skyrmion-antiskyrmion droplets in a chiral ferromagnet. *arXiv preprint arXiv:2009.00890*, 2020.

[69] W. Klingenberg. *A Course in Differential Geometry.* Graduate Texts in Mathematics, 51. Springer New York, New York, NY, 1st ed. 1978. edition, 1978. ISBN 1-4612-9923-3.

[70] MA Lavrent'Ev and BV Shabat. Methods of the theory of functions of a complex variable, 1973.

[71] Levente Rózsa, Julian Hagemeister, Elena Y. Vedmedenko, and Roland Wiesendanger. Localized spin waves in isolated $k\pi$ skyrmions. *Phys. Rev. B*, 98:224426, Dec 2018. doi: 10.1103/PhysRevB.98.224426. URL `https://link.aps.org/doi/10.1103/PhysRevB.98.224426`.

[72] Benjamin Heil, Achim Rosch, and Jan Masell. Universality of annihilation barriers of large magnetic skyrmions in chiral and frustrated magnets. *Phys. Rev. B*, 100: 134424, Oct 2019. doi: 10.1103/PhysRevB.100.134424. URL `https://link.aps.org/doi/10.1103/PhysRevB.100.134424`.

[73] Ran Cheng, Maxwell Li, Arjun Sapkota, Anish Rai, Ashok Pokhrel, Tim Mewes, Claudia Mewes, Di Xiao, Marc De Graef, and Vincent Sokalski. Magnetic domain wall skyrmions. *Physical Review B*, 99(18):184412, 2019.

[74] Maxwell Li, Arjun Sapkota, Anish Rai, Ashok Pokhrel, Tim Mewes, Claudia Mewes, Di Xiao, Marc De Graef, and Vincent Sokalski. Experimental observation of magnetic domain wall skyrmions. *arXiv e-prints*, pages arXiv–2004, 2020.

[75] S. A. Meynell, M. N. Wilson, H. Fritzsche, A. N. Bogdanov, and T. L. Monchesky. Surface twist instabilities and skyrmion states in chiral ferromagnets. *Phys. Rev. B*, 90:014406, Jul 2014. doi: 10.1103/PhysRevB.90.014406. URL `https://link.aps.org/doi/10.1103/PhysRevB.90.014406`.

[76] Jan Müller, Achim Rosch, and Markus Garst. Edge instabilities and skyrmion creation in magnetic layers. *New Journal of Physics*, 18(6):065006, jun 2016. doi: 10.1088/1367-2630/18/6/065006. URL `https://doi.org/10.1088/1367-2630/18/6/065006`.

[77] Markus Garst, Johannes Waizner, and Dirk Grundler. Collective spin excitations of helices and magnetic skyrmions: review and perspectives of magnonics in non-centrosymmetric magnets. *Journal of Physics D: Applied Physics*, 50(29): 293002, jun 2017. doi: 10.1088/1361-6463/aa7573. URL `https://doi.org/10.1088/1361-6463/aa7573`.

[78] Fengshan Zheng, Nikolai S. Kiselev, Luyan Yang, Vladyslav M. Kuchkin, Filipp N. Rybakov, Stefan Blügel, and Rafal E. Dunin-Borkowski. Skyrmion–antiskyrmion

pair creation and annihilation in a cubic chiral magnet. *Nature Physics*, 18(8): 863–868, June 2022. doi: 10.1038/s41567-022-01638-4. URL `https://doi.org/10.1038/s41567-022-01638-4`.

[79] V. M. Kuchkin and N. S. Kiselev. Homotopy transitions and 3d magnetic solitons. *APL Materials*, 10(7):071102, 2022. doi: 10.1063/5.0097559. URL `https://doi.org/10.1063/5.0097559`.

[80] Vladyslav M. Kuchkin, Ksenia Chichay, Bruno Barton-Singer, Filipp N. Rybakov, Stefan Blügel, Bernd J. Schroers, and Nikolai S. Kiselev. Geometry and symmetry in skyrmion dynamics. *Phys. Rev. B*, 104:165116, Oct 2021. doi: 10.1103/PhysRevB.104.165116. URL `https://link.aps.org/doi/10.1103/PhysRevB.104.165116`.

[81] Charles Kind and David Foster. Magnetic skyrmion binning. *Physical Review B*, 103(10):L100413, 2021.

[82] Zhaozhuo Zeng, Chunlei Zhang, Chendong Jin, Jianing Wang, Chengkun Song, Yunxu Ma, Qingfang Liu, and Jianbo Wang. Dynamics of skyrmion bags driven by the spin–orbit torque. *Applied Physics Letters*, 117(17):172404, 2020.

[83] Markus Weißenhofer and Ulrich Nowak. Orientation-dependent current-induced motion of skyrmions with various topologies. *Physical Review B*, 99(22):224430, 2019.

[84] Yuichi Ishida and Kenji Kondo. Theoretical comparison between skyrmion and skyrmionium motions for spintronics applications. *Japanese Journal of Applied Physics*, 59(SG):SGGI04, 2020.

[85] Gregory Malinowski, Olivier Boulle, and Mathias Kläui. Current-induced domain wall motion in nanoscale ferromagnetic elements. *Journal of Physics D: Applied Physics*, 44(38):384005, 2011.

[86] N Papanicolaou and TN Tomaras. Dynamics of magnetic vortices. *Nuclear Physics B*, 360(2-3):425–462, 1991.

[87] Jan Masell, Davi R Rodrigues, Ben F McKeever, and Karin Everschor-Sitte. Spin-transfer torque driven motion, deformation, and instabilities of magnetic skyrmions at high currents. *Physical Review B*, 101(21):214428, 2020.

[88] Stavros Komineas and Nikos Papanicolaou. Skyrmion dynamics in chiral ferromagnets under spin-transfer torque. *Phys. Rev. B*, 92:174405, Nov 2015. doi: 10.1103/PhysRevB.92.174405. URL `https://link.aps.org/doi/10.1103/PhysRevB.92.174405`.

[89] Linge Bai and David Breen. Calculating center of mass in an unbounded 2d environment. *Journal of Graphics Tools*, 13(4):53–60, 2008. doi: 10.1080/2151237X.2008.10129266. URL `https://doi.org/10.1080/2151237X.2008.10129266`.

[90] J.W. Anderson. *Hyperbolic Geometry*. Springer undergraduate mathematics series. Springer, 1999. ISBN 9783764351007. URL `https://books.google.de/books?id=ihcZAQAAIAAJ`.

[91] Vladyslav M. Kuchkin, Pavel F. Bessarab, and Nikolai S. Kiselev. Thermal generation of droplet soliton in chiral magnet. *Phys. Rev. B*, 105:184403, May 2022. doi: 10.1103/PhysRevB.105.184403. URL `https://link.aps.org/doi/10.1103/PhysRevB.105.184403`.

[92] Johann Pfanzagl. *Parametric Statistical Theory*. De Gruyter, 2011. ISBN 9783110889765. doi: doi:10.1515/9783110889765. URL `https://doi.org/10.1515/9783110889765`.

[93] Mikromagnetisch stetige und unstetige magnetisierungskonfigurationen. *Z. Angew. Phys*, 19:530 – 536, 1965.

[94] Point singularities in micromagnetism. *J. Appl. Phys.*, 39:1006–1007, 1968. URL `http://link.aip.org/link/?JAP/39/1006/1`.

[95] Zizhao Gong, Jin Tang, Sergey S. Pershoguba, Zongkai Xie, Rui Sun, Yang Li, Xu Yang, Jianan Liu, Wei Zhang, Xiangqun Zhang, Wei He, Haifeng Du, Jiadong Zang, and Zhao-hua Cheng. Current-induced dynamics and tunable spectra of a magnetic chiral bobber. *Phys. Rev. B*, 104:L100412, Sep 2021. doi: 10.1103/PhysRevB.104.L100412. URL `https://link.aps.org/doi/10.1103/PhysRevB.104.L100412`.

[96] F. Zheng, F. N. Rybakov, N. S. Kiselev, D. Song, A. Kovács, H. Du, S. Blügel, and R. E. Dunin-Borkowski. Magnetic skyrmion braids. *Nat. Comm.*, 12:5316, 2021.

[97] J. Tang, Y. Wu, W. Wang, L. Kong, B. Lv, W. Wei, J. Zang, M. Tian, and H. Du. Magnetic skyrmion bundles and their current-driven dynamics. *arXiv:2108.02487*, 2021.

[98] F. N. Rybakov, A. B. Borisov, and A. N. Bogdanov. Three-dimensional skyrmion states in thin films of cubic helimagnets. *Phys. Rev. B*, 87:094424, Mar 2013. doi: 10.1103/PhysRevB.87.094424. URL `https://link.aps.org/doi/10.1103/PhysRevB.87.094424`.

[99] Haifeng Du, Xuebing Zhao, Filipp N. Rybakov, Aleksandr B. Borisov, Shasha Wang, Jin Tang, Chiming Jin, Chao Wang, Wensheng Wei, Nikolai S. Kiselev, Yuheng Zhang, Renchao Che, Stefan Blügel, and Mingliang Tian. Interaction of individual skyrmions in a nanostructured cubic chiral magnet. *Phys. Rev. Lett.*, 120:197203, May 2018. doi: 10.1103/PhysRevLett.120.197203. URL https://link.aps.org/doi/10.1103/PhysRevLett.120.197203.

[100] Robert Voinescu, Jung-Shen B. Tai, and Ivan I. Smalyukh. Hopf solitons in helical and conical backgrounds of chiral magnetic solids. *Phys. Rev. Lett.*, 125:057201, Jul 2020. doi: 10.1103/PhysRevLett.125.057201. URL https://link.aps.org/doi/10.1103/PhysRevLett.125.057201.

[101] Yizhou Liu, Wentao Hou, Xiufeng Han, and Jiadong Zang. Three-dimensional dynamics of a magnetic hopfion driven by spin transfer torque. *Phys. Rev. Lett.*, 124:127204, Mar 2020. doi: 10.1103/PhysRevLett.124.127204. URL https://link.aps.org/doi/10.1103/PhysRevLett.124.127204.

[102] Stefan Buhrandt and Lars Fritz. Skyrmion lattice phase in three-dimensional chiral magnets from monte carlo simulations. *Physical Review B*, 88:195137, 2013.

A1 Implementation of the fourth order scheme in Mumax

```
OutputFormat =  OVF2_BINARY
TableAdd(Edens_total);

Ms := 384e3;     Msat = Ms; // saturation magnetization
EnableDemag = false;        // turn off DDI

LD := 70.0e-9  // spiral period
Lx := 8*LD     // simulation domain size
Ly := Lx
Lz := 1e-9

nx := 256; ny := 256; nz := 1; // discretization
SetGridSize(nx, ny, nz)
SetPBC(1, 1, 0)
openbc = false

dx := Lx/nx;     dy := Ly/ny;     dz := Lz/nz
SetCellSize(dx, dy, dz)
MinimizerStop = 1e-5;

A     := 4.0e-12;            // Exhange stiffness
D     := 4.0 * pi * A / LD; // DMI coefficient
BD    := D*D/(2*A*Ms);       // saturation magnetic field
B     := 0.65*BD             // magnetic filed value
B_ext = vector(0,0,B)        // magnetic field direction
anisU = vector(0, 0, 1);     // anisotropy axis
Ku1   = 0.0*D*D/(2*A)        // anisotropy value
// parameters correspond to h = 0.65 and u = 0.0

////Initial state \pi-skyrmion
m = uniform(0, 0, 1)
m.setInShape(cylinder(1*LD, Lz).scale(1, 1, 1),
        BlochSkyrmion(1, -1).scale(1, 1, 1))
```

```
// The 2nd order scheme
// Aex = A
// Dbulk = D
// End of the 2nd order scheme

// The 4th order scheme
// nearest exhange and DMI coefficients
Aex = A*(4/3)
Dbulk = D*(4/3)

// second nearest exhange coefficient
NewAex:= A*(-1/12)
prefactorXA := Const( (2 * NewAex) / (dx*dx*Msat.Average()))
prefactorYA := Const( (2 * NewAex) / (dy*dy*Msat.Average()))
prefactorZA := Const( (2 * NewAex) / (dz*dz*Msat.Average()))


left := Mul(Add(Mul(Const(-1),m),Shifted(m,   2, 0, 0)),
        Shifted(Const(1),   2, 0, 0))
left  = Add(left,Mul(Add(Mul(Const(-1),m),Shifted(m,2-nx, 0, 0)),
        Shifted(Const(1),2-nx, 0, 0)))

right := Mul(Add(Mul(Const(-1),m),Shifted(m,  -2, 0, 0)),
        Shifted(Const(1),  -2, 0, 0))
right  = Add(right,Mul(Add(Mul(Const(-1),m),Shifted(m,nx-2, 0, 0)),
        Shifted(Const(1),nx-2, 0, 0)))

backward :=  Mul(Add(Mul(Const(-1),m),Shifted(m, 0,   2, 0)),
        Shifted(Const(1), 0,   2, 0))
backward  =  Add(backward,Mul(Add(Mul(Const(-1),m),
        Shifted(m, 0,2-ny, 0)),Shifted(Const(1), 0,2-ny, 0)))

forward := Mul(Add(Mul(Const(-1),m),Shifted(m, 0,  -2, 0)),
        Shifted(Const(1), 0,  -2, 0))
forward  = Add(forward,Mul(Add(Mul(Const(-1),m),
        Shifted(m, 0,nx-2, 0)),Shifted(Const(1), 0,nx-2, 0)))

down := Mul(Add(Mul(Const(-1),m),Shifted(m, 0, 0, 2)),
        Shifted(Const(1), 0, 0, 2))
up      :=  Mul(Add(Mul(Const(-1),m),Shifted(m, 0, 0,-2)),
        Shifted(Const(1), 0, 0,-2))

leftA     :=  Mul(prefactorXA,    left)
rightA    :=  Mul(prefactorXA,   right)
forwardA  :=  Mul(prefactorYA,  forward)
```

```
backwardA  :=  Mul(prefactorYA, backward)
upA        :=  Mul(prefactorZA,       up)
downA      :=  Mul(prefactorZA,     down)
BcA := Add(leftA,Add(rightA,Add(forwardA,Add(backwardA,Add(upA,downA)))))
AddFieldTerm(BcA)
addEdensTerm(Mul(Const(-0.5),Dot(BcA,M_full)))

// second nearest DMI coefficient
NewD:= D*(-1/6)
prefactorXD  := Const( (2 * NewD) / (2*dx*Msat.Average()))
prefactorYD  := Const( (2 * NewD) / (2*dy*Msat.Average()))
prefactorZD  := Const( (2 * NewD) / (2*dz*Msat.Average()))

overx  := Mul(prefactorXD,Add(Cross(left,constVector(-1,0,0)),
        Cross(right,constVector(1,0,0))) )
overy  := Mul(prefactorYD, Add(Cross(backward,constVector(0,-1,0)),
        Cross(forward,constVector(0,1,0))))

AnisDMI  := Add( overx, overy )
AddFieldTerm(AnisDMI)
addEdensTerm(Mul(Const(-0.5),Dot(AnisDMI,M_full)))
// End of the 4th order scheme


TableSave()

relax();        save(m);        TableSave();
minimize();     save(m);        TableSave();
```

A2 Implementation of quasilinearization method for π-skyrmions

```
#include <stdio.h>
#include <stdlib.h>
#include <fstream>
#include <iostream>
#include <string>
#include <sstream>
#include <cmath>
#include <cstring>

using namespace std;

const double pi = 3.14159265358979323846264338327950;
int    N = 1e5;           // number of points
double L = 8.0;           // Box size in units of Ld
double dr = L/(N+1.);     // discretization step
double h = 0.65;          // External magnetic field in units of Bd
double u = 0.0;           // Anisotropy in units of Ld and Bd
double To = pi, Tn = 0.; // skyrmion boundary conditions
double tolerance = 1e-10, dif = 1;
double p = 1; // parameter for ansatz function

double *T = new double [N], *T0 = new double [N];
double *a = new double [N], *b  = new double [N];


void CalculateF1(double *a){
  for(int i = 0; i < N; i++){
    double r = (i+1)*dr;
    a[i] = -(cos(2*a[i])/r - 4*pi*sin(2*a[i]) +\
    4*pi*pi*r*(h*cos(a[i]) + 2*u*cos(2*a[i])));
  }
}
```

```
void CalculateF2(double *b){
  for(int i = 0; i < N; i++){
    double r = (i+1)*dr;
    b[i] = 0.5*sin(2*b[i])/r - 4*pi*sin(b[i])*sin(b[i]) +\
    4*pi*pi*r*(h*sin(b[i]) + u*sin(2*b[i])) + a[i]*b[i];
  }
}

double Energy(double *t){
  double E = 0;
  E += 0.5*dr*((0.5*(t[1]-To)/dr)*(0.5*(t[1]-To)/dr) +\
   sin(t[0])*sin(t[0])/(dr*dr)) + 2*pi*(dr*0.5*(t[1]-To)/dr) +\
    4*pi*pi*dr*(2*h*sin(t[0]/2)*sin(t[0]/2) + u*sin(t[0])*sin(t[0]));

  for(int i = 1; i < N-1; i++){
    double r = (i+1)*dr;
    E += 0.5*r*((0.5*(t[i+1]-t[i-1])/dr)*(0.5*(t[i+1]-t[i-1])/dr) +\
     sin(t[i])*sin(t[i])/(r*r)) + 2*pi*(r*0.5*(t[i+1]-t[i-1])/dr +\
      0.5*sin(2*t[i])) + 4*pi*pi*r*(2*h*sin(t[i]/2)*sin(t[i]/2) +\
       u*sin(t[i])*sin(t[i]));
  }

  double r = N*dr;
  E += 0.5*r*((0.5*(Tn-t[N-2])/dr)*(0.5*(Tn-t[N-2])/dr) +\
   sin(t[N-1])*sin(t[N-1])/(r*r)) + 2*pi*(r*0.5*(Tn-t[N-2])/dr +\
    0.5*sin(2*t[N-1])) + 4*pi*pi*r*(2*h*sin(t[N-1]/2)*sin(t[N-1]/2) +\
     u*sin(t[N-1])*sin(t[N-1]));
  E *= 2*pi*dr;
  return(E);
}

void SaveTheta(double *t){
  printf("Saving data...\n");
  fstream o;
  o.open("T.csv", ios::out);
  o<<0<<","<<To<<std::endl;
  for(int i = 0; i < N; i++)
    o<<(i+1)*dr<<","<<t[i]<<std::endl;
  o<<L<<","<<Tn<<std::endl;
  o.close();
  printf("Data are saved to T.csv\n");
}

// function calculates discrepancy
// between the two last profiles of Theta
double Difference(double *t0, double *t){
  double res = 0.0;
```

```
  for(int i = 0; i < N; i++)
    res += (t0[i]-t[i])*(t0[i]-t[i])*dr;
  return res;
}

// solving the system of linear equations
// by Gauss back-substitution method
void Solve(double *a, double *b, double *t){
  for (int i = 0; i < N; i++){
    double r = (i+1)*dr;
    a[i] -= 2*r/(dr*dr);
  }
  b[0]   -= To*0.5/dr;
  b[N-1] -= Tn*1.5/dr;

  for(int i = 1; i < N; i++){
    double r = (i+1)*dr;
    a[i] = a[i] - (r/dr-0.5)*(r/dr-0.5)/(dr*dr*a[i-1]);
    b[i] = b[i] - b[i-1]*(r/dr-0.5)/(dr*a[i-1]);
  }
  t[N-1] = b[N-1]/a[N-1];
  for(int i = N-2; i > -1; i--){
    double r = (i+1)*dr;
    t[i] = (b[i]-(r/dr+0.5)*t[i+1]/dr)/a[i];
  }
  for(int i = 0; i < N; i++){
    a[i] = t[i];
    b[i] = t[i];
  }
}

int main ()
{
  //initial ansatz
  for (int i = 0; i<N; i++){
    double r = (i+1)*dr;
    T0[i] = 2.*atan(p*exp(-2*pi*sqrt(h+2*u)*r)/r);
    a[i] = T0[i]; b[i] = T0[i];
  }
  double Eprev = Energy(T0), Enow;
  printf("Energy of the inital state = %.15f\n",Eprev);

  while(dif>tolerance){
    CalculateF1(a); CalculateF2(b); Solve(a,b,T);
    Enow = Energy(T);
    if(Enow>Eprev){
      printf("Algorithm can not reach the tolernace %0.1e.\n",tolerance);
```

```
      printf("Try to improve the initial ansatz!\n");
      dif = tolerance/10;
    }
    else{
      Eprev = Enow;
      dif = Difference(T0,T);
      for(int i = 0; i<N; i++)
        T0[i] = T[i];
      printf("Energy = %0.15f, Error = %0.15f\n",Enow,dif);
    }
  }
  printf("Done!\n"); SaveTheta(T);
  delete T0; delete T; delete a; delete b;
  return 0;
}
```

The initial profile for a π-skyrmion is given by the following ansatz-function

$$\Theta = 2\arctan\left(\frac{p\,e^{-2\pi r\sqrt{h+2u}}}{r}\right), \tag{A2 .1}$$

where parameter p depends on h, u and can be tuned. After performing numerical relaxation, I get the solution for the π-skyrmion. The dashed curves in Fig. A2 .1 **a** represent ansatz (A2 .1) at zero anisotropy and two field values $h = 0.65$ and $h = 0.4$, the parameter $p = 1$, while the solid curves show the result obtained in the Ql method. Fig. A2 .1 **b** shows the same for parameters $h = 0.2$ and $h = 0.1$, parameter p takes the values 20 and 80, respectively. In all cases, the algorithm converges to the π-skyrmion solution.

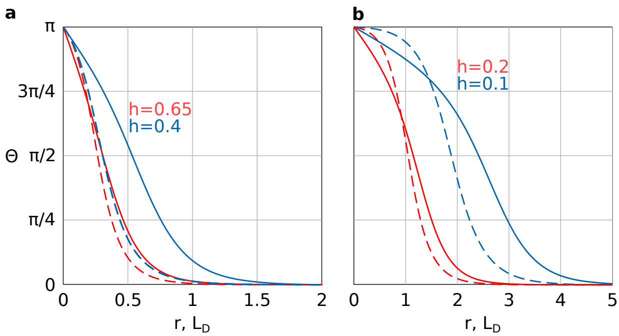

Figure A2 .1: **Skyrmion profile**. **a**, **b** profiles of π-skyrmions, Θ as function of distance r. Dashed curves correspond to ansatz (A2 .1), solid curves are the profiles relaxed by the Ql method. The system size is $8L_{\mathrm{D}}$, 10^5 discretization points are used.

A3 Vector fields visualization

For the general case, $|\boldsymbol{n}| \neq 1$, the magnetization vector field can be visualized by including gray level reflecting the vector length, see Fig. A3 .1. The orientation of the vector is given by spherical angles Θ, Φ and it has a standard color code.

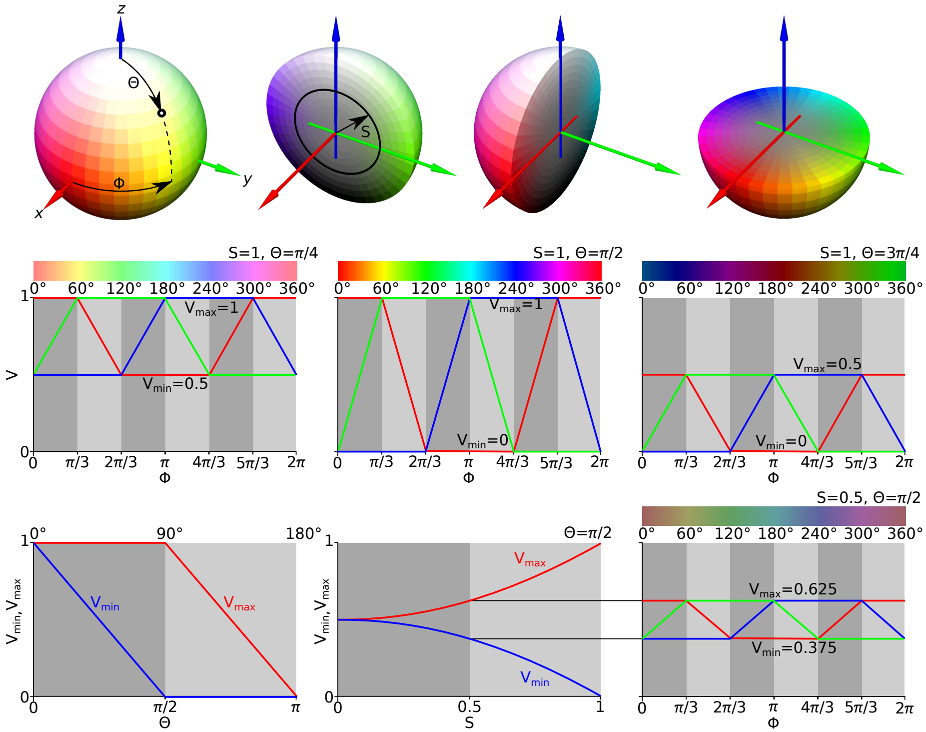

Figure A3 .1: **Color code for the vector field in a general case**. The figure illustrates the approach for encoding the direction of the vector on a sphere by the colors of the HSV (for hue, saturation, value) scheme. Here Θ and Φ are standard polar and azimuthal angles of the vector. Hue of the color is defined by the Φ angle. The length of the vector defines the saturation, S. The position of the vector in the top or bottom semi-sphere determines the value (the brightness) of the color, $V = V_r + V_g + V_b$. The functions, $V_{r(g,b)}(\Phi)$ for each component of red, green and blue, are depicted by the corresponding colors.

A4 Numerical verification of asymptotics

To examine the analytically obtained functions describing asymptotic behaviour of the π-skyrmion and antiskyrmion solutions in the tilted magnetic field (2.10), I have performed numerical energy minimization for each of the states in the domain of the size $L_{\mathrm{x}} = L_{\mathrm{y}} = 8L_{\mathrm{D}}$ with the fourth-order precision scheme and $L_{\mathrm{D}} = 64a$. The Φ function is taken in the form [61],

$$\Phi_{\pm} = \pm\left(\phi + \frac{\pi}{2}\right) + 2\pi x \sin\Theta_{\mathrm{h}} + c_1 \cos\phi, \tag{A4 .1}$$

where signs + and − correspond to π-skyrmion and antiskyrmion, respectively. To fit the function (A4 .1) with numerically obtained data, one needs to find the position of the Sk core. For this, the part of the data $\Theta(x, y) \in [0.05-10^{-6}, 0.05+10^{-6}]$ has been fitted with a circle equation, and its centre, (x_0, y_0), has been identified as the center of the soliton. Then, in the coordinate frame with origin at this center, one can plot $\Phi_{\pm}$ as a function of ϕ for different fixed radii. Due to exponential character of function Θ, it is more informative to plot its logarithm dependencies, the slope of corresponding linear function has to be compared with the value $-2\pi\sqrt{h - \sin^2\theta_{\mathrm{h}}}$, as follows from (2.10).

For parameters $h = 0.65$, $\theta_{\mathrm{h}} = 0.2$ and $u = 0$ from (2.2), one can find $\Theta_{\mathrm{h}} = 0.2$, the calculated value of constant $c_1 = -0.6276$ for the π-skyrmion and $c_1 = 1.667$ for the antiskyrmion. The comparison of numerical and analytical results is given in Fig. A4 .1 **a-c** (π-skyrmion Φ function), **d** (π-skyrmion Θ function) and the same for the antiskyrmion **e-h**. All plots demonstrate good agreement, the case of the antiskyrmion can be improved by including more general form of the Fourier series instead of considering only one harmonic $c_1 \cos\phi$.

For parameters $h = 0.6$, $\theta_{\mathrm{h}} = 0.35$ and $u = 0.1$ from (2.2), one can find $\Theta_{\mathrm{h}} \simeq 0.2655$, the calculated value of constant c_1 is -0.8327 for the π-skyrmion and 1.749 for the antiskyrmion. Interestingly, numerical data for Φ functions shown in Fig. A4 .2 **a-c** for the π-skyrmion and **e-g** for the antiskyrmion are in a good agreement with the analytical result (A4 .1). The attempt to match $\ln\Theta(r)$ profile by a linear function is shown on **d**

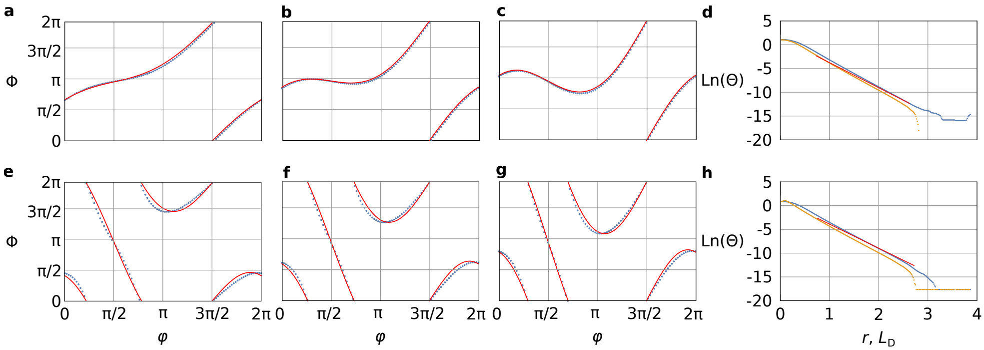

Figure A4 .1: **Asymptotics of the solutions for π-skyrmion and antiskyrmion at $u = 0$.** **a-d** and **e-h** corresponding to the π-skyrmion and the antiskyrmion, respectively, calculated at $h = 0.65$, $\theta_\mathrm{h} = 0.2$. Angular dependencies for $\Phi_\pm$ are shown for fixed radii $r = 1L_\mathrm{D}$ (**a**, **e**), $r = 1.5L_\mathrm{D}$ (**b**, **f**) and $r = 2L_\mathrm{D}$ (**c**, **g**). Functions $\ln\Theta(x, y_0)$ (blue), $\ln\Theta(x_0, y)$ (orange) and the linear function $y = -2\pi r\sqrt{h - \sin^2\theta_\mathrm{h}}/L_\mathrm{D} + 1.5$ for the π-skyrmion (antiskyrmion) are shown in **d** (**h**).

and **h** for the π-skyrmion and the antiskyrmion, respectively. The slope of this function slightly deviates from the value predicted by Eq. (2.27). So in the case of non-zero anisotropy, the asymptotics of the solution are still have to be improved.

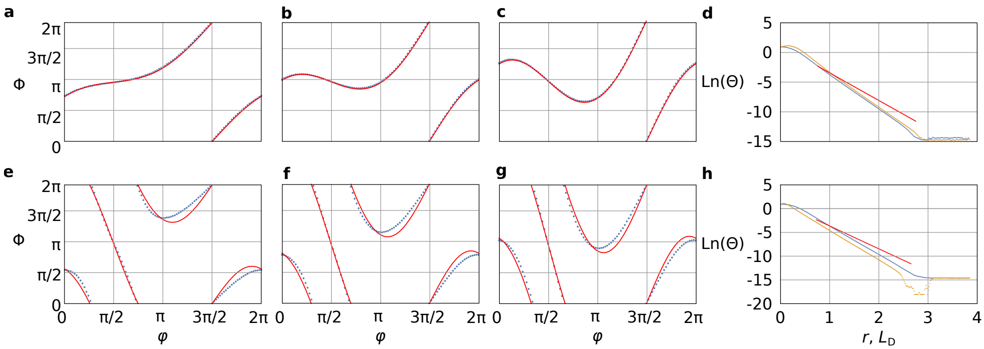

Figure A4 .2: **Asymptotics of the solutions for π-skyrmion and antiskyrmion at $u \neq 0$.** **a-d** and **e-h** corresponding to the π-skyrmion and the antiskyrmion solutions, respectively, obtained for parameters $h = 0.6$, $\theta_\mathrm{h} = 0.35$ and $u = 0.1$. Angular dependencies for $\Phi_\pm$ are shown for fixed radii $r = 1L_\mathrm{D}$ (**a**, **e**), $r = 1.5L_\mathrm{D}$ (**b**, **f**) and $r = 2L_\mathrm{D}$ (**c**, **g**). Functions $\ln\Theta(x, y_0)$ (blue), $\ln\Theta(x_0, y)$ (orange) and the linear function $y = -2\pi r\lambda/L_\mathrm{D} + 1.5$ for the π-skyrmion (antiskyrmion) are shown in **d** (**h**).

A5 Chiral kink ansatz

The most simple ansatz for the 2π-DW with a CK can be constructed as follows. The function of $\Theta = \Theta(x)$ describes the profile of the 2π-DW without a CK as in (3.10) and function Φ depends on y only on the half-plane $x > 0$. By substituting this into the energy functional (1.17) and using (3.16) one obtains,

$$\mathcal{E}_{\mathrm{CK}}^{a} = \int_{-\infty}^{\infty} \left(\frac{I_a}{2} \left(\frac{\mathrm{d}\Phi}{\mathrm{d}y} \right)^2 + 2\pi^2 \left(1 - \sin\Phi\right) \right) \mathrm{d}y, \tag{A5 .1}$$

where $I_a = \int_0^{\infty} \sin^2 \Theta \mathrm{d}x$. I_a can be written as

$$I_a = \frac{k}{2\pi u} - \frac{h}{4\sqrt{2}\pi u^{3/2}} \ln \frac{k + \sqrt{2u}}{k - \sqrt{2u}}. \tag{A5 .2}$$

The minimization of the energy (A5 .1) with respect to $\Phi(y)$ leads to $\Phi(y) = 4\arctan(e^{my}) + \pi/2$ with $m = \sqrt{\frac{2}{I_a}}\pi$ and $\mathcal{E}_{\mathrm{CK}}^{a} = 8\sqrt{2I_a}\pi$. This value for the energy is shown in Fig. A5 .1. In the limiting case $u \to \infty$, formula (A5 .2) allows one to obtain

$$I_a \to \frac{1}{\pi\sqrt{2u}} \left(1 + \frac{h}{2} \frac{\ln u}{u} \right),$$

and the corresponding kink energy decreases as

$$\mathcal{E}_{\mathrm{CK}}^{\mathrm{a}} \to \frac{8\sqrt{2\pi}}{(2u)^{1/4}} \left(1 + \frac{h}{4} \frac{\ln u}{u} \right).$$

The analytic expression for the exact kink energy (see numerical curve on Fig.A5 .1) is unknown but the inequality $\mathcal{E}_{\mathrm{CK}} \leq \mathcal{E}_{\mathrm{CK}}^{\mathrm{a}}$ holds for any ansatz functions. Therefore, the exact kink energy has the upper limit: $\mathcal{E}_{\mathrm{CK}} \leq \frac{8\sqrt{2\pi}}{(2u)^{1/4}} + O\left(\frac{\ln u}{u^{5/4}}\right)$. The fact that the energy of the ansatz goes to 0 at high u suggests that this is a good approximation to the exact kink solution at high u. It fits with the observation that at high u, the contour of the domain wall becomes nearly straight and does not bend much near the location of the CK.

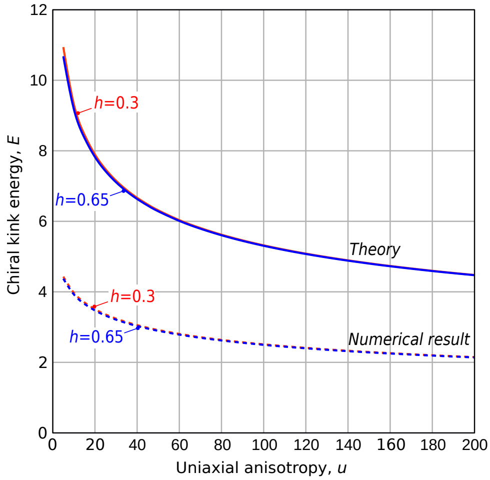

Figure A5 .1: **Energy of the 2π-DW with chiral kink**. The energy dependence for the kink energy $\mathcal{E}_{\mathrm{CK}} = \mathcal{E}_{\mathrm{IS+CK}} - \mathcal{E}_{\mathrm{IS}}$ as a function of anisotropy, u, for two fixed values of magnetic fields $h = 0.3$ and $h = 0.65$. Solid lines correspond to $\mathcal{E}^{a}_{\mathrm{CK}}$, dashed lines are result of numerical calculations with the mesh densities $\Delta l = 256, 512$. This figure has been published in [19].

A6 Saddle points in micromagnetism

Strictly speaking, the LE equations (1.13) can be satisfied not only at the minima of the energy functional but also at the saddle points. However, in practice solving the LE equations numerically is a challenging problem (see **Section** 1.3). When one needs to find the solution at the energy minimum, the most preferable approach is the direct energy minimization. For the search of saddle points, one can reduce the problem to the energy minimization of the functional with an additional constraint to some motion integrals. One of such motion integral is the so-called *magnon number*:

$$\int_\Omega \mathrm{d}\Omega \, (1 - n_\mathrm{z}) \, . \tag{A6 .1}$$

Denoting the fixed value of the integral (A6 .1) as $\mathcal{N}$, one has to minimize the energy functional $\mathcal{E}(\boldsymbol{n})$ with respect of $\boldsymbol{n}$ with an additional constraint $\mathcal{N} = \int_\Omega \mathrm{d}\Omega \, (1 - n_\mathrm{z})$. Numerically, this can done by the penalty function method, for instance. Analytically, such a minimization problem can be formulated using the Lagrange multiplayer, λ:

$$\mathcal{E}^*(\boldsymbol{n}; \mathcal{N}) = \mathcal{E}(\boldsymbol{n}) + \frac{\lambda}{2} \left(\int_\Omega \mathrm{d}\Omega \, (1 - n_\mathrm{z}) - \mathcal{N} \right) . \tag{A6 .2}$$

Applying the Derrick-Hobart scaling approach for stable localized solutions, $\boldsymbol{n}(\boldsymbol{r}) = \boldsymbol{n}(\tilde{\lambda}\boldsymbol{r}')$ with $\tilde{\lambda} = 1$, to the functional (A6 .2), the expression for the Lagrange multiplier can be written as

$$\lambda = -\frac{2\pi}{\mathcal{N}} \int_\Omega \mathrm{d}\Omega \left(\boldsymbol{n} \cdot \nabla \times \boldsymbol{n} + 4\pi u \left(1 - n_\mathrm{z}^2\right) + 4\pi h \, (1 - n_\mathrm{z}) \right) . \tag{A6 .3}$$

Performing the minimization for the functional (A6 .2) and taking into account (A6 .3) for different values $\mathcal{N}$, provide the function $\lambda = \lambda(\mathcal{N})$. The zeros of this function correspond to the extrema of the parent functional $\mathcal{E}(\boldsymbol{n})$. The above approach, however, is not unique. Strictly speaking, any solution satisfying the criterion $\lambda = 0$ corresponds by definition to an extremum of the functional, irrespective of the approach one uses to find this solution. To illustrate this, I check the criterion, $\lambda = 0$, for the saddle points for two representative homotopy transformations: i) between the CD and FM state, and ii) between one Sk with CA and a pair of π-skyrmions. In Fig. A6 .1 **a**, **b**, together with the MEPs I plot the function $\lambda = \mathcal{E}_{\mathrm{DMI}} + 2\mathcal{E}_{\mathrm{anis}} + 2\mathcal{E}_{\mathrm{Zeeman}}$. The minima points on the MEPs satisfy the criterion $\lambda = 0$. The insets in **a** and **b** show the zoomed regions near the saddle points. One can see that the criterion $\lambda = 0$ also holds at saddle points with high accuracy.

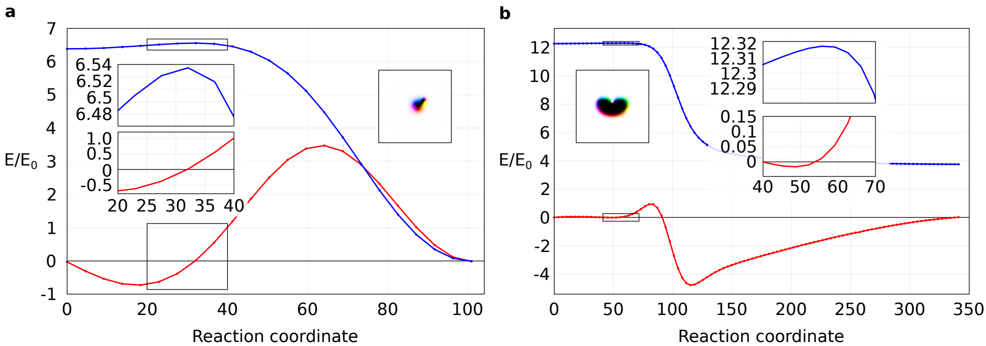

Figure A6 .1: **Energy and λ plots for homotopy paths**. The figures show the energy (blue curve), and λ (red curve) as functions of the reaction coordinate for homotopy transitions of the chiral drop in **a** and π-skyrmion chiral antikink in **b**. Insets show the dependencies near the saddle points. In **a**, the magnetic field $h = 0.65$ and the anisotropy $u = 0$, in **b** the magnetic field $h = 0.01$ and the anisotropy $u = 1.23$.

A7 Velocity space at $\alpha \neq \mathrm{const}$

Using the basic solution of the Thiele equation (5.5), one gets the following relation of the transversal and longitudinal components of the soliton velocity,

$$\frac{v_\perp}{v_\parallel} = -\frac{(\xi-\alpha)Q\Gamma_{\mathrm{xx}}}{Q^2+\alpha\xi\mathrm{det}\hat{\Gamma}+Q(\xi-\alpha)\Gamma_{\mathrm{xy}}}, \tag{A7 .1}$$

from which the expression for α follows

$$\alpha = \frac{Q\xi\left(v_\parallel\Gamma_{\mathrm{xx}}+v_\perp\Gamma_{\mathrm{xy}}\right)+Q^2 v_\perp}{Q\left(v_\parallel\Gamma_{\mathrm{xx}}+v_\perp\Gamma_{\mathrm{xy}}\right)-\xi v_\perp\mathrm{det}\hat{\Gamma}}. \tag{A7 .2}$$

Substituting α in (A7 .2) into $v_\parallel$ or $v_\perp$ in (5.5) leads to the following expression

$$\xi v_\parallel^2\Gamma_{\mathrm{xx}} - \xi v_\parallel\Gamma_{\mathrm{xx}} + 2\xi v_\parallel v_\perp\Gamma_{\mathrm{xy}} + \xi v_\perp^2\Gamma_{\mathrm{yy}} - (Q+\xi\Gamma_{\mathrm{xy}})v_\perp = 0. \tag{A7 .3}$$

It is seen that (A7 .3) is nothing but a general equation for a conic section (ellipse, hyperbola or parabola). To write it in the canonical form, one can introduce the rotated coordinates,

$$v_\parallel = v'_\parallel\cos\zeta - v'_\perp\sin\zeta,\; v_\perp = v'_\parallel\sin\zeta + v'_\perp\cos\zeta, \tag{A7 .4}$$

where angle ζ can be found from (A7 .3) after its substitution into (A7 .4) and requiring the coefficient near $v'_\parallel v'_\perp$ to be zero. That leads to the following equation for ζ

$$(\Gamma_{\mathrm{xx}}-\Gamma_{\mathrm{yy}})\sin 2\zeta = 2\Gamma_{\mathrm{xy}}\cos 2\zeta. \tag{A7 .5}$$

Taking into account (5.10), the solution of (A7 .5) is $\zeta = (\psi + q\pi)/2$ where $q = 0$ or $q = \pm 1$. Then in terms of rotated velocities $(v'_\parallel, v'_\perp)$ equation (A7 .3) can be written as

$$s_+\left(v'_\parallel\right)^2 - \left(s_+\cos\zeta + \frac{2Q}{\xi}\sin\zeta\right)v'_\parallel + s_-\left(v'_\perp\right)^2 + \left(s_-\sin\zeta - \frac{2Q}{\xi}\cos\zeta\right)v'_\perp = 0, \tag{A7 .6}$$

where $s_\pm = \mathrm{Tr}\hat{\Gamma} \pm |S|$. The obvious relation that follows from (5.9) reads $s_+s_- = 4\mathrm{det}\hat{\Gamma}$

and gives the constraint $s_- \geq 0$. Therefore, equation (A7 .6) describes an ellipse ($\det\hat{\Gamma} > 0$) or parabola ($\det\hat{\Gamma} = 0$). If $\det\hat{\Gamma} = 0$ then $s_- = 0$, $s_+ = 2\mathrm{Tr}\hat{\Gamma}$ and (A7 .6) writes

$$\frac{2Q}{\xi}\cos'_{\perp} = 2\mathrm{Tr}\hat{\Gamma}\left(v'_{\parallel}\right)^2 - \left(2\mathrm{Tr}\hat{\Gamma}\cos\zeta + \frac{2Q}{\xi}\sin\zeta\right)v'_{\parallel}. \tag{A7 .7}$$

The general case of the ellipse correspond to $\det\hat{\Gamma} > 0$ from which it follows that $s_- > 0$, and (A7 .6) becomes

$$\frac{\left(v'_{\parallel} - v'_{\parallel 0}\right)^2}{a_+^2} + \frac{\left(v'_{\perp} - v'_{\perp 0}\right)^2}{a_-^2} = 1, \tag{A7 .8}$$

where the ellipse parameters are

$$\begin{aligned} v'_{\parallel 0} &= \frac{1}{2}\cos\zeta + \frac{Q}{\xi s_+}\sin\zeta, \\ v'_{\perp 0} &= -\frac{1}{2}\sin\zeta + \frac{Q}{\xi s_-}\cos\zeta, \\ a_{\pm}^2 = \frac{s_+\left(v'_{\parallel 0}\right)^2 + s_-\left(v'_{\perp 0}\right)^2}{s_{\pm}} &= \frac{1}{4}\left(1 + \frac{Q^2}{\xi^2\det\hat{\Gamma}}\right)\frac{s_+\cos^2\zeta + s_-\sin^2\zeta}{s_{\pm}}. \end{aligned} \tag{A7 .9}$$

The case of high-symmetry Sks ($S = 0$) can be obtained from (A7 .8) letting $\zeta = |S| = 0$, which gives $s_{\pm} = \mathrm{Tr}\hat{\Gamma}$, $v'_{\parallel} = v_{\parallel}$, $v'_{\perp} = v_{\perp}$, $v'_{\parallel 0} = \frac{1}{2}$, $v'_{\perp 0} = \frac{Q}{\xi\mathrm{Tr}\hat{\Gamma}}$, $a_{\pm} = \frac{1}{4} + \frac{Q^2}{\xi^2\mathrm{Tr}\hat{\Gamma}^2}$. Thereby, equation (A7 .8) is equivalent to the circle equation (5.28).

In terms of polar angle $\kappa \in [0, 2\pi]$, the ellipse equation (A7 .8) is equivalent to the following

$$v'_{\parallel} = v'_{\parallel 0} + a_+\cos\kappa,\; v'_{\perp} = v'_{\perp 0} + a_-\sin\kappa. \tag{A7 .10}$$

Now, by switching back to the velocity space $(v_{\parallel}, v_{\perp})$ via (A7 .4) we obtain

$$\begin{aligned} v_{\parallel} &= \frac{1}{2} + \frac{Q}{2\xi}\left(\frac{1}{s_+} - \frac{1}{s_-}\right)\sin 2\zeta + a_+\cos\kappa\cos\zeta - a_-\sin\kappa\sin\zeta, \\ v_{\perp} &= \frac{Q\mathrm{Tr}\hat{\Gamma}}{4\xi\det\hat{\Gamma}} - \frac{Q}{2\xi}\left(\frac{1}{s_+} - \frac{1}{s_-}\right)\cos 2\zeta + a_+\cos\kappa\sin\zeta + a_-\sin\kappa\cos\zeta. \end{aligned} \tag{A7 .11}$$

A8 2π-DW in tilted magnetic field

The equations (6.4) at zero anisotropy, $u = 0$, take the form

$$\begin{aligned} &\Theta'' - 4\pi\Psi' \sin\theta_\mathrm{h} - 4\pi^2 h\Theta = 0, \\ &\Psi'' + 4\pi\Theta' \sin\theta_\mathrm{h} - 4\pi^2 h\Psi = 0. \end{aligned} \tag{A8 .1}$$

By introducing a new complex function, $\zeta = \Theta + i\Psi$, one can rewrite (A8 .1) in the following form

$$\zeta'' + 4\pi i\zeta' \sin\theta_\mathrm{h} - 4\pi^2 h\zeta = 0. \tag{A8 .2}$$

The corresponding characteristic equation

$$\mu^2 + 4\pi i\mu \sin\theta_\mathrm{h} - 4\pi^2 h = 0, \tag{A8 .3}$$

has the following solution $\mu_\pm = -2\pi i \sin\theta_\mathrm{h} \pm 2\pi\sqrt{h - \sin^2\theta_\mathrm{h}}$. Therefore, the solution to (A8 .2) writes as

$$\zeta_\pm = c_\pm \exp\left(\pm 2\pi x\sqrt{h - \sin^2\theta_\mathrm{h}}\right) \exp\left(-2\pi i x \sin\theta_\mathrm{h}\right), \tag{A8 .4}$$

where $c_\pm$ are arbitrary complex constants. By separating the real and imaginary parts of the solution (A8 .4), it can be rewritten as

$$\zeta_\pm = |c_\pm| \exp\left(\pm 2\pi x\sqrt{h - \sin^2\theta_\mathrm{h}}\right) \exp\left(-i(2\pi x \sin\theta_\mathrm{h} + \phi_\pm)\right). \tag{A8 .5}$$

Taking into account the condition that $\zeta \to \infty$ when $|x| \to \infty$ one can write

$$\zeta = c_1 \exp\left(-2\pi|x|\sqrt{h - \sin^2\theta_\mathrm{h}}\right) \exp\left(-i(2\pi x \sin\theta_\mathrm{h} + \phi_\pm)\right), \tag{A8 .6}$$

where $c_1 = |c_+| = |c_-|$ is an arbitrary constant that defines the decay of ζ at $x \to \pm\infty$. After the substitution $\phi_\pm \to \phi_\pm - \pi/2$ and the separation of real and imaginary parts in (A8 .6) one gets the solution (6.5).

A9 Solution for $\Theta(t)$

One can write the solution to equation (7.9) in the integral form,

$$\int_{\Theta_c}^{\Theta(t)} \frac{\mathrm{d}\Theta}{\sin\Theta\,(a_1 - a_2\cos\Theta)} = -\frac{\gamma\alpha t}{1+\alpha^2}. \tag{A9 .1}$$

By denoting $\zeta = \cos\Theta$, (A9 .1) takes an equivalent form

$$\int_{\cos\Theta_c}^{\cos\Theta(t)} \frac{\mathrm{d}\zeta}{(1-\zeta^2)\,(a_1 - a_2\zeta)} = \frac{\gamma\alpha t}{1+\alpha^2}. \tag{A9 .2}$$

depending on the values of a_1 and a_2, the fraction under the integral in (A9 .2) can be presented in a several different forms

$$\frac{1}{(1-\zeta^2)(a_1-a_2\zeta)} = \begin{cases} \dfrac{1}{4a_1}\left(\dfrac{2}{(1\mp\zeta)^2} + \dfrac{1}{1+\zeta} + \dfrac{1}{1-\zeta}\right), a_2 = \pm a_1, a_1 \neq 0, \\ \dfrac{1}{2(a_1^2-a_2^2)}\left(\dfrac{a_1-a_2}{1+\zeta} + \dfrac{a_1+a_2}{1-\zeta} - \dfrac{2a_2^2}{a_1-a_2\zeta}\right), |a_2| \neq |a_1|. \end{cases} \tag{A9 .3}$$

Note, in (A9 .3) I excluded the trivial case $a_1 = a_2 = 0$ following from (7.9) and corresponding to the static solution $\Theta(t) = \Theta_c$. Substituting (A9 .3) into (A9 .2) and performing integration lead to the following solution

$$\frac{2\gamma\alpha t}{1+\alpha^2} = \begin{cases} \dfrac{1}{a_1}\dfrac{1}{\zeta_c \mp 1} - \dfrac{1}{a_1}\dfrac{1}{\zeta \mp 1} + \dfrac{1}{2a_1}\ln\left(\dfrac{1+\zeta}{1+\zeta_c}\dfrac{1-\zeta_c}{1-\zeta}\right), a_2 = \pm a_1, a_1 \neq 0, \\ \dfrac{1}{a_1^2-a_2^2}\ln\left(\left(\dfrac{1+\zeta}{1+\zeta_c}\right)^{a_1-a_2}\left(\dfrac{1-\zeta_c}{1-\zeta}\right)^{a_1+a_2}\left(\dfrac{a_1-a_2\zeta}{a_1-a_2\zeta_c}\right)^{2a_2}\right), |a_2| \neq |a_1|, \end{cases} \tag{A9 .4}$$

where $\zeta_c = \cos\Theta_c$.

A10 Energy minimization with exponential precision

Let me consider the dimensionless micromagnetic energy functional which contains only the exchange and the DMI contributions

$$\mathcal{E}_{\text{ex}} + \mathcal{E}_{\text{DMI}} = \int_{\Omega} \mathrm{d}\Omega \left(\frac{(\nabla \boldsymbol{n})^2}{2} + 2\pi \boldsymbol{n} \cdot \nabla \times \boldsymbol{n} \right), \tag{A10 .1}$$

The corresponding spin lattice Hamiltonian reads

$$\begin{gathered} H_{\text{ex}} + H_{\text{DMI}} + H_0 = \\ -\frac{a}{L_{\mathrm{D}}} \sum_{i,j,k=0}^{N-1} \sum_{q=1}^{M} J_q \left[\boldsymbol{n}_{i,j,k} \cdot \boldsymbol{n}_{i-q,j,k} + \boldsymbol{n}_{i,j,k} \cdot \boldsymbol{n}_{i,j-q,k} + \boldsymbol{n}_{i,j,k} \cdot \boldsymbol{n}_{i,j,k-q} \right] + \\ \frac{2\pi a^2}{L_{\mathrm{D}}^2} \sum_{i,j,k=0}^{N-1} \sum_{q=1}^{M} D_q [(\boldsymbol{n}_{i,j,k} \times \boldsymbol{n}_{i-q,j,k})^x + (\boldsymbol{n}_{i,j,k} \times \boldsymbol{n}_{i,j-q,k})^y + (\boldsymbol{n}_{i,j,k} \times \boldsymbol{n}_{i,j,k-q})^z], \end{gathered} \tag{A10 .2}$$

where $\mathrm{d}x = \mathrm{d}y = \mathrm{d}z = a/L_{\mathrm{D}}$, is the space discretization, N is number of spins in every spatial direction of the cubic sample, each spin interacts with M neighbours, $M < N$. The continuum functional (A10 .1) is the approximate representation of the discrete Hamiltonian (A10 .2) and vice versa. Let me formulate the problem of finding optimal set of coefficients J_q and D_q (for a given M) that minimize the discrepancy between the continuum model (A10 .1) and the discrete model (A10 .2). To find these coefficients, I follow the approach suggested in Refs. [52, 102]. First, I assume that the magnetization, $\boldsymbol{n}$ can be represented by the Fourier transformation

$$\boldsymbol{n}(\boldsymbol{r}) = \tilde{\boldsymbol{n}}(\boldsymbol{k}) e^{i\boldsymbol{k}\cdot\boldsymbol{r}}, \tag{A10 .3}$$

Then, the energy (A10 .2) can be written as

$$
\begin{aligned}
&H_{\text{ex}} + H_{\text{DMI}} + H_0 = \\
&-\frac{a}{L_{\text{D}}} \sum_{\boldsymbol{k}} \sum_{q=1}^{M} J_q \cos(q\boldsymbol{k} \cdot \boldsymbol{a}) \tilde{\boldsymbol{n}}(\boldsymbol{k}) \cdot \tilde{\boldsymbol{n}}(-\boldsymbol{k}) \\
&+\frac{2\pi a^2}{L_{\text{D}}^2} \sum_{i=x,y,z} \sum_{\boldsymbol{k}} \sum_{q=1}^{M} D_q \sin(q\boldsymbol{k} \cdot \boldsymbol{a}) \left[(\tilde{\boldsymbol{n}}(\boldsymbol{k}) \times \tilde{\boldsymbol{n}}(-\boldsymbol{k}))^i \right].
\end{aligned}
\tag{A10 .4}
$$

From the Taylor expansion of (A10 .4) with respect to an argument of sin and cos functions one can get the following equations for coefficients J_q and D_q,

$$
\begin{aligned}
&\sum_{q=1}^{M} q^2 J_q = 1, \sum_{q=1}^{M} q^{2m} J_q = 0, \forall m = \overline{2, M}, \\
&\sum_{q=1}^{M} q D_q = 1, \sum_{q=1}^{M} q^{2m-1} D_q = 0, \forall m = \overline{2, M}.
\end{aligned}
\tag{A10 .5}
$$

As it follows from (A10 .5) at $M = 1$ one has $J_1 = D_1 = 1$, at $M = 2$ then $J_1 = D_1 = \frac{4}{3}$ and $D_2 = 2J_2 = -\frac{1}{6}$. Taking larger number of neighboring spins, M, one gets a better approximation of the micromagnetic functional (A10 .1). The maximal value $M = N - 1$ is the best approximation that can be obtained. The provided below Wolfram Mathematica script calculates these coefficients.

```
Ns = 3;(*Number of spins in one direction*)
Aj = Table[j^(2 i), {i, 1, Ns - 1}, {j, 1, Ns - 1}];
Ad = Table[j^(2 i - 1), {i, 1, Ns - 1}, {j, 1, Ns - 1}];
b = Flatten[{{1}, ConstantArray[0, Ns - 2]} , 1];
(*List of exchange coefficients*)
Jcoefficients = LinearSolve[Aj, b]
(*List of DMI coefficients*)
DMIcoefficients = LinearSolve[Ad, b]
```

List of publications

[1] **Vladyslav M. Kuchkin** and Nikolai S. Kiselev, Turning a chiral skyrmion inside out, Phys. Rev. B **101**, 064408 (2020).

[2] **Vladyslav M. Kuchkin**, Bruno Barton-Singer, Filipp N. Rybakov, Stefan Blügel, Bernd J. Schroers, and Nikolai S. Kiselev, Magnetic skyrmions, chiral kinks, and holomorphic functions, Phys. Rev. B **102**, 144422 (2020).

[3] **Vladyslav M. Kuchkin**, Ksenia Chichay, Bruno Barton-Singer, Filipp N. Rybakov, Stefan Blügel, Bernd J. Schroers, and Nikolai S. Kiselev, Geometry and symmetry in skyrmion dynamics, Phys. Rev. B **104**, 165116 (2021).

[4] Fengshan Zheng, Nikolai S. Kiselev, Luyan Yang, **Vladyslav M. Kuchkin**, Filipp N. Rybakov, Stefan Blügel, Rafal E. Dunin-Borkowski, Skyrmion–antiskyrmion pair creation and annihilation in a cubic chiral magnet, Nat. Phys. **18**, 863–868 (2022).

[5] **Vladyslav M. Kuchkin**, Pavel F. Bessarab, Nikolai S. Kiselev, Thermal generation of droplet soliton in chiral magnet, Phys. Rev. B **105**, 184403 (2022).

[6] Andrii S. Savchenko, **Vladyslav M. Kuchkin**, Filipp N. Rybakov, Stefan Blügel and Nikolai S. Kiselev, Chiral standing spin waves in skyrmion lattice, APL Materials **10**, 071111 (2022).

[7] **Vladyslav M. Kuchkin** and Nikolai S. Kiselev, Homotopy transitions and 3D magnetic solitons, APL Materials **10**, 071102 (2022).

Band / Volume 75
Development of Electrochemical Aptasensors for the Highly Sensitive, Selective, and Discriminatory Detection of Malaria Biomarkers
G. Figueroa Miranda (2021), XI, 135 pp
ISBN: 978-3-95806-589-5

Band / Volume 76
Nanostraw- Nanocavity MEAs as a new tool for long-term and high sensitive recording of neuronal signals
P. Shokoohimehr (2021), xi, 136 pp
ISBN: 978-3-95806-593-2

Band / Volume 77
Surface plasmon-enhanced molecular switching for optoelectronic applications
B. Lenyk (2021), x, 129 pp
ISBN: 978-3-95806-595-6

Band / Volume 78
Engineering neuronal networks in vitro: From single cells to population connectivity
I. Tihaa (2021), viii, 242 pp
ISBN: 978-3-95806-597-0

Band / Volume 79
Spectromicroscopic investigation of local redox processes in resistive switching transition metal oxides
T. Heisig (2022), vi, 186 pp
ISBN: 978-3-95806-609-0

Band / Volume 80
Integrated Control Electronics for Qubits at Ultra Low TemperatureD. Nielinger (2022), xviii, 94, xix-xxvi
ISBN: 978-3-95806-631-1

Band / Volume 81
Higher-order correlation analysis in massively parallel recordings in behaving monkey
A. Stella (2022), xiv, 184 pp
ISBN: 978-3-95806-640-3

Band / Volume 82
Denoising with Quantum Machine Learning
J. Pazem (2022), 106 pp
ISBN: 978-3-95806-641-0

Band / Volume 83
Hybrid hydrogels promote physiological functionality of long-term cultured primary neuronal cells in vitro
C. Meeßen (2022), x, 120 pp
ISBN: 978-3-95806-643-4

Band / Volume 84
Surface states and Fermi-level pinning on non-polar binary and ternary (Al,Ga)N surfaces
L. Freter (2022), 137 pp
ISBN: 978-3-95806-644-1

Band / Volume 85
Dynamical and statistical structure of spatially organized neuronal networks
M. Layer (2022), xiii, 167 pp
ISBN: 978-3-95806-651-9

Band / Volume 86
Persistent firing and oscillations in the septo-hippocampal system and their relation to locomotion
K. Korvasová (2022), 111 pp
ISBN: 978-3-95806-654-0

Band / Volume 87
Sol-Gel-Synthese, Tintenstrahldruck und Blitzlampentemperung von Tantaloxid-Dünnschichten zur pH-Messung
C. D. Beale (2022), xlix, 339 pp
ISBN: 978-3-95806-656-4

Band / Volume 88
Diversity of chiral magnetic solitons
V. Kuchkin (2022), xiv, 155 pp
ISBN: 978-3-95806-665-6

Weitere ***Schriften des Verlags im Forschungszentrum Jülich*** unter
http://wwwzb1.fz-juelich.de/verlagextern1/index.asp

Information
Band / Volume 88
ISBN 978-3-95806-665-6

Mitglied der Helmholtz-Gemeinschaft

JÜLICH
Forschungszentrum